Observing Ocean–Atmosphere Interactions from an AutoNaut Uncrewed Surface Vessel.

Elizabeth Adriana Siddle

A thesis submitted to the School of Environmental Sciences at the University of East Anglia in partial fulfilment of the requirements for the degree of Doctor of Philosophy.

University of East Anglia
School of Environmental Sciences
November 2025

Abstract

A novel Uncrewed Surface Vessel (*Caravela* USV) was successfully tested in its capacity as a platform to measure ocean and atmosphere bulk variables for calculating air-sea heat fluxes. These heat fluxes were then calculated using COARE 3.5 and used to investigate an ocean mixed layer heat budget in a 10 x 10 km square in the Northwestern Tropical Atlantic, as part of the EUREC^{4}A campaign. An optimal estimate of net surface heat flux for the region was made using a combination of observed shortwave, latent and sensible heat fluxes from observed surface properties and ERA5 winds, and ERA5 longwave flux. Compared with this optimal estimate, ERA5 net surface heat flux was biased with $30\,\mathrm{W\,m^{-2}}$ excess heat loss to the atmosphere. I find that cloud cover representation, humidity and sea surface temperature were contributors to this bias. Closure of the ocean mixed layer heat budget was found to be better using surface heat fluxes alone (residual $0.06\,^{\circ}\mathrm{C}$) than when estimates of horizontal advection and entrainment were included (residual $-0.18\,^{\circ}\mathrm{C}$) over the nine whole days spent in the study site, primarily due to uncertainties in the calculations of advection and entrainment. At hourly or daily scales, the effects of horizontal advection become more important to consider. Entrainment should not be neglected in this region at any time scale, as it was responsible for additional heat gain in to the mixed layer due to the presence of a temperature inversion in the barrier layer. The successful use of *Caravela* in this study demonstrates the effectiveness of USVs for surface flux measurement and heat budget closure. Better quantification of flux product biases at regional scales is evidently achievable with USV technology, with implications for improved climate modelling and weather prediction.

Access Condition and Agreement

Each deposit in UEA Digital Repository is protected by copyright and other intellectual property rights, and duplication or sale of all or part of any of the Data Collections is not permitted, except that material may be duplicated by you for your research use or for educational purposes in electronic or print form. You must obtain permission from the copyright holder, usually the author, for any other use. Exceptions only apply where a deposit may be explicitly provided under a stated licence, such as a Creative Commons licence or Open Government licence.

Electronic or print copies may not be offered, whether for sale or otherwise to anyone, unless explicitly stated under a Creative Commons or Open Government license. Unauthorised reproduction, editing or reformatting for resale purposes is explicitly prohibited (except where approved by the copyright holder themselves) and UEA reserves the right to take immediate ‘take down’ action on behalf of the copyright and/or rights holder if this Access condition of the UEA Digital Repository is breached. Any material in this database has been supplied on the understanding that it is copyright material and that no quotation from the material may be published without proper acknowledgement.

Contents

List of Figures

List of Tables

Acknowledgements

This research has received funding to the COMPASS project from the European Research Council under the European Union's Horizon 2020 research and innovation programme (grant agreement no 741120). This work was supported by the Natural Environment Research Council and the ARIES Doctoral Training Partnership [grant number NE/S007334/1]. This work was further supported by a CASE partnership with AutoNaut Ltd. We acknowledge the EUREC^{4}A project and its respective funding, the M161 cruise of the *R/V Meteor* and the crew and scientists involved in this cruise, without which this research would not be possible. We also thank the Barbados Coastguard and Caribbean Institute for Meteorology and Hydrology for facilitating deployment and recovery of Caravela. Thanks to Steve Dorling, WeatherQuest Ltd for supplying Dunstaffnage Weather station data (Dorling, 2019). Thanks to Estelle Dumont, Scottish Association for Marine Science for supplying the Castaway and Data used in chapter 2 (Dumont, 2019). Thank you to SAMS for facilitating Seaglider and Caravela trials. We acknowledge the use of the COARE 3.5 algorithm (Fairall et al., 1996*b*, 2003; Edson et al., 2013). We acknowledge the use of imagery from the Worldview Snapshots application (https://wvs.earthdata.nasa.gov), part of the Earth Science Data and Information System (ESDIS). We acknowledge the use of BCO data via the Aeris data repository for EUREC^{4}A (Jansen et al., 2021). We also acknowledge the use of Meteorology data collected on the *R/V Meteor* in EUREC^{4}A , supplied by private communication with Imke Schirmacher and Ingo Lange. Thanks to Imke Schirmacher for processing the *R/V Meteor* met station data, Ingo Lange for the pre-processing and to both for installation of the instruments. The data used in this publication was gathered in the EUREC^{4}A field campaign and is made available through the Barbados Cloud Observatory, University of Cologne, University of Hamburg and the Max Plank Institute for Meteorology. EUREC^{4}A is funded with support of the European Research Council (ERC), the Max Planck Society (MPG), the German Research Foundation (DFG), the German Meteorological Weather Service (DWD) and the German

Aerospace Center (DLR). ERA5 data, Hersbach, H. et al., (2018) was downloaded from the Copernicus Climate Change Service (2023). The results contain modified Copernicus Climate Change Service information 2020. Neither the European Commission nor ECMWF is responsible for any use that may be made of the Copernicus information or data it contains. (Hersbach et al., 2018, 2020; Copernicus Climate Change Service, 2023). This study has been conducted using E.U. Copernicus Marine Service Information; GLORYS12V1 https://doi.org/10.48670/moi-00021 (E.U. Copernicus Marine Service Information (CMEMS), 2023).

Writing the personal acknowledgements section of this thesis felt almost as scary as the thesis itself, not because I disliked it, but because finding the right words to thank those below was a surprisingly difficult task.

First to Karen Heywood and Ben Webber, for taking a chance on a keen student with zero knowledge of oceanography. You have both been an incredible support throughout the last 6 years of academic and personal challenges, of which there were too many to keep count. I honestly don't think I would have been able to finish this PhD were it not for you patience and support, for that I cannot thank you enough. Academically, thank you the last minute proof reading, from the scribbled diagrams to detailed calculations, for explaining the simple topics when I lose track to discussing the niche and complex. Your input into this work has made this research possible, this thesis could not and would not have happened without you.

Thanks go to the AutoNaut team for their expertise and assistance in the work of this thesis. In particular, thanks to Peter Bromley, Sarah Heasman and Terry Hibben who took supervisory responsibilities in this work, for each taking the time for technical discussion and for their feedback on this work.

Thanks to Liam Fernand for his assistance in the role of independant research impact adviser within this project. A further thank you for the coffee's and career advice, which helped me to look beyond academia.

To Simon Josey and Adrian Matthews, the examiners of this work. A genuine thank you for making the viva such an interesting, relaxed and enjoyable experience and for your great suggestions to improve this thesis.

To the UEA glider group members past and present. Thank you for taking the time to teach me how work with this amazing technology, for involving me in so many opportunities and deployments, for helping me to pilot and being a generally wonderful group of people to hang

out with.

I cannot thank the Glider group without highlighting the major role Gareth Lee has played in these last 6 years. Thank you for taking the time to teach me, from the basics to the complicated bits. For the morning coffees and for letting me hide from my thesis in the workshop. It has been a pleasure and a privilege to learn from you. I found my direction in science because of your guidance, you gave me the confidence to step off the traditional academic career path and follow what I loved. It's because of your influence that my next stage in life is as a 'Glider Engineer' and that I will never forget.

To Callum Rollo for your patience, friendship, scientific and technical teachings. For taking me under your wing when I first showed up at UEA, guiding me through my first research cruise, teaching me Python, and helping me through many academic hurdles. For every bike ride, every paddle, your great tolerance to my horrible attempts at playing chess and a friendship which I hope will last a lifetime, saying thank you doesn't feel like enough. May we continue to cross paths in the world of oceanography, hopefully next time it wont be because I bricked some software again...

I want to take time to thank James Lee for his independent mentorship, support, friendship and encouragement long after I left the field of atmospheric chemistry. For every evening spent discussing academia over a pint, thank you.

To Dan Skinner, Eliza Karlowska and Jack Mustafa, the original 'Tropical Hour Squad', thank you for you unwavering friendship and support. To you and the honorary members Becky Shaw and Meg Childs, I couldn't have asked for a more accepting and supportive group to grow with these past few years. May we always find a way to regroup and occasionally discuss the MJO...

To many other PhD student friends and office mates over the years, this experience would not have been the same without our laughs, smiles, dances and rants. To those still in office 3.16, I wish you all the best in the rest of your PhD journeys. In case of emergency, I have left one last jar of jelly beans on my desk.

To my family and friends long past, thank you for coming on this journey alongside me. Its been most turbulent and unexpected, but with your support, I made it in the end. And specifically to my parents and brother, for every long drive up and down the country, every food package and dog walk, every home cooked meal and the patience of watching a 4 year PhD turn into nearly 6, thank you.

To Andreas, for every late evening spent with me writing, for every meal and cup of tea made, for every tear shed on your shoulder (and there were many), thank you for reminding me of what's most important in our little lives.

Lastly, to the little girl who liked science, you made it further than you ever could have dreamed.

There are no stupid questions.

1

Introduction

Synopsis

In this introduction I provide an overview of our region of interest - the northwestern tropical Atlantic, providing context to the importance of this region in improving SST products. General ocean processes pertaining to the ocean mixed layer heat budget are explained and the ocean mixed layer heat budget itself defined. I discuss the EUREC^{4}A campaign from which the data in this thesis were obtained and describe mixed layer heat budget studies relevant to the latter parts of this thesis. There are limited studies providing 'ground-truth' observations on short timescales in the tropics. I focus the work of this thesis on this gap in observational comparison, looking for biases in air-sea fluxes in the region with the collected observations and investigating the mixed layer heat budget to better understand SST evolution, which is not accurately represented in models and reanalysis on small spatial scales. The technology used to address this observational gap is an uncrewed surface vessel, which in itself is an active area of development in terms of ocean observing strategy. This chapter outlines gaps in knowledge in flux product parameterisations and the need to supply in situ measurements for SST validation, and it is within this research gap that I focus the work of this thesis.

1.1 Motivation

The uppermost layer at the ocean surface is known as the ocean mixed layer and is important as it controls the relationship between the sea surface temperature (SST) and the atmosphere through air-sea interactions (Treguier et al., 2023). Air-sea interactions encompass a wide breadth of processes including the exchange of heat, momentum, moisture and gases. Here I focus mainly on the exchange of heat.

SSTs feed back into the atmospheric system as drivers of global scale processes and teleconnections through ocean heating and cooling of the atmosphere. For example the El Niño southern oscillation (ENSO) (Neelin et al., 1998) is a global climate variation related to conditions in the tropical Pacific. Every 2-7 years, ENSO transitions between El Niño, La Niña and a neutral phase. El Niño events exhibit reduced eastern boundary upwelling with surface SST warming and La Niña is associated with eastern Pacific SST cooling and stronger westward winds. As a global scale phenomenon, ENSO is able to excite other modes of variability in the Indian and Atlantic oceans (Cai et al., 2019). However this is not a one way system, variation in the Indian ocean SSTs can accelerate the transition from El Niño to La Niña and SSTs in the Atlantic oceans can affect the spatial structure, strength and evolution of ENSO (Cai et al., 2019). Another phenomenon affected by tropical SSTs and fluxes is the Madden-Julian Oscillation (Madden and Julian, 1971; Flatau et al., 1997; Matthews, 2004; Karlowska et al., 2024). High frequency, small scale interactions are believed to be a part of complex climate feedback mechanisms which are potentially important in climate systems at much larger spatial and temporal scales than their own (Bernie et al., 2007; Hu et al., 2015; Seo et al., 2023).

Across the globe, tropical regions suffer from poor sampling of humidity and air temperature near the surface as satellites cannot resolve this information with high vertical resolution (Foltz et al., 2025). This is further difficult to rectify because the in-situ observations are still limited for validating satellites and sparse in their own right. It is thought that many of the relationships between satellite and in situ measurements are dependent on localised and complex dynamics, such that it is difficult to correct humidity and air temperature remote observations and results in uncertainty and biases in derived net heat fluxes in the tropics (Yu, 2019; Cronin et al., 2019; Gentemann et al., 2021; Foltz et al., 2025).

To understand the importance of air-sea interactions, global flux products with quantified biases are needed, alongside high spatial and temporal resolution observations of essential ocean and climate variables. Quantifying and improving upon flux product biases allows for the development of better flux algorithms, which has wider impacts on the improvement of future climate prediction and extreme weather event predictions including tropical cyclones and hurricanes (Black et al., 2007; Grist et al., 2010; Tilinina et al., 2018; Aristizábal Vargas et al., 2024; Reshma and Singh, 2024). Ocean observations have directly improved extreme weather event prediction (Mainelli et al., 2008; Dong et al., 2017), such that there are already direct socioeconomic benefits of improving ocean observation coverage.

1.2 Air-sea interactions

Within the context of this thesis, air-sea interactions describe the fluxes of heat between the atmosphere and the ocean. There is currently only one method of measuring air-sea heat fluxes in situ and this is the eddy correlation method (Crawford et al., 1993; Edson et al., 1998). Whilst this method is able to provide in situ turbulent fluxes (turbulent fluxes being latent and sensible heat fluxes which are driven by the turbulent motion of air), it is a complicated and costly method. Flow distortion is a significant issue, such that specialist buoys or vessels are needed to minimise this effect (Yu, 2019). Also there is the unavoidable issue at sea of platform motion which requires high frequency sampling and rigorous quality control to correct for (Edson et al., 1998). Unfortunately the specialist nature of the set-up required for eddy correlation measurements means that it is not viable to provide global coverage of air-sea turbulent fluxes (Landwehr et al., 2015). Most researchers instead turn to a parameterisation to represent air-sea heat fluxes, in the form of the bulk flux approach. The advantage of the bulk flux method is the wide availability of the essential ocean and climate variables which are needed to run a bulk flux algorithm, through satellite remote sensing, ship observations, autonomous technologies and numerical weather prediction models (Yu, 2019). The bulk approach is fed with values of near-surface air temperature, SST or ocean skin temperature depending on formulation, humidity, wind velocity and surface currents which all can be modelled or observed (Cronin et al., 2019). If available, additional observations of wave state can be input to improve bulk flux calculation (Edson et al., 2013), but this is not necessary to run a bulk flux algorithm.

Bulk surface turbulent heat fluxes can be represented according to the following equations

$$Q_{sen} = \rho_{air} c_p C_H S (T_s - T_{air}) \tag{1.2.1}$$

$$Q_{lat} = \rho_{air} L_v C_E S (q_s - q_{air}) \tag{1.2.2}$$

where Q_{sen} represents the sensible heat flux and Q_{lat} represents the latent heat flux. Of the variables used to compute these quantities, ρ_{air} is the density of air; c_p is the specific heat capacity; C_H is the sensible heat transfer coefficient; S the wind speed with respect to the ocean surface current; T_s the sea surface temperature; T_{air} the air temperature; L_v is the latent heat of evaporation, C_E is the latent heat transfer coefficient, q_{air} the specific humidity and q_s the saturation humidity at the SST.

The inclusion of parameterised transfer coefficients in bulk flux algorithms relies on the use of Monin-Obukhov similarity theory (Monin and Obukhov, 1954), which accounts for the effects of atmospheric stability on fluxes. Transfer coefficients also account for ocean surface roughness (Prakash et al., 2019). Transfer coefficients in bulk flux algorithms are obtained in one of two ways. The first is by using eddy correlation measurements and ocean variable measurements to directly derive and then parameterise said coefficients in bulk flux algorithms (Cronin et al., 2019; Fairall et al., 1996*b*, 2003; Edson et al., 2013). The second way that transfer coefficients can be obtained is by empirically derived flux profiles (Yu, 2019; Liu et al., 1979).

There are two additional flux components important in calculating a net heat flux, the net shortwave Q_{sw} and net longwave Q_{lw} flux. Below I show the formulations described by Cronin et al. (2019) and Yu (2019). Q_{sw} is the difference between downwelling and upwelling shortwave radiation at the surface. The downwelling shortwave radiation includes direct and diffuse solar radiation reaching a horizontal plane at the Earths surface. The upwelling shortwave radiation is the component of that radiation reflected by the Earth's surface. The equation takes the form

$$Q_{sw} = SW \downarrow (1 - \alpha) \tag{1.2.3}$$

where $SW \downarrow$ is the downwelling shortwave radiation and α the albedo representing surface reflection.

Q_{lw} is the difference between downwelling and upwelling longwave radiation at the surface. The downwelling longwave radiation includes thermal radiation from the atmosphere and clouds reaching the surface. The upwelling long-wave radiation includes an estimation of thermal radiation is that emitted by the ocean and some reflected downwelling radiation.

$$Q_{lw} = \epsilon \sigma_{SB} T_{skin}^4 + (1 - \epsilon) LW \downarrow - LW \downarrow \tag{1.2.4}$$

where $\epsilon = 0.97$ represents emissivity and is assumed equal to absorptivity, σ_{SB} is the Stefan-Boltzmann constant, T_{skin} the ocean skin temperature and $LW \downarrow$ the downwelling longwave radiation. The ocean skin temperature is the temperature measured at a depth of approximately 10 - 20 μm and is cooler than the bulk SST due to heat loss from the ocean surface to the atmosphere (Fairall et al., 1996*b*; Yan et al., 2023). In bulk flux algorithms,

T_{skin} is often determined from input SSTs and used for calculation of more accurate turbulent fluxes (Fairall et al., 1996*b*).

The net heat flux term Q_0 between the atmosphere and ocean is the sum of the above four components, accounting for the difference in direction for Q_{sw} (positive downwards) and Q_{lw}, Q_{sen} and Q_{lat} (all positive upwards in the forms given above).

$$Q_0 = Q_{sw} - Q_{lw} - Q_{sen} - Q_{lat} \tag{1.2.5}$$

1.2.1 Flux Products

Various methods of parameterisation of the bulk fluxes exist, which result in a range of global flux products with differing values for global ocean mean energy budget (visible in 1.1). This figure shows global flux product budget closure between $-20\,\mathrm{W\,m^{-2}}$ and $25\,\mathrm{m^2}$ across 12 flux products, highlighting that many of the products are unable to fully close the energy budget in their present forms. Places where flux products differ in their parameterisations include the transfer coefficients, for example in the surface roughness relationships via the Charnock parameter (Charnock, 1955). Some flux parameterisations include cool skin and warm layer effects (Yan et al., 2023), which over 70 days in the tropics were found to reduce heat loss to the atmosphere by $11\,\mathrm{W\,m^{-2}}$ and increase heat loss by $4\,\mathrm{W\,m^{-2}}$ respectively (Fairall et al., 1996*a*). Some products account for effects of cloud cover and cloud types on radiative fluxes more than others (Clark et al., 1974; Josey et al., 1997, 1999; Berry and Kent, 2009). Each flux product also has its own biases in wind speed, temperature, humidity and cloud cover, all of which contribute additionally to biases. Often the bulk variables fed into flux products come with different uncertainties based upon their sources, which causes further divergence in flux product results. Generally, reanalysis products each develop their own bulk parameterisation schemes (Dee et al., 2011; Hersbach et al., 2020; Saha et al., 2021). Satellite derived flux products are based upon the COARE algorithm (Fairall et al., 1996*b*, 2003; Edson et al., 2013), which was developed following the tropical ocean global atmosphere coupled ocean atmosphere response experiment (TOGA COARE). Meanwhile, the NOC flux product (Josey et al., 1999; Berry and Kent, 2011) based on ship observations uses the formulae of Payne (1972); Clark et al. (1974); Reed (1977); Smith (1988).

A 'correct' flux product would have an annual global integration (a budget) of almost 0, to obey the conservation of energy between heat flux gains and losses,assuming no net ocean heating. Many flux products cover the global ice free ocean rather than the entire ocean; in

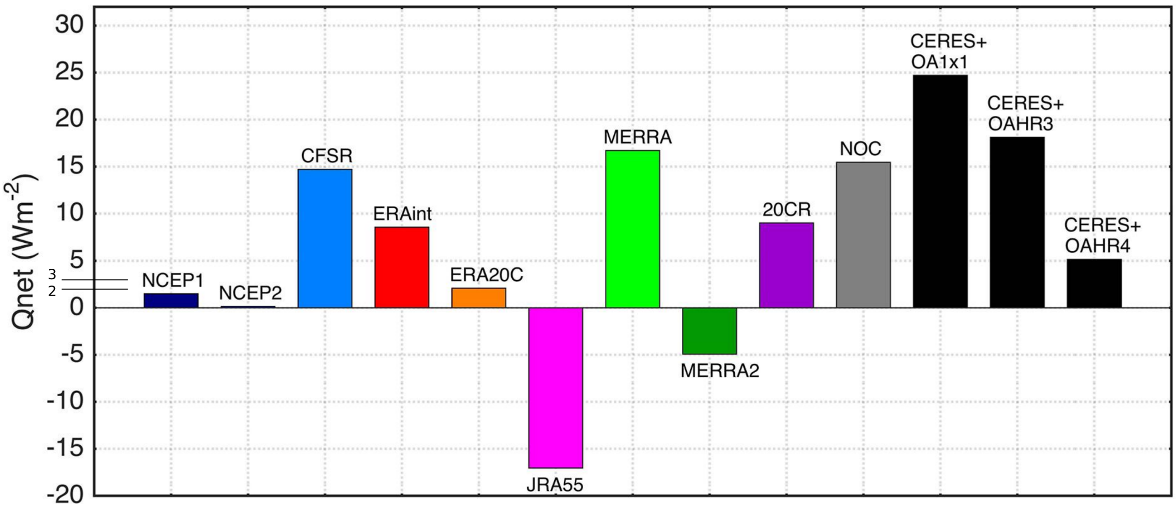

Figure 1.1: Global ocean mean energy budget of 12 flux products. Abbreviations: 20CR, Twentieth Century Reanalysis; CERES, Clouds and the Earth's Radiant Energy System–Energy Balanced and Filled; CFSR, Climate Forecast System Reanalysis; ERA-20C, European Centre for Medium Range Weather Forecasts Twentieth Century; ERA-Interim, European Centre for Medium Range Weather Forecasts Interim; GPCP, Global Precipitation Climatology Project; JRA-55, Japanese 55-Year Reanalysis; MERRA, Modern-Era Retrospective Analysis for Research and Applications; NCEP, National centre for Environmental Prediction; NOC, National Oceanography Centre; OAFlux-1 × 1, 1 °gridded Objectively Analyzed Air–Sea Fluxes; OAFlux-HR3 and -HR4, high resolution (0.25 °gridded) Objectively Analyzed Air–Sea Fluxes analysis computed from Coupled Ocean–Atmosphere Response Experiment (COARE) version 3 and version 4, respectively. The 2 - 3 $\mathrm{W\,m^{-2}}$ closure goal of a global ice-free surface budget is explicitly noted on the axis. This figure was adapted from Cronin et al. (2019).

this case the global integral of net surface flux should be 2 - 3 $\mathrm{W\,m^{-2}}$ if these bulk parameterisations were correct in their assumptions (Bengtsson et al., 2013; Yu, 2019). Many flux products do not close the budget and so there must be biases within each flux product. Figure 1.1 shows the global net heat budget closure for 12 flux products, demonstrating significant variation in closure between different products. NCEP2 has the best global ocean mean energy budget closure of the 12 flux products, with almost total budget closure. However Cronin et al. (2019) and Yu (2019) note none of these 12 products close the budget within the expected threshold whilst also achieving a 1:1 balance of turbulent to radiative fluxes . This figure highlights the substantial effect of different parameterisations on the budget closure, which further highlights the need for more in-situ observations and validation experiments to improve these products budget closure.

The air-sea heat flux scientific community set out the aim for global flux resolution, which is a 10 km, 3 hourly heat flux over the global ice-free ocean with random uncertainty of 15 $\mathrm{W\,m^{-2}}$ and a bias of less than 5 $\mathrm{W\,m^{-2}}$ at 1 day time scales (Cronin et al., 2019). To do this, significant developments in ocean and atmosphere observing systems are needed. Achieving these targets is only realistic with satellite coverage, but for this satellite coverage to be accurately recording the essential flux variables, it must be paired with an in situ observing network for reference measurements (Cronin et al., 2023). The need for bias quantification and improved observations are the motivation for the work contained within this thesis.

1.3 Mixed layer heat budget

1.3.1 Equations and Assumptions

Air-sea interactions cause heat gain and loss into the ocean, which affects the ocean surface mixed layer. The heat content exchange within this layer plays a significant role in controlling the SST. To understand the temporal evolution of SSTs, a mixed layer heat budget is often used to quantify the dominant processes contributing to heat exchanges in the mixed layer (Stevenson and Niiler, 1983), where understanding these processes feeds into better predicting climate and weather systems. Additional benefits are mapping SSTs helps decipher the role of temperature stratification in biological productivity, and temperature on atmospheric interactions and ocean dynamics. Many studies use mixed layer heat budgets to investigate heat exchange on a variety of timescales, from changes over a short observation period (Delnore, 1972; Godfrey and Lindstrom, 1989; Vijith et al., 2020; du Plessis et al., 2022) to intra-seasonal (McPhaden, 2002; Halkides et al., 2015), seasonal (Foltz et al., 2013; Roberts et al., 2017) and annual (Niiler and Stevenson, 1982; Foltz and McPhaden, 2006) variation.

The ocean mixed layer heat budget consists of a three dimensional balance of multiple processes, which affect the local SSTs. The mixed layer heat budget equation can be written as

$$h\frac{\partial T_a}{\partial t} + h\boldsymbol{v_a}\cdot\nabla T_a + \nabla\cdot\left(\int_{-h}^{0}\hat{v}\hat{T}dz\right) + (T_a - T_{-h})\times\left(\frac{\partial h}{\partial t} + \boldsymbol{v_{-h}}\cdot\nabla h + w_{-h}\right) = \frac{Q_0 - q_{-h}}{\rho c_p} \tag{1.3.1}$$

where h is depth, T the ocean temperature, v is horizontal velocity, subscript a denotes the average value between depth h and the surface, w is the vertical velocity, $\nabla \equiv (\frac{\partial}{\partial x}, \frac{\partial}{\partial y})$, Q_0 is the net surface heat flux, q_{-h} diffuse heat flux at depth h, ρ the sea water density, c_p the specific heat capacity of seawater, $\hat{v}$ is deviation from the vertically-averaged horizontal velocity where $v = v_a + \hat{v}$ and $\hat{T}$ the deviation from the vertically-averaged temperature $T = T_a + \hat{T}$ (Stevenson and Niiler, 1983; Moisan and Niiler, 1998). In the above equation, the terms from left to right represent the local storage of heat, horizontal advection, vertical temperature and velocity covariance, entrainment and the air-sea net heat flux adjusted for penetrative shortwave radiation and turbulent mixing at the base of the mixed layer respectively (Foltz et al., 2003).

Building on eq 1.3.1, the mixing terms are explicitly resolved in the form of the equation of Wells et al. (2009) based on the work of Stevenson and Niiler (1983), with derivation available in Hadfield (2007).

$$h\frac{\partial T_a}{\partial t} + h\boldsymbol{v_a} \cdot \nabla T_a + \nabla \int_{-h}^{0} \hat{v}\hat{T}dz + (T_a - T_{-h}) \times \left(\frac{\partial h}{\partial t} + \boldsymbol{v_{-h}} \cdot \nabla h + w_{-h}\right) + hk_{x,y} \cdot \nabla^2 T_a + k_z\frac{\partial^2 T}{\partial z^2} = \frac{Q_0 - Q_{pen}}{\rho c_p} \qquad (1.3.2)$$

Here the horizontal diffusion of temperature $hk_{x,y} \cdot \nabla^2 T_a$ and vertical diffusion of temperature $k_z\frac{\partial^2 T}{\partial z^2}$ are defined, where $k_{x,y}$ and k_z are the horizontal and vertical diffusion coefficients respectively. The correction to the net heat flux is reduced to Q_{pen}, which represents the penetrative shortwave heat flux. Stevenson and Niiler (1983) and Moisan and Niiler (1998) take the approach in which h is the depth of a chosen isotherm, in order to assess low frequency SST variation (Stevenson and Niiler, 1983). The limitations of this approach fall in both selecting an appropriate isotherm and the use of an isotherm deeper than the mixed layer depth increasing the degree of error in the heat content over depth h (Hadfield, 2007). An alternative approach identifies the mixed layer depth as depth h, (Hadfield et al., 2007; Foltz and McPhaden, 2005). Alternatively, to simplify the equation, h can be chosen to be the depth of the isotherm that has minimal heat transfer across it, where h lies deeper than the main thermocline. In this circumstance, q_h is then negligible and the entrainment rate small as the bottom surface is treated as a material surface (Moisan and Niiler, 1998).

For clarity, the form of the budget equation which is used for the work within this thesis is

$$\frac{\partial T_a}{\partial t} = -(\boldsymbol{v_a} \cdot \nabla T_a) - \frac{(T_a - T_{-h})}{h} \times \left(\frac{\partial h}{\partial t} + \boldsymbol{v_{-h}} \cdot \nabla h + w_{-h}\right) + \frac{Q_0 - Q_{pen}}{\rho c_p h} \qquad (1.3.3)$$

where the terms excluded in analysis in this thesis have been removed. The justifications for these exclusions are given in chapters 4 and 5. Within this thesis, I take h to be the mixed layer depth.

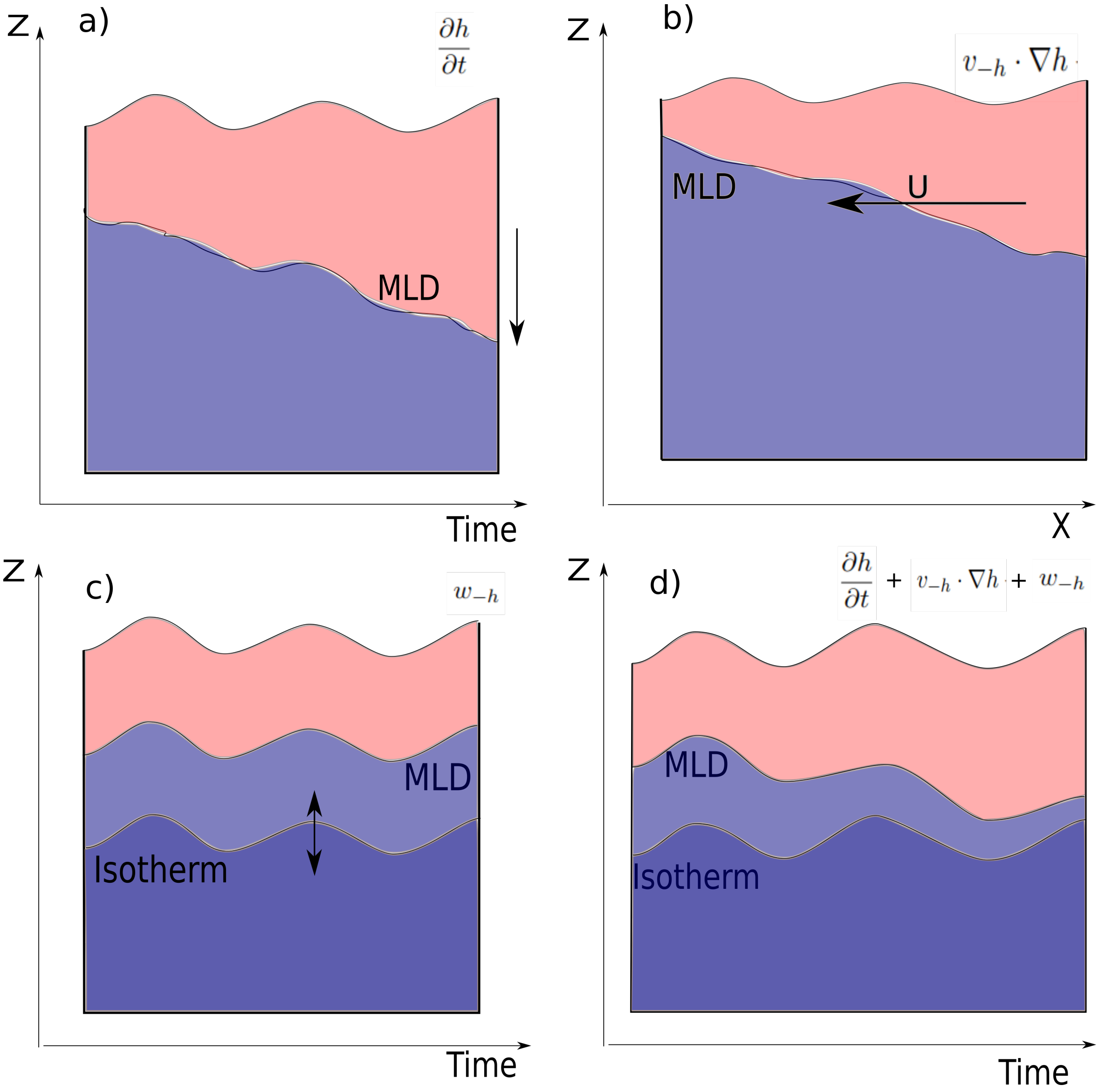

Figure 1.2: Schematic diagrams of the processes contributing to entrainment in the ocean mixed layer. Red regions show relatively warm waters of the mixed layer, with relatively colder water below in blue. MLD is the mixed layer depth and Isotherm denotes an isotherm below the MLD. a) mixed layer depth tendency component with an example of mixed layer deepening b) the lateral induction component with an example of mixed layer deepening. U denotes a horizontal velocity. c) vertical velocity component showing vertical oscillation of water mass. d) Example of MLD evolution due to the three combined components of entrainment.

1.3.2 Entrainment

The entrainment term within the mixed layer heat budget consists of three components, each representing the component of entrainment from a subtly different process. The total entrainment is given by $\frac{(T_a - T_{-h})}{h} \times \left(\frac{\partial h}{\partial t} + v_{-h} \cdot \nabla h + w_{-h}\right)$ .Figure 1.2 shows a schematic of each of these processes. The first is $\frac{\partial h}{\partial t}$ which is the evolution of the mixed layer depth with time at a location. The second and third component 'correct' this for processes which change the mixed layer depth, but are not necessarily due to the mixed layer itself evolving at this location. The second term of the entrainment is the lateral induction term $v_{-h} \cdot \nabla h$, which represents the horizontal movement of water advecting a sloping mixed layer base. To calculate the lateral induction, gradients of the mixed layer depth across the region of interest are needed, along with the current velocity of the mixed layer base. The third term contributing to entrainment is w_{-h}, which represents the vertical velocity of the region. This term accounts for processes like internal tides which will move the mixed layer base in the vertical, but are not changing the water properties in the mixed layer itself. The vertical velocity can be obtained by taking a fixed isotherm below the mixed layer and tracking its depth evolution.

In most areas of open ocean, the entrainment will be responsible for cooling the mixed layer as a stable water column often means water below the mixed layer is cooler than the mixed layer. Exceptions to this include polar regions and estuaries. Sometimes circumstances are described in which there is a sub surface temperature inversion below the mixed layer, which causes mixed layer heating during entrainment. In this area of the tropics, one must be mindful of the possibility of this occurrence, discussed more in section 1.4.2.

1.3.3 Horizontal Advection

The horizontal advection is described by $-v_a \cdot \nabla T_a$ and is the horizontal movement of water. To determine this quantity, one needs good spatial coverage of the region of interest to determine temperature gradients. v_a is the sum of wind driven Ekman velocity and geostrophic velocity and I do not separate these components within the scope of this thesis. High vertical resolution over the upper ocean is needed to determine the horizontal advection, as it is calculated as an average over the mixed layer.

Horizontal advection is thought to be an important process in the tropics. In the 10°- 20° latitudes, the horizontal advection standard deviation is larger compared to the rest of the tropical Atlantic, due to increased wind stress and spatial variation in Ekman currents (Foltz and McPhaden, 2006). Horizontal advection has strong negative correlation with air-sea fluxes in the NWTA due to strong meridional advection which is countered to some degree by zonal advection (Foltz and McPhaden, 2006). The horizontal advection is therefore an important process to be considered and should not be neglected from an NWTA heat budget.

1.4 Ocean Features

1.4.1 The ocean mixed layer depth

Within an ocean surface mixed layer, temperature and salinity profiles are uniform with depth due to the turbulent mixing from wind and wave input. There are many ways to define an ocean mixed layer, as the definition itself is rather arbitrary. The definition chosen for a study is often dependent on the timescales of the investigation being carried out (de Boyer Montégut et al., 2004). Mixed layer depth varies spatially and temporally, with temporal variation often due to ocean mixed layer processes i.e. surface forcing, lateral advection, internal waves (de Boyer Montégut et al., 2004). In tropical regions mixed layers are of the order of 10 m - 100 m whereas they can reach depths around 500 m in the winter of subpolar regions (Monterey and Levitus, 1997). Of the many ways to determine mixed layer depth, within this thesis I focus here on threshold definitions. This involves finding the depth of a density a given threshold amount away from that at a reference depth. Reference depths tend to be to ocean surface or 10 m to avoid the effects of diurnal heating. Some examples of studies using density thresholds are Monterey and Levitus (1997); Foltz et al. (2003); de Boyer Montégut et al. (2004).

Similar to the MLD is the isothermal layer depth (ILD). The ILD is calculated using a temperature based threshold method, again where there are many papers suggesting various temperature threshold values (Monterey and Levitus, 1997; Kara et al., 2000; de Boyer Montégut et al., 2004). Sometimes the temperature threshold condition is used to represent the MLD, however density based criteria are generally regarded as more reliable for the MLD (Lukas and Lindstrom, 1991). The temperature threshold criterion is known to fail in regions with salinity barrier layers (Sprintall and Tomczak, 1992), which is something one needs to be mindful of in the tropics. Inherently, the existence of barrier layers shows that temperature criteria will not accurately represent a mixed layer depth, such that a density threshold, gradient method or specific algorithm (Holte and Talley, 2009)) should be used to determine MLD.

1.4.2 Barrier layers

A barrier layer (BL) is an important ocean feature which can prohibit heat exchange between the mixed layer and the deeper ocean. The barrier layer itself is the distance between the top of the thermocline and the bottom of the mixed layer (Sprintall and Tomczak, 1992) and is found when the pycnocline, halocline and thermocline do not occur at the same depth. An example of an ocean profile with a barrier layer is in Figure 1.3. Barrier layers are formed by different mechanisms depending upon the region they are found, but are often attributed to salinity stratification (Lukas and Lindstrom, 1991). Barrier layer thickness can be anywhere between 10 m and 50 m (Sprintall and Tomczak, 1992). Typically the process of entrainment will bring cold water into the mixed layer from below, however the presence of a barrier layer can inhibit this process, bringing same temperature or potentially warmer water into the mixed layer. A persistent BL affects the transfer of heat to the deeper ocean, causing mixed layer SST anomalies which in turn affect air sea interactions (Fernández et al., 2024). In the tropical North Atlantic (TNA), it is not uncommon for horizontal advection to then dominate heat transfer to balance air-sea fluxes. Forced ocean and coupled ocean–atmosphere models may have trouble reproducing the observed seasonal cycle of SST in the TNA if they do not properly represent the barrier layer (Foltz and McPhaden, 2009). It is important to obtain more observations of mixed layer depth and barrier layer thickness to accurately model entrainment processes and capture SST evolution. The work carried out in this thesis quantifies entrainment in a barrier layer region to help address this gap. The barrier layers of the NWTA are discussed in more detail in section 1.6.

1.4.3 Diurnal warm layers

A mixed layer will experience daytime warming with the rise in solar insolation. Sufficient turbulent mixing will redistribute this heating such that the temperature varies very little with depth in the mixed layer. Under low wind, high solar insolation conditions, it is possible a diurnal warm layer (DWL) to form (Kawai and Wada, 2007). Typical characteristics of a DWL are 1 - 10 m depth and 0.1 °C to 1 °C SST anomaly from the bulk SST (Kawai and Wada, 2007). A DWL formed under wind speeds below $2\,\mathrm{m\,s^{-1}}$, with an exponential form, can have a surface temperature anomaly from the bulk SST as much as 3 °C (Soloviev and Lukas, 1997). A diurnal warm layer is a region in the upper few metres of the mixed layer in which solar radiation absorption causes temperature stratification strong enough to suppress mixing (Price et al., 1986; Fairall et al., 1996*b*). Thus the warm layer develops throughout the day with strengthening stratification from continued solar input to the ocean and decays overnight with turbulent mixing when the solar input is not present. Even though the diurnal warm layer decays over night, it raises daily mean SST compared with no diurnal warm layer formation (Mujumdar et al., 2011). A higher daily mean SST will affect air-sea interactions,

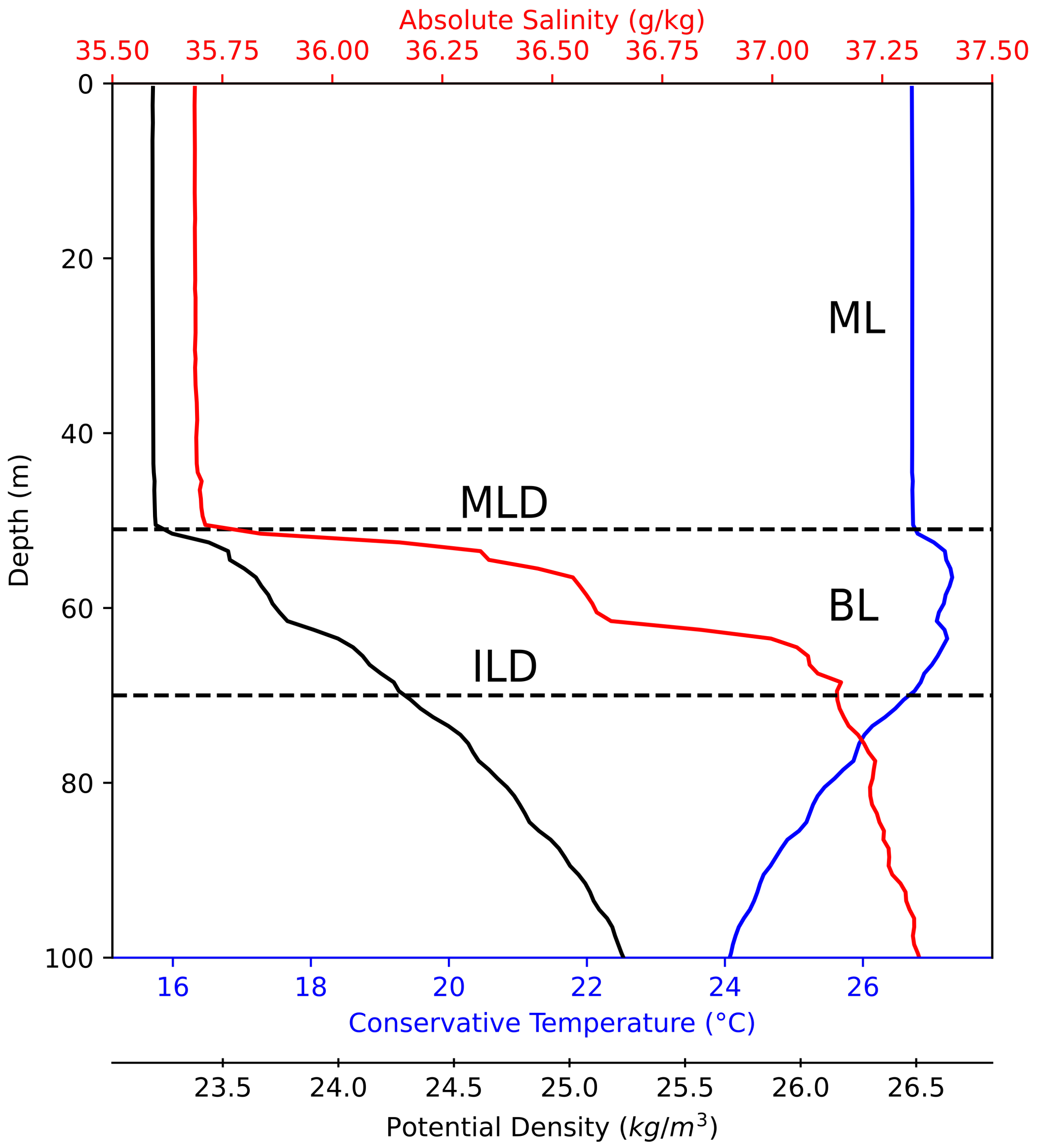

Figure 1.3: Example profile of a barrier layer from Seaglider data in the EUREC^{4}A campaign, where the barrier layer also contains a temperature inversion. The mixed layer (ML), mixed layer depth (MLD), isothermal layer depth (ILD) and barrier layer (BL) are labelled.

so it is important to quantify this feature in an air-sea interactions context. A Seaglider study in the equatorial Indian ocean found daily mean SSTs could increase by 0.2 °C in the presence of a diurnal warm layer and that diurnal warm layer formation typically occurred with wind speed less than $6\,\mathrm{m\,s^{-1}}$ (Matthews et al., 2014).

1.5 Ocean observing systems

To improve understanding of the interplay between oceanic and atmospheric processes and the heat exchanged between them, high resolution observations from the ocean and atmosphere interface are needed (Domingues et al., 2019; Cronin et al., 2019; Yu, 2019). As technology advances, various networks are able to provide in-situ ocean and lower atmosphere measurements for validation of satellite measured variables and flux products. Notable observing strategies include satellites (Zhang et al., 2004; Wallcraft et al., 2009; Zhang et al., 2009; Rodríguez et al., 2019; Nagamani et al., 2012); buoys (Bourlès et al., 2008; Johns et al., 2021); ocean gliders (Rudnick, 2016); the ARGO network (Roemmich et al., 2019); surface drifters (Hansen and Poulain, 1996); ships (Kent and Berry, 2005; Kent et al., 2007) and uncrewed surface vessels (USVs) (Patterson et al., 2025).

Given that USVs are the platform investigated in this thesis, it is pertinent to review them in more detail.

1.5.1 USVs

An expanding area of technological advancement for ocean and atmospheric essential variable measurement is the USV. Whilst some USVs are powered with an engine which supplements power supply and allows constant motor use, these USVs are not the focus of this work. Here I am interested in renewable USVs, i.e. those powered by solar and propelled by wave motion and possibly supplemented by a thruster system. There are many USVs of this type being developed around the world, where some literature about these USVs includes Caccia et al. (2005); Hine et al. (2009); Fer and Peddie (2013); Gentemann et al. (2020); Siddle et al. (2021). In the ocean observing world, although USVs are a relatively new technology, they have already proven their use in many scientific disciplines. Successful use cases include hurricane measurement (Foltz et al., 2022), tropical cyclone measurement (Lenain and Melville, 2014), volcanic area monitoring (Tada et al., 2024) and Antarctic circumnavigation (Nicholson et al., 2022). USVs are able to measure many of the Global Ocean Observing System (GOOS) essential ocean and climate variables, such that they have the potential to form a global network which could provide the desired monitoring capability requirements for air-sea fluxes. Of the published USV deployments, Zhang et al. (2019) demonstrate the ability of a singular USV to provide a vast amount of observations pertaining to air-sea interactions though the deployment of a Saildrone USV, which observed 18 different essential variables in the SPURS campaign. There is a rapidly growing list of studies in which USVs have successfully undertaken air-sea interaction studies around the globe (Wills et al., 2023; Iyer et al., 2022; Sivam et al., 2024; Zhang et al., 2019; Grare et al., 2021; Nagano et al., 2022; Thomson and Girton, 2017; Swart et al., 2019).

The specific advantages of using USVs over other ocean measurement platforms and networks include the ability to measure close to the air-sea interface with minimal flow distortion compared with a ship. As USVs have some form of forward propulsion system, they can move around the ocean to target areas of particular interest or follow a pertinent feature. This brings a freedom to the ability to measure the air-sea interface not found with moored buoys, more control over the area studied than drifters and lower cost than ships. It also allows USVs to intentionally be sent into hazardous conditions without risk to life. Another great cost advantage of USVs, depending on the study location, is that USVs can be deployed from and returned to land, which avoids the costly, environmentally damaging and restrictive time dependence on ship availability. Some sensors on USVs will require more detailed quality control (QC) due to vessel motion than others, but vessel motion correction is well established on ships and similar principles can be applied to USVs. However there are few guidelines in the USV community for quality control, and no cross platform standardisation. Methodology and implementation of QC varies between vessel types and individual users. If USVs are to become a global network to aid in satellite validation and flux product development, the hurdle of first forming a USV community to tackle regulation of scientific use must be addressed (Patterson et al., 2025). Research is emerging to establish guidelines on common USV measurements, for example downwelling radiation (Riihimaki et al., 2024).

Whilst there are many plus sides to USV use, one must also acknowledge the potential for limitations. For USVs operating over a satellite network, operation range is a non-issue, however a local communications network can limit range of operations to a few km or less. The ability of the USV to recognise obstacles becomes important if out of sight of the operator. Some USVs support cameras, but for many this is a resource too power consuming to support. AIS (Automatic Identification System) can be used to warn nearby vessels, but is reliant upon other vessels having AIS capability. Radar, the most popular system of conventional vessels may struggle to pick up a USV (Liu et al., 2016). Use location is another issue, with limited solar irradiance at high latitudes proving challenging for solar-powered USVs and further constraining available power. There are also challenges associated with the physicality of a USV. Being sent into more dangerous conditions than manned vessels brings greater risk of damage, however USV have been shown to successfully record inside of hurricaines (Zhang et al., 2023). Lastly on the physical nature of a USV, the proximity to the water surface of sensors compared to a ship is a scientific advantage, but can bring the potential for salt contamination and water damage. Additionally, quality control of sensor data to account for wave motion on the vessel must not be overlooked. Regulation in USV use can also be an issue depending on the nation under which one operates. The rules around USV use are rapidly evolving and users must ensure they are up to date with the latest regulations before undertaking operations.

A global community with the desire to address these challenges has formed under the United Nations Decade of Ocean Science for Sustainable Development programme, called The Observing Air–Sea Interactions Strategy (OASIS) (Cronin et al., 2023). In April 2025. further global progress on the coordination and collaboration of USV use was made through endorsement by the GOOS Observations Coordination Group under UNESCO-IOC of 'SUN Fleet' as an emerging ocean observing network. The work described in this thesis is intended to feed into the establishment of widely agreed USV protocols for data collection and quality control.

1.6 The Northwestern Tropical Atlantic

The tropical Atlantic is of interest due to its SST variability directly influencing hurricanes in the USA and regional rainfall and droughts in Africa and Brazil (Bourlès et al., 2008), making the study of the region beneficial both scientifically for global climate understanding, and societally for extreme weather event prediction. As discussed earlier and visible in Figure 1.4, this region also has significant SST variability and capturing this will be useful in improving flux products through satellite validation, in situ measurements feeding into global reanalysis products and process studies from the observations themselves.

1.6.1 Oceanography

To understand the temperature gradients and currents of the NWTA for calculation of horizontal advection, one must first be aware of the broad scale regional circulation. The NWTA area has a complex ocean current system (Figure 1.5). The westward flowing North Equatorial Current (NEC) forms part of the North Atlantic Subtropical Gyre and is forced by the trade winds. The Equatorial Undercurrent (EUC) and North Equatorial Undercurrent (NEUC) are eastward zonal flows which may also be supplied by a branch of the NEC (Bourles et al., 1999). The EUC is a strong eastward current on the equator whereas the NEUC is a comparatively weak eastward current in the region of the North Equatorial Counter Current (NECC). The North Equatorial Counter Current (NECC) falls south of the NEC, and is a retro-flection of the North Brazil Current (NBC) occurring between 3 °N and 10 °N (Hormann et al., 2012). The NECC disappears from the surface

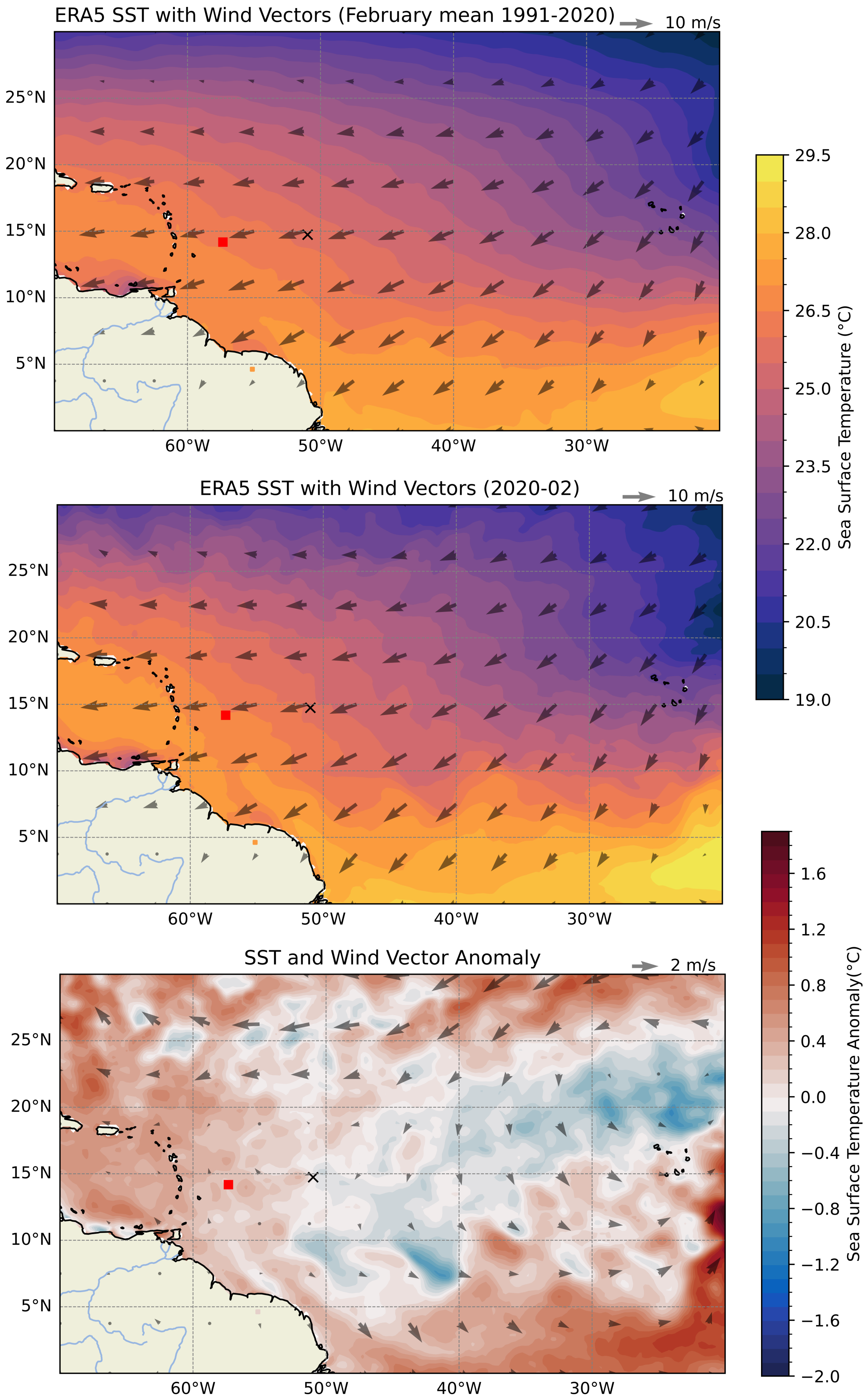
ERA5 SST with Wind Vectors (February mean 1991-2020)

ERA5 SST with Wind Vectors (2020-02)

SST and Wind Vector Anomaly

Figure 1.4: (caption on next page)

Figure 1.4: Figures of average SST and wind field for a 30 year February mean (top) and February 2020 (middle). Wind and SST anomaly for February 2020 compared to 30 year climatology (bottom). Red box denotes the study site measured in February 2020 and used in this thesis. Black cross shows location of NTAS buoy. Data from Hersbach et al. (2023).

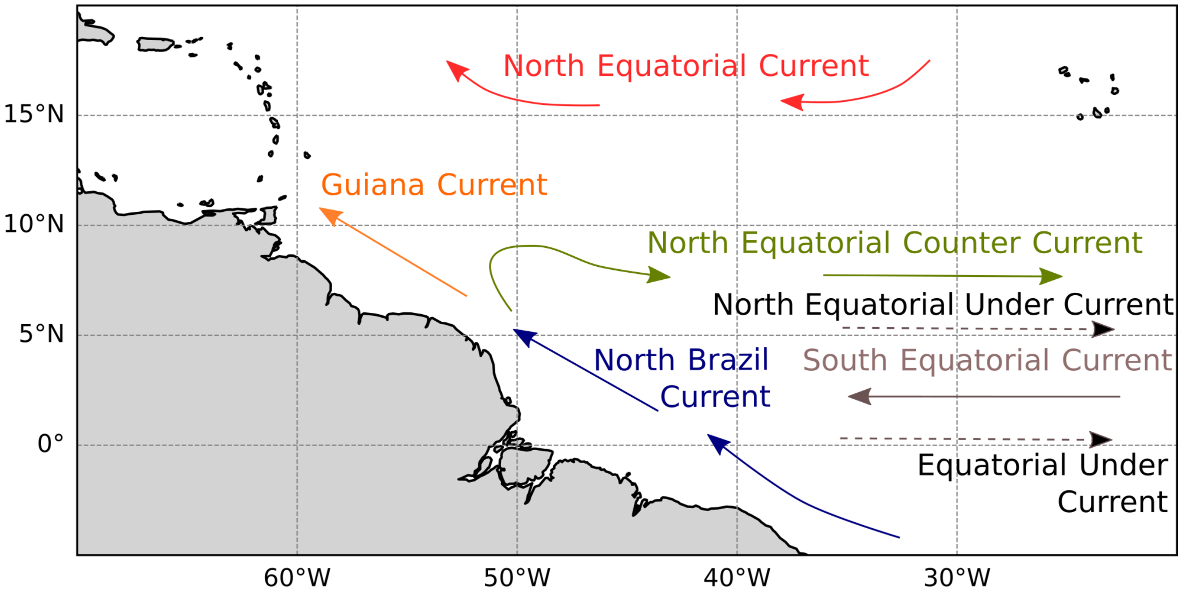

Figure 1.5: Schematic map showing the major surface currents of the western tropical Atlantic Ocean, where solid lines are surface currents and dashed lines subsurface.

between January and May such that surface flow is westward everywhere in the western tropical Atlantic (Philander, 2001), due to changing position of the Inter Tropical Convergence Zone (ITCZ) towards the southern hemisphere. The Guiana current continues from the NBC along the coat of South America towards the Caribbean. Another important feature of the NWTA is the discharge of the Amazon and Orinoco rivers. Most fresh surface waters in the western tropical Atlantic can be attributed to Amazon run-off (Pailler et al., 1999). These fresh waters affect the upper ocean salinity distribution, causing the NWTA to be a particularly heterogenous area of the ocean, which has consequences for the ocean mixed layer budget through stratification.

Looking at the anomaly in Figure 1.4 in the context of the ocean currents, there is a strong influence and abnormally warm North Equatorial Current flow in 2020. Warmer SSTs along the North Brazil and Guiana Currents are also visible, entrapping a cooler SST region in the centre of the TNA. Winds around the study site are similar to the climatology, but stronger than the average when looking North of 20° and East of 50°. This figure also highlights a stark difference in conditions between the study site and the NTAS buoy (discussed in section 1.8). The study site has SSTs around 0.2 °C above the climatologic mean, whereas the NTAS buoy sits in a region where SSTs transition west to east from above to below climatological mean. The NTAS buoy is a vital mooring in providing air-sea interactions data for the tropics. Yet the spatial heterogeneity of Figure 1.4 highlights the need for observations to facilitate air-sea interacts study in more NWTA locations.

Across the wider NWTA, 6 different surface water masses were identified in the Jan-Feb period of 2020 (Fernández et al., 2024; Olivier et al., 2022). Of these 6 water masses, the dominant water mass seen in the location of this thesis' study site is North Atlantic Subtropical Water (NASW). It is characterised by SSS $< 36.07\,\mathrm{g\,kg^{-1}}$ and SST centred on 26.72 °C, representing the coldest surface waters of the NWTA (Fernández et al., 2024). A conservative temperature - absolute salinity diagram of the top 250 m using Seaglider data in February 2020 is shown in Figure 1.6. The top 70 m show the water contained in the mixed layer, with the shallowest waters having characteristics consistent with North Atlantic Subtropical Water. Below this (expected around 50-200 m) (Fer et al., 2010; Sheehan et al., 2023) there are characteristics of Subtropical Underwater (STUW) with a characteristic salinity maximum layer below the mixed layer. Subtropical underwater is defined as 22-25 °C and 37-37.6 $\mathrm{g\,kg^{-1}}$ (Rollo et al., 2022). Water masses for the region from various EUREC^{4}A platforms show similar characteristics (L'Hégaret et al., 2023).

A 30 year mean of SSTs (Figure 1.4) shows variation across the ocean basin from 19 °C in the northeast to 25 °C and higher in the west of the basin. Warmer waters are advected along the coast of South America by the NBC, particularly visible in February 2020 in Figure 1.4. The work of this thesis is concerned with a study carried out in the red box of Figure 1.4 during February 2020, such that I anticipate observing ocean surface temperatures on the order of 27 °C.

Barrier layers are an important feature in this region, with the 50 - 60 °W, 15 - 20 °N region in boreal winter dominated by 50 m thick barrier layers, decaying to thicknesses of 10 - 25 m in boreal summer (Sprintall and Tomczak, 1992). The formation mechanism of barrier layers in the coastal and western NWTA is thought to be due to surface freshwater advection from river outflow being advected northwestward towards the Caribbean (Foltz and McPhaden, 2008) with the assistance of the Guiana current in boreal summer and autumn (Hu et al., 2004). Meanwhile subduction of high-salinity, warm waters from the Northern Hemisphere Subtropical Gyre occurs, with the river outflow remaining at the surface forming a wintertime barrier layer (Sprintall and Tomczak, 1992; Balaguru et al., 2012; Tanguy et al., 2010). BLs centred around 18 °N, 60 °W are treated as a separate BL system with strong winter temperature inversions (Mignot et al., 2007). These BLs are thought to be due to advection of freshwater into the region by the North Brazil Current, by anticyclonic eddies

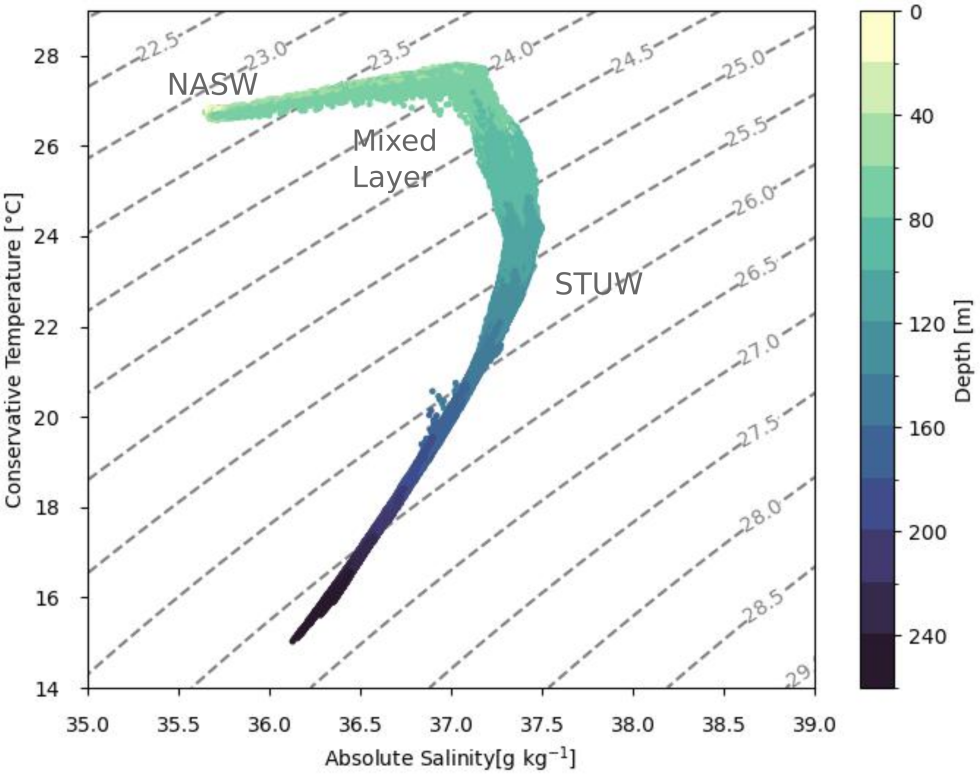

Figure 1.6: Conservative temperature - absolute salinity diagram using Seaglider data from the EUREC^{4}A campaign in the northwestern tropical Atlantic in February 2020, showing the top 250 m of the ocean in this region. Grey lines denote potential density contours and the diagram is coloured by depth of measurement. NASW (North Atlantic Subtropical Water) and STUW (Subtropical Under Water) are water mass labels.

and northward Ekman currents (Mignot et al., 2007). With a maximum advection in summer and autumn, the warm waters below the advected fresh water are then trapped at these times, resulting in the subsurface temperature inversions seen in the region (Mignot et al., 2007; de Boyer Montégut et al., 2007). In winter, the stratification in salinity is maintained and the surface temperature cools through poleward transport of fresh equatorial mixed layers. The wind-induced mixing leads to a deepening of both the MLD and ILD, but the two deepen at different rates and a BL is maintained in-between (Mignot et al., 2012). Due to the strong winter and summer BL formation in the NWTA, the subsurface temperature can exceed the surface temperature by up to 1 °C (Mignot et al., 2012). These BL are shown in the observations discussed later in this thesis.

1.6.2 Meteorology

The winds in the region east of Barbados are known colloquially as the trades. These consistent surface trade winds are typically north-easterly winds in the January, February period (Acquistapace et al., 2022). This consistent wind is due to Hadley cell circulation of air in the atmosphere, where convergence of air at the ITCZ results in rising air forming deep convective clouds as it cools and leading to localised precipitation. The Hadley cell results in dry air sinking in a region of high pressure around 30 °N. Along the ocean surface, air flows from this region of high pressure to low, resulting in the southward component of the flow in the trade winds. The westward component is due to the Coriolis force acting upon the air parcel and results in a total southwestward flow. In Boreal winter, to redistribute higher seasonal solar insolation in the southern hemisphere, the ITCZ shifts southwards, which leaves consistent winds and less precipitation in the TNA. Consistent with the trade winds expected from movement of the ITCZ, both the 2020 and 30 year means (Figure 1.4) show winds on the order of $10\,\mathrm{m\,s^{-1}}$ with a mostly westward and small southward component near to our study region marked in red.

Cloud cover is another important consideration in air-sea fluxes and is at the core of the EUREC^{4}A campaign (discussed in section 1.7). In the NWTA, broken shallow clouds form within the lowest kilometres of the atmosphere called trade-cumuli, where the base of these clouds are influenced by the warm moist air below (Bony et al., 2017). Figure 1.7 shows examples of cloud cover in the NWTA from 2 days of the EUREC^{4}A campaign using images from NASA worldview (https://worldview.earthdata.nasa.gov/) (NASA Worldview Snapshots, 2020). Cloud cover is very variable in this region with 4 distinct cloud types identified (Stevens et al., 2020). An understanding of the cloud cover of the region has important implications on surface radiative fluxes and can result in downwelling solar biases if not correctly parameterised in flux products. This thesis looks for biases in ERA5 surface fluxes and considers whether cloud cover representation may be responsible for any bias found.

1.7 The EUREC^{4}A campaign

The EUREC^{4}A (Elucidating the Role of Cloud-Circulation Coupling in Climate) project was designed to investigate the relationship between trade-cumuli in the tropical Atlantic and their interactions (Bony et al., 2017). EUREC^{4}A developed from a Barbadian-French-German collaboration led by Bjorn Stevens, Sandrine Bony and David Farrell. The project expanded across multiple sub projects, national funded research projects and collaborations to encompass multiple themes and ended up with the following experimental facets (Stevens et al., 2021):

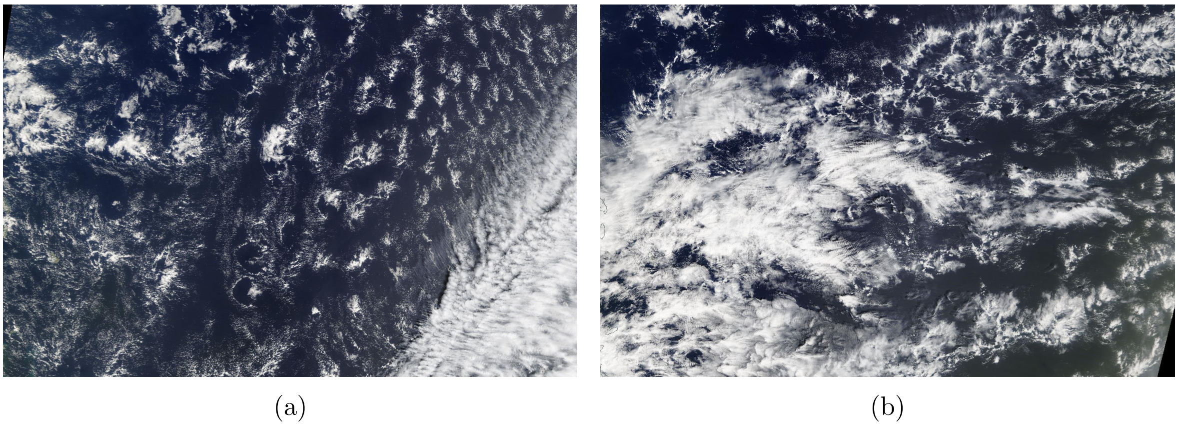
(a) (b)

Figure 1.7: Images from NASA worldview snapshots (https://worldview.earthdata.nasa.gov/) (NASA Worldview Snapshots, 2020), showing cloud structure over the region 10 - 20 °N and 61 - 45 °W for the (a) 9th and (b) 14th February 2020. The coastline of Barbados and some of the Lesser Antilles is included in the left of the figure for spatial context.

- (i) quantify the relative role of micro and macrophysical factors in rain formation;
- (ii) quantify different factors influencing the mass, energy, and momentum balances in the sub-cloud layer;
- (iii) identify processes influencing the evolution of ocean mesoscale eddies;
- (iv) measure the influence of ocean heterogeneity, i.e., fronts and eddies, on air–sea interaction and cloud formation;
- (v) provide benchmark measurements for a new generation of both fine scale coupled models and satellite retrievals.

The core research of EUREC^{4}A took place between 20th January 2020 and 20th February 2020 based from Barbados, expanding as far south as 5 °N and as far east as 50 °W.

One of the collaborations which occurred alongside EUREC^{4}A was the ATOMIC (Atlantic Tradewind Ocean-atmosphere Mesoscale Interaction Campaign) project, a US project let by NOAA. ATOMIC ran from 7th January to 11th July 2020 between Barbados and 51 °W (Quinn et al., 2021). The overall collaborations between EUREC^{4}A , ATOMIC and many other project led to the use of four ships, four research aircraft, the Barbados cloud observatory and multiple autonomous platforms, isotopologue measurements, satellite measurements and models (Stevens et al., 2021).

Within the campaign, the University of East Anglia (UEA) team stationed *Caravela* (discussed in chapters 2 and 3) at the intersection between the HALO aircraft's planned flight circle, and the planned transect of the *R/V Meteor*. *Caravela* and the Seagliders deployed into the same location were then available to provide an SST validation time series at the bottom of the atmospheric profile, to aid the overall cloud-circulation coupling investigation of EUREC^{4}A (Vogel et al., 2022). For our own investigations with *Caravela* , the *R/V Meteor* would occasionally pass by, providing validation opportunities. The proximity of the NTAS buoy to the Eurec4a project was also a benefit. The NTAS buoy is one of a handful of air-sea interactions buoys around the world,is an OceanSITES Ocean Reference Station, and is World Meteorological Organization station number 48401. It is capable of meteorological and oceanographic measurements and was conceptualized to study local air-sea interactions (Weller et al., 2022).

1.8 Historical Analysis of the Tropical North Atlantic

When discussing other published research, I try throughout this thesis to maintain a consistent sign convention of positive flux representing heat gain by the ocean.

A relevant study to this thesis was the use of SWIFT drifters were alongside Wavegliders to investigate SST gradients and air-sea fluxes (Iyer et al., 2022). The average latent and sensible heat fluxes of Iyer et al. (2022) were $-157\,\mathrm{W\,m^{-2}}$ and $-6.6\,\mathrm{W\,m^{-2}}$ respectively. Multiple fronts were observed in the Iyer et al. (2022) study with the average temperature gradient over a front $0.008\,°\mathrm{C\,km^{-1}}$, standard deviation $0.005\,°\mathrm{C\,km^{-1}}$. Another study to come out of the EUREC^{4}A campaign which is relevant to this thesis is the work of Fernández et al. (2023, 2024). They use ship and Saildrone data to investigate the latent heat flux variations between January and April 2020 of the NWTA with the COARE 3.5 algorithm. In terms of flux product biases, ERA5 had a bias of the order $-10\,\mathrm{W\,m^{-2}}$ in latent heat flux based on ERA5's own flux parameterisation compared with inputting ERA5 bulk variables into COARE 3.5 (Fernández et al., 2023). These studies are of a similar time frame and location to the work of this thesis, providing an independent comparison to ascertain that potential biases identified in the flux product are due to the flux product and not the observations.

Generally at short timescales of days to a week, turbulent heat flux spatial variation is due to spatial differences in SSTs, where warm SSTs perturbations result in heat loss from the ocean (Seo et al., 2023). Much of the existing regional literature is on substantially larger spatial scales and longer timescales. Changes in ocean temperature and heat content in the North Atlantic on seasonal timescales are dominated by air-sea interactions and local heat storage with horizontal advection playing a significant role (Böning and Herrmann, 1994; Wang and

Carton, 2002). On inter annual timescales, SST anomalies are thought to be caused by air-sea interactions (Dong and Kelly, 2004). Model studies run over the NWTA suggest annual changes of the tropical ocean heat content are dependent upon both air-sea interactions and ocean heat transport with equal importance (Grist et al., 2010). A 28 year monthly mean surface heat flux of the NWTA is approximately $-15\,\mathrm{W\,m^{-2}}$ (Bishop et al., 2017). A bias of $50\,\mathrm{W\,m^{-2}}$ in air-sea interaction representation is responsible for a 0.5 °C SST anomaly in the tropical North Atlantic (Wen et al., 2017). Typical fluxes using the NTAS buoy in the NWTA for February averaged between 2001 and 2012 are approximately latent flux $-170\,\mathrm{W\,m^{-2}}$; sensible $-7\,\mathrm{W\,m^{-2}}$; shortwave $220\,\mathrm{W\,m^{-2}}$ and longwave $-60\,\mathrm{W\,m^{-2}}$, with net flux between 0 and $-50\,\mathrm{W\,m^{-2}}$ (Bigorre and Plueddemann, 2021). It is clear that heat budget processes are highly dependent on time and spatial scale, which makes comparing studies of various seasons, lengths and regions somewhat difficult. Scale variation must be accounted for in any comparison made, but quantifying the exact effects of these differing scales is not usually possible. The disagreement and difficulty comparing between studies over various scales is the reason more heat flux studies are needed, particularly in an important heat uptake area like the tropics. One could use a flux product to investigate spatial heterogeneity, but the literature identified that flux products contain a host of biases which are not well quantified at the regional level. There is a distinct need for additional observations of bulk variables to calculate fluxes, for quantification of biases in flux products, for validation of observing remote observing systems to enhance observational capacity and understanding of processes contributing strongly to the mixed layer heat budget. These open areas of further study brings us to the scope of this thesis.

1.9 Research Scope of this Thesis

The University of East Anglia developed a bespoke USV called *Caravela* in conjunction with AutoNaut Ltd, to investigate air-sea interactions and transport an autonomous underwater vehicle (AUV). The purpose of this thesis is to investigate the capabilities of this *Caravela* platform, in both a technical and scientific capacity.

The specific questions posed to investigate in this thesis are as follows:

1. *Can an adapted autonomous surface vessel provide a viable platform for air-sea interaction studies?*

2. *How do observational heat fluxes compare to global reanalysis product ERA5?*

3. How well do observed surface processes alone close the heat budget?

4. Considering air-sea interactions and ocean processes, can we close the heat budget on a local scale?

This thesis is structured as follows

Chapter 2 provides an overview of the deployment of *Caravela* in the EUREC^{4}A campaign (as published in 'Weather'), together with dataset descriptions. Chapter 3 discusses the *Caravela* vessel and its data management and quality control; this chapter addresses question 1. Chapter 4 investigates the air-sea fluxes calculated from EUREC^{4}A and compares them with ERA5, addressing questions 2 and 3. Chapter 5 revisits the calculations of chapter 4, with additional terms of the mixed layer heat budget; it addresses question 4. Chapter 6 provides a summary of the thesis alongside recommendations for future work.

2

Research motivation and overview

Synopsis

This chapter was published as the article ‘First measurements of ocean and atmosphere in the tropical North Atlantic using *Caravela* , a novel uncrewed surface vessel’, in the RMETS journal ’Weather’ . I supplement this with section 2.5 to describe datasets used for analysis in this thesis and for clarity within the context of the thesis.

2.1 Introduction

In the tropics, air–sea interactions are an important driver of weather and climate variability and can seed extreme weather events. Robust, accurate and widespread observations at the air–sea interface can improve our understanding of air–sea interaction, help to validate coupled climate models and improve the initial conditions for weather forecasts. A crucial component of the air–sea interaction is the exchange of heat and moisture at the surface. When observing these fluxes, satellites and vessels can only take us so far. To make the next step in understanding air–sea interactions, a comprehensive network of flux measurement platforms, able to sample for extended periods of time, is needed (Cronin et al., 2019).

Nowadays, there are a range of instruments spread across global oceans to capture in situ measurements as part of systems like the Global Ocean Observing System (GOOS) and the EUMETNET Surface Marine Programme. Some examples relevant to the collection of observations at the air–sea interface include the Argo network, moored and drifting buoys, and ships. However, these systems have their limitations: vessels are costly and thus only provide sparse coverage, while moorings rely on deployment and maintenance from a ship, another costly procedure. Argo floats have provided a step change in global coverage of ocean observations, but they typically only surface at 10-day intervals and so are unsuited to studying air–sea interactions on short time scales. Drifting buoys also require deployment by vessel and cannot be targeted to a region of interest, and most drifting platforms only measure near-surface ocean temperature and atmospheric pressure, in addition to recording their position. There are efforts to incorporate a range of meteorological and ocean sensors onto drifters (Centurioni et al., 2019) but their Lagrangian nature still limits their use when a set location is to be studied.

The development of autonomous surface vessels allows targeted measurements of a wide suite of surface ocean and atmospheric data in particular regions of interest, over long time periods. These vessels will be a key component of future global in situ arrays of observation platforms for air–sea fluxes with high spatial resolution and minimal reliance on ship time. Ideally, these surface vessels would be non-polluting and powered by renewable resources, such as waves, wind and sun.

2.2 Autonomous vehicles

The use of autonomous vessels in air–sea interaction studies allows for measurements very close to the water surface, with minimal disturbance to the surrounding air and water parcels. Other advantages include: the ability to launch and recover the vessels from the shore, cutting down costs and reliance on ship time for study; the lack of emissions and low carbon footprint; and the ability to reach previously inaccessible areas. Examples of autonomous vessel deployments to date include Saildrones as part of the SPURS-2 campaign (Zhang et al., 2019), to demonstrate their feasibility as air–sea interaction observational platforms, a wave glider studying air–sea interaction in Drake passage (Thomson and Girton, 2017) and the OCARINA platform developed by Bourras et al. (2014), deployed off the west coast of France as part of FROMVAR. It is apparent that the use of surface vehicles in flux determination is still in its very early stages. The focus is currently on data acquisition, quality testing and determining the combinations of conditions under which autonomous surface vehicles struggle to operate.

2.2.1 AutoNaut

Following these studies, the University of East Anglia (UEA) worked with AutoNaut Ltd to develop an uncrewed surface vessel, named *Caravela* . Previous uses of AutoNaut vessels include scientific deployments (Johnston and Pierpoint, 2017),surveillance (Johnston and Poole, 2017) and environmental campaigns through AutoNaut's involvement in The Ocean Cleanup. [1]

The UEA's *Caravela* is a 5m-long surface vessel (shown during deployment in Figure 2.1 and described in Figure 2.2), with 0.8 m draft and 1.5 m high mast. AutoNaut's Wave Foil Technology generates the vessel's forward motion. This uses sprung foils at the front and aft of the vessel, which articulate to draw energy from the vessel's pitch and roll (Johnston and Pierpoint, 2017). The larger the waves, the more energy generated and the faster the forward motion of the vessel. An auxiliary thruster is also fitted on the aft foil to aid propulsion in difficult conditions. *Caravela* is a robust vessel, designed to withstand rough ocean conditions and in the event of capsize, self-right. *Caravela* can be operated in three different ways depending on proximity to the pilot. Up to 200 m from the pilot, a joystick can be used to drive *Caravela* and engage the thruster, to allow for controlled movement at launch and retrieval sites. Up to around a kilometre from the pilot, *Caravela* can operate under 'local controls' in which the pilot sends commands from the piloting interface (called RCW) to *Caravela* over UHF radio. Finally, when beyond line of sight, the pilot can send commands from RCW over the Iridium satellite network. Within these piloting regimes, *Caravela* can operate under three modes: station mode, where *Caravela* circles a location at a specified radius, typically 25 m; heading mode, in which a heading is set and kept regardless of course over ground; or track mode in which a series of waypoints are set and *Caravela* automatically adjusts heading to reach these points. This large range of operational modes opens many possibilities for meteorological and oceanographic measurement with an AutoNaut vessel.

Caravela has a modular monohull, allowing for integration of different sensor types and minimising risk of damage in case of water ingress. Four lithium-ion batteries recharged by three solar panels spanning *Caravela* 's surface are responsible for powering the onboard computer and sensors. The sensor package fitted on *Caravela* was selected to support the determination of air–sea fluxes and is described in Table 2.1, with locations on the platform shown in Figure 2.2.

---

[1] https://theoceancleanup.com/

Figure 2.1: Photograph of *Caravela* (an AutoNaut vessel) in front of the German *R/V Meteor* during the EUREC^{4}A campaign. (Credit: Callum Rollo.)

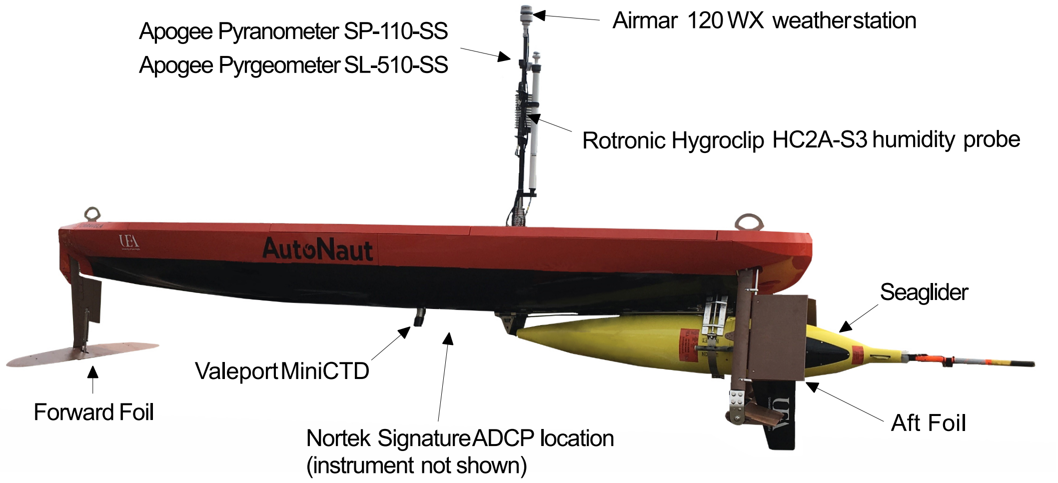

Figure 2.2: Labelled photograph of *Caravela* and a Seaglider, describing the locations of meteorological and oceanographic sensors. The Nortek Signature1000 ADCP is not included in the figure but would be mounted below *Caravela* , level with the CTD.

Instrument	Measurements
Apogee Pyrgeometer SL-510-SS	Incoming longwave radiation (5 - 30 µm)
Apogee Pyranometer SP-110-SS	Incoming shortwave radiation (360 - 1120 nm)
Rotronic Hygroclip HC2A-S3 humidity probe	Air temperature, Humidity
Airmar 120 WX weather station	Wind velocity, Air temperature, Barometric pressure
Nortek Signature1000 ADCP	Near surface current velocity
Valeport MiniCTD	Sea surface temperature (SST), Conductivity, Water pressure

Table 2.1: Description of the parameters measured by *Caravela* during the EUREC^{4}A deployment and the associated sensors.

Caravela's novel aspect is its ability to transport and release a profiling ocean glider, specifically a Seaglider. The Seaglider is a separate underwater autonomous vehicle piloted over Iridium, capable of profiling the ocean to 1000 m through changes in its buoyancy. The Seaglider is visible inside *Caravela's* release mechanism in Figure 2.2. The benefits of developing a Seaglider transport system are that the Seaglider can be deployed in a remote or challenging area, without the cost of sending a ship or endangering personnel. Additionally, the Seaglider can rest in *Caravela* 's glider release mechanism for a long period of time without significant battery wastage. This opens the opportunity to time the deployment of a Seaglider to study an event, like a monsoon or phytoplankton bloom, again without reliance on ship availability for deployment. The release mechanism does not allow for Seaglider recovery to *Caravela* , so it is still necessary to consider ship availability to collect the Seaglider. However, this provides many more opportunities for deployment than if a ship was needed for both deployment and recovery.

2.3 Deployment of an AutoNaut – data quality

The first full scientific deployment of *Caravela* took place from January to March 2020, as part of the EUREC^{4}A campaign (Bony et al., 2017; Stevens et al., 2021). EUREC^{4}A was developed to investigate the coupling between clouds, circulation and climate but expanded to cover many themes within meteorology and oceanography that feed into climate research. UEA's contribution involved the preparation of *Caravela* in Barbados, where the vessel was deployed with the aid of the Barbados Coastguard on 22nd January 2020.

Caravela travelled from Barbados to the study site and back over 33 days. This included 11 days occupying a 10 km wide hourglass-shaped sampling pattern at the study site (upper right of Figure 3). On the outward journey, *Caravela* covered approximately 150 km before the Seaglider was released to travel independently to the study site. Average speed over ground was approximately $0.34\,\mathrm{m\,s^{-1}}$ whilst carrying the Seaglider, compared with $0.49\,\mathrm{m\,s^{-1}}$ across the whole deployment. Unfortunately, we suspect entanglement of the Seaglider in Sargassum slowed *Caravela* , hence releasing the Seaglider earlier than planned on the outward journey. Fortuitously, *Caravela* and the Seaglider arrived separately at the study site within a day of one another, giving us an almost co-located dataset between the two platforms during outward transit.

The Airmar 120WX (Airmar) and Rotronic Hygroclip HC2A (Hygroclip) both measured

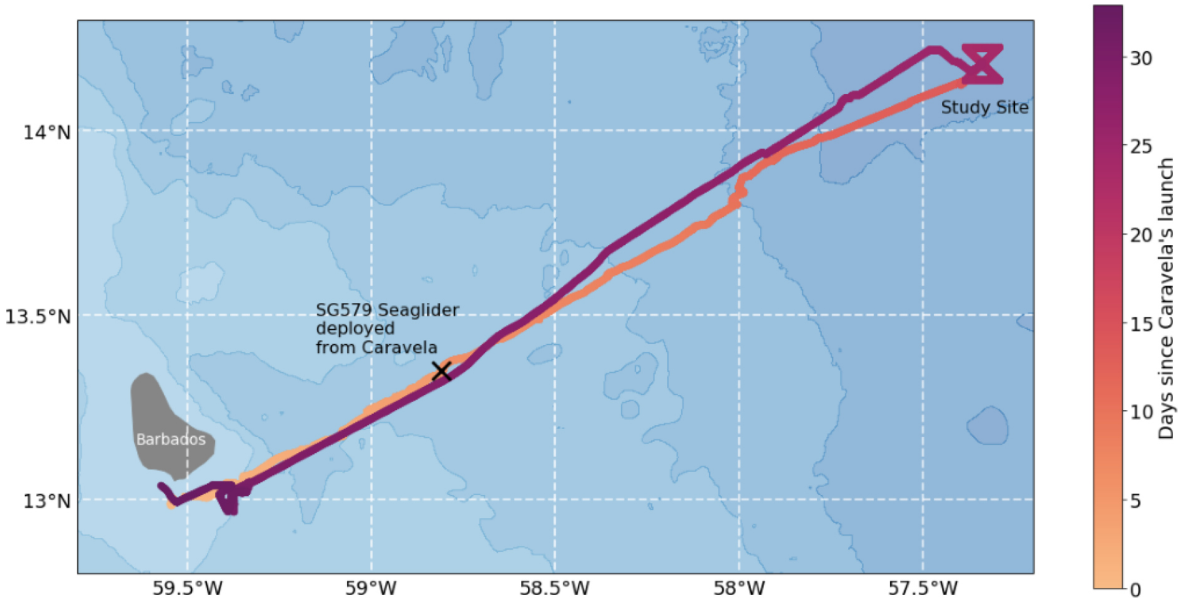

Figure 2.3: Track taken by *Caravela* during the EUREC^{4}A campaign, coloured by days since deployment from Barbados. The study site is labelled at the top right, where *Caravela* repeated the same bowtie pattern for 11 days. The release location of the Seaglider from the transport system below *Caravela* is marked in the Figure. Bathymetry is shown in blue with contours at 1000 m depth intervals.

air temperature on *Caravela* . When analysed, we discovered these instruments showed poor agreement.The timeseries of these air temperatures and comparison to the *R/V Meteor* are visible in Figure 2.4 and Figure 3.6. The complete time series taken from the *R/V Meteor* during the campaign is not always in the vicinity of *Caravela* . Using only when the *R/V Meteor* and *Caravela* are within 10 km of one another, the mean difference of the Hygroclip is 0.33 °C larger than the R/V Meteor, with RMS 0.48 °C. For the Airmar, the mean difference is 1.39 °C less than the *R/V Meteor* with RMS 1.50 °C. Both instruments on *Caravela* were shaded and well ventilated. The Airmar is situated at the top of the mast (1.5m), approximately 0.5m above the Hygroclip. Comparisons with data from the *R/V Meteor* (Figure 2.4) shows consistency with the Hygroclip sensor. The Hygroclip time series stopped on 18th February due to sensor failure but we are satisfied with the quality of data obtained from the Hygroclip before failure. However, the Airmar does not provide the accuracy required to detect small temperature variations important in heat fluxes. It is often used as a sailing or fishing instrument and whilst useful for these applications, is not appropriate for our needs in terms of air temperature measurement. The Airmar instrument is also responsible for apparent wind data. This analysis is in progress so comprehensive assessment of the quality of Airmar wind data will be addressed in subsequent publications.

A time series of *Caravela's* SST whilst at the study site was compared with Seaglider SST data (Figure 2.5). This uses three different Seagliders deployed in the study site throughout

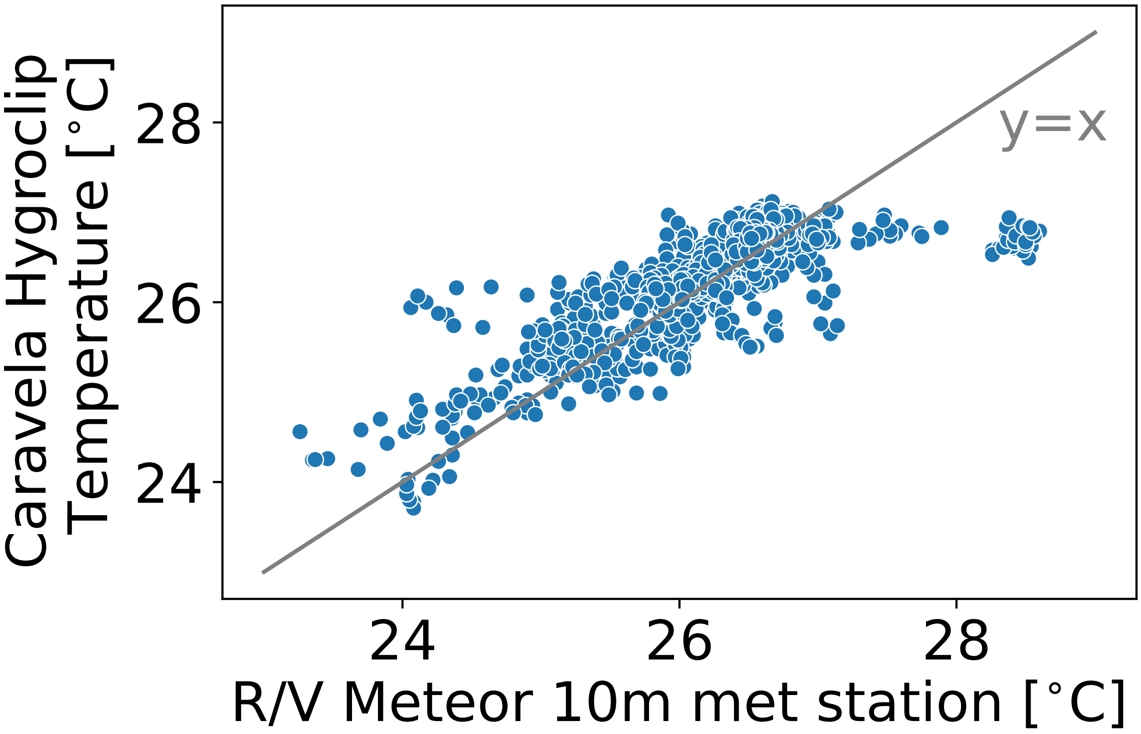

Figure 2.4: Comparison of air temperature measurement between a weather station on the *R/V Meteor* and *Caravela* 's Hygroclip instrument, when the vessels are within 10km of one another. The median Hygroclip temperature value per minute was matched to the *R/V Meteor* data. From this we see that *Caravela* 's Hygroclip data agrees well the *R/V Meteor* and does not require correction.

EUREC^{4}A , the one released from below *Caravela* and two deployed from the *R/V Meteor*. We would expect to see a diurnal cycle in SST, which is clearly visible between 10th - 14th February. The measurements from the two platforms are consistent, albeit with substantial spatial and temporal variability evident. Downwelling longwave (5 - 30 µm) and shortwave (360 - 1120 nm) radiation were measured by *Caravela* throughout the EUREC^{4}A campaign because accurate measurements of these parameters are vital for heat flux estimation. The total air–sea heat flux is the sum of four fluxes: net longwave and shortwave radiative fluxes; surface latent heat flux; and sensible heat flux. Variability in incoming solar radiation throughout the day impacts surface heat flux and causes the diurnal cycle in SST (Figure 2.5). Figure 2.6 shows the diurnal cycle in shortwave (i.e. solar) radiation. We see significant variation of around 100 W m^{-2} in the longwave radiation (Figure 2.6).

2.4 Future work

Caravela offers continuous measurements of surface fluxes and surface conditions that are co-located with the HALO aircraft's flight circle during the EUREC^{4}A campaign, as well

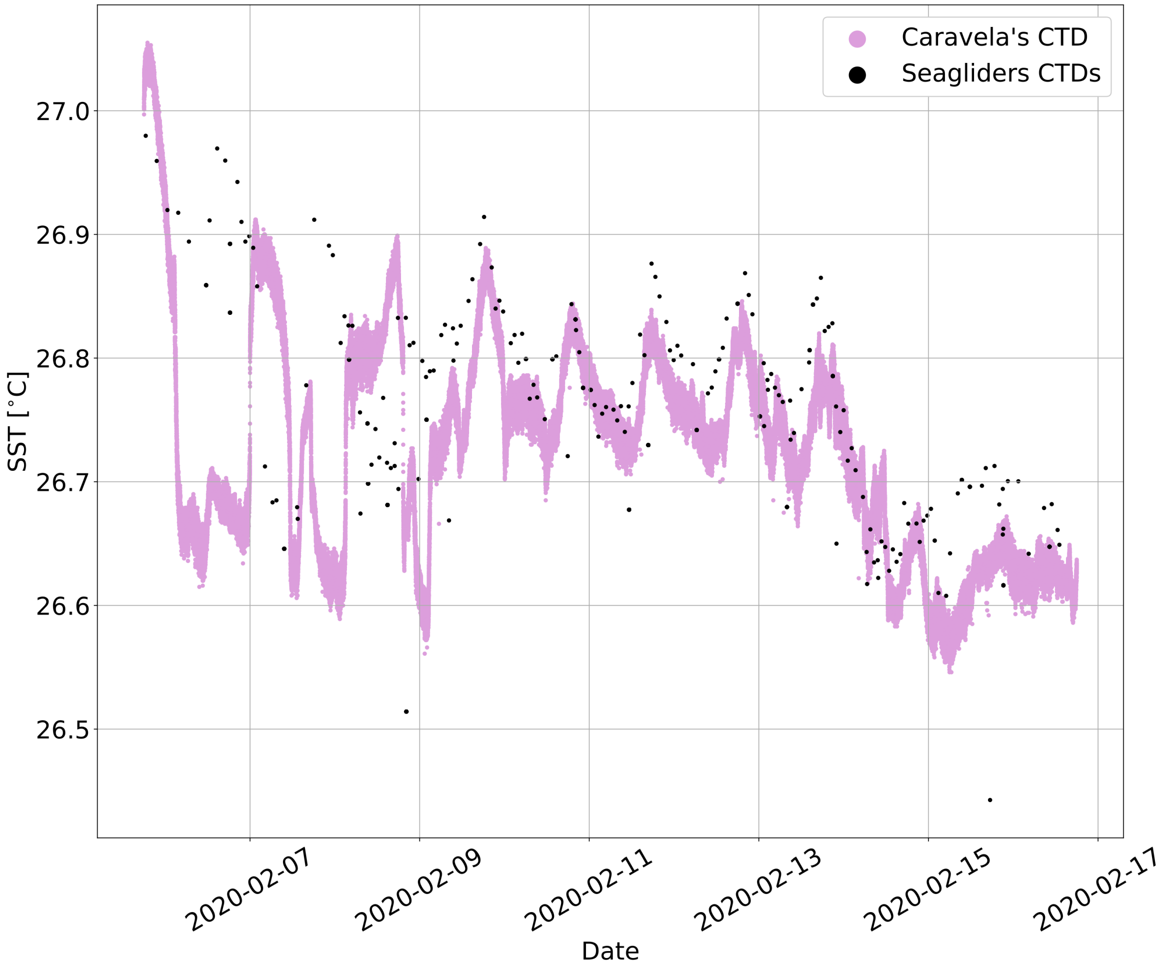

Figure 2.5: Time series of sea surface temperature (SST) data from *Caravela* , measured 0.2 m below the surface with data from three Seagliders at the same study site. The Seaglider data shows one measurement per dive, recorded nearest to the surface as the Seaglider ascended. Clear diurnal cycling in both Seaglider and *Caravela* data between 10th and 14th February can be seen, with spatial and temporal variability.

as complements the measurements taken from the *R/V Meteor* on a meridional transect at 57°14.7′ W. *Caravela's* data will be valuable outside of our heat and momentum flux research, providing a stationary time series in EUREC^{4}A where many other platforms had large spatial coverage. Having *Caravela* provide measurements in the marine boundary layer, co-located with flights by the HALO aircraft, will enhance atmospheric analysis within the wider scope of EUREC^{4}A by providing true data at sea level. Without this, much coarser resolution satellite data or ship data further up from the sea surface would have been relied upon. This has scope to enhance the quality of boundary layer heat fluxes and understanding of the impacts on clouds at a local scale in the wider campaign.

UEA's future work with *Caravela* will first build on the observations from EUREC^{4}A , calculating local heat and momentum fluxes between the ocean and atmosphere. Using time series of upper ocean heat content from the profiling gliders, we will estimate an upper ocean heat budget at the study site with the purpose of determining the dominant SST variability

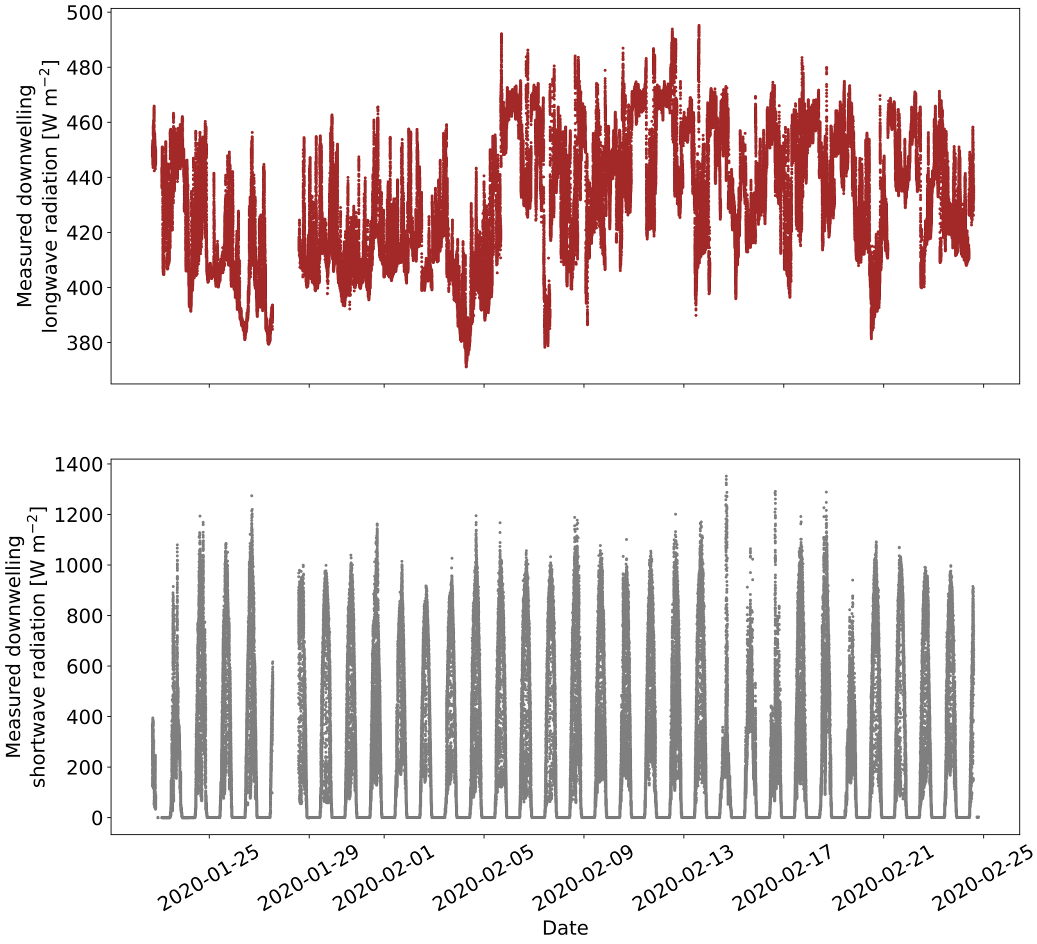

Figure 2.6: Time series of measured downwelling longwave (top) and shortwave (bottom) radiation on *Caravela* during the EUREC^{4}A deployment. These instruments performed well on *Caravela* ; investigation into the impacts of vessel motion on these measurements is ongoing.

driver in the region. This would allow us to differentiate between SST variability based on surface heat fluxes and subsurface processes like mixing, entrainment or advection. We intend to do this work with observations alone, utilising data from *Caravela* , the Seaglider transported to the study site by *Caravela* and the two other Seagliders that were deployed from the *R/V Meteor*. Deriving the ocean mixed layer heat budget based solely on ocean and atmosphere observations is rare. If the analysis is successful, we intend to undertake a similar deployment in Antarctica, where in situ observations are even more scarce. We hope this work will provide a foundation for future air–sea interaction research based only on the use of autonomous observations.

2.5 Wider thesis datasets

Whilst this research is predominantly based upon observations recorded during the EUREC^{4}A campaign, investigations are supported by reanalysis products, allowing for cross validation and a picture of the regional ocean behaviour. A brief overview of the reanalysis data within this thesis is given below:

2.5.1 ERA5

ERA5 is an atmospheric reanalysis product from European Centre for Medium-Range Weather Forecasts (ECMWF), replacing the ERA5-Interim product. Available resolution is 31 km spatially with 1 hour time resolution (Hersbach et al., 2018, 2020; Copernicus Climate Change Service, 2023). ERA5 is forced at the ocean interface with SST from the HadISST2 dataset prior to 2007, and the Operational Sea Surface Temperature and Ice Analysis (OSTIA) after this time. ERA5 can be accessed from the Copernicus Climate Data Store and is available at various temporal resolutions (hourly, daily, monthly). The product used within this thesis is the ERA5 hourly data on single levels from 1940 to present. This dataset is used in chapter 4 and 5.

2.5.2 GLORYS12V1

GLORYS12V1 is the Global Ocean Physics Reanalysis product (shorthand GLORYS) including daily and monthly temperature, salinity, currents, sea level, mixed layer depth and ice parameters throughout the full ocean depth. GLORYS is available on a regular grid at 1/12° (approximatively 8 km) and on 50 standard levels. This is an eddy-resolving reanalysis product with the model component being NEMO. The ocean surface is driven by atmospheric conditions from ERA-Interim, but this has more recently been exchanged for ERA5 (Jean-Michel et al., 2021). This dataset is used in chapter 5.

3

The *Caravela* Cookbook: Recipes for Vessel Upkeep and Scientific Use

Synopsis

This thesis uses a range of data derived from ocean platforms and reanalysis. Whilst processing of Seaglider data is fairly well established, handling data from the AutoNaut surface vessel is comparatively less established. Seagliders have been used scientifically for the last two decades, with a range of literature investigating the impact of Seaglider motion on data quality from their sensors. However, surface vessels are an emerging technology. At the time of writing, there is no community standard for data processing from uncrewed surface vessels. This chapter looks at data throughout testing and use of the AutoNaut vessel since 2019, considers changes made to ease data handling and usability, as well as sensor upgrades to improve confidence in the data. I discuss sensor data quality control, what worked and what did not, with the aim that this information is helpful for future users of the vessel. Scientific analysis and conclusions drawn from the data are discussed in later chapters.

3.1 An Introduction to USVs

Uncrewed surface vessels (USVs) describe a group of vessels which sit on the ocean surface with varying degrees of autonomy, and often rely on a human pilot or captain to oversee the vessels' operation (Patterson et al., 2022). These vessels are cost effective, safer (Bai et al., 2022) solutions to the high cost and demand for scientific ship time. Depending on design, USVs can be deployed and recovered from a larger ocean vessel or from land, enhancing global observational programmes and filling gaps in spatial and temporal ocean coverage.

The development of USVs spans multiple industries including scientific, defence, wind farm management, fisheries management (Osen et al., 2019; Handegard et al., 2024) and coastal monitoring (Zaghi et al., 2016; Kum et al., 2018). Because of the broad range of applications, USVs are an important emerging technology. USV uptake has been hampered by high upfront costs, difficult and disparate legal frameworks and sometimes limited customer confidence in the technology (Patterson et al., 2022), as well as further development needed for safe widespread use of USVs (Nemoto, 2024).

There are many variations of USVs. Saildrone vessels are large, including a 5 m wing above water and 2.5 m draft, with an extensive sensor suite described by Gentemann et al. (2020). Meanwhile the Waveglider incorporates an underwater tethered glider with a surface float, using wave energy for forward propulsion (Hine et al., 2009). Saildrone takes a more unusual approach to their use, with the Saildrone company owning the vehicles and selling the data to scientists. Many other manufacturers sell the USVs to be owned and operated by facilities carrying out the science. The large range of vessels, uses and designs continues to grow with uptake in USVs, and vessels are continually innovated to meet new needs. I focus this chapter on the AutoNaut USV owned by the University of East Anglia.

3.2 *Caravela* : An AutoNaut Uncrewed Surface Vessel

Following on from the overview in chapter 2, *Caravela* is a product of a partnership between the UEA and AutoNaut Ltd, to enhance the capabilities of the standard AutoNaut USV to transport and deploy a Seaglider autonomous underwater vehicle. The Seaglider is a separate autonomous underwater vehicle piloted over Iridium, capable of profiling the ocean to 1000 m depth through changes in its buoyancy. The benefits of developing a Seaglider transport system are that the Seaglider can be deployed in a remote or challenging area, without the cost of sending a ship or the risk of endangering personnel. Additionally, the Seaglider can rest in *Caravela* 's glider release mechanism as long as is required by the user. This opens the opportunity to time the deployment of a Seaglider to study an event with uncertain timing, like a tropical cyclone or phytoplankton bloom, again without reliance on ship availability for deployment. The release mechanism does not allow for Seaglider recovery to *Caravela* , so it is still necessary to consider ship availability to collect the Seaglider. However, this provides many more opportunities than if a ship was needed for both deployment and recovery. This set up could lead to a change in the way missions are planned, i.e. rather than an open ocean mission, projects could be designed unidirectionally, from remote release of a Seaglider in the open ocean, transiting to a coastal region for recovery by a small boat. The other main difference between *Caravela* and a standard AutoNaut vessel is the rear foil system. As the Seaglider needs to be deployed from under the aft of the vessel, it is not possible to have a standard aft foil system. Instead the aft foil has been replaced by a triangular rig, where the bottom of the triangle still acts as a wave foil and the two upward-pointing sides act as angled rudders (Figure 2.2). The Seaglider passes through the centre of this triangle and is gripped inside a band further forward on the hull. This transport of the Seaglider does slow the vessel compared with a standard AutoNaut system (see chapter 2), however the benefit of the ability to deploy the glider outweighs the loss in speed over ground.

3.3 Vessel sensors

Caravela's sensor configuration and data storage has evolved during the time of this PhD project. Through this chapter I will cover noteworthy changes to the data storage protocols and data quality control methods from *Caravela* deployments - namely our short trials deployments and the EUREC^{4}A (Elucidating the role of clouds-circulation coupling in climate) (Stevens et al., 2021) project deployment. *Caravela* was also deployed on the PICCOLO (Processes Influencing Carbon Cycling: Observations of the Lower limb of the Antarctic Overturning) project, however this deployment falls outside the scope of this thesis.

Caravela is designed to study the fluxes of heat and momentum between the atmosphere and ocean. Therefore, I take measurements of radiative fluxes (shortwave and longwave) and the bulk parameters enabling turbulent flux calculations. Sensors are summarised in Table 3.1 and Table 3.2. All meteorological instruments on the vessel are located on the mast, at various heights as depicted in Figure 2.2 and Table 3.2. Measurement heights are defined as height above the vessel's waterline with the mast aligned vertically in flat water, unless otherwise specified, and do not account for pitch or roll of the vessel changing the height above the sea surface. Measurement heights and depths should be reverified with each campaign as a change in payload or ballast on the vessel will affect the waterline and sensor heights are variable on the mast. The sensor package on *Caravela* was chosen to give a cost effective and accurate picture of bulk parameters which feed into air sea fluxes (for more detail on the bulk formulation of fluxes, see chapter 4). The turbulent fluxes require high precision SSTs, available from a fixed CT sail (Conductivity Temperature sensor) under the vessel hull. Wind measurements are available relative to the vessel hull from an

Airmar unit, which also provides air temperature. Further air temperature and humidity measurements are available from a Rotronics HygroClip HC2-S3 probe (henceforth referred to as HygroClip). To determine radiative fluxes, *Caravela* measures downwelling shortwave and longwave radiation with Apogee sensors. There is some redundancy built in with the meteorological measurements, in that the HygroClip probe measures air temperature as well as the Airmar system, however this is the only measurement with redundancy. All other variables do not have a back up system.

Measurement	Instrument	Depth
Sea Temperature	Valeport miniCTD	0.27 m from waterline
	Seabird SBE 49 FastCAT	0.43 m from deck
Salinity	Valeport miniCTD	0.27 m from waterline.
	Seabird SBE 49 FastCAT	0.43 m from deck
Current	Nortek Signature 1000 ADCP	0.5 m

Table 3.1: Ocean measurement capabilities of *Caravela*

Measurement	Instrument	Height relative to ocean surface	Frequency
Wind Speed and direction	Airmar 120WX	1.25 m	2Hz
Relative Humidity	Hygroclip HC2A - S3	0.67 m	1 Hz
Air temperature	Airmar 120 WX	1.25 m	1 Hz
	Hygroclip HC2A - S3	0.67 m	1 Hz
Downwelling Longwave radiation	Apogee SL-510 Pyrgeometer	Variable height on mast	1 Hz
Downwelling Shortwave radiation	Apogee SP-110 Pyranometer	Variable height on mast	1 Hz

Table 3.2: Meteorological measurement capabilities of *Caravela*

3.4 An overview of processing development and sensor evolution

Multiple short test missions, and the EUREC^{4}A campaign mission are used to critically review the set up of *Caravela* (Table 3.3).

Date	Event description	Location
September 2019	UEA team training	Oban, Scotland
November 2019	Sensor testing	Chichester, England
January 2020	EUREC^{4}A	East of Barbados
April 2022	Sea trials 1	Littlehampton, England
June 2022	Sea trials 2	Chichester, England
June 2023	Sea trials 3	Oban, Scotland

Table 3.3: Timeline of *Caravela* deployments and tests.

3.4.1 Oban 2019 training

Early experience of the vessel and training in hands-on use happened during the 2019 trials in Oban, Scotland. The vessel was successfully built with assistance from the AutoNaut team and collected data for short periods between 2nd and 6th September 2019 in the coastal waters around the Scottish Association for Marine Science (SAMS). At this stage, the sensor suite was not fully integrated, see Table 3.4. The main purpose of this deployment was to develop familiarity with vessel piloting among the UEA team, so lack of data was not an immediate concern. The functioning sensor suite did include the Valeport miniCTD and Airmar 120WX. Some navigational data were also returned over Iridium. A comparison of Airmar air temperature against the nearest available data; the Met Office weather station in Dunstaffnage, Scotland was carried out (Figure 3.1) Dorling (2019). This weather station is an automatic station located at 56.451° N, 5.439° W, 3 m above sea level near to the SAMS site (Figure 3.2). Data was provided by private communication. *Caravela* air temperature measurements were on average 2.2 °C lower than Dunstaffnage weather station, however *Caravela* recorded a higher temperature than Dunstaffnage at 13:40 on 4th September. The limited time of deployment and variable distance from the weather mean it is difficult to deduce much about the sensor from this comparison, but it justifies the need for further sensor validation described in section 3.4.2. The SST was compared with near surface measurements from a handheld CTD device (Dumont, 2019) used in the vicinity of

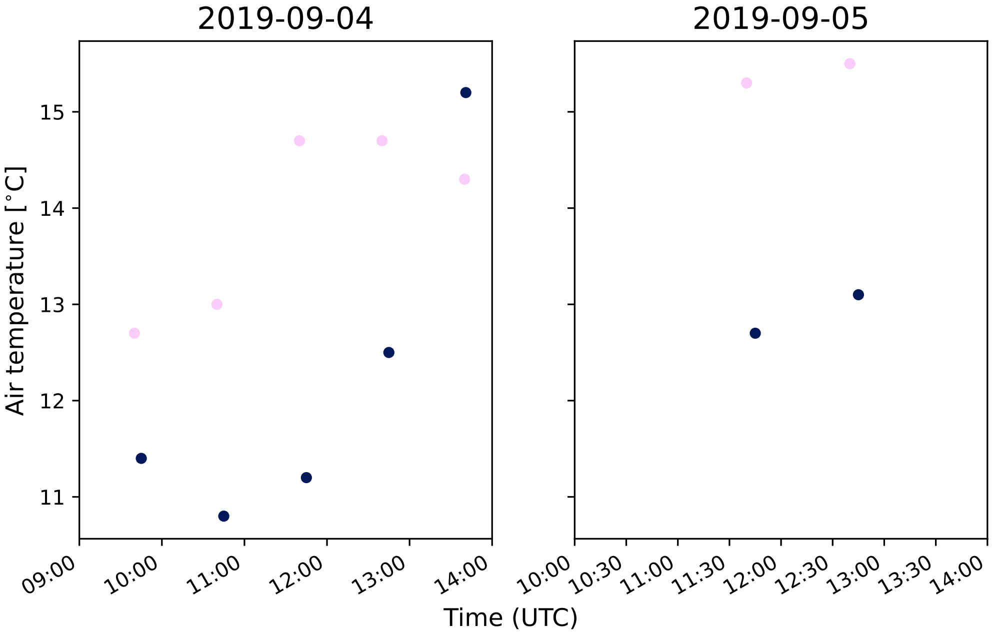

Figure 3.1: Comparison of air temperature measured from the Dunstaffnage weather station (pink) and *Caravela* 's Airmar sensor (blue).

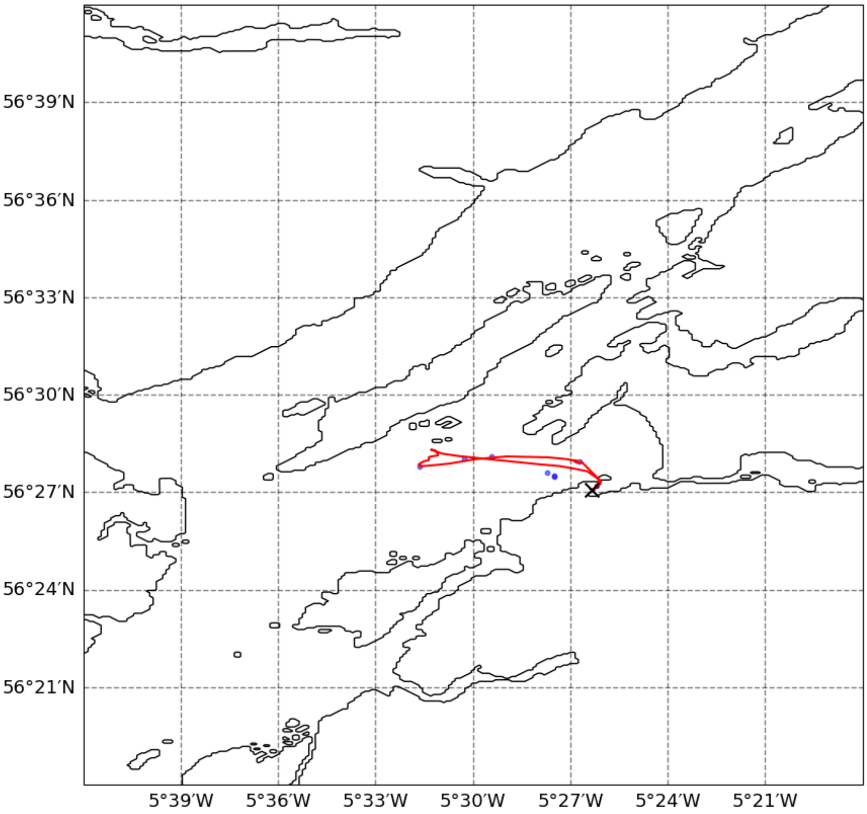

Figure 3.2: Map showing track taken by *Caravela* on 3rd September 2019 (red), locations of CTDs taken on 3rd, 4th and 5th September 2019 (blue) and location of the Dunstaffnage weather station (black X)

	UEA team training	Sensor testing	Eurec^{4}a	Sea trials 1	Sea trials 2	Sea trials 3
Apogee Pyrgeometer SL-510-SS		X	X	X	X	X
Apogee Pyranometer SP-110-SS		X	X	X	X	X
Rotronic HygroClip HC2A-S3 humidity probe		X	/	X	X	X
Airmar 120 WX weather station	X	X	X	X	X	X
Nortek Signature1000 ADCP			X	X	X	X
Valeport MiniCTD	X	X	X			
Seabird Fastcat CTD				X	X	X

Table 3.4: Shows which sensors were available during each deployment, marked by X. Deployments where a sensor failed are marked by /.

Caravela whilst on Loch Linnhe, visible in Figure 3.2 (data provided by private communication). There are 11 handheld CTD measurements across the 3 days in the water at 0.15m depth, comparable to the Valeport miniCTD depth. The handheld CTD consistently measured higher temperatures than *Caravela* ,with a mean difference of 0.17 °C and standard deviation of 0.03 °C. The calibration status of the handheld device is unknown and so it is possible that it is this responsible for the offsets rather than *Caravela* . To assess this further, I include the temperature data from Seaglider SG579 in Figure 3.3. The Seaglider temperature was believed at this stage to be correct and raised concerns over a temperature offset in *Caravela* 's CT sail, however it was later found that the SG579 CT sail used in this deployment and EUREC^{4}A had a temperature offset (discussed in chapter 4). Measurements of salinity between the Seaglider and *Caravela* are consistent, Figure 3.4, however there is some offset to the handheld CT. It is much more likely that the handheld CTD was the victim of sensor drift than the new *Caravela* CT, especially since the Seaglider was in good agreement of *Caravela* . Of note, there is some large and unrealistic salinity spiking in the *Caravela* data which should be quality controlled in future deployments.

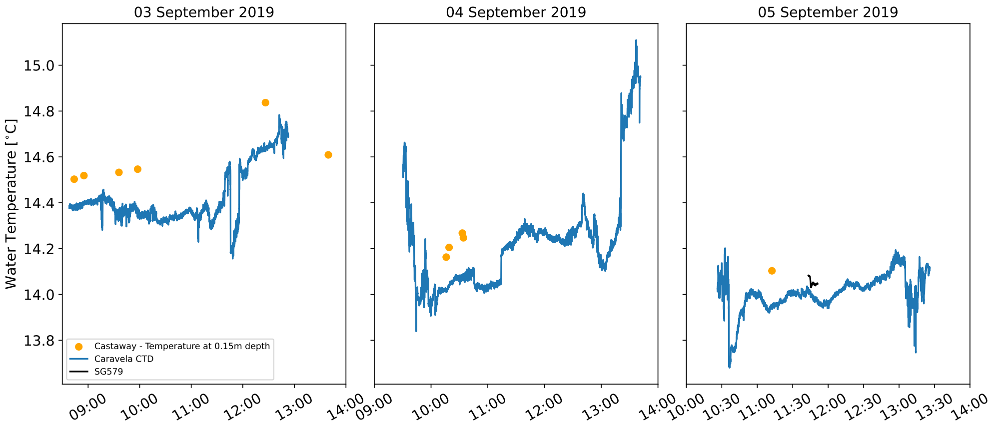

Figure 3.3: Time series of in-situ water temperature measurements from *Caravela* (blue), a handheld CTD and Seaglider SG579 (black).

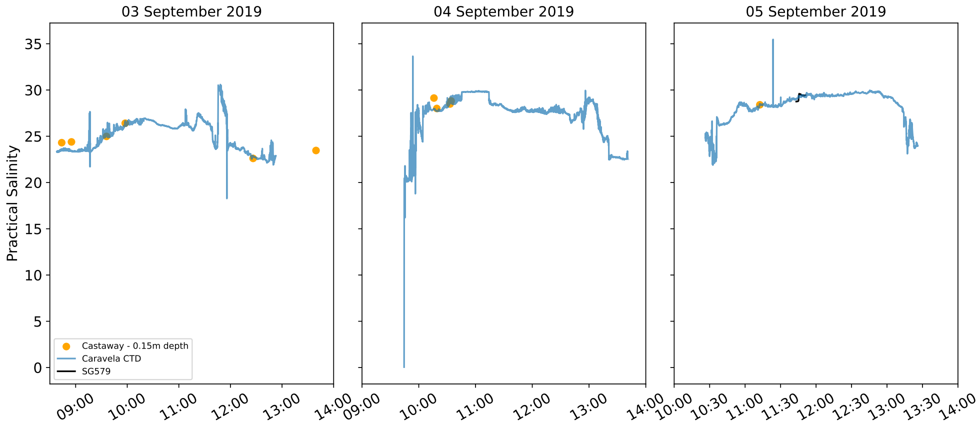

Figure 3.4: Time series of practical salinity measurements from *Caravela* (blue), a handheld CTD and Seaglider SG579 (black).

3.4.2 November 2019 Sensor Testing

The November 2019 sensor trials involved on-land testing of sensors to interrogate the data return and handling. Functioning sensors included the Valeport miniCTD (used in air), Airmar 120WX, Hygroclip and both Apogee radiation instruments. The Acoustic Doppler current profiler (ADCP) was not available for testing at this point. Measurements often began when *Caravela* was indoors, before being moved outside of the facility to start its land measurement period for a few hours each day. The vessel was brought back indoors during the afternoon. During these indoor/outdoor transitions, sharp temperature changes are visible (Figure 3.5). At 9 am 6th November 2019, the Airmar sensor initially recorded higher temperatures than the HygroClip. Whilst it is difficult to explain why the airmar read higher temperatures inside the building than the HygroClip, the slower response to being moved outside can be assumed to be a combination of the vessel supplying 10 minute averages for the Airmar sensor and the lower quality of the sensor. The Airmar accuracy

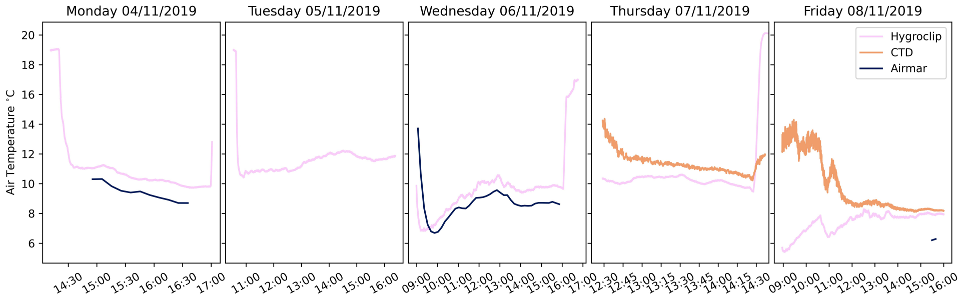

Figure 3.5: Time series of air temperature measurement from the Airmar, Hygroclip and CTD on land in Chichester, November 2019.

is ±1.1 °C at 20 °C and the HygroClip ±0.1 °C at 23 °C. Comparison of air temperature measurements across sensors using raw 1 Hz HygroClip data and 10 minute averaged airmar data files showed an offset between the Airmar and HygroClip, with the HygroClip sensor routinely recording higher than the Airmar sensor. There is a difference in positioning on the mast, but this height difference is on the order of 0.5 m and would not account for this temperature difference between sensors. The HygroClip is inside a 'beehive'-style radiation shield, which should reduce the effects of direct solar heating on the sensor. The lower temperature of the Airmar than HygroClip indicates that direct heating of the Airmar sensor was not a significant issue here (Figure 3.5). The CTD was turned on whilst the vessel was in air, so the CTD temperature has been included for interest. Whilst the Hygroclip is the better instrument for our air temperature requirements in terms of accuracy and response time, an independent air temperature validation would still be beneficial.

During this trial, it became apparent that the data output could be made more user-friendly in that the .csv delimiters (marker used to separate values or columns of data within the file) were inconsistent and data files did not all contain accurate headings or metadata. AutoNaut provided updates to the vessel to include data headings and a consistent comma delimiter for all .csv data files in subsequent deployments.

3.4.3 Barbados 2020 - EUREC^{4}A Campaign

The first full scientific deployment of *Caravela* took place from January to March 2020, as part of the EUREC^{4}A campaign (Bony et al., 2017; Stevens et al., 2021). EUREC^{4}A was designed to investigate the coupling between clouds, circulation and climate but expanded to cover many themes within meteorology and oceanography. A more detailed description of EUREC^{4}A is provided in chapters 1, 2 and 4. The *Caravela* vessel was deployed with the aid of the Barbados Coastguard on 22nd January 2020. *Caravela* traveled from Barbados to the study site and back over 33 days. This included 11 days occupying a 10 km wide hourglass-shaped sampling pattern at the study site, seen in chapter 2 Figure 3. Below I cover in more detail some of the specific technological investigations and calibrations that took place during this campaign.

Distance Traveled

Calculation of distance traveled by *Caravela* during the deployment is not a simple task, and depends greatly on the time interval between gps fixes over which the distance is being calculated. *Caravela* tracks are not straight, and have many small adjustments and loops which add to the actual distance traveled between two points. The back up location supply (yellowbrick system) was located inside *Caravela* and could be used to give a distance traveled using approximately hourly location fixes. When the *Caravela* GPS was used, I opted to calculate distance traveled using GPS fixes every two minutes. Take for example the distance traveled between deployment from Barbados and the release of the Seaglider. Using location map from the yellowbrick, I approximate this distance at around 150 km. However if the higher resolution locations are taken from the *Caravela* GPS, the total distance traveled to glider release is calculated as 296 km. This is a substantial difference in distance traveled estimates, which will in turn affect the accuracy in calculations of speed over ground. Care should be taken to consider the reason behind needing a distance traveled, as the distance calculated is highly dependant on the GPS fix interval. Average speed over ground was approximately $0.34\,\mathrm{m\,s^{-1}}$ whilst carrying the Seaglider, compared with $0.51\,\mathrm{m\,s^{-1}}$ without the Seaglider, when calculated using the the speed over ground reported in NMEA strings in the GPS_SystemTime_01 files. The aforementioned 'loops' in *Caravela* 's track were observed by the pilots during the campaign. It was observed that *Caravela* traveled slowly whilst transporting the Seaglider, speeding up after the glider was released and travelling faster again on the transit back from the study site to Barbados. This return leg to Barbados aligned more so with the easterly trade wind, whereas the outward transit was against these trade winds. It is likely that the alignment with wind and waves has a significant affect on the speed and manoeuvrability of the vessel, and this should be carefully considered in future mission planning.

Glider Transportation

Whilst a glider is being transported inside the release mechanism of *Caravela* , it needs to be ready to perform as if it had been launched from a ship. This means the glider undergoes its usual testing and sealaunch routine before being loaded into the release mechanism on land. Whilst inside the release mechanism, the glider will repeatedly try to call the Iridium satellite service (unaware that it is trapped underwater) at a set interval (given by a value called T_RSLEEP). Each of these failed attempts to make a call will use some of the gliders battery. To estimate the battery consumption of the glider whilst in the *Caravela* release mechanism, I take the last battery measurements available during pre-deployment preparation and the first available battery measurement during the EUREC^{4}A deployment, which is at the end of the gliders first dive. For the 24 V battery,1.097 Ah were consumed in the period between battery measurements (15th Jan to 28th Jan), with approximately 0.83 Ah of this attributable to the gliders first dive. For the 10 V battery, 2.976 Ah were consumed in this same period, with approximately 0.03 Ah attributable to the gliders first dive. The battery usage should be taken as upper bound of what was used while the glider was within the glider mechanism, as some useage may be due to final checks between 15th Jan and deployment of the systems of 22nd Jan. For context, in the 295 dive deployment, the 24 V battery used a total of 41.928 Ah and the 10 V battery 27.813 Ah. The total capacity available to the glider from each battery is 145 Ah for the 24 V battery and 95 Ah for the 10 V battery. Assuming all useage was attributable to the 6 days the glider spent inside the glider mechanism at sea from the 22nd to 28th Jan and no useage occured in 15th to 22nd Jan, then these calls used 3.1 % of the gliders 10 V battery capacity 0.2 % of the gliders 24 V capacity. Whilst this battery useage was not significant on this mission, it raises need for careful mission planning for a longer deployment where the glider may need to stay in the release mechanism for many weeks. This can be mitigated by extending the period the glider is asleep between call attempts. The above campaign used a sleep period of 60 minutes. If the glider battery conservation was a concern, this could be reduced to every few hours or even once a day, so long as the gliders release could be planned to occur just before the call is due. Overall the development of the *Caravela* glider release mechanism improves the endurance of a Seaglider mission, reducing the battery use from having the glider dive to reach a target location. With careful pre-planning, a glider could be held in a release mechanism for multiple weeks and launched for a notable oceanic event, which is often not possible with conventional ship work.

Matching Sensor Data

Data from *Caravela* 's sensors is often stored under a set of files per sensor. To be able to use data across multiple sensors together, the data taken and the time needs to be matched together and paired to a location. I do this using the timestamp of the data. During analysis of this deployment, discrepancies in the timestamps between the two sensors providing GPS locations were identified. The vessel set up at this time involved a Veethree GPS receiver and a Garmin GPS receiver. According to the data storage manual, the timestamp in the GPS_SystemTime files is the payload PC time, and that it is synchronised to within one second of the GPS time. We found these timestamps were often not synchronised to within one second and that there were instances were the timestamps differed as much as seven minutes. Not having a consistently correct timestamp on the GPS means we cannot accurately match sensor measurements to a location, which is problematic for any spatial analysis of the measurements onboard *Caravela* . Investigations by AutoNaut uncovered that there were buffering instances in the onboard PC which caused these timestamp discrepancies. By only using GPS data from the Garmin unit, we could overcome this issue. Extracting the data from the Garmin GPS is unfortunately non trivial. The data is contained in *Caravela* 's Serial_export directory, file nomenclature example Serial_Export_01_2020_01_15_12.dat . These files contain lines of NMEA strings. Each of these NMEA strings can be thought of as a sentence holding comma delimited characters, followed by a checksum. Whilst investigating these timestamp issues, we also decided that a more accurate positioning system was needed to accurately correct the relative wind measurements and the ADCP. The vessel was later upgraded with a GNSS system which should be used when correcting wind and ADCP in future deployments.

Wind Measurements

Unfortunately it was found within the EUREC^{4}A deployment that there was the ability for physical rotation of the meteorological sensor mast. Whilst this should have had limited impact on all other sensors mounted on the mast, it leaves scope for large uncertainties in the wind measurements. Wind measurements were reported relative to the heading of the vessel, so I needed to have confidence in both the relative wind angle and vessel heading to derive observed winds. Subsequently the design of the mast was changed to pin the mast in place and reduce the chances of the wind sensor angle becoming offset for future deployments. It is worth noting to future builders of the vessel that the alignment of the Airmar sensor needs to be checked before deployment. The sensor notch should align forward, parallel to the centre line of the vessel. Given the uncertainty in the mast alignment during deployment, issues in synchronising the GPS units with timestamps and knowledge of the need for a more accurate GPS systems for correcting wind measurements, it was chosen that ERA5 winds would be used to supplement analysis of Chapters 4 and 5. I may have been able to average out the effects of the timestamp matching problem and have tested a calculated 'true' wind against ERA5 or the *R/V Meteor*. Instead it was determined that the limited time the ship was close by to *Caravela* , the difference in measurement height between the ship and *Caravela* and time constraints of the thesis also favoured the use of ERA5 reanalysis data for this variable in chapters 4 and 5.

Air Temperature Validation

The Airmar and HygroClip air temperature measurements show poor agreement, which was previously noted in the trials deployments (Figure 3.5). Comparisons with measurements from the *R/V Meteor* show consistency with the HygroClip and not the Airmar sensor. The stated accuracy of the Airmar (±1.1 ° C at 20 °C) is much lower than that of the Hygroclip (±0.1 K @ 23 °C) so some discrepancy was expected, but not as much as shown in Figure 3.6. The lower air temperature measurements reported by the Airmar in both this and the Chichester deployment indicate an offset in the Airmar sensor. This has not been further investigated or corrected as I instead utilise the HygroClip air temperature. I recommend the use of the HygroClip temperature values for any scientific purposes in future campaigns.

To validate the HygroClip temperature measurements, I select measurements where the distance between *Caravela* and the *R/V Meteor* was 1 km, averaging the data using the median at 1 Hz (Figure3.7). The *Caravela* HygroClip measurements show similar trends to the temperature data available from the *R/V Meteor*. On 5th February there are rapid decreases in temperature readings at 16:30 and 17:15 from *Caravela* which are not present in the ship data. 11 days later there is a second period of co-location of the vessels. The HygroClip sensor does appear to be reading somewhat higher than the ship. I instead used measurements from a 10 m weather station on the front of the *R/V Meteor* bow to further validate the HygroClip sensor (Figure 2.4). These meteorological station data were provided by private communication. Based on the agreement with the Meteor weather station data in Figure 2.4, I decided a correction to the HygroClip air temperature was not required.

The Hygroclip time series stopped on 18th February due to sensor failure. The Hygroclip

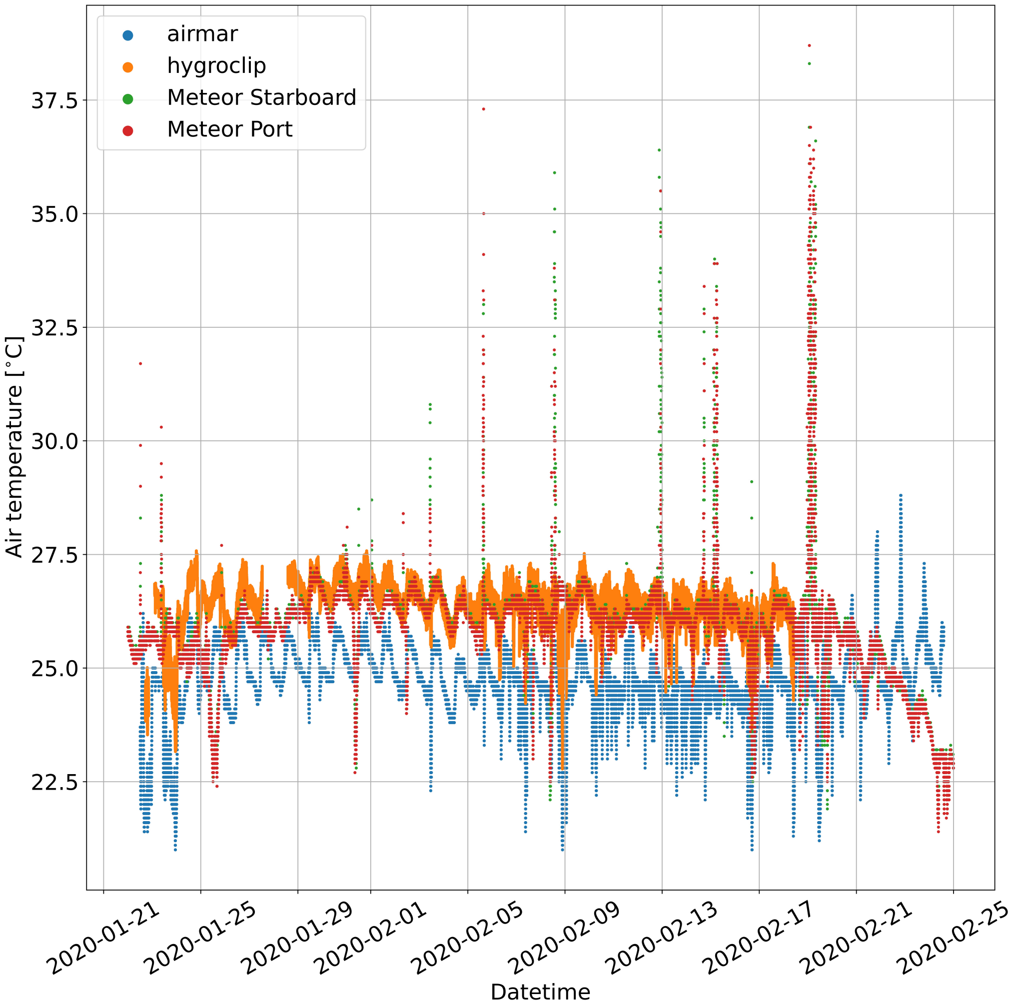

Figure 3.6: Time series of air temperature measurement during EUREC^{4}A . Red and green points describe the *R/V Meteor* port and starboard measurements respectively.

sensor has since been repaired and is recommended be used for air temperature measurements in future campaigns.

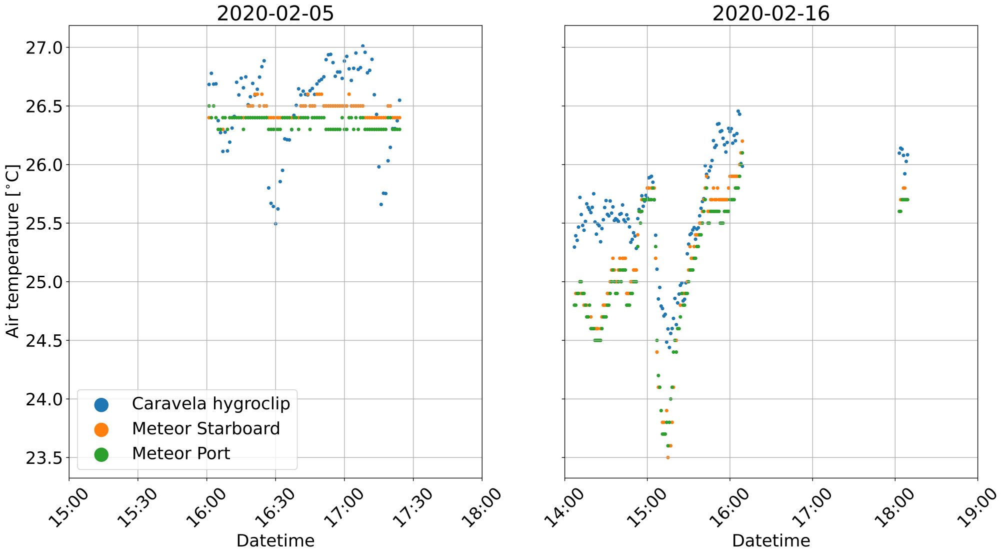

Figure 3.7: Time series of air temperature measurement during EUREC^{4}A . Orange and green points describe the *R/V Meteor* port and starboard measurements respectively and blue *Caravela* 's HygroClip sensor. 1 minute medians are shown, where the two vessels are less that 1 km apart.

CTD

The CT sail used in this deployment was an unpumped CT sail. There is spiking in the conductivity values from this CT sail, I investigate the possibility that there is some link between this spiking and *Caravela* 's motion in Figure 3.8. It appears that times where the vessel speed over ground spikes, the conductivity measured by the CT sail also spikes. This indicates a relationship between the vessel speed and accuracy of the conductivity measurements. Whilst I do not know the exact cause, it is likely that the flow rate over the CT sail is contributing to the conductivity spiking. To combat this, a pumped CT sail was later installed instead to regulate flow rate and hopefully improve measurement quality.

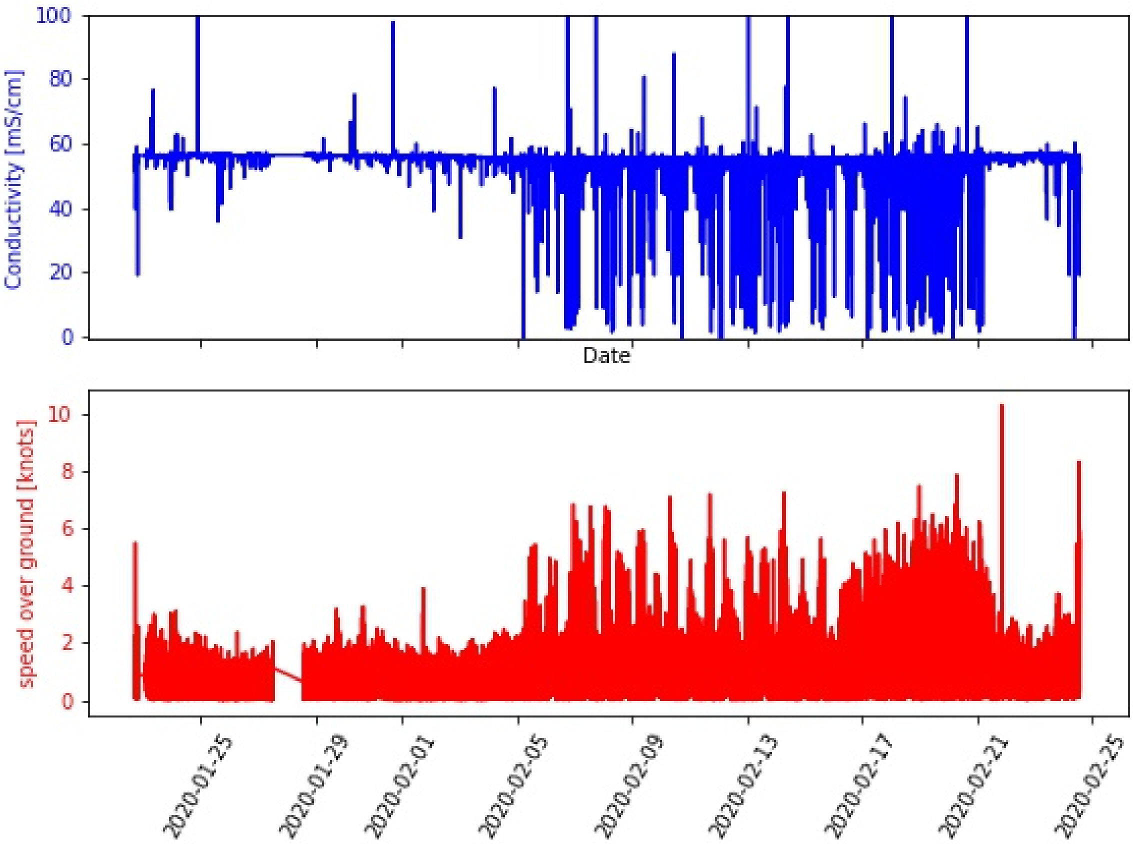

Figure 3.8: Timeseries of Conductivity values from *Caravela* (top panel) and speed over ground as reported by the vessels onboard estimates (bottom panel)

Downwelling Radiation

EUREC^{4}A was the first deployment in which I could independently verify the radiation measurements from *Caravela* . To do this, I use data from the Barbados Cloud Observatory (BCO) (Stevens et al., 2016) available through the EUREC^{4}A data repository (https://eurec4a.aeris-data.fr/) (Jansen et al., 2021). At the end of the campaign, *Caravela* was piloted along north, south, east and west legs toward the south of Barbados for approximately one day. It is these measurements in close proximity to Barbados that I use to compare to the BCO.

Figure 3.9 shows the timeseries of downwelling shortwave radiation from *Caravela* , the BCO and ERA5. The magnitudes of downwelling shortwave radiation are consistent across datasets on the 21st February, however *Caravela* reports lower values on 22nd February. *Caravela* also detects a midday decrease in longwave radiation. The BCO radiation is broken down into diffuse and direct components (not shown). The diffuse component also shows a midday decrease in measured radiation on 21st February, but not on the 22nd. These downwelling radiation observations do have some differences, but the general similarities in measurement

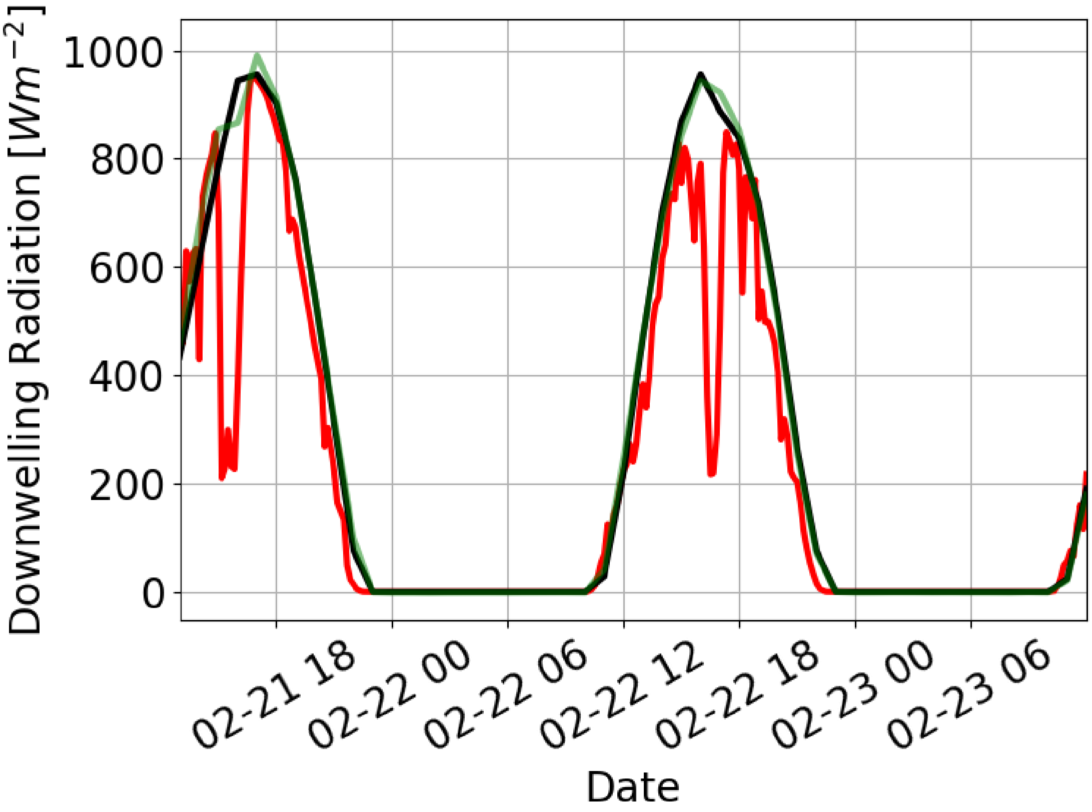

Figure 3.9: Downwelling shortwave radiation measured by *Caravela* (red), the Barbados Cloud Observatory (green) and ERA5 (black)

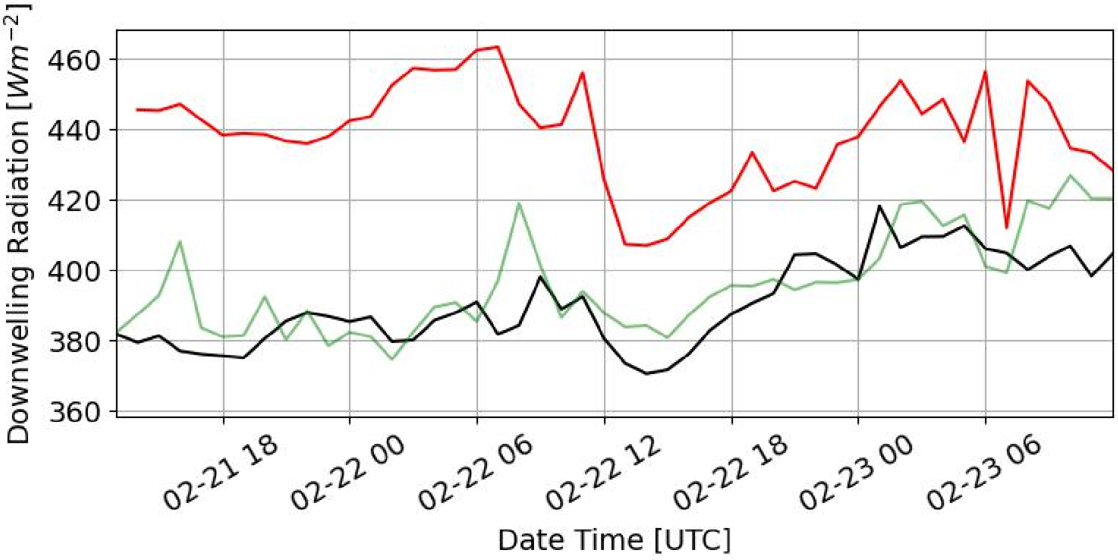

Figure 3.10: Downwelling longwave radiation measured by *Caravela* (red), the Barbados Cloud Observatory (green) and ERA5 (black).

magnitude gives us confidence that the measurements from *Caravela* are reasonable.

The downwelling longwave radiation measurements are also compared to ERA5 and the BCO (Figure 3.10). On average, *Caravela* measurements of downwelling longwave are 35 W/m^2 higher than the BCO. The much better agreement of the BCO to ERA5 than *Caravela* indicates that there is some kind of offset in *Caravela* 's longwave measurements. This is discussed more so in chapter 4.

3.4.4 Littlehampton Sea Trials 2022

The Littlehampton trials involved a day at sea with *Caravela* , completing the manufacturer required acceptance tests after changes to the data handling and boat hardware. The main upgrade in the preceding period was the addition of a VectorNav GNSS system for more accurate vessel heading, pitch and roll and GPS location than the Garmin and Veethree GPS units. The biggest driver for this was accurate calculation of the vessel's heading for derivation of true wind velocity from the Airmar and true current velocity from the ADCP. AutoNaut also updated the data pathway such that the Airmar 120WX NMEA strings now report to the payload PC onboard the *Caravela* , under the directory NMEA_LOGGER_02.

During this sea trial, we used an empty Seaglider faring within the release mechanism. During tow out of the harbour the Seaglider faring slipped out of the release mechanism and surfaced unexpectedly. To install a glider into the release mechanism, *Caravela* must be on land/deck where the mechanism can be accessed. By the time we had returned to harbour after the rest of the tests, the tide was too low to repeat the release mechanism testing. It is likely that the accidental release is due to not winding the Seaglider release mechanism tightly enough. From experience, we have found that the mechanism needs to be a few turns tighter than the manual describes. A small strip of rubber was also added to the glider release mechanism to improve friction with the glider body and limit the chance of accidental release in rough conditions.

Whilst at sea, we had some trouble getting *Caravela* to travel as expected when transferring from SSSCP to Iridium. When transferring from one communications method to the next, the vessel would change dorection by 180° without being instructed to do so. This was subsequently addressed by AutoNaut after the campaign and was an issue with the configuration of the heading after the new GNSS install.

There was also a fault with the CTD cable so the new Seabird CTD could not be tested. As a result of revealing these issues, we concluded that a further round of testing should be conducted before on the upgraded vessel.

3.4.5 Chichester Sea Trials 2022

These trials were a continuation of those in Littlehampton two months prior, to address some handling issues noticed during the in-water testing at Littlehampton. After this Chichester deployment, *Caravela* performed well and was fit for use from the UEA team's perspective. Following on from mast alignment concerns in EUREC^{4}A , we had identified a free axis of rotation where the mast was connected to the hull which was rectified with additional grub screws. The Airmar unit had also worked loose on top of the mast, which is detrimental to wind measurements. All wind measurements are relative to the centre line of the vessel, so the sensor needs to stay aligned to the centre line both by the mast join the the hull, and its own seating on the mast. The Airmar was tightened on the mast and marked with a dash for forward alignment. Care should be taken to confirm the mast and Airmar are secure and aligned with every use in the future.

3.4.6 Oban 2023

This sea trial involved user tests of the vessel to verify that she was fit for use prior to the PICCOLO Antarctic deployment. No significant issues were identified during this test, however the joystick communications did appear unreliable. Our primary use of the joystick up to this point had been steering the vessel whilst she is towed during launch and recovery. If the rear rudder system is disconnected, the vessel can be towed behind without need for active steering and this was demonstrated successfully.

3.4.7 PICCOLO

Analysis of the PICCOLO deployment falls outside of the scope of this thesis.

3.5 Data Processing

Due to the relatively recent growth of the uncrewed surface vessel industry, at the point of writing there is no agreed community standard for data handling and processing. As a result of this, data quality control and handling have been implemented based upon the research needs of the science discussed later in this thesis. An overview of how science sensor data have been managed is given below.

It is unknown whether there is a sensor lag between triggering of a sensor recording measurement and the data being recorded. Given that the sensors record data individually and the vessel's maximum speed will be no more than a few $\mathrm{m\,s^{-1}}$, any issue due to measurement lag should be negligible compared with the limit of accuracy of a GPS location, therefore this is not investigated further and assumed to not be an issue when aligning sensor measurements.

3.5.1 Quality Control

Quality control was applied to raw sensor data during post processing. Below I outline the methods applied to the data. Table 3.5 outlines QC markers that can be used on *Caravela* data. The following QC description was trialled on *Caravela* 's CTD data.

Flag Value	Description
0	Unprocessed data
1	Data has passed all processing applied to this dataset
2	Value beyond chosen upper limit
3	Value below chosen lower limit
4	Value identified as bad during median filter despiking

Table 3.5: Flags used to identify spurious data within the *Caravela* observations

Data is flagged with a 0 before processing and data that passes all checks is given a flag of 1. Note only one 'flag identifier' is retained per data point, although it is possible that a data point has been flagged for multiple other reasons. For example, a data point with a flag 4 identified during median despiking may have earlier been flagged with a 2 for being outside the defined upper bound, but only the last flag applied during processing remains visible, i.e. flag value 4.

Despiking was carried out using a median filter method (Brock (1986)), assessed to be the most versatile despiking method for large scale standardized surface-atmosphere exchange data (Starkenburg et al. (2016)). To improve processing, data beyond the feasible upper and lower bounds are removed before despiking begins. Initially a first pass filter is applied using a rolling median value at position i over 2N+1 values, such that N is the order of the pass. When i is either the first or last values in a dataset, the raw measurements are used as there is not enough data to form a rolling window. All data is retained during this median calculation. The difference, D_i, between the measured data and median is computed. The values of D_i are represented in a histogram, where the bin size should be twice the measurement resolution and the number of bins odd such that they centre on $D_i = 0$ (Brock (1986)). The first empty bin in the distribution of D_i is identified as the threshold and D_i values beyond these threshold as spikes. It is worth noting the limitation of this method is that spikes longer in duration than 2N+1 cannot be identified but that passes of order N = 3 or higher risk removing valid signal fluctuations (Brock (1986)).

In application to *Caravela* CTD data, the high frequency of the data means that spikes can be larger than a 7 point window of an N=3 filter pass. Points which appear as anomalous spikes by eye are thus not identified by the algorithm. Realising that this method may not in fact be appropriate without running at much higher order and risking elimination of real data variation, it is recommended for future work to consider development of a more robust despiking algorithm specific to each sensor. A simpler approach of identifying data like flagging data using standard deviations from the mean may capture the most extreme part of a spike, but also risks identifying data within the generally accepted variability range. Another method that could be applied is that used in Argo floats where a measurement change of a certain quantity within 500 dbar is considered a spike (Wong et al. (2023)). This is defined as

$$\text{Test value} = |V2 - (V3 + V1)/2| - |(V3 - V1)/2|$$

where V2 is the measurement being tested, and V1 and V3 are the values above and below (Wong et al. (2023)). For this thesis, I opt instead to calculate 10 minute median values from all sensors. Whilst this is not the most robust method of quality control, it ensures elimination of outlying data and preserves resolution to enough of a degree for the scope of heat budget analysis (chapter 4 and 5). By using 10 minute medians, this also eliminates most instances of the earlier discussed mismatching timestamps issue (section 3.4.3) experienced with the data in the EUREC^{4}A campaign. It is possible that using a 10 minute median is also removing some real small scale fluctuations, hence the recommendation of a future despiking algorithm. It is hoped that wider community push towards surface vessel inter-comparability in the future brings standardised processing and guidelines for surface vessel data.

3.6 Summary

This Chapter looked to address the first question posed in this thesis *Can an adapted autonomous surface vessel provide a viable platform for air-sea interaction studies?*. Given the successful deployment of the EUREC4A and PICCOLO campaigns, this question can quickly be answered with a yes. It is certainly possible to gather the necessary essential ocean and meteorological variables required for bulk-flux calculations of air-sea interactions with an autonomous surface vessel. In addition, a vessel adapted to carry a Seaglider and facilitate complimentary underwater studies, such as *Caravela* , brings a new and novel way to plan and conduct air-sea interaction studies,with more possibilities for studies beyond research vessel based work.

Uncrewed surface vessels are still an emerging and developing technology. At the time of writing, the scientific community is coming together to develop recommendations for best practice and data handling, but there is no standardised way of using or processing surface vessels sensor data. It is up to the user or manufacturer to facilitate data output appropriate to the scientific niche of each USV. We have worked alongside AutoNaut to enhance the usability and improve the sensor suite of the USV *Caravela* , such that it should be a robust vessel for measuring physical air-sea interaction processes. As with any cutting edge technology, there is still scope for improvements in sensor quality and data handling. Additional learnings, recommendations for future work and improvements on this vessel that fall outside of the scope of the body of this thesis are discussed in Chapter 6. A short summary of important findings not in the manuals for *Caravela* users are included below.

3.7 Specific recommendations for future *Caravela* users

Here is a 'highlight' list of recommendations/ checks from this authors experience with the *Caravela* vessel.

- Prior to deployment, align the mast such that the Airmar 0° reference is parallel to the *Caravela* vessel centre line. Wind is reported relative to the vessel so the alignment matters.
- Sensor heights and depths should be rechecked for a deployment, as a change in payload or ballast will change the vessel waterline for sensor depths. For the meteorological sensors, the sensor height should be measured prior to deployment, as the position on the mast can change for all except the Airmar.
- If deploying a Seaglider, do not use the number of turns of the glider mechanism stated in the original manual. Turn until the mechanism feels secure around the glider, but

do not overtighten.

- Ensure the ADCP is correctly aligned within the vessel housing. At the time of writing, the ADCP has never been processed. Alignment of the output with the GNSS system will be needed to utilise the ADCP data.
- The pumped CTD system has been run on *Caravela* but not independently tested, the best available dataset to do this will be PICCOLO campaign data, and this should be checked by the next user.
- Sensor calibration dates should be checked well in advance of the next deployment. The CTD is likely to need calibration and I recommend the longwave radiation sensor is returned to manufacturer for calibration based on the offsets found in the EUREC^{4}A campaign.

4

Upper Ocean Mixed Layer Heat Budget

Synopsis

In this chapter I quantify the air-sea heat fluxes using observations from the EUREC^{4}A project, as well as an ERA5 reanalysis product. Biases are identified in the ERA5 heat fluxes in the surface net heat fluxes. The mixed layer heat budget is calculated with observations and I assess how well the heat budget can be closed using the net heat flux term only.

4.1 Introduction

The upper ocean mixed layer heat budget is an important tool for discerning the dominant heat transfer processes driving SST variability in a region (see chapter 1 for more detail). Historic assessment of ocean mixed layer heat budgets in the tropical North Atlantic have shed light on the dominant processes of the region. Yu et al. (2006) found that the dominant driver of annual SST evolution north of 10 °N was air-sea heat flux. More specifically, north of 10°N, the dominant flux component was the shortwave radiative flux. North of 8°N, evidence suggests SST changes are driven by seasonal changes in shortwave radiation and latent heat loss (Foltz et al., 2003). The whole western tropical Atlantic heat budget was investigated by Nogueira Neto et al. (2018), where a site in the northwestern zone between 10 °N and 20 °N, west of 35 °W captured the North Equatorial Current and Counter Current and a year-mean net surface heat flux of $-21.2\,\mathrm{W\,m^{-2}}$, which dominated the mixed layer heat budget. In a complementary study to EUREC^{4}A , Iyer et al. (2022) finds sensible heat flux of $-6.6\,\mathrm{W\,m^{-2}}$ and latent heat flux of $-157\,\mathrm{W\,m^{-2}}$, for January to February 2020, using COARE 3.6. Bigorre and Plueddemann (2021) evaluated annual averages from the NTAS buoy in the tropical North Atlantic. The NTAS buoy lies approximately 690 km from the study site, visible in Figure 1.4.Extracting February only from the period 2001 - 2012 for comparison with my observations, the sensible and latent heat flux were around $-7\,\mathrm{W\,m^{-2}}$ and $-170\,\mathrm{W\,m^{-2}}$ respectively. Whilst not in the tropical North Atlantic, Vijith et al. (2020) gives the first mixed layer budget closure from observations alone and its methodology is applicable to the tropical Atlantic. If air-sea heat fluxes dominate SST variability in the NWTA, then it is vital to identify any biases in flux products in this region, such that SST variability can be better represented. Whilst air-sea interactions over large time and space scales are reasonably well studied, the effects of submesocale and mesoscale processes on the atmosphere and air-sea interactions are less well understood (Seo et al., 2019). Individual observational studies can provide high spatial resolution over a small area, to help elucidate the effects of small scale SST variability on air-sea interactions, and are highly desirable in addressing this knowledge gap.

Multiple studies have assessed and quantified the difference between observations and reanalysis products in terms of air-sea heat fluxes around the globe (Josey, 2001; Song, 2020; Han et al., 2022; Al Senafi et al., 2019). Most reanalysis products contain biases, but ERA5 and its predecessor ERA-Interim have been shown to perform best in terms of surface flux biases (Sanchez-Franks et al., 2018; Pokhrel et al., 2020). Josey (2001) investigated a region of the northeastern tropical Atlantic and observed an underestimation of net heat gain into the ocean, by ERA-Interim of $32 \pm 9\ \mathrm{W\,m^{-2}}$, predominantly due to underestimated shortwave flux gain to the ocean and overestimated latent heat loss compared with buoy observations. The reanalysis product ERA5 was shown to underestimate the magnitude of turbulent fluxes in the Bohai Sea, China, with ERA5 reporting average sensible heat flux as only 70% of that measured by a buoy. (Song, 2020). In the East China Sea, ERA5 overestimated the magnitude of all four flux components compared with observations, the largest being a $45.3\,\mathrm{W\,m^{-2}}$ overestimate of the latent heat flux magnitude (Han et al., 2022). These few studies highlight air-sea flux biases in ECMWF fluxes in various locations, with the magnitude of biases in each flux component dependant upon location and temporal scale investigated. It is therefore important to increase capacity to calculate bulk fluxes from in-situ measurements across global oceans, such that the regional drivers of flux biases can be better quantified, and hopefully improved in future ECMWF products.

This chapter will use a bulk formula approach to investigate a region of the NWTA, where ocean heat budget analyses and observations are historically limited. I will investigate whether variability in mixed layer temperature and therefore SST can largely be accounted for by surface fluxes and quantify biases in the surface fluxes given by the ERA5 reanalysis

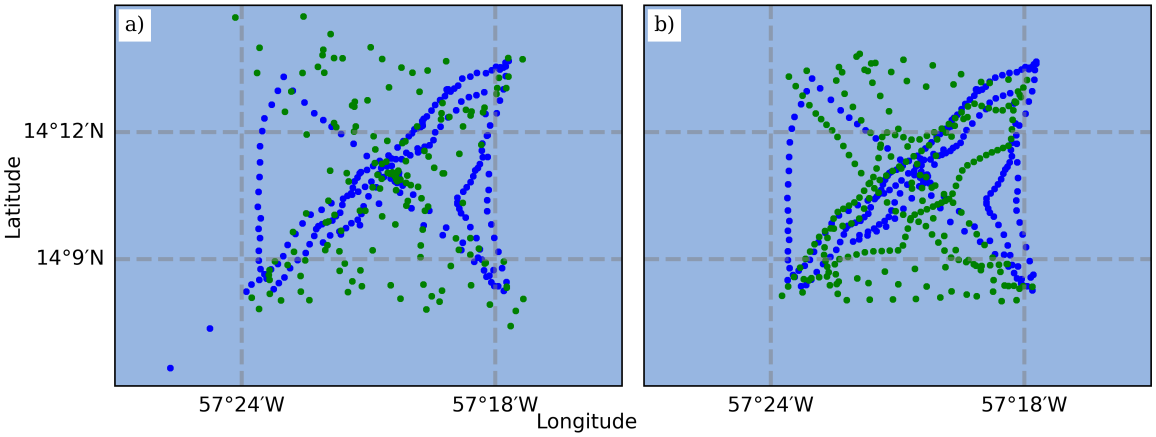

Figure 4.1: a) Locations at the end of each glider dive. b) Locations of 1 hour, 1 m interpolated glider data. SG579 is blue and SG637 is green.

product for this region.

4.2 Observations and Methodology

The EUREC^{4}A campaign was introduced in section 1.7. Within the scope of the research in this chapter, I base all analysis on the 10 km x 10 km site, restricted to 6th February 2020 12:30:00 - 16th February 2020 08:30:00, where the two Seagliders and *Caravela* were inside this site. The following sections describe data handling methods applied to make the Seagliders, *Caravela* and ERA5 comparable. All analysis was carried out using UTC date times. Comparisons of *Caravela* observations to observations from the EUREC^{4}A campaign are discussed in Chapters 2 and 3.

4.2.1 Seagliders

This section explains the data processing of the SG579 and SG637 to enable calculation of equation 4.2.3, specifically the temperature tendency term, mixed layer depth and verify the specific heat capacity.

Three Seagliders were used during this campaign, one deployed from another autonomous system (*Caravela* , see Chapters 2 and 3) and two Seagliders deployed from the *R/V Meteor* into a 10 km square henceforth referred to as the 'study site'. SG579 completed a bowtie pattern, SG637 completed a complementary pattern at 90° to SG579 (Figure 4.1a). Figure 4.1b shows the glider locations after processing onto a regular grid, described further in this section. SG620 acted as a virtual mooring at the central intersection of the other two Seagliders. SG620 was recovered on 5th February 2020 and plays little role in the scope of this research. This heat budget study focuses on data collected in the study site after recovery of SG620.

Data from Seagliders SG579 and SG637 were passed through the UEA Seaglider toolbox commit version 3f16640, available from https://bitbucket.org/bastienqueste/uea-seaglider-toolbox/src/toolbox/. Raw engineering files from the glider were uploaded into the toolbox and manually flagged for anomalous values in the temperature and conductivity or salinity profiles. As part of the toolbox, a hydrodynamic flight model regression (Frajka-Williams et al. (2011)) was applied to the dataset and a conductivity thermal lag correction was calculated and applied (Garau et al. (2011)). After processing through the toolbox, glider data underwent a second round of quality control (QC) to deal with unrealistic near surface data where the gliders were performing surfacing manoeuvres. Salinity values below 32 on the practical salinity scale were removed, as these are unrealistic for this region in February according to data in the World Ocean Atlas (Reagan et al., 2023, 2024). All glider descents were removed to eliminate the possibility of solar heating and lack of CT sail flushing during the surface manoeuvre. A pressure geometry correction was applied to the conductivity and salinity measurement depths to account for the distance between CT sail and pressure sensor within the Seaglider. For SG579, any CT measurements associated with depths above the surface (0 m) were removed, as these are unrealistic based on the behaviour of a Seaglider during its surface manoeuvre. For the top 10 m of both gliders, temperature, conductivity and absolute salinity data points more than two standard deviations away from top 10 m median were also flagged. This decision was made due to a wide spread of anomalous data at the surface, particularly in the conductivity and salinity due to the reduced flushing of the CT sail during the surface manoeuvre of the Seaglider. All flagged data points were removed before further analysis and the remaining data are shown in Figure 4.2 panels a and b and Figure 4.3 panels a and b.

For each Seaglider, data were initially processed by profile. The conductivity and in-situ temperatures (with flagged data removed as described above) were linearly interpolated onto

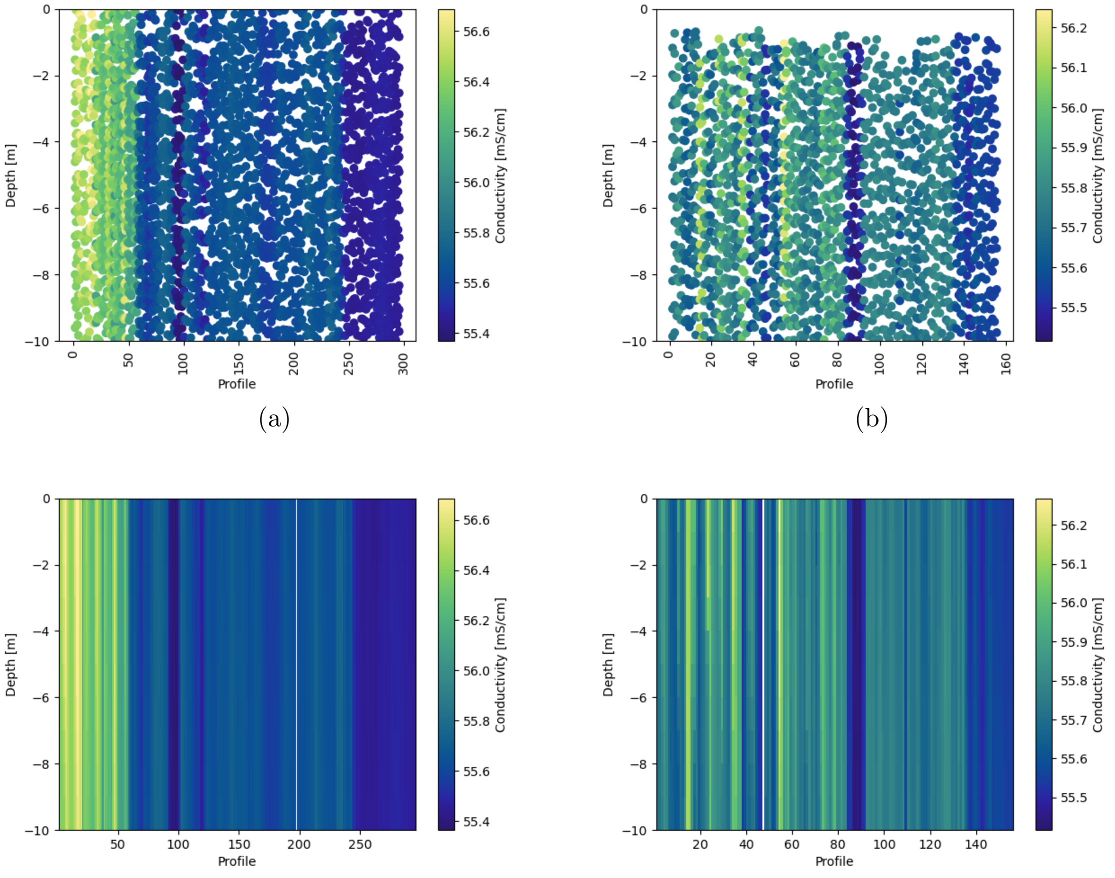

(a) (b)

(c) (d)

Figure 4.2: Conductivity measured by SG579 (left) and SG637 (right). a,b after removing data points that failed quality control. c,d after linear fit applied and missing near-surface values extrapolated from this fit.

a 1 m regular depth grid, starting at a depth of 0.5 m. These are shown in Figure 4.3 c, d for temperature. Missing near surface values were then filled using a fit of the clean data of the top 10 m (4.3 e, f) and (4.2 c, d); this procedure will now be explained.

Profiles were fitted with a linear approximation for conductivity. For temperature I used both a linear and exponential fit to the glider data points after flagged data were removed, to consider the possibility of diurnal warm layer formation in the region. In this region, it is important to consider the possibility of diurnal warm layers due to the effects on surface fluxes. Increased daytime SST, for example due to a diurnal warm layer, increases the longwave and turbulent fluxes thus decreasing net flux into the ocean and causes cooling of the mixed layer. On average, reduction in net flux due to this process in the North Atlantic is $5\,\mathrm{W\,m^{-2}}$ (Cornillon and Stramma, 1985; Bellenger and Duvel, 2009) and on daily scales, diurnal warm layers can perturb fluxes above $10\,\mathrm{W\,m^{-2}}$ (Bellenger and Duvel, 2009). On the other hand, our location in the NWTA's trade wind region has winds in the region of $10\,\mathrm{ms^{-1}}$ according to ERA5. At winds of $7\,\mathrm{ms^{-1}}$ or above, I expect minimal to no diurnal warm layer formation

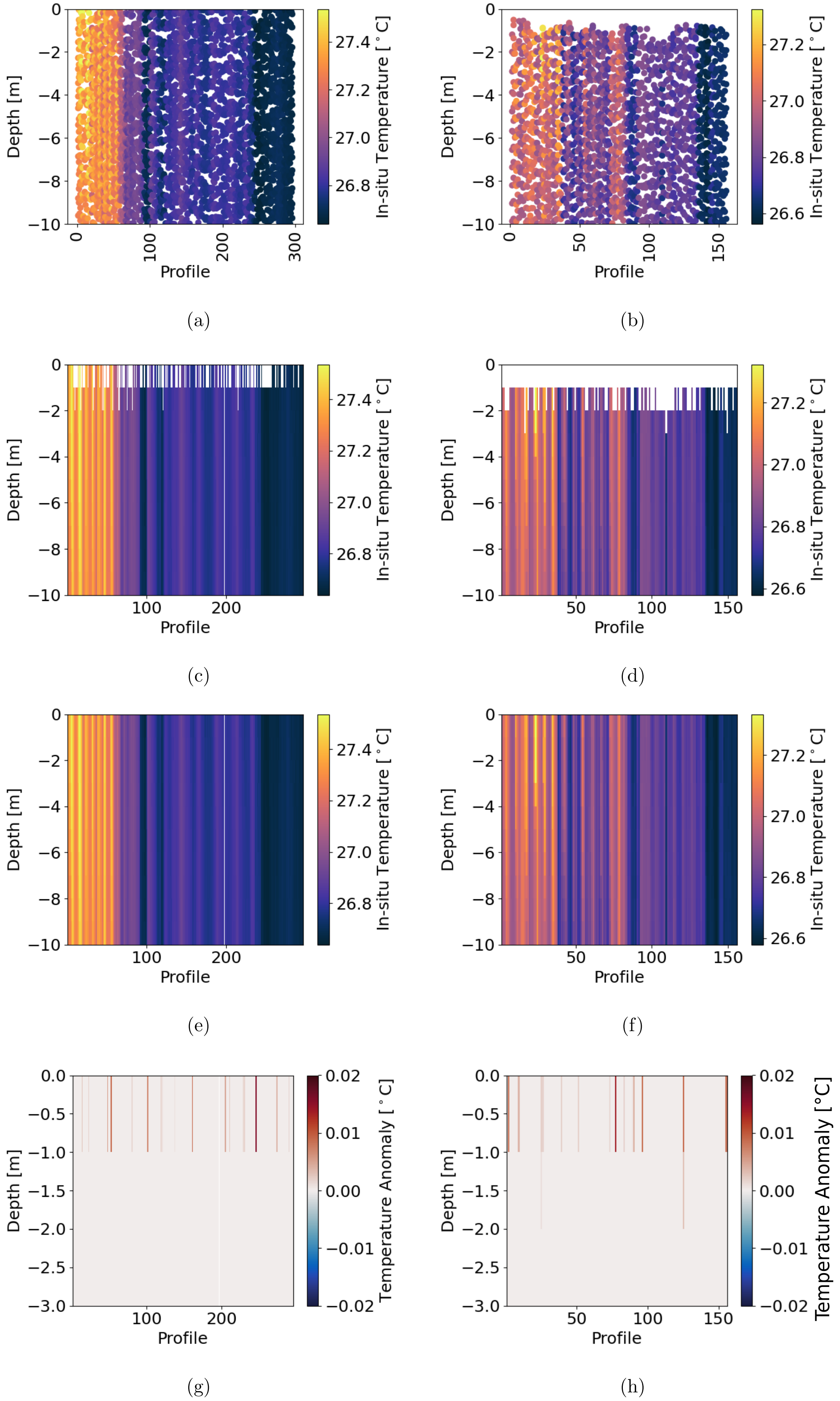

(a)

(b)

(c)

(d)

(e)

(f)

(g)

(h)

Figure 4.3: (caption on next page)

Figure 4.3: SG579 (left) and SG637 (right) in situ temperature data cleaning methodology. (a,b) data that passed quality control. (c,d) after cleaning and interpolation. (e,f) after surface extrapolation. (g,h) difference in temperature when using linear fit vs exponential fit as exponential minus linear (shown only for values derived from the exponential fit).

(Figure 10 of Matthews et al. (2014)). However, Matthews et al. (2014) do detect a residual diurnal cycle in high wind, low solar radiation conditions. In February, average diurnal SST amplitude variation is less than 0.2 °C for the NWTA (Bellenger and Duvel, 2009).

To investigate the possibility of diurnal warm layer formation, I apply two different fits to the surface temperature measurements. When extrapolating the Seaglider data to the surface I use a linear fit over the top 10 m and an exponential of the form:

$$(be^{(-x/c)}) + a \tag{4.2.1}$$

based on the representation of diurnal warm layer formation (Matthews et al., 2014)

$$T_{dh}(d) = T_{dh0}e^{-d/H} + \epsilon \tag{4.2.2}$$

where Matthews et al. (2014) define $T_{dh}(d)$ as the magnitude of diurnal warming at depth d, and T_{dh0} at corresponding depth 0, i.e. SST, H the scale depth and ϵ a residual constant. I take a to represent the foundation SST, whereas Matthews et al. (2014) use ϵ as a residual after removal of the 6am SST. The foundation SST is the temperature at the base of the diurnal temperature gradient experienced in the mixed layer, assuming the previous days diurnal stratification has decayed. Otherwise, b is comparable to T_{dh0} and c comparable to the scale depth. The exponential fit of this form was generated for each Seaglider profile individually. For every glider profile, a root mean square error (RMSE) was produced alongside a linear and an exponential fit. For any glider profile with an exponential fit that did not converge using equation 4.2.1, the linear fit was used to produce surface temperatures. For profiles where both a linear and exponential fit converged, the fit with the lowest RMSE was used (Figure 4.4) such that the possibility of diurnal warm layer formation is included in the processing. Additionally, the linear fit extrapolation was used for profiles that had limited data in the top 2 m as the the accuracy of a fit could not be verified (Figure 4.4 b). In excluding the possibility of an exponential fit where there is little data available in the top 2 m, I remove the possibility of producing exponentially-fitted surface values where the profiles exponential fit produces surface temperatures 0.1 °C larger than the profiles linear fit. The

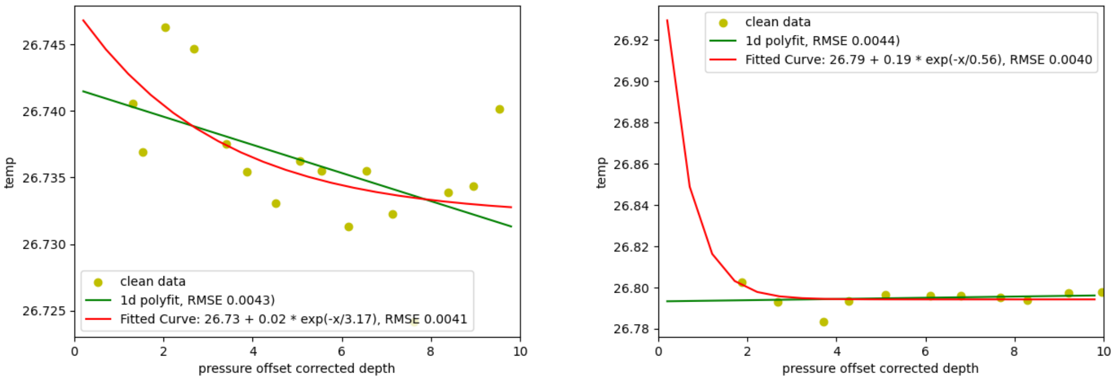

(a) (b)

Figure 4.4: Examples of exponential fits to test for near surface diurnal warm layers. a) shows a successful implementation of a diurnal warn layer exponential fit. b) shows an example where I manually reject the exponential fit due to lack of near surface data.

inclusion of these exponential fit produced values on profiles with no near surface data would increase error in the heat budget by falsely raising the mixed layer temperature. Many profiles where temperature data is available through most of the top 10 m (Figure 4.4 a) have a difference of tenths or hundredths of a degree between the linear and exponential surface fit, indicating that most profiles do not contain diurnal warm layers, consistent with what I expect from Matthews et al. (2014). For SG579, 135 missing near surface temperature values were approximated with the linearly fitted function and 17 by the exponential approximation. For SG637, 201 missing near surface temperature values were approximated with the linearly fitted function and 16 by the exponential approximation. The difference in temperature between the linear and exponential fitted values are visible in Figure 4.3 g,h, the difference between the two approximations being no larger than 0.02 °C.

Profiles are linearly interpolated at each depth level (0.5 m to maximum dive depth) onto hours, marked by half past the hour, to give a 1 m, 1 hour resolved dataset. Both glider time series are cut to the date time range 6th February 2020 12:30:00 - 16th February 2020 08:30:00, which begins when both these gliders and the surface vessel *Caravela* are inside the EUREC^{4}A study site and ends when the gliders are changed to shallow dives, ready for recovery to the ship.

Inter-comparison of temperature data from *Caravela* and the two gliders (not shown) raises concerns that SG579 may have an offset in the temperature observations. Using 0.5 m temperature from both Seagliders, SG579 has a mean difference more than Caravela temperatures of 0.06 °C, whereas SG637 mean difference is 0.02 °C, such that 637 is in better agreement with Caravela . To quantify and correct for this offset in SG579,

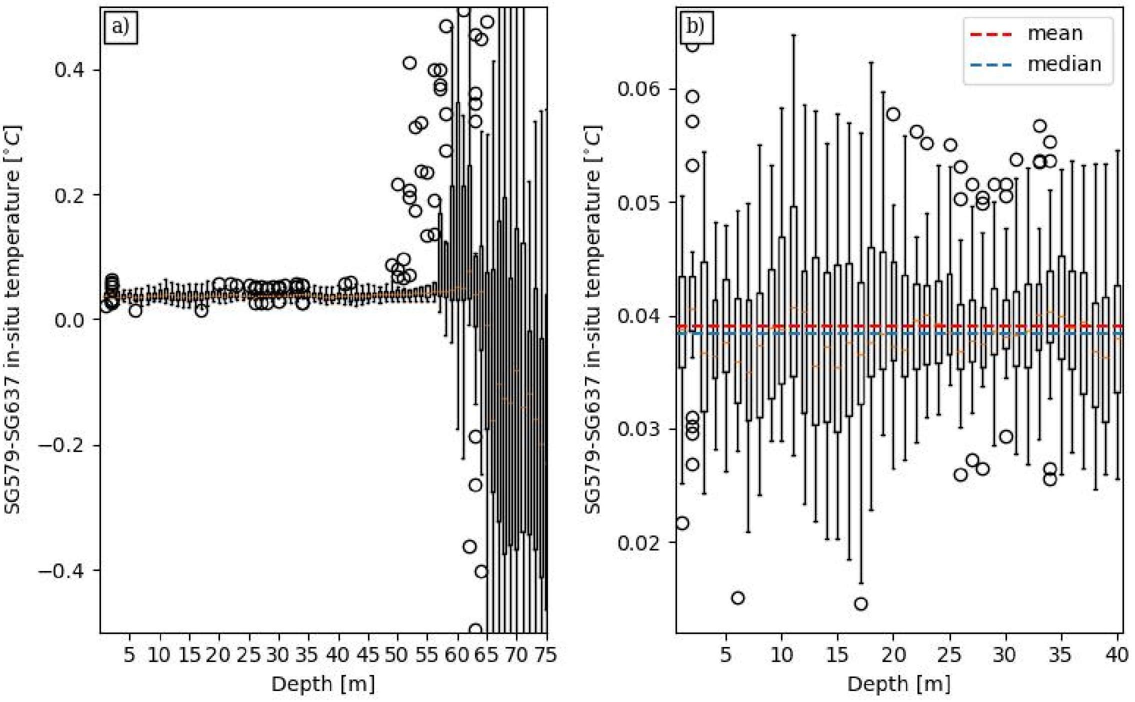

Figure 4.5: Difference in temperature (SG579 - SG637) at each 1 m depth after Seaglider data processing (described in text), shown as a boxplot over all data points where the gliders are within 1 km of each other. Each box spans the 1st to 3rd quartile with an orange line at the median. Whiskers extend to the furthest datapoint 1.5 times inside the interquartile range from the box. Circles highlight datapoints outside of this range. a) shows all data within the varying depth mixed layer, b) shows the top 40 m with a depth mean temperature offset(red) and depth median temperature offset (blue).

temperature measurements are compared where SG579 and SG637 are within 1 km of each other (Figure 4.5a,b). SG637 in-situ temperatures are subtracted from SG579 in-situ temperatures at every time and depth. A boxplot over the temperature differences is plotted for the top 75m depth in Figure 4.5a. Throughout the time period, the mixed layer depth (calculated and discussed later in this chapter) varies by 30 m. This study is interested in correct representation of the ocean mixed layer, so I determine the in-situ temperature correction by taking depths which consistently fall with the mixed layer, ie the top 40 m. The median temperature difference over the top 40 m is 0.038 °C. This value is subtracted from all SG579 in-situ temperature values assuming a fixed relationship between depth and temperature offset.

All other physical parameters subsequently used were calculated on 1 hour, 1 m resolved dataset using properties calculated using the TEOS-10 GibbsSeaWater package (McDougall and Barker, 2011). From here onwards, I use Conservative Temperature Θ and Absolute Salinity S_A. Time series of these and potential density anomaly σ_Θ from SG637 and SG579 are shown in Figures 4.6 and 4.7 respectively.

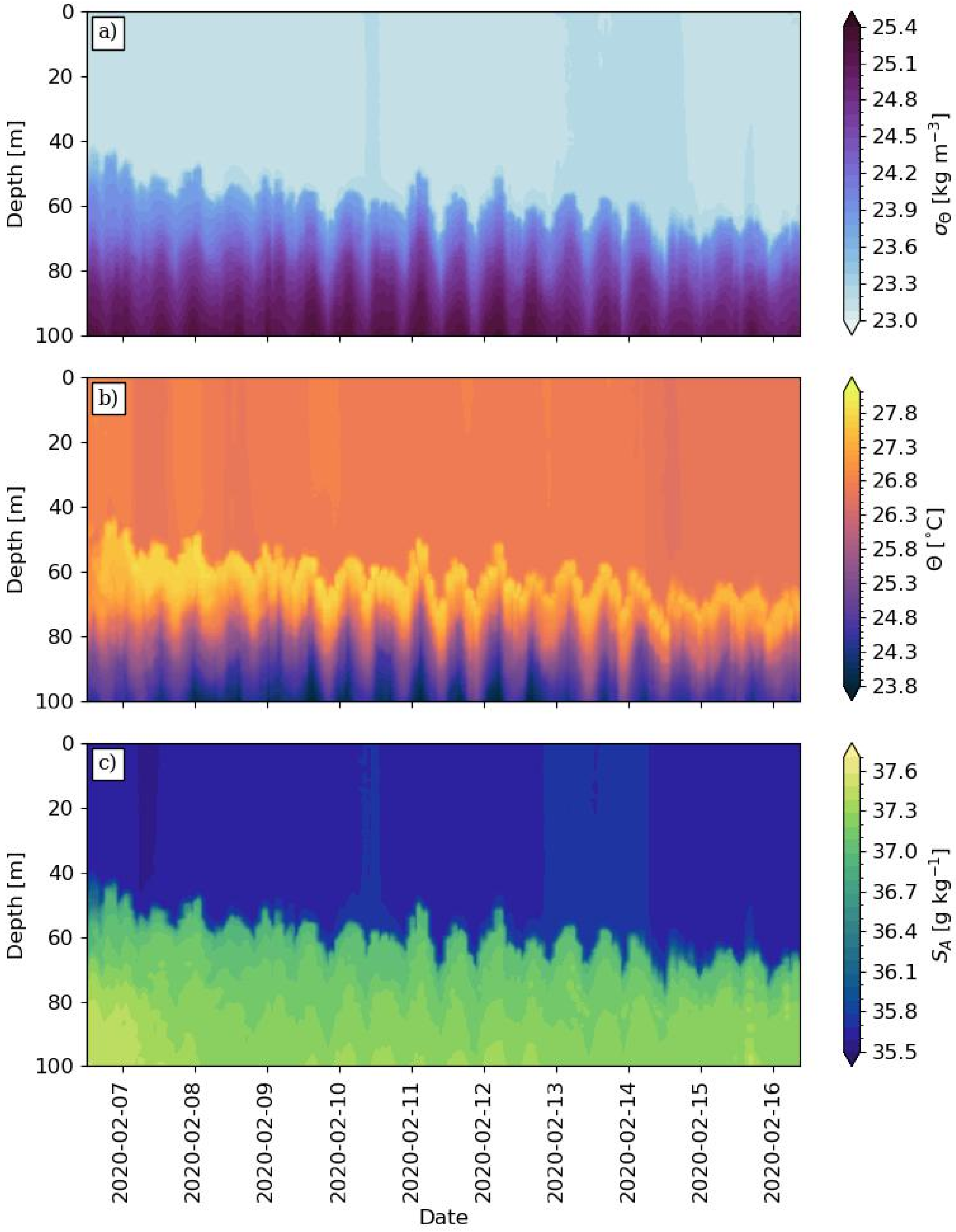

Figure 4.6: SG579 1 m 1 hour processed dataset, showing a) potential density anomaly, b) conservative temperature and c) absolute salinity in the top 100 m.
Processing described in text.

For investigation of the mixed layer heat budget (section 4.5), the study site is treated as a point location and the mixed layer heat budget investigated with a time series. To have a single time series of the ocean state for this thesis, the hourly average of the in-situ temperature and conductivity from the processed SG579 and SG637 observations is taken. Ocean variables of interest are derived with GibbsSeaWater in the same way as the individual glider methodology and this is thus referred to as SGavg.

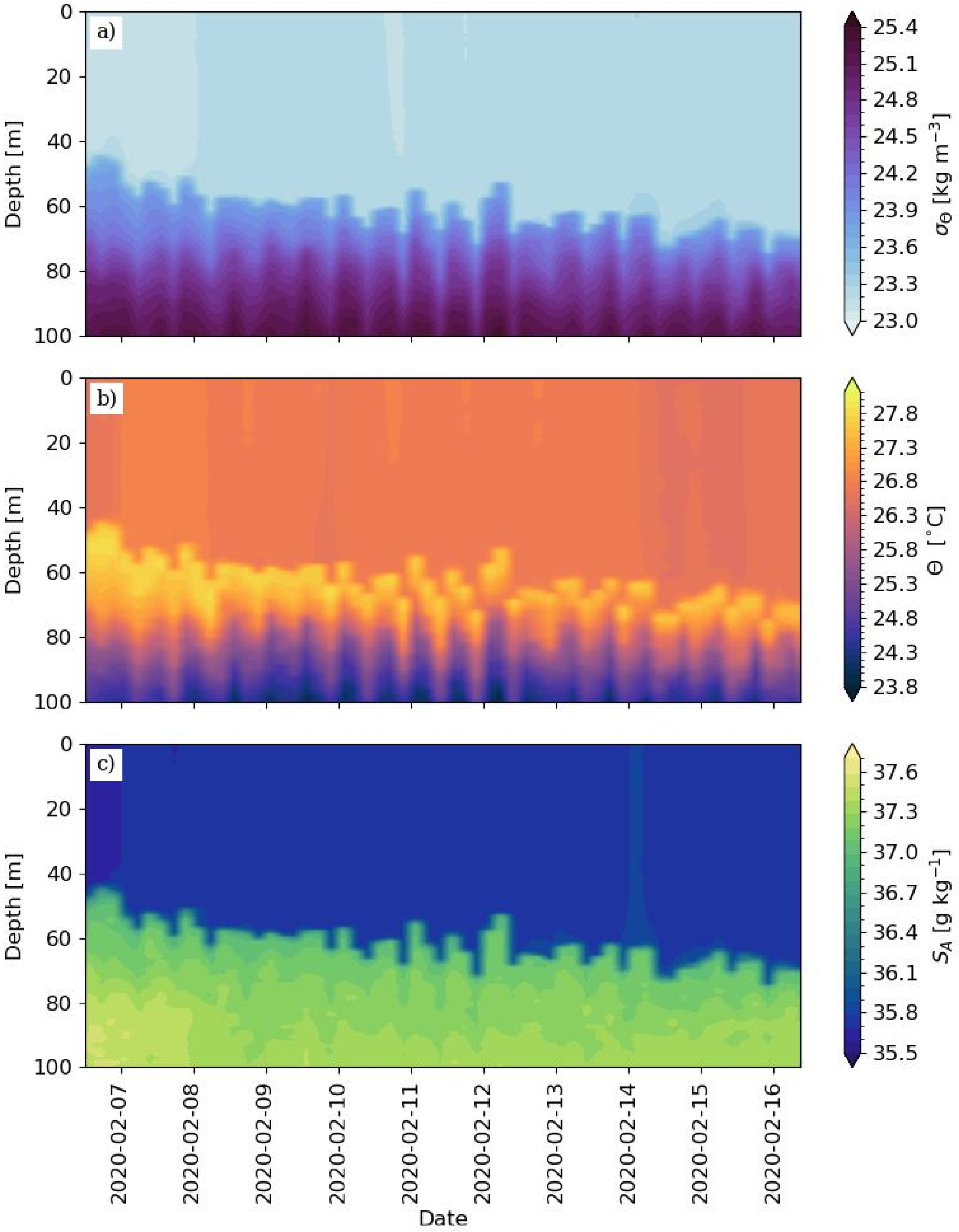

Figure 4.7: SG637 1 m 1 hour processed dataset, showing a) potential density anomaly, b) conservative temperature and c) absolute salinity in the top 100 m. Processing described in text.

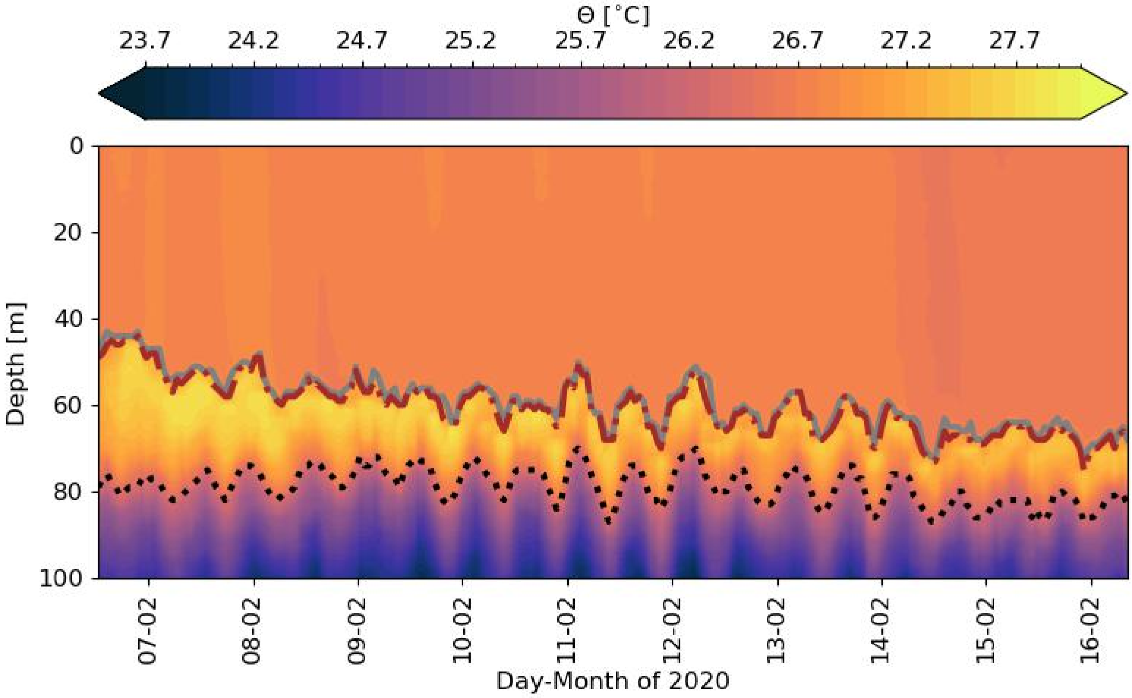

Figure 4.8: Conservative temperature glider average SGavg (see text). Mixed layer depth definitions are Foltz et al. (2003) (black line), Kara et al. (2000) (brown line) and Monterey and Levitus (1997) (grey line).

The Mixed Layer Depth

The mixed layer depth (MLD) is important in defining the bottom of the surface ocean mixed layer used in a mixed layer heat budget. In this thesis, the mixed layer is calculated using the SGavg dataset from Seaglider observations. Three approximations of the MLD were tested (Figure 4.8) according to different temperature and density based mixed layer depth thresholds. The scheme of Foltz et al. (2003) was deemed inappropriate for this study as the temperature based threshold (depth at which temperature is 0.5°C below SST) captures the sub surface temperature inversion in the barrier layer. For the purposes of investigating heat exchange and fluxes, I prioritise a definition that captures the actively mixing layer. Thus the mixed layer depth was calculated using a density based threshold of 0.125 $\mathrm{kgm^{-3}}$ from the surface, according to (Monterey and Levitus, 1997) and a density based criterion using the density difference found from a temperature difference $\Delta T = 0.8°C$ (Kara et al., 2000). The calculated MLD's are visible in Figure 4.8c. For simplicity, I take the Monterey and Levitus (1997) definition of MLD. This definition gives a time varying MLD between 43 m and 73 m on SGavg.

Mixed layer observations using the above definition are plotted in Figures 4.9 and 4.10. This allows us to examine the representation of study site mixed layer by the SGavg dataset compared to the individual glider observations. Throughout the time series Figure 4.9 , both SG579 and SG637 observe a diurnal cycle in the mixed layer temperature. From the start point to 11th February, transitions between warmer and cooler waters are seen at different times between SG579 and SG637, indicating the presence of a front. Increased variation in SST is also seen in *Caravela* observations (section 4.3) until 10th February. Meanwhile in Figure 4.10, absolute salinity of the mixed layer varies on 6th and 7th February on both Seagliders, supporting the assumption that a front passes through the study site. After this point, salinity measurements are consistent for each individual glider until 10th February where SG579 sees a brief 1 day increase in absolute salinity. An increase of the same magnitude is seen again by this glider between 12th and 14th February. In SG637, from 7th February onwards, mixed layer salinities are consistent, apart from a short period of salinity increase on 14th February. The mixed layer depth will be revisited later in section 4.5 when calculating the mixed layer heat budget.

4.2.2 *Caravela*

To enable comparability with the Seagliders and ERA5 later in this work, hourly median data from *Caravela* was generated. This was defined as data points up to and including the hour, with the label being the right hand side of the hour interval, such that a 15:00 data point is a median of all data 14:00-15:00, and inclusive of 15:00.

For *Caravela* 's CTD data, a simple quality control regime based on realistic physical limits of ocean measurements was applied before the hourly median was generated. This was used to remove wildly unrealistic conductivity values thought to occur when the vessel speed affected CTD flushing. By using a median over an hour of 2 Hz data, I ensured any spiking due to inadequate CTD flushing was not seen in the analysed dataset. For all other parameters, an hourly median was sufficient in removing erroneous data.

Caravela wind data were not used here (see chapter 3). Instead, ERA5 10 m wind velocity data were used for the analyses described in this chapter and chapter 5. ERA5 will be described moreso in section 4.2.3.

Turbulent fluxes were calculated from *Caravela* observations using the bulk formulae in the form of the COARE 3.5 algorithm (Fairall et al., 1996*b*, 2003). COARE 3.5 python was used, in which the warm layer and surface wave options are unavailable. I anticipate very little impact from warm layers in our study, as investigated above with the Seagliders. Surface

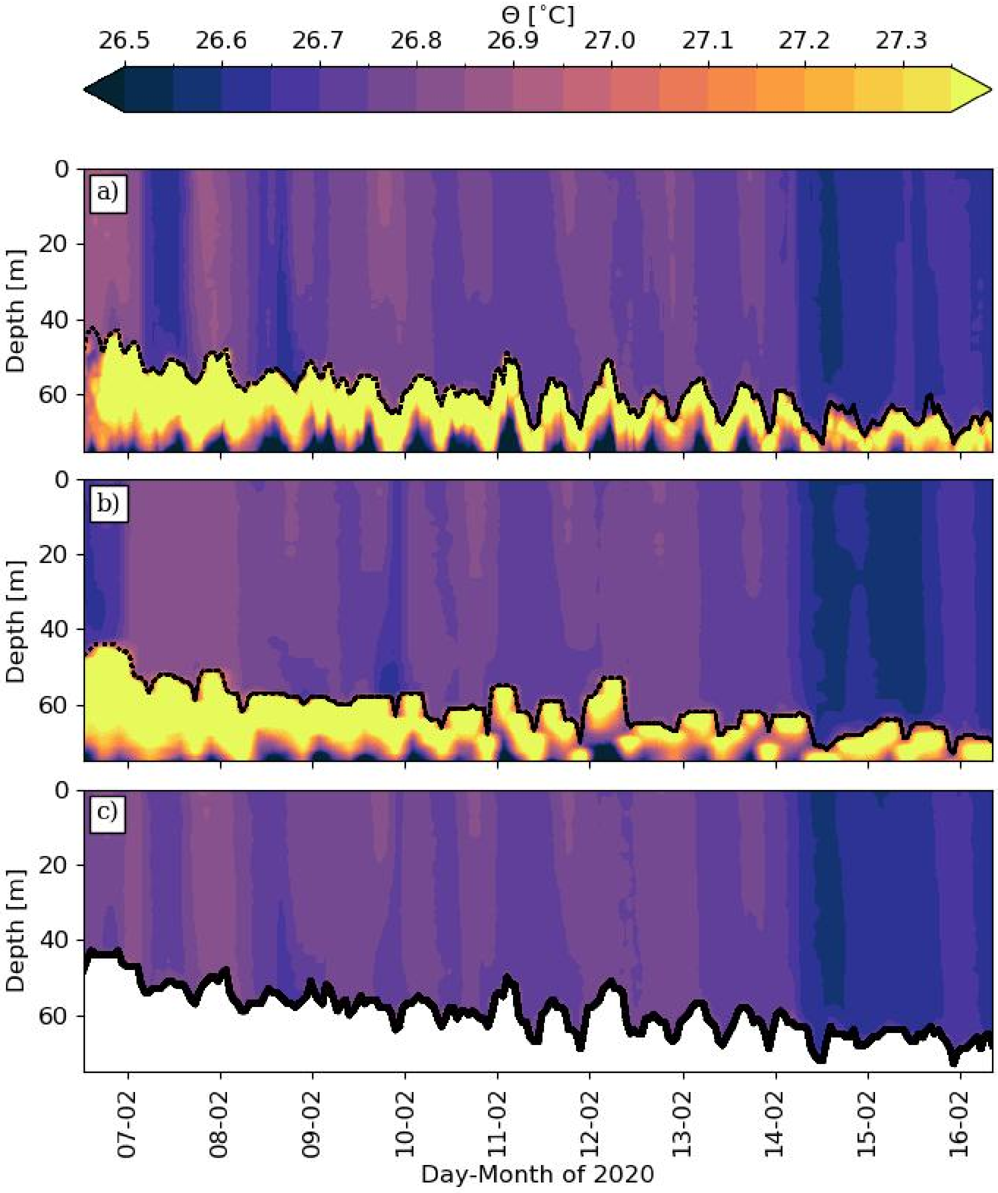

Figure 4.9: Conservative temperature with colour bar range restricted to mixed layer temperature values a) SG579, b) SG637 and c) SGavg. For SGavg, observations below the mixed layer depth are not shown. Mixed layer depth (black lines) were calculated for glider individually as well as SGavg.

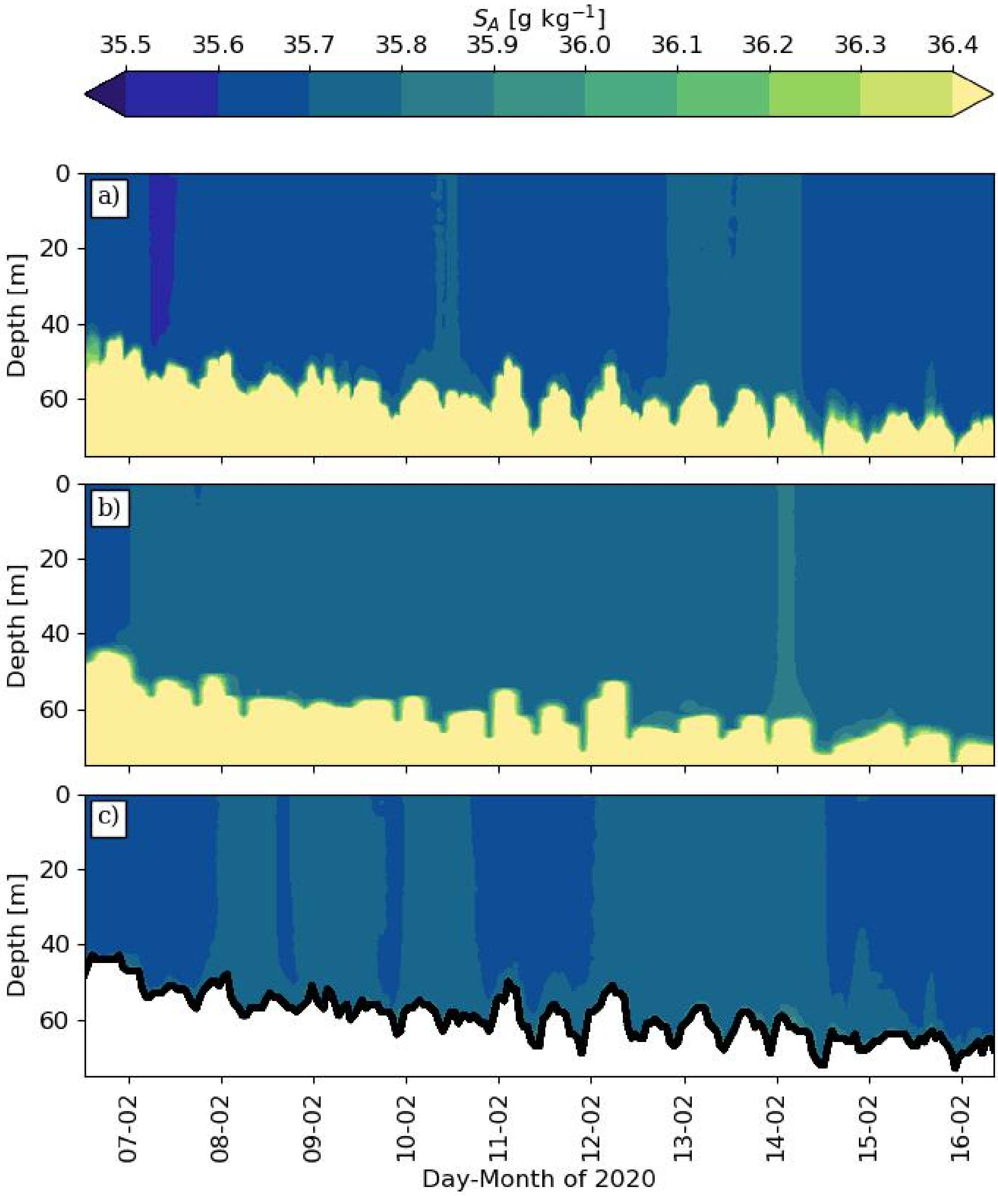

Figure 4.10: Absolute Salinity with colour bar range restricted to mixed layer temperature values a) SG579, b) SG637 and c) SGavg. For SGavg, observations below the mixed layer depth (black line) are not shown. Mixed layer depths were calculated for glider individually as well as SGavg.

wave data are not available from *Caravela* . The COARE 3.5 bulk formula is designed to process surface relative winds. The inclusion of surface currents for a surface-relative wind would reduce the heat flux if current is assumed to flow parallel to mean wind speed, however this may not hold with eddying or upwind currents(Song, 2020). In the Bohai Sea with an upwind flow, monthly mean turbulent heat flux increases $2\,\mathrm{W\,m^{-2}}$ for surface relative wind compared to absolute wind, with a $10\,\mathrm{W\,m^{-2}}$ difference at the hourly scale (Song, 2020) so it is important to consider the surface current effects on fluxes as intended in the COARE algorithm. Within the scope of this thesis, ERA5 absolute winds are used. surface currents are assumed small (according to model data are less than $0.22\,\mathrm{m\,s^{-1}}$, see chapter 5) and thus neglected. It is acknowledged that based on literature findings of surface current correction there could be a component of error in the fluxes from this assumption.

When calculating radiative fluxes, the longwave flux should be calculated using skin temperature. As the observations from *Caravela* were of bulk SST not skin temperature, this bulk SST was used in calculating the upwelling component of longwave radiative flux and so will be an addition source of error in the net heat fluxes presented here.

4.2.3 ERA5

An overview of the ERA5 reanalysis product is available in section 2.5.1. This thesis uses the 'ERA5 hourly data on single levels from 1940 to present' product (Hersbach et al., 2018, 2020; Copernicus Climate Change Service, 2023). The main parameter of interest from ERA5 is the average net heat flux at each hour, for validation of fluxes derived from observations. ERA5 accumulated fluxes are provided in $\mathrm{Jm^{-2}}$, the net flux Q_0 is calculated in $\mathrm{W\,m^{-2}}$ by summing the four heat flux components in $\mathrm{W\,m^{-2}}$ and calculating the average flux over the preceding hour at each time step (ECMWF, 2024). The spatial resolution of ERA5 is relatively coarse for the 10 km square of our observations. For each ERA5 parameter, I calculate the mean of values at the four ERA5 grid points surrounding the study site (Figure 4.11). The difference in using a median vs mean over the points surrounding the study site is very small, the mean being average of $0.25\,\mathrm{W/m^2}$ larger than the median, with root mean square difference of $2.3\,\mathrm{W/m^2}$.

ERA5 winds were used to supplement observations and observational fluxes calculated in this thesis. The ERA5 wind time series is visible in Figure 4.12 where the mean wind speed is $9.8\,\mathrm{ms^{-1}}$ and direction north-easterly. The mean of the four ERA5 grid points shown above was again used.

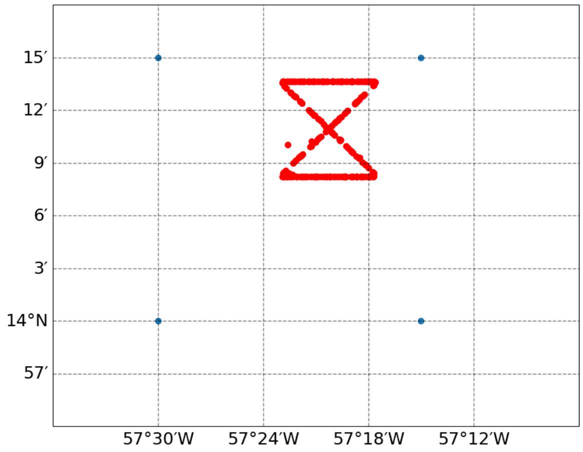

Figure 4.11: ERA5 grid point locations used in comparison (blue) and *Caravela* 's track around the study site (red).

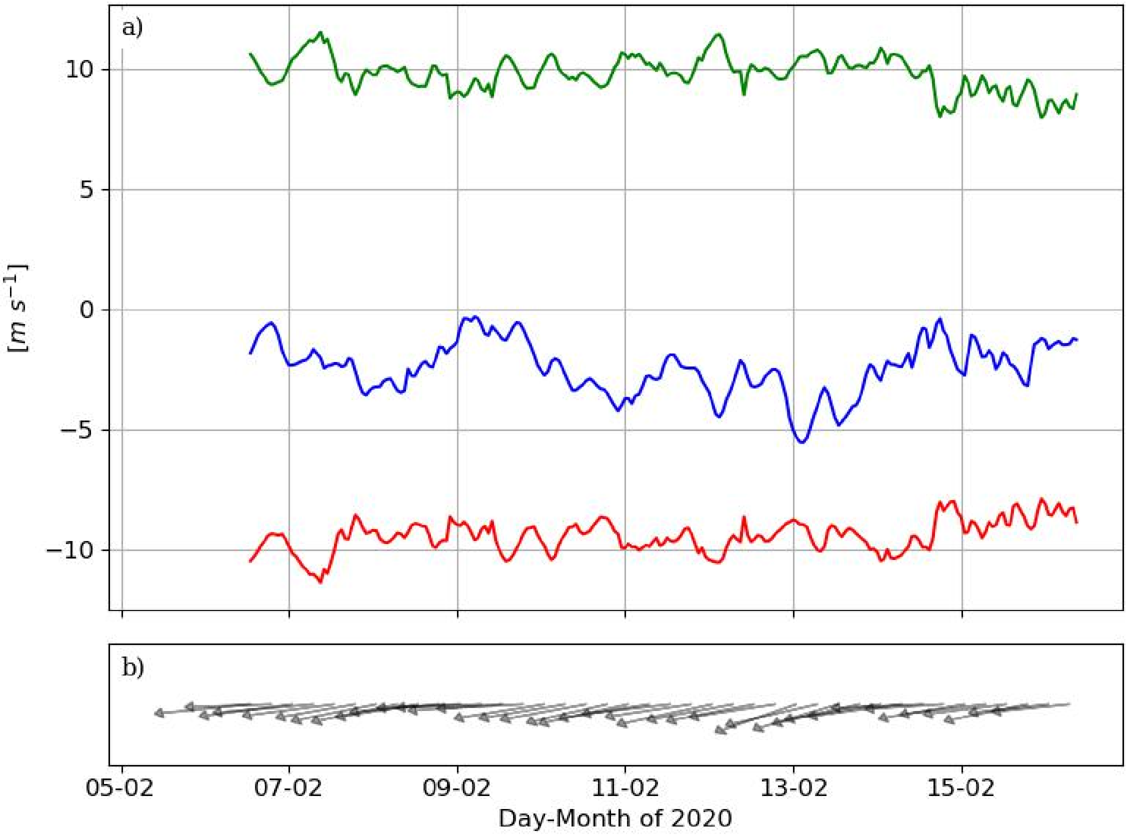

Figure 4.12: a) 10 m wind speed from ERA5 with magnitude (green), u component (red) and v component (blue) where positive values are northerly and easterly. b) direction wind comes from at 6 hour intervals, with the time series corresponding to the base of the arrow. Arrow length has no meaning.

4.2.4 Heat Budget Calculation

The ocean mixed layer heat budget consists of a three dimensional balance of multiple processes, which affect the local SSTs. A detailed discussion of the full equation can be found in chapter 1. In this chapter, I neglect all processes other than the air-sea net heat flux component of the ocean heat content equation, such that an assessment of the heat budget closure is based on the following equation:

$$\frac{\partial T_a}{\partial t} \approx \frac{Q_0 - Q_{pen}}{\rho c_p h} \tag{4.2.3}$$

where the term on the left represents the temperature tendency. The term on the right the net air-sea heat flux adjusted for penetrative solar radiation, where T_a is the average temperature of the mixed layer, Q_0 the sum of the four surface heat flux terms, also called the net surface heat flux, Q_{pen} the flux of solar radiation penetrating through the base of the mixed layer, ρ the seawater density, c_p the specific heat capacity (3997 J/kg/K) and h the mixed layer depth. Many studies have used this equation (or similar versions excluding Q_{pen}) to investigate seasonal and annual SST changes and their relationship to air-sea interactions (Yu et al., 2006, 2007; Virmani and Weisberg, 2003; Pinker et al., 2020).

4.3 Results: Air-Sea Heat Flux

To assess the mixed layer heat budget, observations and ERA5 are used to calculate the terms in equation 4.2.3. In this section, the focus is on the net heat flux Q_0 term, shown as a sum of its components in equation 1.2.5. For clarity in the rest of this section, ERA5 fluxes will be henceforth denoted by Q_{xxx-e} and fluxes calculated from observations by Q_{xxx-o}, where xxx refers to the relevant flux component, i.e. net (net), latent (lat) , sensible (sen), longwave (lw) or shortwave (sw).

4.3.1 Shortwave fluxes

The sea surface albedo is typically assumed to be 6% for this region of the tropical Atlantic (Foltz et al., 2003; Cogley, 1979) and this value was used to calculate observational fluxes. The mean ERA5 albedo for the study period was back-calculated to be 0.063, consistent with the chosen 6% value.

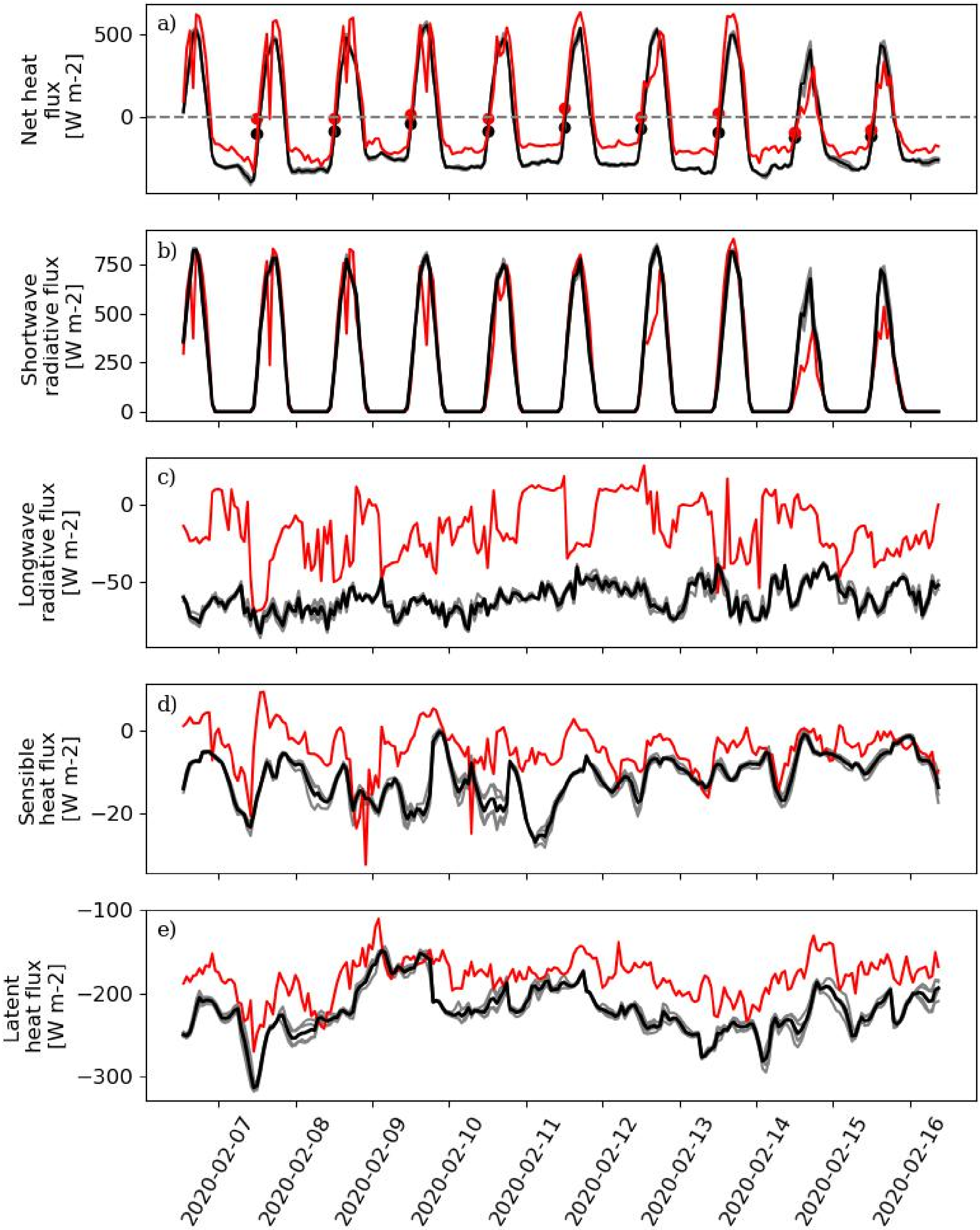

Figure 4.13: Air-sea heat flux components of the upper ocean heat budget derived from *Caravela* temperatures, humidity and radiation measurements with ERA5 winds (red lines), ERA5 fluxes at the four grid points surrounding the study site (grey lines), and mean of these four locations (black line). (a) Net surface heat flux, (b) shortwave radiative flux, (c) longwave radiative flux, (d) sensible heat flux, and (e) latent heat flux. Black and red circles in (a) are daily averaged net fluxes, marked at 12:00 UTC of the day.

The time series of the net shortwave fluxes Q_{sw-o} and Q_{sw-e} are visible in Figure 4.13b. During the 12th, 14th and 15th of February, ERA5 clearly overestimates Q_{sw-e} compared to Q_{sw-o} with a maximum hourly difference of $356\,\mathrm{W\,m^{-2}}$, $350\,\mathrm{W\,m^{-2}}$ and $350\,\mathrm{W\,m^{-2}}$ within each respective day. The downwelling shortwave estimation in ERA5 will be impacted by representation of local cloud cover , supported by Figure 4.14. There is notable difference in the clear sky and downwelling solar radiation fluxes reported by ERA5 on the 14th and 15th February, which are two of the three aforementioned days *Caravela* observations show less downwelling radiation than ERA5. It is known that the surface irradiance bias of ERA5 varies with the cloudiness, where ERA5 overestimates surface irradiance with cloudy conditions and slightly underestimates with clear-sky conditions (Urraca et al., 2018). In the Bermuda region (the closest site available in this study), these cloudy overestimates are in the order of 0 to $40\,\mathrm{W\,m^{-2}}$ and clear sky underestimates 0 to $30\,\mathrm{W\,m^{-2}}$. This thesis' results suggest that ERA5 is overestimating net shortwave radiation flux, therefore overestimating surface irradiance and underestimating cloud cover, on these three stated days. Over these three days, the mean daily Q_{sw-e} is $197\,\mathrm{W\,m^{-2}}$ larger than Q_{sw-o} . Within the daytime hours of the remaining time series, the first five days show decreases in Q_{sw-o} during the middle of the day that are missing inQ_{sw-e} . This implies a transient cloud cover increase in the observations, again not captured within ERA5 reanalysis. Given the observations are able to capture cloud cover variation missed in the ERA5 reanalysis, I use Q_{sw-o} in subsequent analysis.

4.3.2 Longwave fluxes

When estimating radiative bulk fluxes, skin temperature was unavailable directly from observations so SST has been used instead. Surface emissivity of 0.97 is assumed, in line with other near-surface studies (Bellenger and Duvel, 2009).

Figure 4.13c shows differences between the ERA5 and observational hourly-averaged net longwave flux, with a maximum of $82\,\mathrm{W\,m^{-2}}$, with Q_{lw-o} being smaller in magnitude (more positive value) than Q_{lw-e}. Q_{lw-o} observations change between positive and negative flux contributions throughout the time series, whereas Q_{lw-e} is a consistently negative contributor (heat transfer from ocean to atmosphere). To investigate further, the upwelling and downwelling components of the longwave fluxes are plotted in fig 4.15. The upward component of the longwave flux is the first two terms of equation 1.2.4. Upwelling longwave from ERA5 is calculated as the difference in the net and downwelling longwave radiation

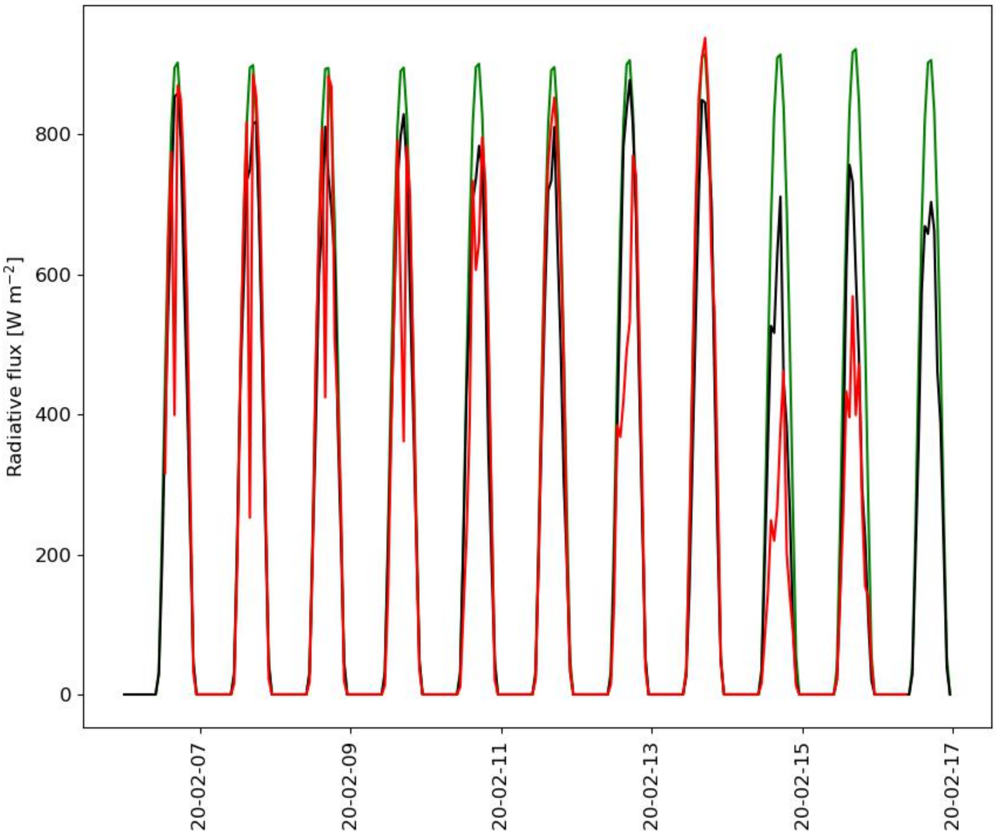

Figure 4.14: Timeseries of observed downwelling solar radiation from *Caravela* (red), downwelling solar radiation for ERA5 (black) and clear sky downwelling solar radiation from ERA5 (green).

variables because upwelling radiation was not available for download. ERA5 and observed upwelling longwave fluxes are always within $5\,\mathrm{W\,m^{-2}}$ of one another, whereas the observations in downwelling longwave flux are on average $47\,\mathrm{W\,m^{-2}}$ larger than ERA5. This difference is not consistent throughout the time at the study site, nor is the variability in the difference between ERA5 and observations consistent. This could in part be explained by the underestimation of scattered cloud cover in ERA5. However, based on a comparison of downwelling longwave fluxes to the Barbados cloud observatory, Section 3.4.3, the bias appears to be in the observations from *Caravela* . Causes of biases in the Caravela measurements could be due to salt contamination and sea spray with proximity of the sensor to the ocean surface, however similar contamination would then be expected in the other meterological sensor on the vessel. Due to the onset of the COVID pandemic and logistical challenges, the vessel was not accessable for many months after the deployment, meaning there was no post calibration available to assess this data. I take the ERA5 estimate of longwave flux to be the more reliable of the two. Therefore this will be used henceforth for the heat budget calculations.

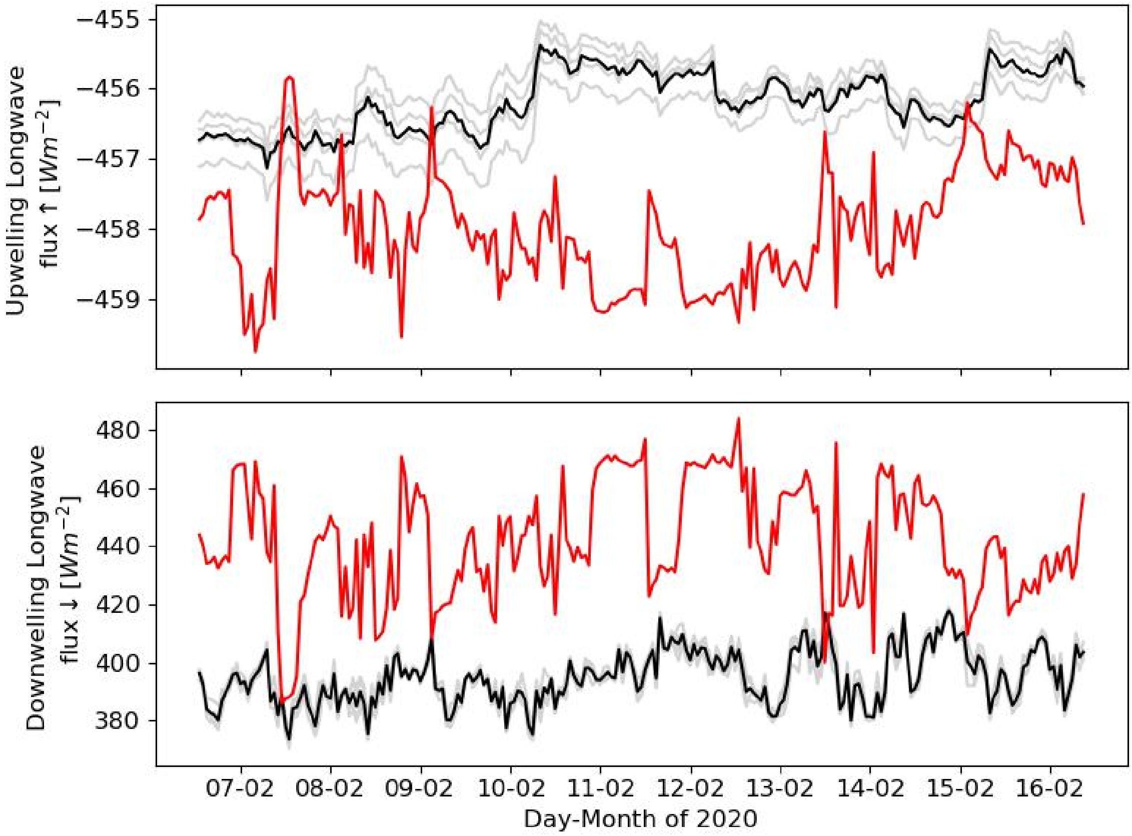

Figure 4.15: a) Upwelling component of longwave radiative flux from observations (red) and four ERA5 locations surrounding the study site (grey) with the mean of ERA5 (black), b) downwelling longwave radiative flux

4.3.3 Sensible heat Flux

Sensible heat flux output calculated using the COARE 3.5 algorithm (Fairall et al., 1996*b*) is visible in Figure 4.13d. Over the time spent in the study site, mean hourly Q_{sen-e} was 11 W m^{-2}, standard deviation 6 W m^{-2}, while mean Q_{sen-o} was 4 W m^{-2} with standard deviation 6 W m^{-2}. Q_{sen-e} predominantly estimates larger heat losses to the atmosphere than Q_{sen-o}. There are instances in the *Caravela* time series of short term positive sensible heat fluxes in the daytime (Figure 4.13). These align with times where observed air temperature is larger than the SST in Figure 4.16b,c,d on 7th and 9th February. ERA5 and *Caravela* have similar SSTs (Figure 4.16b except for 12th February to 14th February, where ERA5 SST are an average of 0.15 °C less than *Caravela* observed SST. ERA5 2 m air temperature is compared to *Caravela* Hygroclip air temperature observations (0.67 m) in Figure 4.16c. Observed air temperature is on average 0.68 °C warmer than ERA5, except for two instances on the 8th and 10th February, where observed air temperature briefly decreased below ERA5. The instances on 8th February and 10th February correspond to where Q_{sen-o} has larger losses to the atmosphere than Q_{sen-e}. Increases in observed humidity are also noted in Figure 4.16a on these two days. This may be associated with an atmospheric front or cold pool passing through the study site, which ERA5 may not well represent on short timescales. There are notable differences in the observed and ERA5 sensible flux until 12th February, where observed sensible heat flux is on average $9.7\,\mathrm{W\,m^{-2}}$ larger than ERA5 (less negative value and thus less heat loss to the atmosphere). After the 12th February, the difference reduces to *Caravela* observing an average of $3.8\,\mathrm{W\,m^{-2}}$ larger value (less heat loss to the atmosphere) than ERA5. Observed SSTs were cross-validated with the Seaglider data (Figure 2.5). Air temperature was compared with observations from the *R/V Meteor* (Figure 2.4) and no concerns over calibration of *Caravela* raised. This lends confidence in the observations from *Caravela* and thus I assume differences between observations and ERA5 are down to ERA5 errors. Figure 4.16 highlights the SST- air temperature difference is consistently larger in ERA5 than observations throughout the timeframe. Mean temperature difference SST - air temperature for ERA5 is $1.05\,^{\circ}\mathrm{C}$ and for Caravela observations $0.43\,^{\circ}\mathrm{C}$. If the difference of $0.62\,^{\circ}\mathrm{C}$ is added to Caravela observations, it equates to a mean additional $7.98\,\mathrm{W\,m^{-2}}$ heat loss to the atmosphere throughout the timeseries, or mean sensible heat flux of $-12.97\,\mathrm{W\,m^{-2}}$ across the timeseries. Mean ERA5 sensible heat flux is $-11.36\,\mathrm{W\,m^{-2}}$. Such that most of the difference in mean flux across the timeseries is accounted for by the differences in SST and air temperature between products. The differences in representation of wind speed and transfer coefficient formulation between ERA5 and COARE 3.5 must also play a role in the discrepancies seen between fluxes, but is less influential than temperature offset. Due to the notable difference in temperatures, I take the observational quantities such that I use Q_{sen-o} for calculation of net heat flux.

4.3.4 Latent Heat Flux

Average hourly Q_{lat-o} is $-181\,\mathrm{W\,m^{-2}}$ and Q_{lat-e} is $-221\,\mathrm{W\,m^{-2}}$, with ERA5 estimating on average $40\,\mathrm{W\,m^{-2}}$ more heat loss into the atmosphere than observations suggest. ERA5 overestimates the magnitude of heat loss into the atmosphere compared with observations for all times except a brief period in the early hours of 8th February and again 9th February. These periods where the latent heat fluxes are almost in agreement align with short periods in Figure 4.16a where ERA5 and observed humidities agree. ERA5 humidity is not available directly, so it was back calculated according to the available 2 m air and dew-point temperature. Generally, ERA5 is underestimating the relative humidity compared with observations, with *Caravela* on average observing $3.4\,\%$ more than ERA5, with a maximum difference of $11\,\%$. ERA5's consistent underestimation of humidity from

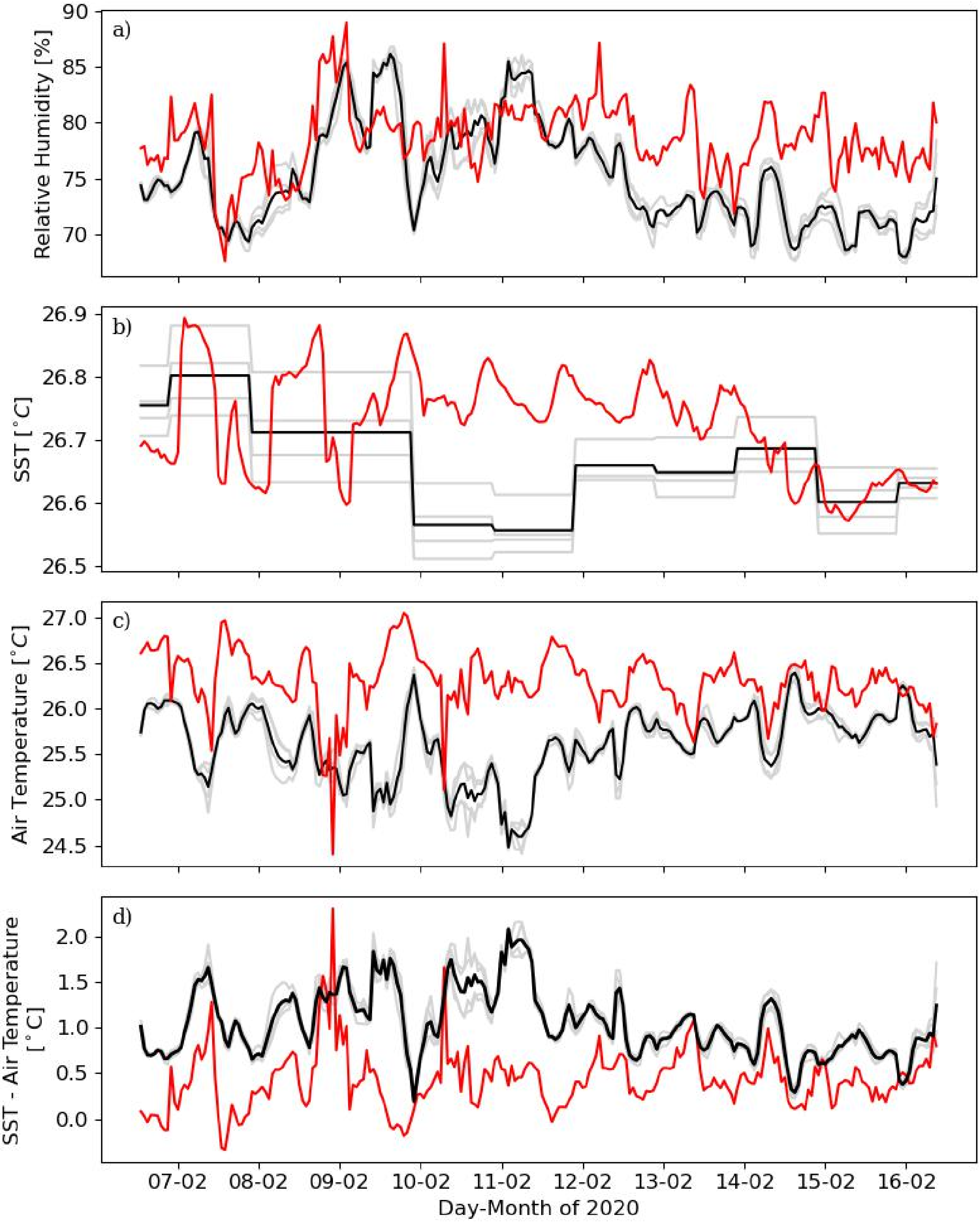

Figure 4.16: Observations in the EUREC^{4}A study site from *Caravela* (red), at each ERA5 grid point surrounding the study site (grey) and mean over the ERA5 values (black). a) Relative humidity observations with ERA5 value calculated from ERA5 2 m air and dew point temperature. b) SST. c) air temperature. d) shows the difference in SST minus air temperature.

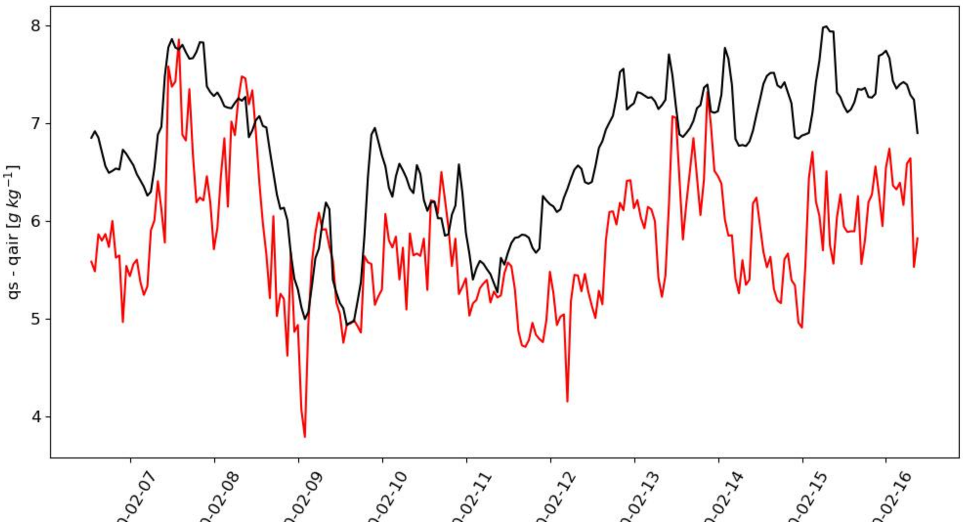

Figure 4.17: Difference in qs and qair from *Caravela* (red) and mean over the ERA5 grid points surrounding the study site (black).

12th February to the end of the time series aligns with its overestimation of the magnitude of Q_{lat} losses to the atmosphere for the same time period. Figure 4.17 shows the difference in saturation humidity at SST and specific humidity of the air at 10 m, derived from COARE 3.5 for both *Caravela* observations and met/ocean variables from ERA5. The mean $q_s - q_{air}$ in the observed timeseries is $5.80\,\mathrm{g\,kg^{-1}}$, compared to a mean $6.70\,\mathrm{g\,kg^{-1}}$ from ERA5. The ratio of the mean ERA5 difference to mean observed difference is 1:0.86. The ratio of $Q_{lat-e} : Q_{lat-o}$ is 1:0.83. The ratios are almost the same which supports the humidity bias being responsible for the latent heat flux bias. The small difference in ratio is likely due to difference in transfer coefficient scheme used in the bulk formulae, and the impact of differing transfer coefficients was also noted in sensible heat fluxes. The effect of the transfer coefficient formulation is therefore small compared to the humidity bias itself. In the net heat flux calculation, I opt to use the observationally derived latent heat flux Q_{lat-o}.

4.3.5 Net Surface Heat Flux

The net surface heat flux (Figure 4.13a) is dominated by the shortwave radiative fluxes during the daytime, offset largely by heat loss to the atmosphere in the form of latent heat fluxes. The max, min and mean differences in daily average fluxes between Q_{net-o} and Q_{net-e} (where Q_{net-o} are larger in magnitude than Q_{net-e}) are $31\,\mathrm{W\,m^{-2}}$, $117\,\mathrm{W\,m^{-2}}$ and $75\,\mathrm{W\,m^{-2}}$ respectively, excluding the 6th and 16th February where there is not a full day of data. For hourly fluxes, Q_{net-o} are on average $76\,\mathrm{W\,m^{-2}}$ larger than Q_{net-e}, with differences

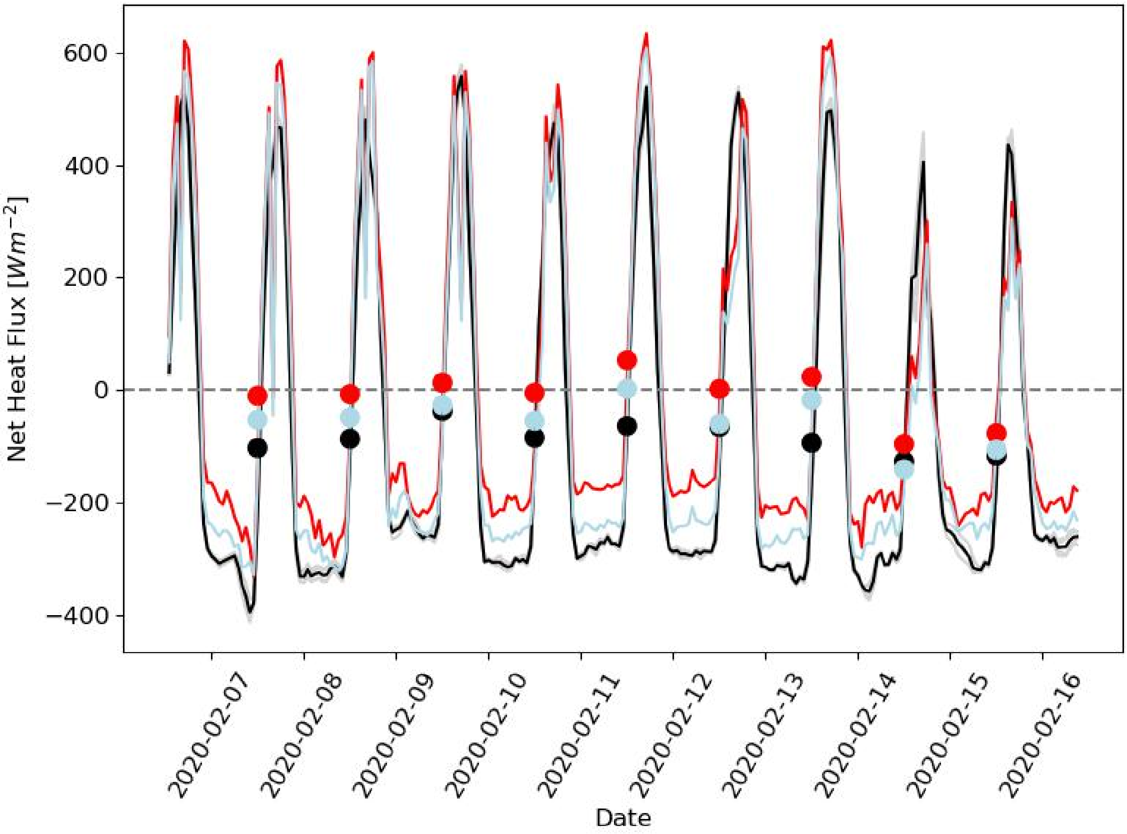

Figure 4.18: Net heat flux as a time series within the EUREC^{4}A study site using ERA5 reanalysis (black), *Caravela* observations (red) and a combination of ERA5 longwave flux with observed shortwave, latent and sensible flux (blue). Daily averages are show as circles at 12:00 UTC for each complete day.

ranging between 250 W m^{-2} larger Q_{net-o} and 412 W m^{-2} larger Q_{net-e} . Differences between observations and reanalysis in all four heat flux terms lead to these considerable discrepancies in net heat fluxes. In terms of daily mean flux, for Q_{net-o}, heat gain to the ocean occurs in four of the nine complete days available in the study site and heat loss to the atmosphere in five of these nine days. For Q_{net-e}, the daily averaged flux is always negative, representing a consistent heat loss to the atmosphere. For each of the net surface heat flux components, I discussed which of ERA5 and observations were thought to provide the better estimate for each term. This is observed shortwave, latent and sensible heat flux with ERA5 longwave flux. Figure 4.18 shows the net surface heat flux when using this combination of components, henceforth referred to as Q_{net-x}, compared to Q_{net-o} and Q_{net-e}. The mean daily flux of Q_{net-x} is -56 W m^{-2}. Daily Q_{net-x} shows heat loss to the atmosphere for all days except 11th February, where a 2 W m^{-2} heat gain to the ocean was observed.

4.4 Penetrative solar radiation

Turbulent and longwave fluxes are considered to be surface effects occurring in the top few millimetres of the mixed layer. Meanwhile, shortwave radiation may penetrate tens of metres into the ocean and through the base of a shallow mixed layer. Solar radiation penetrating through a chosen depth is defined as Q_{pen}. If the heat budget is calculated to fixed depth below the thermocline as in Moisan and Niiler (1998) or to a sufficient depth that Q_{pen} is small , Q_{pen} can be assumed negligible. In this study, I am interested in the mixed layer heat budget, where the MLD is above the subsurface temperature maximum or thermocline and shallow enough that penetrative solar radiation is significant, so the Q_{pen} term must be considered.

Q_{pen} has various estimation methods based on water mass classification and chlorophyll concentrations. Q_{pen} according to Wang and McPhaden (1999),

$$Q_{pen} = 0.45 Q_{surf} \exp\left(-\gamma h\right) \tag{4.4.1}$$

assumes a 25 m e-folding decay of shortwave radiation, where Q_{surf} is the surface shortwave solar radiation, γ is $0.04\,\mathrm{m}^{-1}$. A higher value of γ is used in instances of high biological productivity.

A chlorophyll-based approximation by Morel (1988) accounts for local biological productivity in the form of chlorophyll concentration.

$$Q_{pen} = 0.47 Q_{surf} \exp -(0.027 + 0.0518 CHL^{0.428}) h \tag{4.4.2}$$

Various papers compare these two formulations. Scannell and McPhaden (2018) opt to use the chlorophyll approximation due to the importance of chlorophyll concentration in productive waters with shallow mixed layers. They study the southeastern tropical Atlantic and see a $12\,\mathrm{W\,m^{-2}}$ to $26\,\mathrm{W\,m^{-2}}$ bias seasonally between the two Q_{pen} approximations, with the chlorophyll-based model always resulting in lower penetration across the mixed layer base, i.e. more absorption in the mixed layer (Scannell and McPhaden, 2018). Foltz et al. (2003) tested the two equations I describe above. Of the three PIRATA mooring locations in their paper, 12°N 38°W is the closest geographically to the study site of this thesis. This location showed strong seasonality in Q_{pen} due to MLD variation, but some of the smallest differences between

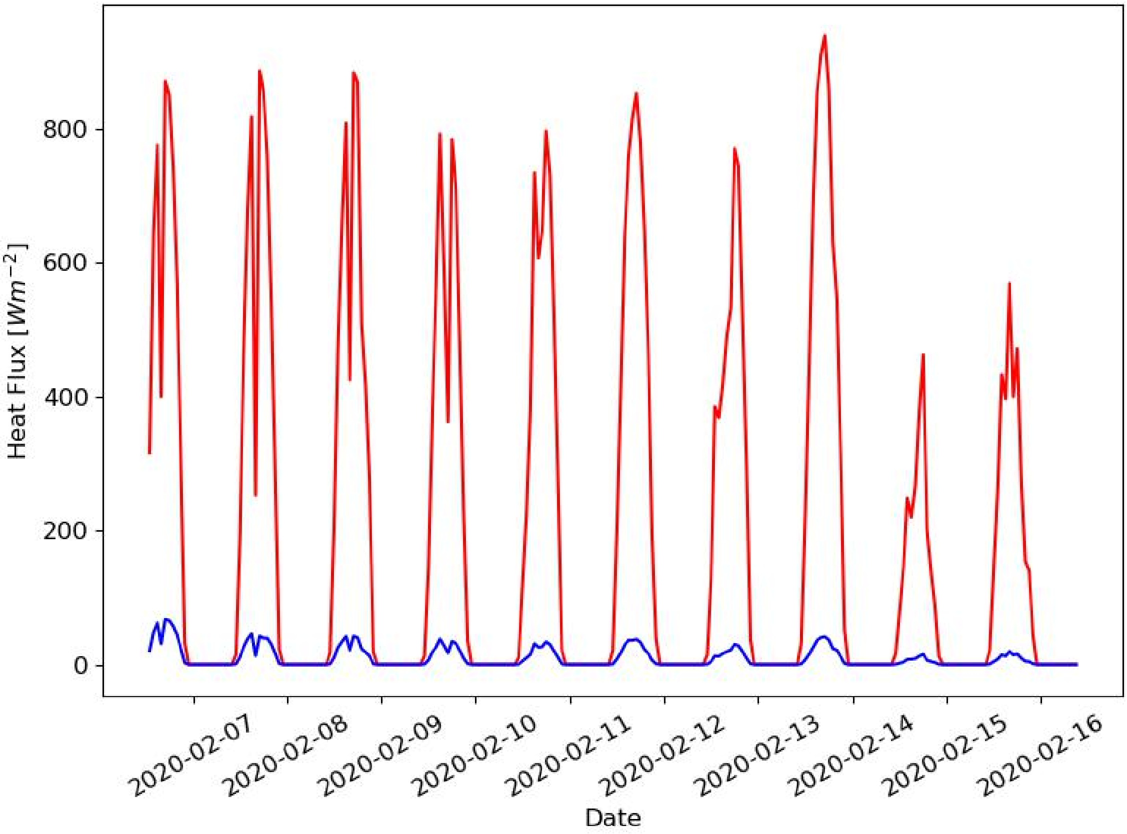

Figure 4.19: Time series of observed surface downwelling solar radiation (red) and calculated penetrative solar radiation at the mixed layer depth (blue) using $Q_{pen} = 0.45Q_{surf}\exp(-\gamma h)$

the two Q_{pen} formulations in February. The Wang and McPhaden (1999) approach gives lower absorption than the chlorophyll approximation in this study, in agreement with Scannell and McPhaden (2018), with nearly constant bias at all locations. Liu et al. (2021) show that the Northwestern Atlantic heat content, off the US coast, is very sensitive to ocean optical properties and solar attenuation schemes. They use different methods of calculation to the formulae covered in this thesis, but advocate for the use of an optical-based parameterisation from ocean colour satellites over a chlorophyll-based solar attenuation scheme, seeing up to a 30 % difference in their two schemes. Within this thesis, the chlorophyll based approximation assuming chlorophyll concentration of 0.1 gives Q_{pen} between 1.6 % and 6.4 % of downwelling solar radiation at the ocean surface. To avoid assumptions on chlorophyll concentration, I approximate Q_{pen} using the Wang and McPhaden (1999) formulation. Q_{pen} is then calculated to be between 2.4 % and 8 % of downwelling solar radiation at the ocean surface, Figure 4.19.

4.5 Mixed layer heat budget

4.5.1 Net Heat flux Contribution to Mixed Layer Heat Budget

The individual terms from the chosen combination of $Q_{sw-o}, Q_{lw-e}, Q_{lat-o}, Q_{sen-o}$ are shown in Figure 4.20a as hourly fluxes, along with the penetrative solar radiation correction Q_{pen} and net surface heat flux Q_0. Other contributing terms to the net heat flux component of the heat budget are mixed layer density (Figure 4.20b) and MLD (Figure 4.20c). The mixed layer density and depth are determined from SGavg. The net flux contribution to the heat budget using these terms is shown in Figure 4.20d, alongside the temperature tendency $\frac{dT_a}{dt}$; the mixed layer averaged temperature from SGavg used to calculate this tendency is shown in 4.20b. $\frac{dT_a}{dt}$ is compared to the net heat flux contribution to the heat budget, with a residual R given as the temperature tendency minus the heat flux contribution (Figure 4.20e).

The mean temperature tendency is $-0.0006\,^{\circ}\mathrm{C\,h^{-1}}$ with a standard deviation of $0.008\,^{\circ}\mathrm{C\,h^{-1}}$. The mean net heat flux contribution to the heat budget is $-0.0008\,^{\circ}\mathrm{C\,h^{-1}}$ with a standard deviation of $0.004\,^{\circ}\mathrm{C\,h^{-1}}$. Notice the standard deviation is an order of magnitude larger than the mean in both formulations, such that the hourly changes are highly variable. Over the whole time series, the correlation coefficient is 0.39, and the root mean squared difference is $0.008\,^{\circ}\mathrm{C\,h^{-1}}$, indicating that the net heat flux is weakly correlated to the temperature tendency on these short time scales. The residual ranges from $0.022\,^{\circ}\mathrm{C\,h^{-1}}$ to $-0.033\,^{\circ}\mathrm{C\,h^{-1}}$. The net heat flux contribution to the mixed layer heat budget better reproduces the overall pattern of the tendency term from the 10th February onwards, with the correlation improving to 0.5 with root mean square difference $0.006\,^{\circ}\mathrm{C\,h^{-1}}$ when considering these days alone. From 6th to 10th February, there are large fluctuations in the temperature tendency that are not reflected in the flux term, indicating other processes are also playing a role in the heat budget, as well as during the rapid temperature decrease on 14th Feb. On the 14th and 15th February, net surface heat flux is considerably lower than the previous eight days, due to reduced shortwave radiative flux. These days also have larger variation in longwave flux than previous days, indicating a change in the cloud conditions during this time.

The magnitude of the temperature tendency is well represented by the net heat flux contribution from 10th to 14th February and a reduction in the range of the residual is seen in this time period too. Before the 10th and after the 14th February, increases in the magnitude of the residual align with variation in the temperature tendency. The temperature tendency does not display a clear diurnal cycle on these days, indicating ocean processes such as advection and mixing may be playing an important role. Whilst the net heat flux is thought to dominate the ocean mixed layer heat budget in the area on longer timescales (Foltz et al., 2003), at the hourly scale, other processes become important and must be considered. The budget can be closed with a root mean square difference of $0.006\,^{\circ}\mathrm{C\,h^{-1}}$ using a 6 hour running mean in $\frac{dT_a}{dt}$, but consideration of other oceanic processes must be made to fully close the budget at such high temporal resolution.

4.5.2 Cumulative Temperature Tendency

The temperature tendency describes the rate of change of temperature within the study site region. The accumulation of this temperature change is comparable the the integral of the right side of equation 4.2.3. Looking at the budget in cumulative terms allows for assessment of the closure across the whole time spent in the study site, thus assessment of the dominance of net heat flux on the timescale of 10 days as opposed to hourly.

The cumulative net heat flux contribution to the heat budget and temperature tendency are shown in Figure 4.21, alongside the cumulative temperature tendency of the individual gliders. The cumulative budget is taken from time 0, which is 12:30 on 6th February 2020, and the cumulative values are calculated for every hour thereafter.

The budget can be closed over the 10 days from 12:30 UTC 6th February to 08:30 UTC 16th February, to within $0.07\,^{\circ}\mathrm{C}$. At the end of the accumulation period, net heat fluxes account for $-0.2\,^{\circ}\mathrm{C}$, whereas the temperature tendency indicates a temperature change in the mixed layer of $-0.13\,^{\circ}\mathrm{C}$. The root mean square difference between temperature tendency and net heat flux contribution throughout this time is $0.05\,^{\circ}\mathrm{C}$. Overall the heat fluxes do a good job of closing the heat budget alone on the scale of the campaign, at shorter time scales the advection likely causes the short-term fluctuations and mixing/entrainment may also contribute to the tendency.

4.6 Discussion

The representation of ocean mixed layer SGavg gives a high resolution insight into the behaviour of the mixed layer which is not obtainable without the Seaglider measurements. Even within a small sampling site of sides 10 km, there is marked variability in T_a between the two Seagliders at different locations in the study site. SG637 seeing an almost $0.2\,^{\circ}\mathrm{C}$

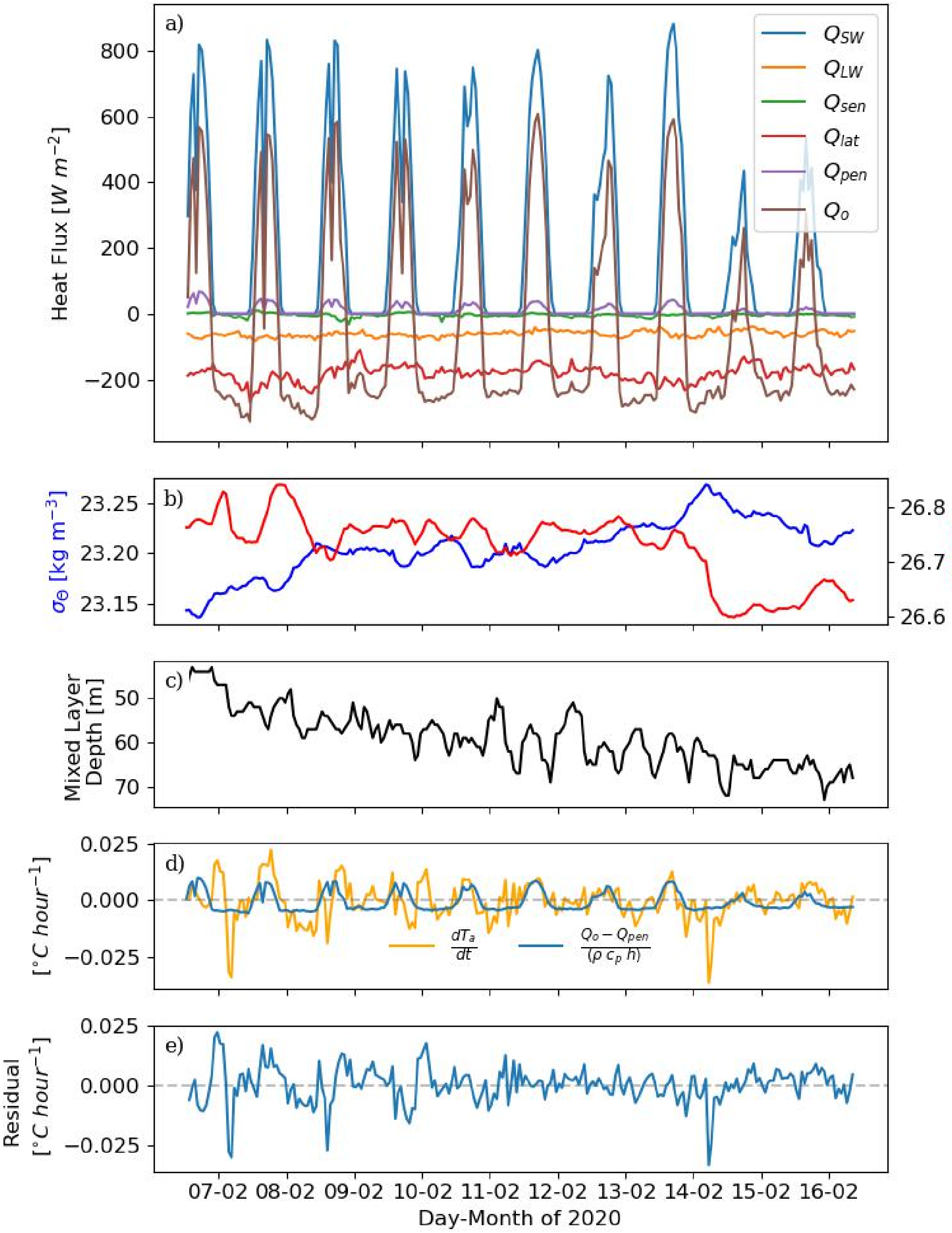

Figure 4.20: Time series of heat budget. a) Net surface heat flux and the flux components used to calculate it, along with Q_{pen} correction. b) Mixed layer average potential density anomaly (blue) and conservative temperature (red). c) mixed layer depth. d) Temperature tendency (orange) and the net heat flux contribution to the mixed layer heat budge (blue). e) Residual left by this approximation of the mixed layer heat budget.

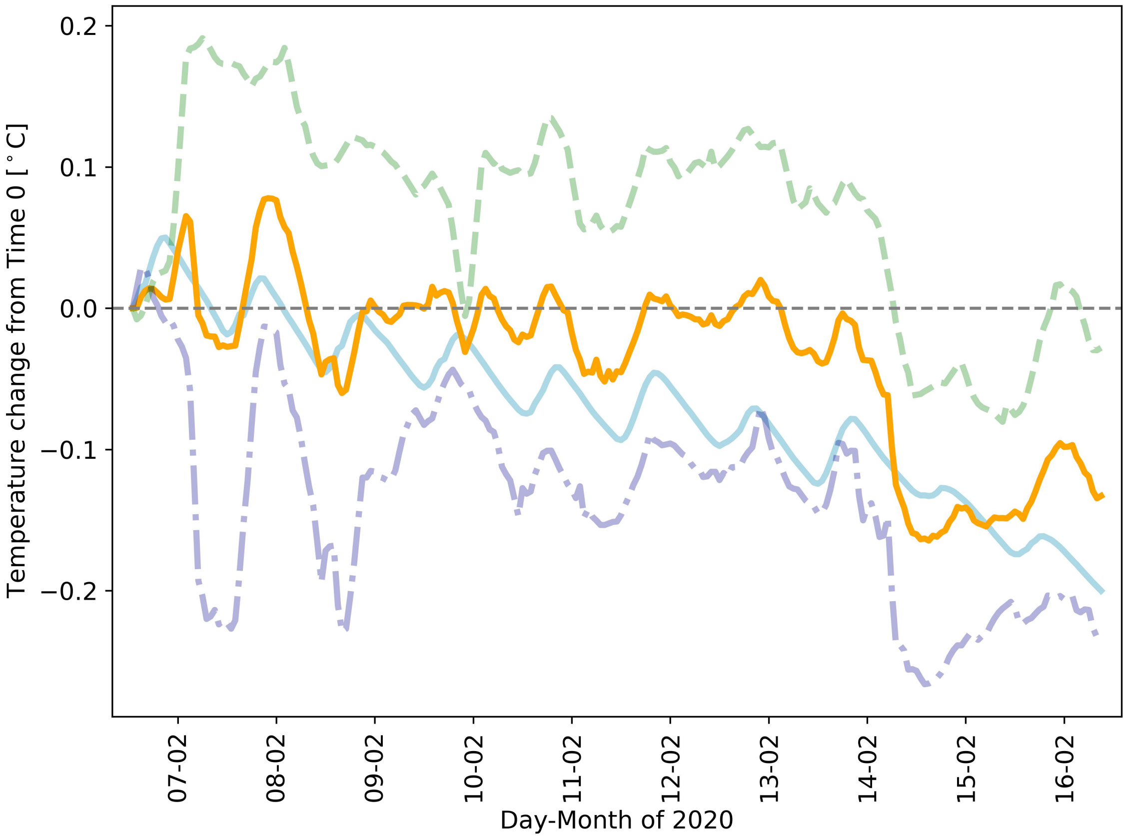

Figure 4.21: Temperature change from Time 0 in campaign, comparing cumulative glider averaged mean mixed layer temperature per hour (orange) with cumulative net heat flux contribution to the ocean heat budget per hour (light blue). Dotted lines show the mean mixed layer temperature tendency from each individual Seaglider, SG579 (blue dashed line) and SG637 (green dashed line).

increase in T_a within the first 12 hours of the study 'Time 0'. SG579 observes rapid changes of the same order of magnitude to SG637 between 6th and 9th February, indicating it crosses the same front multiple times as it moves around the study site under a different pattern. SG637 experiences another cooling event during the night of 9th February, but after this both gliders show very similar trends in T_a. SGavg then combines these temperatures seen at different positions within the study site, which creates the appearance of rapid warming and cooling within the site, particularly noticeable on 7th February. Whilst these changes are true and observed, they are the product of spatial and temporal variation in the study site. This work assumes spatial homogeneity in the site to treat the site as a point location, however at timescales as short as hourly, spatial variability inside the site does have an impact. The study could have benefitted from a different sampling pattern that reduced the movement of the Seagliders within the site and so eliminated the observation of spatial changes around the site. The right angled orientation of three platforms (Vijith et al., 2020), where the gliders form two end points and a third platform forms the point at the right angle, would have produced time series appropriate for a mixed layer heat budget whilst removing the impact of platform movement within the site. Nonetheless, the campaign undertaken in this thesis has produced ocean mixed layer time series which allow investigation into closing the mixed layer heat budget in terms of net heat flux and quantifying biases in reanalysis products, which is still a useful and worthwhile scientific endeavour. Overall, the budget closed fairly well, but there are some uncertainties in the treatment of the data and the choice of variables that I discuss in more detail below.

Processing of the Seaglider data looked into the possibility of diurnal warm layer formation in the study site whilst filling missing near surface during the quality control process. A linear and exponential fit was made to the top 10m of each glider profile and of the 369 near surface temperature values missing across both gliders, 33 were filled using the exponential fit. In many of the profiles, the difference between linear and exponential fit for the 0.5 m temperature value was on the order of 0.01 °C or less. If the linear fit were used, the filled temperature would be at most 0.02 °C lower, as seen in Figure 4.3g,h. Changing surface approximation will play no significant role in skewing the mixed layer averaged temperatures which were used for the heat budget of the chapter. The *Caravela* CTD has an accuracy of ±0.01 °C, so in most instances the difference in surface extrapolation is within the error of *Caravela* temperatures to which the glider SSTs are comparable.

Beginning with the air-sea heat fluxes calculated from observations and ERA5, Q_{net-e} and Q_{net-o} produced daily averaged heat fluxes with a mean difference of $75\,\mathrm{W\,m^{-2}}$. This difference is considerably larger than the target flux bias of $5\,\mathrm{W\,m^{-2}}$in a 25 km gridded product (Cronin et al., 2019). I discern that three of the four components of net surface heat flux provided by ERA5 are thought to have biases compared to our regional observations in the NWTA. Possible biases in the ERA5 longwave flux have not been quantified in this thesis due to offsets discovered in the observations of downwelling longwave radiation. Using a best estimate of $Q_{sw-o}, Q_{lw-e}, Q_{lat-o}, Q_{sen-o}$, for the net surface heat flux gives $30\,\mathrm{W\,m^{-2}}$ less mean daily heat loss to the atmosphere than suggested by ERA5, indicating ERA5 carries a net heat flux bias in the NWTA region much larger than the target bias of a gridded product (Cronin et al., 2019).

The greatest bias identified in ERA5 surface fluxes lies in the shortwave radiative flux term, with differences in ERA5 and observed net shortwave flux on the hourly scale as large as $356\,\mathrm{W\,m^{-2}}$. Direct comparisons cannot usually be made between a point observation and gridded product due to local variability that the gridded product will be unable to represent, however differences on this order of magnitude are still suggestive of a misrepresentation of processes or bias in the reanalysis product. Biases in irradiance from ERA5 have been identified in previous studies, with overestimation of surface irradiance during cloudy conditions and underestimation of surface irradiance during clear conditions (Urraca et al., 2018). A study using the PIRATA moorings, an array over the equatorial Atlantic (Trolliet et al., 2018) drew similar conclusions on the performance of ERA5, finding that instances of cloud free conditions also underestimate surface solar irradiance for daily observations. Conditions from 6th to 13th February involved intermittent cloud cover with varying cloud structure. Cloud conditions were visually assessed using satellite images on NASA Worldview, using the Corrected Reflectance (True Color) Terra/Modis base layer (NASA Worldview Snapshots, 2020). This transient cloud cover is likely responsible for observed decreases in net longwave flux, which is not represented in ERA5. On 14th and 15th February, the cloud structure changed and cloud coverage of the region was much denser. On these days, ERA5 overestimates net shortwave flux (by $76\,\mathrm{W\,m^{-2}}$ and $42\,\mathrm{W\,m^{-2}}$ and so must be overestimating solar irradiance, which is in line with conclusions drawn by Urraca et al. (2018). The underestimation of irradiance with clear conditions is harder to assess in this campaign, as the rest of the time spent at the study site is with intermittent cloud cover. However, ERA5 clearly does not represent this finer variable cloud structure well, as ERA5 overestimates net shortwave flux for five of the remaining days and underestimates net shortwave flux for three days. Overall it is clear that whilst ERA5 improves on tropical fluxes compared to its predecessor ERA-Interim (Li et al., 2021), there is still a way to go in accurate cloud representation (Bony et al., 2017).

Latent heat fluxes are the next biggest contributor after the shortwave flux to the observed net surface heat fluxes. The mean air-sea latent flux calculated from the observations is $-181\,\mathrm{W\,m^{-2}}$.This latent flux is larger in magnitude than $-157\,\mathrm{W\,m^{-2}}$ from Iyer et al. (2022) and $-170\,\mathrm{W\,m^{-2}}$ from Bigorre and Plueddemann (2021). Bigorre and Plueddemann (2021) results are from February average fluxes from 2001-2012 using NTAS buoy data (around 51 °W, 15 °N) and Iyer et al. (2022) January - February 2020, approx 51 °W - 57 °W, 13.5 °N - 16 °N. Differences between latent flux in these studies are likely due Iyer et al. (2022) being over a larger and more easterly area, and spatial differences from (Bigorre and Plueddemann, 2021). Figure 1.4 shows both these studies typically have cooler SSTs than our study site, which could indicate lower surface evaporation, thus the lower latent heat flux to the atmosphere. For the tropical Atlantic, net surface heat flux, specifically the shortwave and latent flux contributions, are responsible for changes seen in the mixed layer heat content (Foltz et al., 2003), so it is pertinent to correctly represent this flux to close the budget. Apart from a few short periods, ERA5 overestimates the magnitude of heat lost to the atmosphere when compared to observations in the NWTA with an average hourly overestimate of 39 W m^{-2}. Studies on the PIRATA moorings show annual mean latent heat flux at 15 °N, 38 °W is -120 W m^{-2} and at 12 °N, 38 °W is -130 W m^{-2} (Foltz et al., 2003), lower than observed in this study and identified by ERA5, however that is likely be a product of location differences and lack of seasonal influence in an annual mean value in the paper. Even though I do not expect a February value to align with an annual mean, it is useful to get an indication of flux magnitudes from other studies. Latent heat flux can be expected to be larger in boreal winter due to stronger winds (Foltz et al., 2003) enhancing evaporation at the surface, such that the observations within our campaign are assumed reasonable. Decomposing the turbulent fluxes into bulk variables provided by ERA5 and observed bulk variables, differences in representation of relative humidity between the ERA5 and the observations were noted. It was assumed that the ERA5 mean underestimation of relative humidity of 3.4 % relative to observations was a contributor to the bias seen in latent heat flux. Investigation into ERA5 flux bias in the tropical Indian ocean shows a root mean square error in latent heat flux of 29 W m^{-2} over three buoys (Pokhrel et al., 2020), 10 W m^{-2}, lower than the bias identified in this work. It must be acknowledged that observed relative humidities were not independently verified within this campaign, so the observed flux may contain some unquantified errors. Overall the 39 W m^{-2} bias in ERA5 compared to observations is substantial and further validation (like that intended to be obtained in the EUREC^{4}A campaign) will benefit turbulent flux representation in this region.

The mean air-sea sensible flux is 4 W m^{-2}. This sensible flux is comparable to -6.6 W m^{-2} of Iyer et al. (2022) and -7 W m^{-2} of Bigorre and Plueddemann (2021), although slightly smaller than the values in their studies. The mean bias in sensible heat flux from ERA5 was 7 W m^{-2} compared to observations, much smaller than for the previous two fluxes. Root mean square error in sensible fluxes compared to three buoys in the tropical Indian ocean was found to be around 6 W m^{-2} (Pokhrel et al., 2020), such that differences in this turbulent flux are in line with other similar studies. ERA5 was earlier shown to be underestimating air temperature by 0.68 °C and SST by 0.15 °C, leading to a larger air-sea temperature difference than in observations and an increased loss of heat to the atmosphere in the sensible flux compared to observations.

Biases identified in the turbulent fluxes in this study cannot be due to winds, as ERA5 winds were used for the observed flux calculations. However, it is possible that ERA5 is not representing these winds accurately, leading to further biases that cannot be quantified within the scope of this thesis. The validation of fluxes from ERA5 would further benefit from locally observed wind measurements and this should be possible in future campaigns given that adjustments to the *Caravela* platform were made to facilitate accurate wind observations following Chapter 3 of this thesis. The wind has not been adjusted for surface currents in this study, however it is thought that currents will be negligible with wind speeds of around $10\,\mathrm{ms}^{-1}$, such that this omission will not significantly impact the fluxes.

The net surface heat flux from this study can be best represented for the region with $Q_{sw-o}, Q_{lw-e}, Q_{lat-o}, Q_{sen-o}$ where the mean hourly net flux is $-50\,\mathrm{W\,m^{-2}}$. In terms of closure of the heat budget within this study, the heat budget can be closed with a root mean square difference of $0.006\,^{\circ}\mathrm{C\,h^{-1}}$ using a 6 hour running mean over $\frac{dT_a}{dt}$ or to within $0.07\,^{\circ}\mathrm{C}$ over the 10 days spent inside the study site, equivalent to $22\,\mathrm{W\,m^{-2}}$.

To assess how well our study represents expected fluxes and heat budget closure compared to other studies, similar net heat flux studies are considered. At 15 °N, 38 °W a PIRATA array mooring has been used to calculate the ocean heat budget (Foltz et al., 2003). A monthly mean for February indicates net surface heat flux in the region of $-50\,\mathrm{W\,m^{-2}}$ to $-100\,\mathrm{W\,m^{-2}}$ in line with our best representation of net surface heat flux. The residual in the heat budget using the full sum of terms in this equation was between $20\,\mathrm{W\,m^{-2}}$ to $30\,\mathrm{W\,m^{-2}}$ for February, such that our closure with net heat flux alone is as good as this study. Another study quantifying net surface heat flux in the tropical Atlantic uses the OAFlux product and identifies February net surface heat flux of between $-40\,\mathrm{W\,m^{-2}}$ and $-60\,\mathrm{W\,m^{-2}}$ for the region around 14 °N, -57 °W (Yu et al., 2006). One must note that the variability in local ocean and weather conditions on the scale of a week to a month mean that I do not anticipate the literature exactly matching the values found in this thesis. However one could expect them to be similar in value, and that is what I assess for here. The best representation of net surface heat flux being comparable to the above literature for this region in February supports the conclusions of this thesis that shortwave and turbulent fluxes are biased for ERA5 in this region. The monthly temperature change based on net heat flux contribution to the heat budget (excluding Q_{pen} correction is between $0\,^{\circ}\mathrm{C}$ and $-0.25\,^{\circ}\mathrm{C}$ (Yu et al., 2006), which is less than mean temperature change identified in our study (equivalent to $-0.4\,^{\circ}\mathrm{Cmonth}^{-1}$). It is entirely possible that for the period of time at the study site, temperature losses were larger than the monthly average identified by Yu et al. (2006). In terms of the hourly mixed layer heat budget closure, the residual does suggest that other mixed layer heat budget processes could play a role as important as the net heat flux contributions at short timescales, and so a heat budget should also consider processes like advection in a high temporal resolution study.

4.7 Conclusions

In summary, I have demonstrated that a novel combination of autonomous platforms and reanalysis data can be used to assess the mixed layer heat budget on regional scales, over short time periods. When only considering the net heat flux contribution to the mixed layer heat budget, the mixed layer heat budget is closed remarkably well, to within 0.07 °C over 10 days. This addresses Question 3 of this thesis *'How well do observed surface processes alone close the heat budget?'*. However at hourly to daily timescales, it becomes important to consider spatially variability when closing the budget, even within a small site as this.

An observational study of this type gives a unique opportunity to assess fine temporal scale variation and compare to existing flux products, as considered in Question 2 of this thesis, *'How do observational heat fluxes compare to global reanalysis product ERA5?'*. Comparisons to ERA5 highlights places where the ERA5 reanalysis dataset is lacking, namely its estimation of scattered or intermittent cloud cover, humidity and air temperature representations in the NWTA. These biases compared to observations coupled with COARE 3.5, result in average ERA5 sensible heat flux showing $5\,\mathrm{m}^{-2}$ more loss to the atmosphere than observations. ERA5 latent heat flux has on average $40\,\mathrm{m}^{-2}$ more loss to the atmosphere than observations. These differences are notable and highlights the need to understand the impacts of regional differences in flux products.

To improve the observational portion of the study, the calibration of the measured longwave sensor needs to be reassessed and the ability to directly measure wind from the vessel fixed. This chapter identifies biases in shortwave and latent fluxes in ERA5 reanalysis in the northwestern tropical Atlantic, and shows that improved representation of these fluxes will improve accuracy of regional air-sea heat fluxes, which could help reduce error in a mixed layer heat budget and bring SST accuracy for improvement of future climate simulations.

5

Further investigation into an ocean mixed layer heat budget

Synopsis

In this chapter, I follow on from the ocean mixed layer heat budget investigation in chapter 4. Different methodologies for calculating horizontal advection from *Caravela* and Seaglider observations are tested alongside GLORYS reanalysis. Entrainment is investigated from Seaglider observations at the mixed layer base. I anticipated entrainment and advection would play significant roles in this heat budget, and the results indicate both processes contribute notably to heat exchange in the mixed layer. This chapter set out to improve upon the budget closure from chapter 4 by including these two additional processes, however I found the budget closure to be worse than with the net heat flux contribution alone, likely due to uncertainties in the horizontal advection and entrainment.

5.1 Introduction

In the previous chapter, the closure of the heat budget was investigated using only the net heat flux term of the heat budget equation (full equation 1.3.2). In this chapter, the heat budget is recalculated with consideration of oceanic processes neglected in Chapter 4, specifically horizontal advection and vertical entrainment, to see if this reduces the residual and further improves mixed layer heat budget closure.

Horizontal advection is produced by ocean currents flowing up or down a temperature gradient, bringing colder or warmer water (respectively) into a specified location. Horizontal advection of heat is influenced by submesoscale ocean features, eddies and large scale circulation, affecting local SSTs. Vertical advection is near-zero within the mixed layer because of the lack of vertical temperature gradient, but vertical advection across the mixed layer base results in entrainment. Vertical entrainment directly influences mixed layer depth through incorporation of deeper waters into the mixed layer, changing the mixed layer average temperature based on the properties of the entrained water. The entrainment term is typically separated from the vertical mixing term in mixed layer heat budgets. The differences in vertical mixing and entrainment are subtle yet important. Vertical mixing represents diffusion of heat across the mixed layer base, and can occur without any change in mixed layer depth. Meanwhile entrainment represents a bulk process that is estimated from mixed-layer depth changes and must involve vertical mixing, whether or not the mixing is observed. As a result, observational budget estimates that include both entrainment and mixing may double-count the effects of mixing. Here I do not have the observations to quantify the vertical mixing so I estimate entrainment instead. In the tropical Atlantic, entrainment is an important process during periods of strong wind stress and vertical stratification changes. These processes alongside air-sea fluxes drive SST variability, from daily to seasonal and inter-annual timescales (Nogueira Neto et al., 2018; Foltz et al., 2013).

In previous heat budget studies around the world, the contributions of oceanic processes and air-sea interactions have been investigated. Various examples are described in the following paragraphs to evaluate the current knowledge of the drivers of SST variability.

The seasonal cycle of the equatorial mixed layer heat budget was investigated using a numerical simulation of the tropical Atlantic (Peter et al., 2006), in which the SST balance at the equator was reported to be due to heat gain by surface net heat fluxes and eddies, and heat loss by vertical subsurface processes. Eddy heat transport has been shown to be significant only within 5 degrees of the equator based on studies in the Pacific (Moisan and Niiler, 1998; Hansen and Paul, 1984). Foltz et al. (2003) assessed the Atlantic seasonal cycle at 15 °N 38 °W and found that in January and February, entrainment, the zonal component of horizontal advection and eddy advection contributed to heat losses, whilst the meridional advection contributed to heat gains in the mixed layer. The heat storage rate is between $-100\,\mathrm{W/m^2}$ and $-50\,\mathrm{W/m^2}$ from January to February for this region, suggesting that seasonal cooling dominates at this time of year. This is the same time of year as our investigation, within 1 degree of latitude, but around 20 degrees to the east of our investigation.

Nogueira Neto et al. (2018) investigated the annual mean contribution of various processes to the heat budget. Taking their box 1 region representing the NWTA (northwestern tropical Atlantic), between 10 °N and 20 °N, west of 35 °W, they calculate the annual mean contributions of surface fluxes ($-21.2\,\mathrm{W\,m^{-2}}$), horizontal advection ($1.65\,\mathrm{W\,m^{-2}}$), and entrainment ($-3.8\,\mathrm{W\,m^{-2}}$), yielding a residual of $17.7\,\mathrm{W\,m^{-2}}$ compared with the heat storage value of $-5.7\,\mathrm{W\,m^{-2}}$, with net surface fluxes the dominant contributor to heat storage (Nogueira Neto et al., 2018). This study has a large residual which contains the errors of the other terms in the heat budget and gives an idea for how well the budget in this region can be closed on an annual time scale.

Whilst air-sea interactions dominate the heat budget across the NWTA on longer timescales, I set out to ascertain if this relationship is sustained at sub-seasonal timescales. The data used in this chapter are a combination of in-situ observations and reanalysis products. The in-situ observations are from *Caravela* and the two Seagliders SG579 and SG637, as used in chapter 4, with processing described in section 4.2.1. Wind speed is obtained from ERA5 as described in chapter 4. I use the GLORYS12V1 reanalysis product to provide independent mixed layer temperature and horizontal velocity estimates. GLORYS12V1 is an eddy rich ocean reanalysis product at 1/12 °on 50 standard levels (E.U. Copernicus Marine Service Information (CMEMS), 2023; Jean-Michel et al., 2021) (introduced in Section 2.5.2). This dataset is henceforth referred to with the shorthand GLORYS. Conservative temperature field from GLORYS surface data and observed surface data from our study are visible in Figure 5.1.

5.2 Theory and Methods

In Chapter 4, processes contributing to the ocean mixed layer heat budget outside the net heat flux were ignored. Here I consider said other processes. To do this with daily mean values for entire days across all calculated terms, the study in this chapter is restricted in time to 00:00 UTC 7th February to 24:00 UTC 15th February, or nine whole days in the study site.

One method to investigate the surface heat balance is that of Wang and McPhaden (1999), where the horizontal advection, entrainment and surface heat flux terms are compared with the temperature tendency, with all other terms treated as components of a residual heat flux. The advantage of using a residual term is that this includes accumulated errors of the other terms in the equation (Nogueira Neto et al., 2018) and is similar to the approach I took in the previous chapter. In this chapter, I again take the approach of comparing the temperature tendency to the heat budget with a residual, but this time with additional terms from the ocean heat budget than in chapter 4.

Starting from Equation 1.3.2, simplify to the form

$$\frac{\partial T_a}{\partial t} = \frac{q_0 - q_{pen}}{\rho c_p h} - \boldsymbol{v_a} \cdot \nabla T_a - \frac{(T_a - T_{-h})}{h} \times \left(\frac{\partial h}{\partial t} + w_{-h} \right) + R \tag{5.2.1}$$

where R represents the residual in the budget closure due to the terms not represented and the uncertainties in the calculated terms. It is common to simplify the ocean mixed layer heat budget to focus on terms of interest within a particular study (du Plessis et al., 2022; Liu et al., 2010; Dong et al., 2007). Using a residual allows one to also account for the terms of equation 1.3.2 that are not explicitly calculated in a simplified form of the heat budget.

Reasoning for excluding terms from our Equation 5.2.1 are as follows. The velocity temperature covariance term has been estimated to contribute less than 10 % of other terms in the heat budget equation (Swenson and Hansen, 1999), so I assume that this term is negligible and can be ignored, in line with many other heat budget investigations (Wang and McPhaden, 1999; Foltz and McPhaden, 2005; Hadfield et al., 2007). For the entrainment term, the mixed layer depth tendency $\frac{\partial h}{\partial t}$ and vertical advection w_{-h} terms can be estimated with in situ observations, however I do not have the spatial resolution for the $\boldsymbol{v_{-h}} \cdot \nabla h$ component of entrainment representing lateral induction in our observations alone. I therefore estimate the entrainment with the depth tendency and vertical advection components, excluding lateral induction. The diffusion terms included in Equation 1.3.2 predominantly resolve eddy behaviour. Horizontal diffusion is assumed to have no significant impact on the heat budget in the open ocean when the budget is undertaken over a large area (30°–10°S, 100°–80°W) (Zheng et al., 2010) but can be locally significant in eddy-rich areas like coastal upwelling regions (Kolodziejczyk and Gaillard, 2013). At the scale of the observations collected in this study (9 whole days and 10 km), horizontal diffusion due to eddies will be largely captured within the horizontal advection term therefore I expect this term to be negligible. For the vertical diffusion or mixing term on short time scales, diffusivity of temperature across the base of the mixed layer without entrainment is likely a much smaller term than I am concerned with, especially on short time scales and is thus neglected. For vertical heat transfer at the base of the mixed layer, I estimate vertical entrainment and ignore vertical diffusion, assuming the entrainment calculations on such short timescales is capturing any heat exchange caused by vertical diffusion. The temperature tendency term is the same used in Chapter 4 and is described in Section 4.5.2 (Figure 4.21).

5.2.1 Horizontal Advection

Horizontal advection is the $-(\boldsymbol{v_a} \cdot \nabla T_a)$ term of the heat budget equation where $\boldsymbol{v_a}$ is the horizontal velocity averaged between the surface and depth h and T_a is the ocean temperature averaged between the surface and depth h.

Horizontal advection can be estimated from ocean reanalysis data, and the GLORYS product was chosen for this purpose. I also attempt to utilise observations for the calculation of advection, given the coverage of observations within the study site. I estimate both the temperature gradients and velocities used to calculate advection from GLORYS and observations, and describe each of the methods below. Positive values refer to northwards and eastward movement when looking at temperature gradients and velocities. The results of each method are visible in Figure 5.5 and the pros and cons of each discussed in Section 5.10. Methods labelled T describe temperature gradient component calculations and methods labelled V describe velocity term calculations. Due to large uncertainties with observational determination of advection, ultimately the GLORYS based calculation (methods T3 and V2) are used to represent advection in the final heat budget (Section 5.3), with a comparison made to methods T2 and V2. Depending on the method used to calculate each term of the horizontal advection, the resolution of the term will either be hourly or daily.

Method T1: Observations from *Caravela* This method takes in-situ SST observations from *Caravela* alone to determine daily temperature gradients across the study site. Usually the temperature used in the horizontal advection calculation in mixed layer heat budgets is the average mixed layer temperature. As vertical ocean profiles are not available from *Caravela* , I use the near surface SST to estimate advection. The study site is divided into four quadrants. The *Caravela* time series resampled to hourly medians to remove outliers and for consistent temporal resolution with the glider data and ERA5. Each hourly *Caravela* data point is assigned a quadrant based on the median location within said hour. The time series of in-situ ocean temperature measurements is separated by quadrant in Figure 5.2 . Using this time series, a daily mean ocean temperature was calculated for each quadrant (Figure 5.2 panel b), as well as mean vessel location on each day (Figure 5.2 panels c and d). To calculate the temperature gradients, the site is split into halves, so each of $\frac{dT}{dx}$ and $\frac{dT}{dy}$ have two estimates within the site. The north estimate is defined as $Q2 - Q1$, south as $Q4 - Q3$, east as $Q2 - Q4$ and west as $Q1 - Q3$. The temperature change is taken to be the daily mean temperature difference between a given pair of quadrants. The distance needed to calculate the gradient is calculated using the difference in daily mean longitudes in a pair of quadrants for $\frac{dT}{dx}$ and difference in daily mean latitudes in a pair of quadrants for $\frac{dT}{dy}$. To obtain an overall $\frac{dT}{dx}$ and $\frac{dT}{dy}$, an average of the two site half estimates is taken. For days when *Caravela* did not enter a quadrant of the study site, no gradient has been calculated for that half of the site and the daily average is taken to be the calculated value for other quadrant pair in the site.

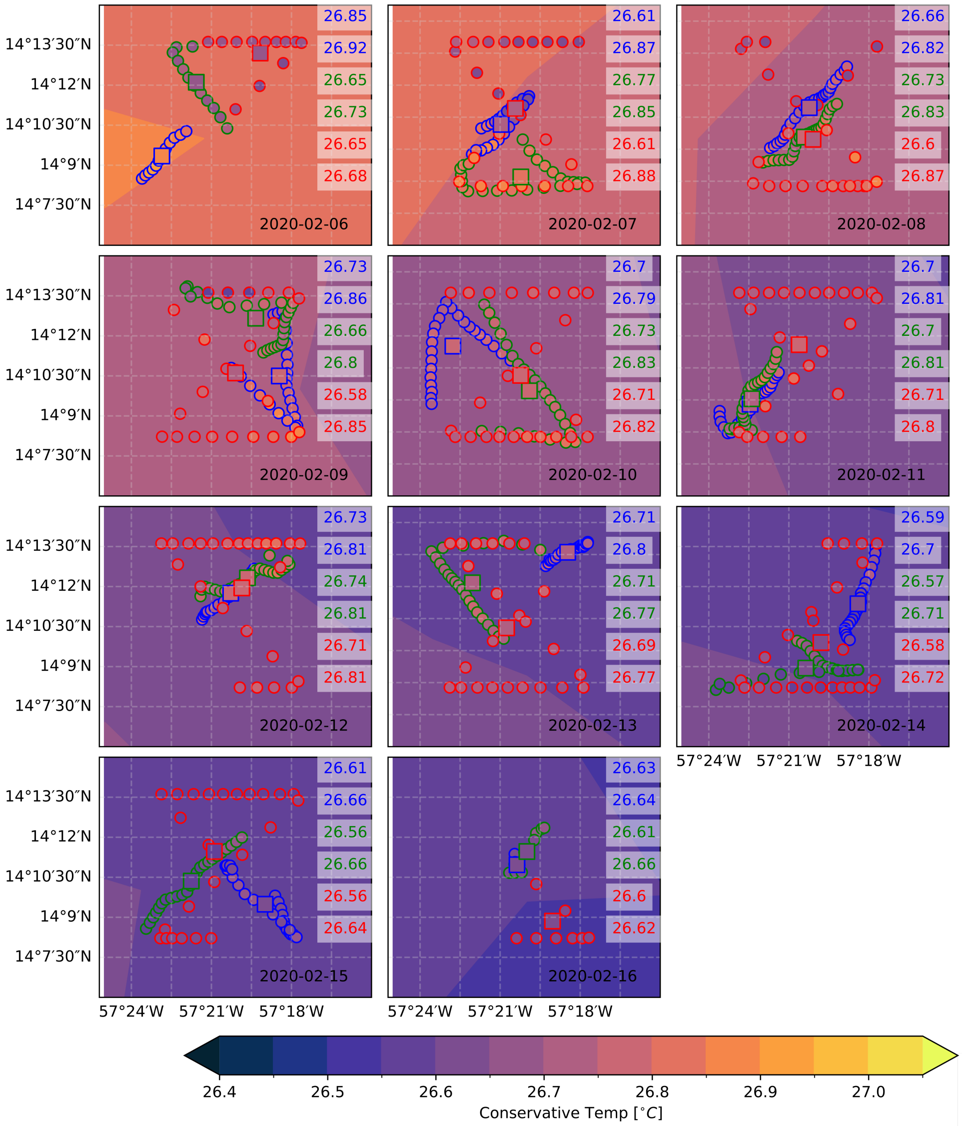

Figure 5.1: SST values in the EUREC^{4}A study site between 6th and 16th February 2020. The background contour shows conservative temperature from 0.494 m depth level of GLORYS. Observations are shown in circles with 0.5 m depth values of SG579 (blue) and SG637 (green) and the fixed depth CTD measurement from *Caravela* (red). Squares denote the daily average for each platform. Values printed on each day are the max and min hourly observation in the corresponding colour used for each platform.

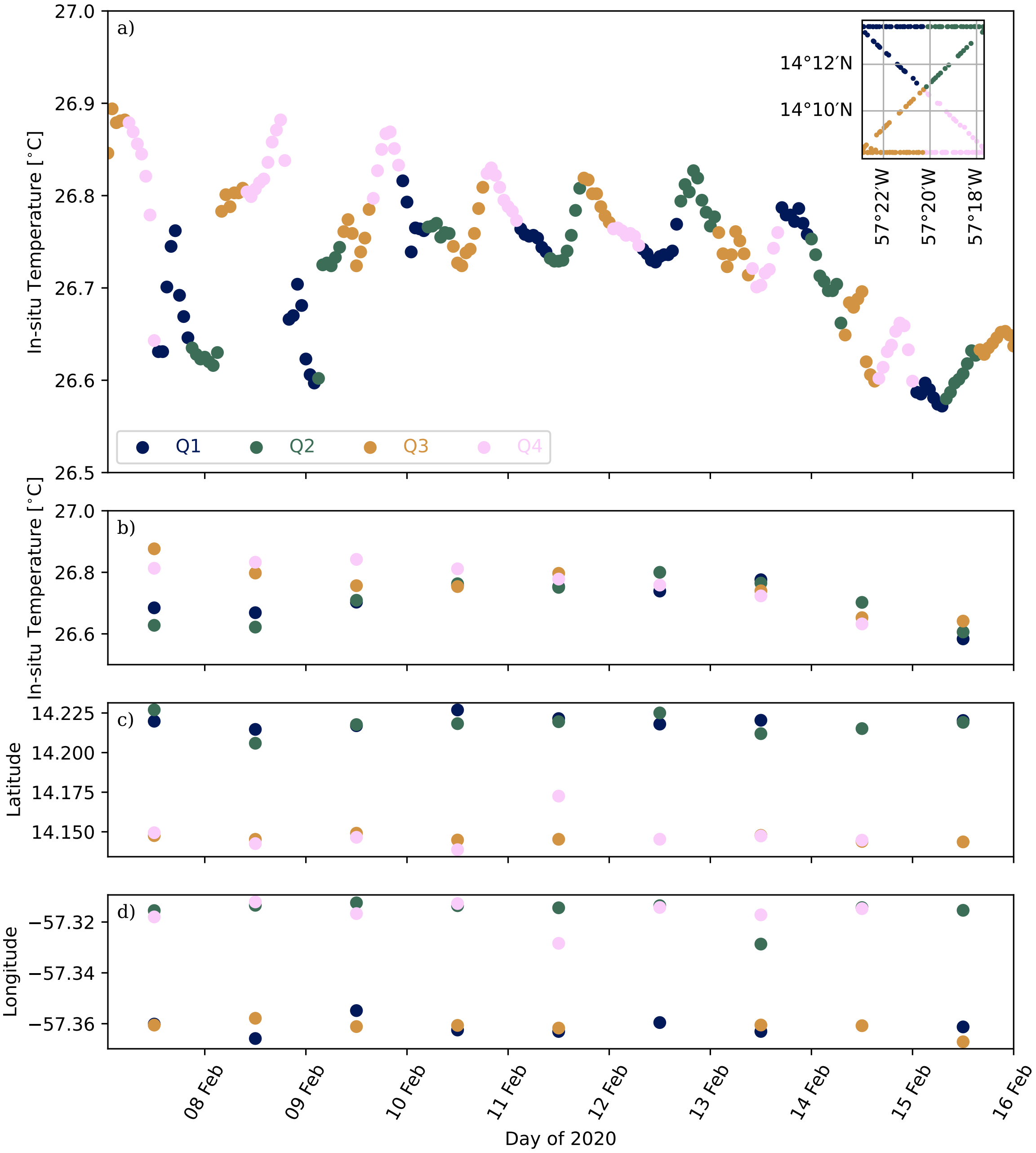

Figure 5.2: a) Time series of in-situ ocean temperature measurements from the *Caravela* vessel, labelled by 00:00 hours on each day of 2020 (UTC). The study site and time series are divided into and coloured by quadrants ((a) inset). b,c and d show daily mean values of temperature, latitude and longitude respectively at 12:00 UTC of the relevant day.

Method T2: Multi platform Observations This method takes observations from both Seagliders and *Caravela* to determine hourly temperature gradients across the study site. In method T1, using only *Caravela* data necessitates aliasing values at different points in the diurnal cycle into the gradient calculation. By using *Caravela* and the Seagliders in T2, the temperature gradient is calculated across data taken within the same hour bracket, eliminating the problem of diurnal aliasing. In this method, I take the conservative temperature of each platform to determine the temperature gradient. Conservative temperature from *Caravela* has been calculated with the fixed absolute salinity value of 35.62 g/kg (the median salinity within the study site) to eliminate anomalous conservative temperature values from salinity spikes. As I am using 3 moving platforms, the vessels are unlikely to be orthogonal or aligned along the latitude and longitude axes for any hourly measurement (see schematic Figure 5.3). To estimate temperature gradients whilst accounting for the configuration of the three vessels, I follow the method of (Vijith et al., 2020) in which the measured temperature differences $\Delta T_a, \Delta T_b$ between *Caravela* and a glider are used to calculate the temperature gradients in x and y, and are given by

$$\Delta T_a = T_a - T_{Caravela} = \frac{\partial T}{\partial x}\Delta x_a + \frac{\partial T}{\partial y}\Delta y_a \tag{5.2.2}$$

$$\Delta T_b = T_b - T_{Caravela} = \frac{\partial T}{\partial x}\Delta x_b + \frac{\partial T}{\partial y}\Delta y_b \tag{5.2.3}$$

where a and b represent the two Seagliders respectively. $\Delta x_a, \Delta x_b$ and $\Delta y_a, \Delta y_b$ are respectively the x and y components of the distances between glider a or b and *Caravela* . Rearranging the above for a and b gives the temperature gradients in the form

$$\frac{\partial T}{\partial x} = \frac{\Delta T_b \Delta y_a - \Delta T_a \Delta y_b}{\Delta x_b \Delta y_a - \Delta x_a \Delta y_b} \tag{5.2.4}$$

$$\frac{\partial T}{\partial y} = \frac{\Delta T_b \Delta x_a - \Delta T_a \Delta x_b}{\Delta y_b \Delta x_a - \Delta y_a \Delta x_b} \tag{5.2.5}$$

It is these temperature gradients from equations 5.2.4 and 5.2.5 which are subsequently used in the horizontal advection calculation.

Method T3: Reanalysis This method estimates daily temperature gradients from the depth weighted mean of conservative temperatures derived from the GLORYS reanalysis

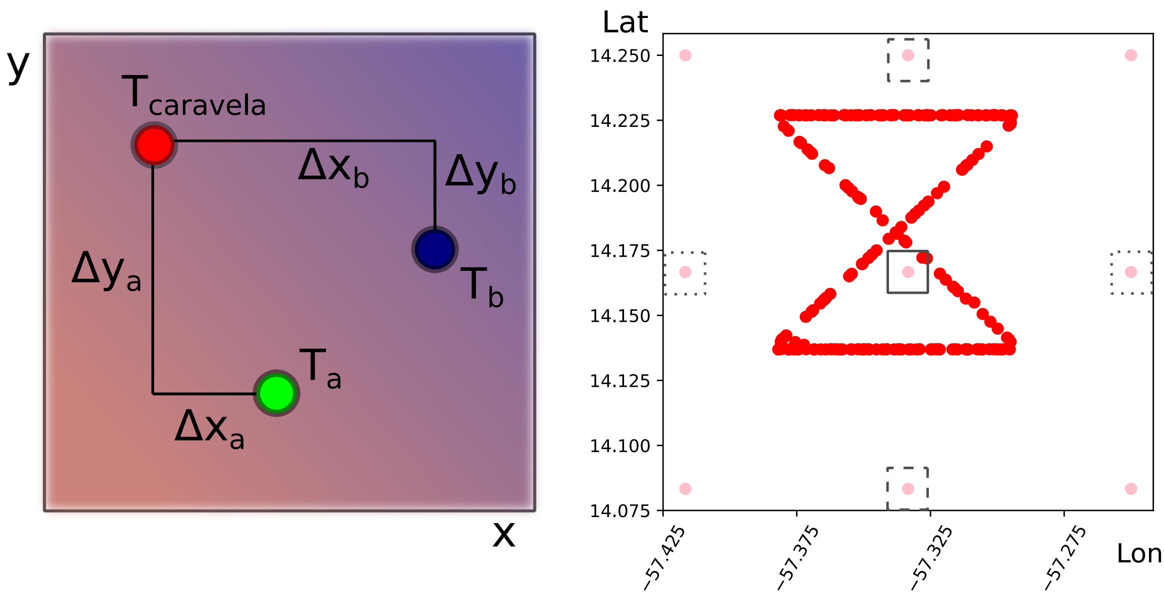

Figure 5.3: Schematic to show how temperature gradients are calculated. Left is an example of vessel locations SG579 (green circle), SG637 (blue circle), *Caravela* (red circle) for method T2 (see text). Shading is used to give an example of an SST field in the background. Right shows *Caravela* data (red) and GLORYS grid points (pink) for method T3 . For dT/dx, locations identified with dotted lines are used, for dT/dy dashed line location are used. The solid line around the centre GLORYS point is the location of velocity values used in V2.

product (Figure 5.3). $\frac{\partial T}{\partial x}$ and $\frac{\partial T}{\partial y}$ are calculated by taking the gradients in temperature between two GLORYS grid locations in x and y and the distance between these grid points.

Method V1: Glider Surface Drift Between each profile, the Seaglider takes time to sit at the surface to transmit data. As a buoyant platform, the Seaglider will drift during this communications phase. This drift can be used as a proxy for the ocean surface currents. The effect of winds on the drift of the glider should be minimal as only the antenna and a small portion of the tail lies above the water, but stokes drift from surface waves may affect the movement of the glider, and the surface current is not necessarily representative of the mixed-layer average currents. The surface drift is estimated using the GPS location at the end of the previous dive, just before the next dive and the time spent at the surface. I assume linear travel between the two points on this short timescale of up to 15 minutes. Glider surface drift values are timestamped at the start time of the drift. A daily mean of the surface drifts is then used as a proxy for surface current velocity when calculating advection.

Method V2: GLORYS This method takes horizontal velocities u and v supplied directly by GLORYS at the location closest to the centre of the study site, see bold outlined grid point in Figure 5.3. I compare both the depth weighted mixed layer average velocities and surface velocities in Figure 5.5.

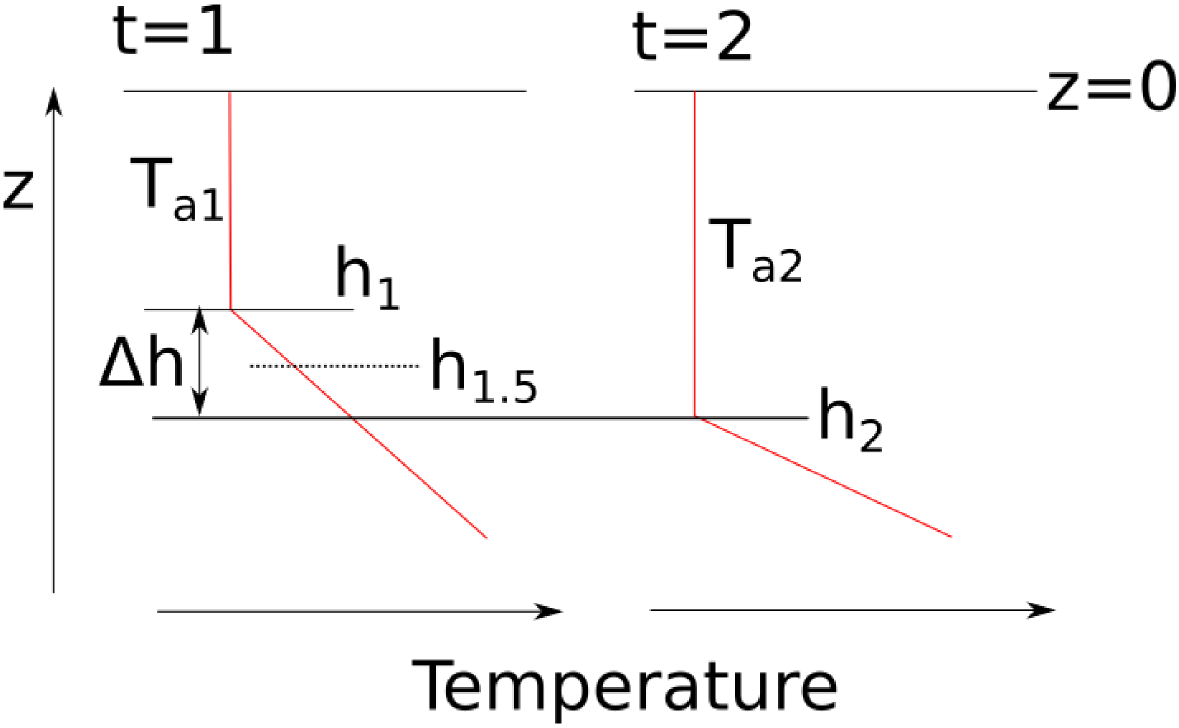

Figure 5.4: Schematic to illustrate the values used in the calculation of entrainment. t represents two consecutive timesteps; T_{a1} and T_{a2} the mixed layer average temperatures at each timestep; h_1 and h_2 the mixed layer depth at each time step, $h_{1.5}$ the depth halfway between h_1 and h_2 at which the entrained water temperature is found and Δh the mixed layer depth change.

5.2.2 Entrainment

The entrainment term formulation used in this mixed layer heat budget is $-\frac{(T_a - T_{-h})}{h} \times \left(\frac{\partial h}{\partial t} + w_{-h}\right)$, neglecting the lateral induction component as earlier described. I calculate entrainment over each one hour time interval from time 1 to time 2. For this method, the multiplier $\frac{T_a - T_{-h}}{h}$ from equation 1.3.3 is replaced with $\frac{T_{a1} - T_{-h1.5}}{h_2}$. Using T_{a1},the depth weighted mean temperature at time 1 (explained schematically in Figure 5.4). $T_{-h1.5}$ replaces T_{-h}, where $T_{-h1.5}$ is the temperature interpolated at time 1 at the midpoint between the mixed layer depths at time 1 and 2, i.e. the temperature at $z = -h_{1.5}$ in Figure 5.4. This is to represent the water that will be entrained within this time step. The divisor h is taken to be the mixed layer depth at time 2, ie $h2$. The mixed layer tendency term $\frac{\partial h}{\partial t}$ is the difference in mixed layer depth at each time step, where a positive value denotes a deepening of the mixed layer. w_{-h} is calculated by taking the change in depth within the time step of the 26 °C isotherm, which lies below the sub-surface temperature inversion. Without accounting for vertical advection in this way, the entrainment term would be dominated by short term depth fluctuations from internal tides.

There are arguments for and against the inclusion of detrainment (where the mixed layer becomes shallower) in the entrainment calculation. To exclude detrainment, when $\frac{\partial h}{\partial t} \leq 0$, the entrainment is set to 0. Many papers take the approach that entrainment is an irreversible process in both heat and salt budgets and so a value is only calculated when the mixed layer deepens within a time step (du Plessis et al., 2022; Ren and Riser, 2009; Dong and Kelly, 2004). However Kim et al. (2006) outline the need for the inclusion of detrainment. Assuming colder water lies below the mixed layer, mixed layer shoaling will typically cause slightly colder water to be shed in the lower mixed layer due to a small vertical temperature gradient in the mixed layer, causing the vertically-averaged mixed-layer temperature to warm slightly. In the context of this study, the warmer water below the mixed layer will result in water shed in detrainment being above T_a, thus cooling the mixed layer average temperature.

5.3 Results

5.3.1 Horizontal Advection

The first mixed layer heat budget term assessed is the horizontal advection using the various methodologies described above. The temperature gradients and velocities calculated according to each method are shown in Figure 5.5. The T1 and T2 temperature gradients are much larger than that suggested by GLORYS. Concerns with method T1 diurnal cycle aliasing lead us to calculate the budget with advection from GLORYS method T3 and observational method T2. For the velocity component, the glider drift approximation differs between the two gliders, with the offset in the u component increasing from the 10th February. I am unable to explain or why this would have occurred as both gliders remained in the study site. It is possible that glider 637 experienced more drift due to sitting differently in the water, or it may be that courser measurements and GPS error contribute to bigger discrepancy. The GLORYS product velocity is chosen for further analysis such that a reliable mixed layer average velocity is used in the advection calculation. The results that lead to these choices are described below. Horizontal advection over the whole study site period is consistent between methods V2,T2 and V2,T3, indicating advection is being well represented overall. At the daily scale, these methodologies differ, such that there is room for improvement in higher resolution accuracy of temperatures and currents.

Figure 5.5d shows the $\frac{\partial T}{\partial x}$ values, with method T3 (GLORYS) have a mean gradient $-1.9 \times 10^{-6}\,^{\circ}\mathrm{C\,m^{-1}}$, and in the same direction for each studied day. In 5.5e, $\frac{\partial T}{\partial y}$ values from method T3 have a mean of $-9 \times 10^{-7}\,^{\circ}\mathrm{C\,m^{-1}}$ with temperatures warmer in the north 7th to 9th of

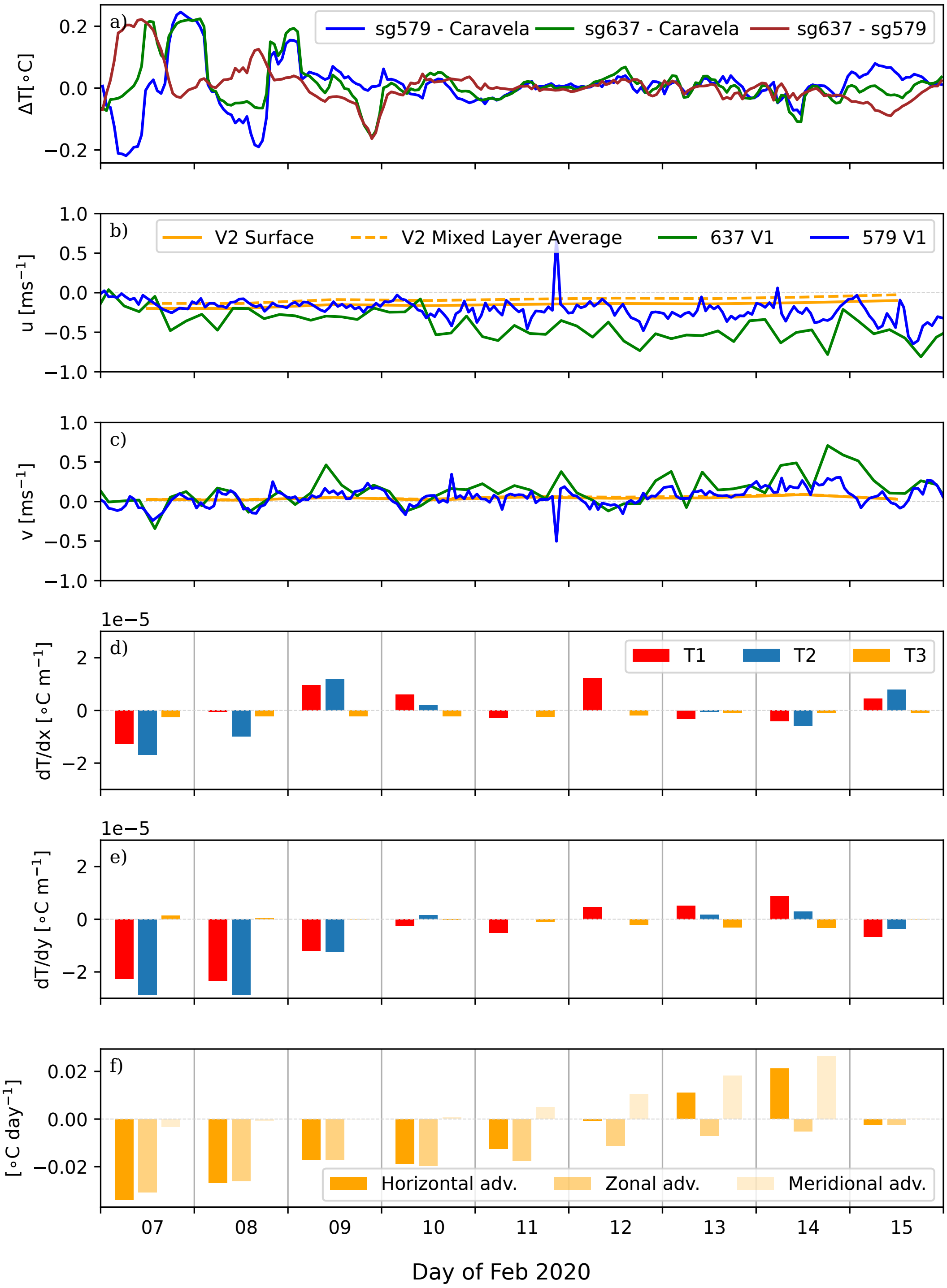

Figure 5.5: Components of horizontal advection based on methods T1,T2,T3,V1 and V2 described in text. Differences in conservative temperature at the surface between platform pairs (a). U (b) and V (c) components of horizontal velocity using method V1 with glider 579 (blue) and glider 637 (green). Method V2 takes GLORYS data at the surface (orange solid line) and averaged over the mixed layer (orange dashed line) dT/dx (d) and dt/dy (e) from *Caravela* T1, glider and *Caravela* observations T2 and GLORYS T3 methods. (f) The horizontal advection from GLORYS, split into zonal and meridional contribution

February and cooler towards the north thereafter. Meanwhile methods T1 and T2 change temperature gradient direction day to day, but both T1 and T2 methods do agree on the gradient direction apart from for $\frac{\partial T}{\partial y}$ on 10th February. The methods T1 and T2 however do not typically agree with T3 in either magnitude or direction.

Method T1 gives daily estimates of temperature gradient in Figures 5.5 and 5.6. On 8th and 11th February, there are differences between $\frac{\partial T}{\partial x}$ calculated over the northern and southern halves of the study site. Differences in sign of the east and west halves of the study site for $\frac{\partial T}{\partial y}$ occur on 10th February. On the 12th, 14th and 15th February, *Caravela* did not enter one of the quadrants in the site, so the temperature gradients could not be calculated over both halves. For all other days, the gradient direction is the same across both halves of the study site. As *Caravela* travels round the bowtie shape, she always travels directly from an east to west quadrant or vice versa. When looking at $\frac{\partial T}{\partial y}$, this method means north to south always involves transit through another quadrant first, for example Q1-Q3 involves *Caravela* travelling through Q2 between Q1 and Q3. This additional time (between 5 and 8 hours spent in Q2) means $\frac{\partial T}{\partial y}$ is aliasing the diurnal cycle and associated surface warming or cooling between Q1 and Q3, as well as any advective process. The diurnal cycle and approximately daily period of the route around the study site is responsible for differing signs found for temperature gradient in the northern and southern half of the site on 8th February. For the southern half of the site, the gradient captures the SST warming throughout the morning across Q3 and Q4, leading to a positive $\frac{\partial T}{\partial x}$. For the northern estimate, observations in Q1 and Q2 on this day are almost 24 hours apart, such that the gradient captures the temperature difference from one night to the next, during which time *Caravela* may have also crossed an oceanic front. These differences in the temperature gradient across halves of the site are a product of the sampling strategy. Because of this and diurnal cycle aliasing, I cannot further use method T1 to reliably calculate temperature gradients for horizontal advection.

Due to the design of the deployment, method T2 had sampling issues which produced erroneously large temperature gradients, as well as spiking in temperature gradient values (Figure 5.7f,g). Anomalous values were as large as $0.001\,^{\circ}\mathrm{C\,m^{-1}}$, which is unfeasible based on GLORYS temperature fields (Figure 5.1) . The campaign was designed such that the timings of the platforms moving round the site would produce repeated right angled triangles between platforms, however varying vessel speeds meant this did not occur as often as expected in reality. Frequently there is unrealistic spiking in temperature gradients when platforms were too close together, a pair of platforms was too close together in x or y space or the angle between the three platforms was too small or large. To obtain a better

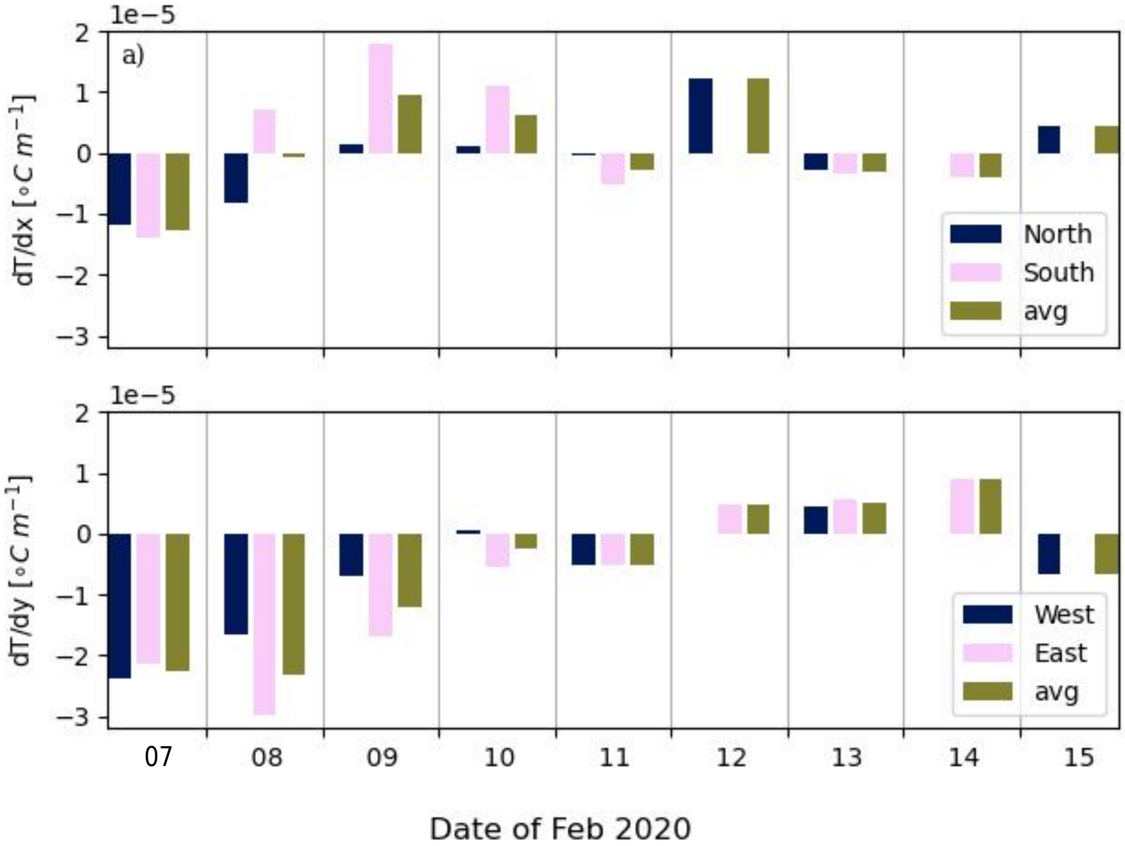

Figure 5.6: Daily mean $\frac{\partial T}{\partial x}$ (top) and $\frac{\partial T}{\partial y}$ (bottom) over the study site, with an approximation over each half of the study site (north,south,east or west half) and average of these halves.

estimate of the the temperature gradients from this method, the results had to be quality controlled and I identified filters based on these three conditions (Figure 5.8). The angle test was determined by taking the bearing from *Caravela* to each glider (between $-180°$ and $180°$), taking the magnitude of the difference between SG579s and SG637s bearings and correcting so this falls within the range 0°-180°. This angle is that formed from one glider, to *Caravela* to the other glider. An example of an optimal orientation (Figure 5.8a) has $\frac{\partial T}{\partial x}$ $0.000\,009\,°\mathrm{Cm}^{-1}$ of and $\frac{\partial T}{\partial y}$ of $-0.000\,003\,°\mathrm{Cm}^{-1}$. Meanwhile platforms alignment failing the angle QC test (Figure 5.8b) have $\frac{\partial T}{\partial x}$ of $0.0001\,°\mathrm{Cm}^{-1}$ and $\frac{\partial T}{\partial y}$ of $-0.0001\,°\mathrm{Cm}^{-1}$, over an order of magnitude larger. After some experimentation with thresholds, QC was set as a minimum area of triangle enclosed by the platforms of $3\,000\,000\,\mathrm{m}^2$, at least 500 m between *Caravela* and a Seaglider in either x or y direction and the angle formed between both gliders and *Caravela* between 15 ° and 165 °.

Figure 5.7 highlights the importance of mission planning, with much of the spiking behaviour in $\frac{\partial T}{\partial x}$ and $\frac{\partial T}{\partial y}$ removed in panels g and h once I filter for platform position. However this does leave no valid estimates of temperature gradient available on 11th or 12th of February and may filter out important times when gradients and the associated horizontal advection were large.

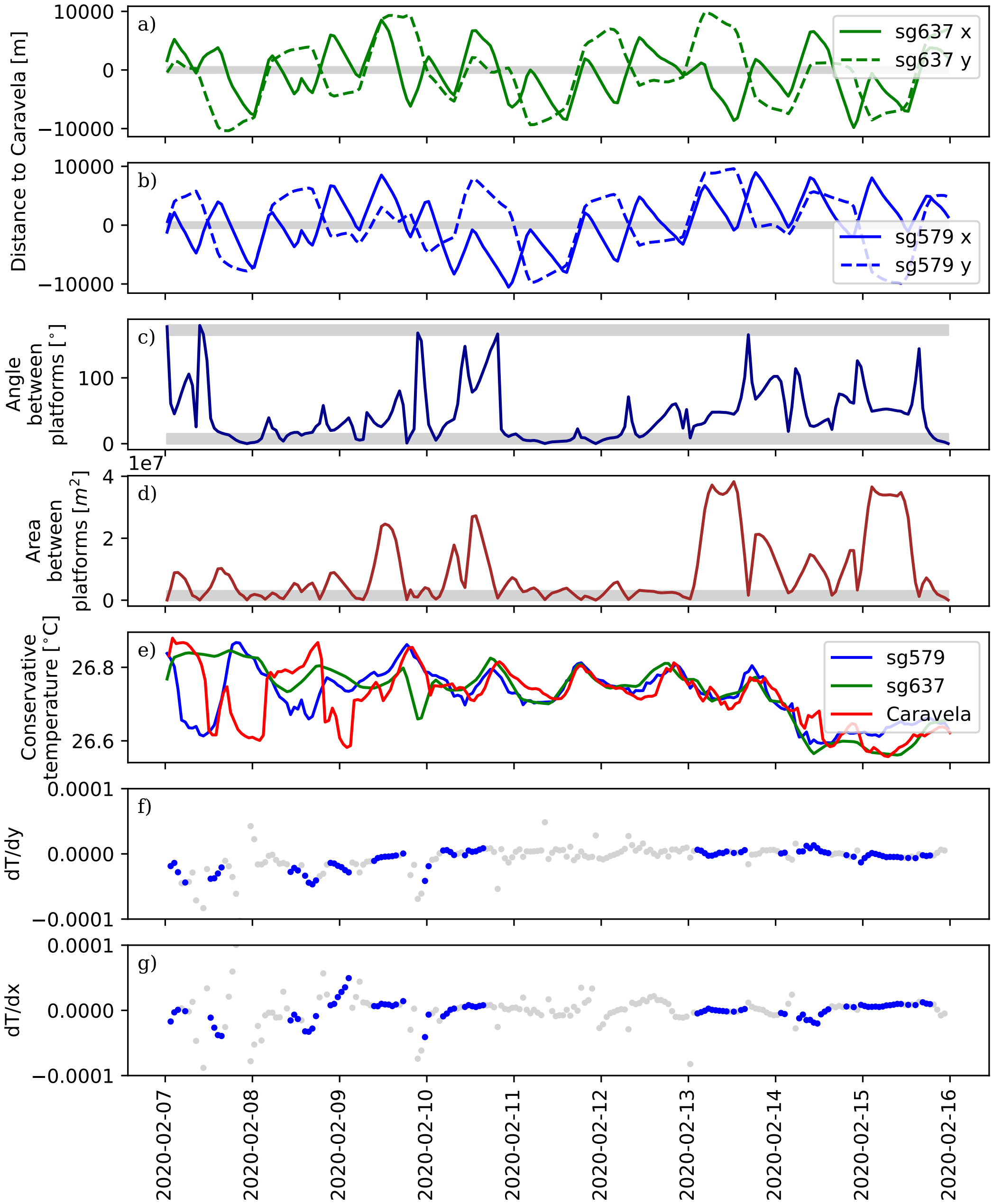

Figure 5.7: Temperature gradients and components of the calculation for method T2 (see text). Distance from Seaglider SG637 (a) and SG579 (b) to *Caravela* where a negative distance indicates the glider is south or west of *Caravela* . x components of distance are given by a solid line and y component a dashed line. c) The angle formed between platforms by going from SG579 to *Caravela* to SG637. d) The area of the triangle formed by the three platforms if each platform is treated as a vertex. QC tests are shown in plots a,b,c,d as grey regions, defined as (a,b); less than 500 m between *Caravela* and a Seaglider in either x or y. c); angle formed between both gliders and *Caravela* is not between 15° and 165°and d); minimum triangle area enclosed by platforms is 3 000 000 m^2. e) Shows Conservative temperature measured by the three platforms with the Seaglider values being the 0.5 m interpolated values after processing. f,g) Calculated temperature gradients dT/dx and dT/dy with all data in grey (y-axis limits do hide some anomalous values) and values that passed all QC tests in blue. Values that fail QC tests are those which fall inside grey regions in a-d.

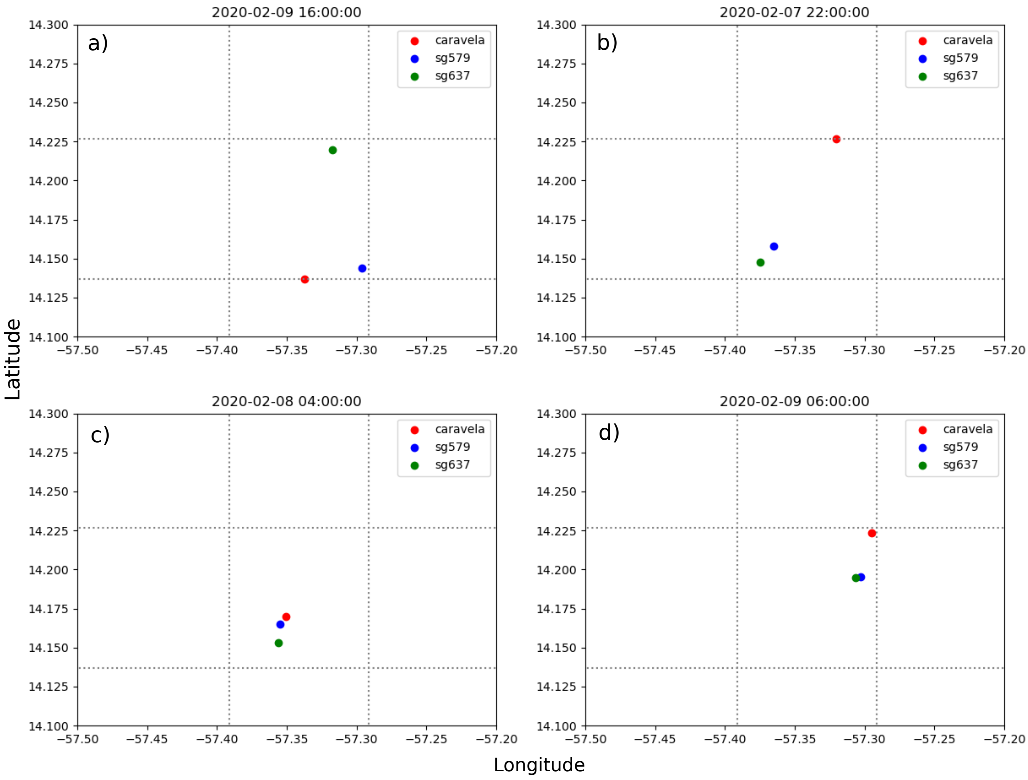

Figure 5.8: Examples of platform orientation within the study where a) desirable platform orientation within study site, b) platforms forming a line rather than triangle, c,d) platforms forming a triangle of small area.

For days with remaining estimates, the standard deviation is substantial. On 9th February standard deviation is $2.1 \times 10^{-5}\,{}^{\circ}\mathrm{C\,m^{-1}}$ for a mean $\frac{\partial T}{\partial x}$ of $1.2 \times 10^{-5}\,{}^{\circ}\mathrm{C\,m^{-1}}$ and standard deviation of $1.3 \times 10^{-5}\,{}^{\circ}\mathrm{C\,m^{-1}}$ for $\frac{\partial T}{\partial y}$, where the mean gradient is $-1.3 \times 10^{-5}\,{}^{\circ}\mathrm{C\,m^{-1}}$. It is possible that adjustment of the QC thresholds will reduce the standard deviation and that platform layout based errors have not been entirely removed, although the larger the QC threshold, the more real data is also lost. I later calculate the heat budget with advection from these T2 temperature gradients as a comparison to GLORYS, but acknowledge the substantial uncertainty retained by using this method. Calculation of horizontal advection with three platforms is certainly possible, but requires better pre-planning of the platform orientation.

For the velocity components of the advection, Figure 5.5b,c shows the zonal and meridional current velocities respectively. The surface and mixed layer average velocities for V2 are visible in Figure 5.5b,c for comparison to the velocities derived from Seaglider surface drift V1. In the meridional direction, the mean of daily velocities is $0.06\,\mathrm{m\,s^{-1}}$ for SG579, $0.15\,\mathrm{m\,s^{-1}}$ for SG637 and $0.04\,\mathrm{m\,s^{-1}}$ for the surface level of GLORYS. In the zonal direction, the mean of daily velocities is $-0.21\,\mathrm{m\,s^{-1}}$ for SG579, $-0.41\,\mathrm{m\,s^{-1}}$ for SG637 and $-0.15\,\mathrm{m\,s^{-1}}$ for the surface level of GLORYS. The weighted mean mixed layer averaged velocities from GLORYS are $-0.08\,\mathrm{m\,s^{-1}}$ for the zonal component and the meridional component $0.05\,\mathrm{m\,s^{-1}}$. The average GLORYS surface velocities are consistent with the surface drifts calculated from SG579 in method V1. Glider SG637 surface drifts have larger magnitudes, particularly in the zonal component. Whilst it is unclear why the gliders are recording different surface drifts, a hypothesis is that SG637 sat much higher in the water whilst on the surface, causing it to experience a larger component of surface drift due to wind action than the other glider. Correlation between daily ERA5 10 m wind and SG637 surface current is 0.33 for the v component and -0.45 for the u component, which indicates wind may be partly responsible. The directionality of SG637s surface drift is much less consistent than SG579 (not shown). Another possible explanation is that GPS errors have compounded in SG637 surfacing to give unrealistic drifts. The orange dashed lines in Figure 5.5b,c show velocities averaged over the mixed layer from GLORYS data. In the zonal component of velocity, there is significant shear within the mixed layer giving a mixed layer averaged zonal velocity around half that of the surface current. As the advection should be calculated with a mixed layer averaged velocity and there is velocity shear in this mixed layer, the glider surface drift will not be an appropriate proxy for mixed layer averaged currents and so a weighted mean of GLORYS levels is used to calculate advection within the study site.

The calculated time series of horizontal advection using methods T3 and V2, ie GLORYS reanalysis, is shown in Figure 5.5f. The mean of daily horizontal advection for the nine entire days spent at the site is $-0.009\,°\mathrm{C/day}$ with standard deviation $0.017\,°\mathrm{C/day}$. The mean of the daily zonal components is $-0.015\,°\mathrm{C/day}$ with standard deviation $0.009\,°\mathrm{C/day}$ and the mean of the daily meridional advection component $0.006\,°\mathrm{C/day}$ with standard deviation $0.010\,°\mathrm{C/day}$. According to GLORYS, horizontal advection is responsible for heat loss from the study site for all days in the campaign except for 13th and 14th February, where the meridional component of advection strengthens and the zonal component weakens compared to previous days. Overall horizontal advection is responsible for heat losses in the mixed layer heat budget in this study, such that heat entering the site through other processes is being advected away.

5.3.2 Entrainment

For the entrainment term, I calculate the entrainment both including and excluding the effects of detrainment (Figure 5.9). Cumulatively across the time spent in the study site, the inclusion of detrainment accounts for $0.09\,°\mathrm{C}$ less warming of the mixed layer. The vertical velocity component of entrainment modulates the heat exchange, reducing the cumulative heat gain to the mixed layer by 0.25 °C relative to an entrainment value based only on mixed layer depth tendency. Whilst the entrainment term is commonly thought of as a cooling term, the temperature inversion found below the mixed layer here results in entrainment of water warmer than the mixed layer average temperature into the mixed layer, thus causing mixed layer warming. When the mixed layer shoals and detrainment occurs, heat appears to be lost from the mixed layer. As the detrainment term has a significant affect on heat exchange within the entrainment process, I take the estimate of entrainment including detrainment to calculate the heat budget.

The entrainment calculated here is particularly large. Assuming the entrained water temperature is 27.3 °C, with the average mixed layer temperature 26.7 °C, the mixed layer depth deepening from 46 m to 73 m and an average MLD of 60 m, the entrainment over the nine days would be 0.27 °C, which is fairly close to the entrainment estimate in Figure 5.9. The mixed layer deepens substantially (27 m) during the study with the entrained water much warmer than the mixed layer Figure 4.9. The 26°C isotherm oscillates down to 85 m at the start of the time series, to 88 m at the end of the time series. Between the mixed layer and the 26 °C isotherm on 7th February there is substantially more heat than by the end of the time series. If all this heat entered the mixed layer that would lead to substantial warming (as is assumed in entrainment calculation). In reality, the warm barrier layer may have been mixed with water below or advected horizontally, where this possibility is unquantified through neglecting lateral induction. Hence a large uncertainty and probable large positive bias in the entrainment estimate in Figure 5.9.

5.3.3 Mixed Layer Heat budget

The GLORYS V2,T3 method of calculating advection combined with entrainment and detrainment and the net surface heat flux gives the budget closure shown in Figure 5.10b (brown line). The net heat flux and advection terms contribute to cooling of the ocean mixed layer, whilst the entrainment contributes to warming the ocean mixed layer. We assess the budget based on cumulative daily changes in temperature in the mixed layer (Figure 5.10b and Table 5.1). Chapter 4 concludes that air-sea interactions (light blue line) give a good estimate of temperature tendency (orange line) over the nine days spent in the study site, with the net heat flux term leading to a 0.06 °C colder ocean than the cumulative daily temperature tendency. When entrainment and advection are included as

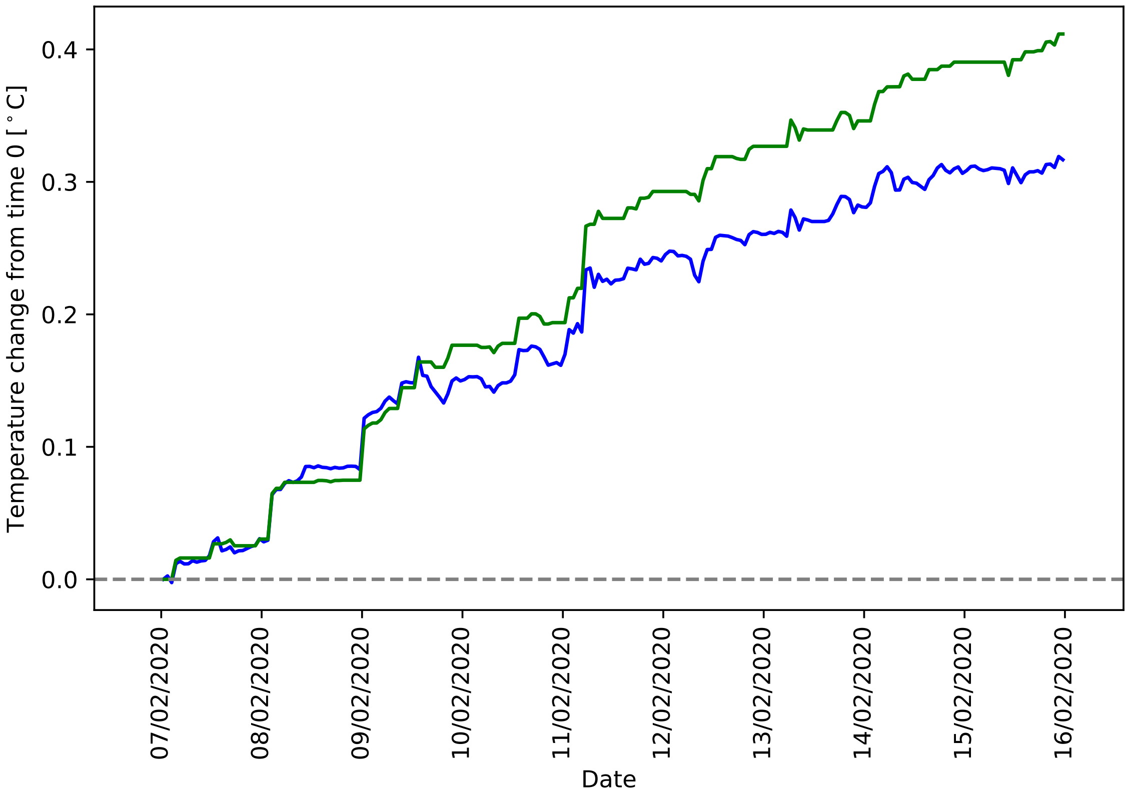

,

Figure 5.9: Time series of cumulative hourly temperature change in the ocean mixed layer due to entrainment without detrainment (green) and entrainment with detrainment (blue)

	Cumulative temperature change after nine days °C	Equivalent heat flux W m^{-2}	Residual °C	Residual W m^{-2}
Temperature tendency	-0.15	-47	-	-
H. Advection	-0.08	-25	-	-
Entrainment	0.32	100	-	-
NHF	-0.21	-66	0.06	19
NHF + H. Advection + entrainment	0.03	9	-0.18	-56

Table 5.1: Summary of contribution to mixed layer heat budget of various budget terms and total heat budget using the chosen calculation methods for advection (V2,T3) and entrainment (with detrainment). Colours to cross refer to data plotted in Figure 5.10 are temperature tendency (orange), Horizontal advection (pink), net heat flux (light blue), entrainment (dark blue) and the sum of advection from methods V2,T3, entrainment with detrainment and net heat flux (brown) . The residual is the total temperature tendency minus nine day accumulation of the heat budget approximation using net heat flux alone and the sum of terms.

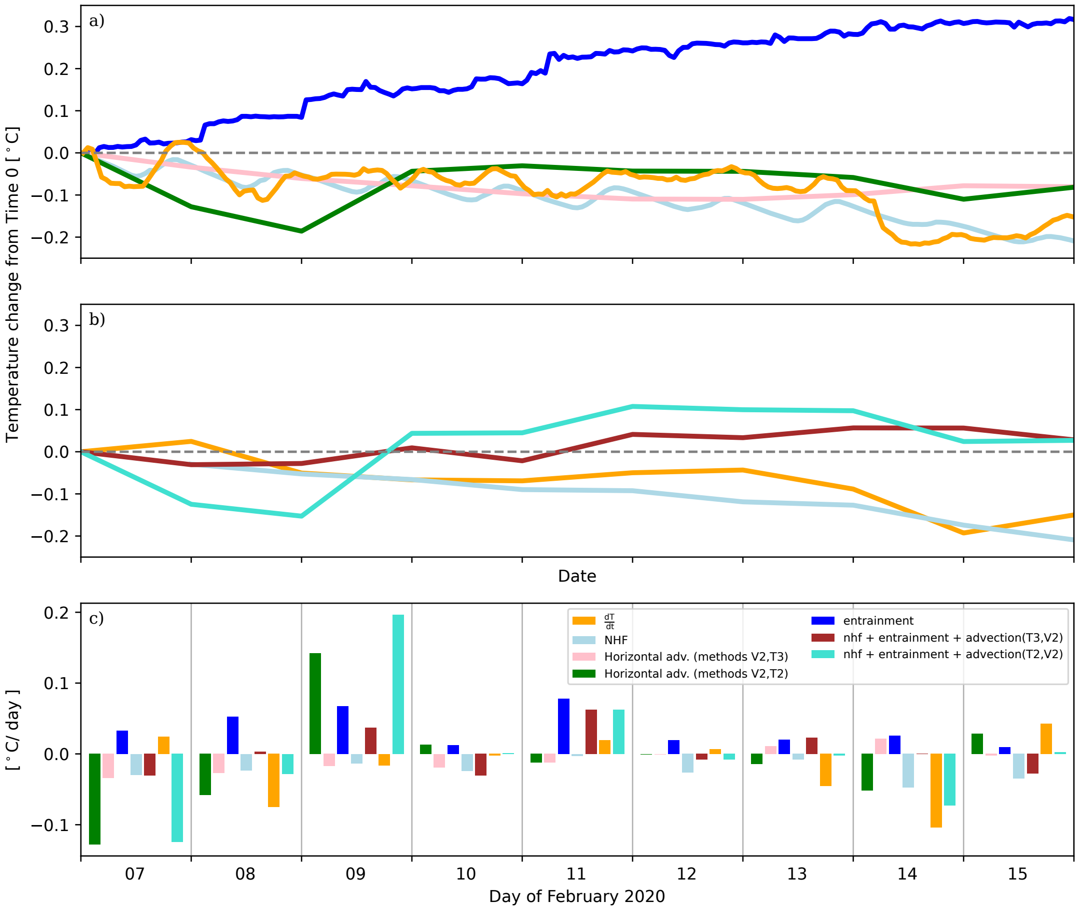

Figure 5.10: Temperature change from time 0 (00:00:00 2020-02-07 UTC) due to each component of the heat budget; Net heat flux with penetrative solar correction (light blue); horizontal advection from methods T3 and V2 (pink); horizontal advection from methods T2 and V2 (green) with missing values on 11th and 12th February replaced with those from GLORYS advection; entrainment with detrainment (dark blue); temperature tendency (orange). (a) hourly changes for all variables except horizontal advection, which are daily. (b) cumulative sum of daily means the heat budget, with the sum of net heat flux, horizontal advection from methods T3 and V2 and entrainment terms (brown) and sum of net heat flux, horizontal advection from methods T2 and V2 and entrainment terms (turquoise). (c) mean contribution to temperature change for each day inside the study site. X axis ticks denote 00:00 UTC of each day.

well as net heat flux, the accumulation until 15th February gives a total heat gain to the mixed layer of 0.03 °C. The accumulation of temperature tendency within the mixed layer shows a total change of −0.15 °C. The calculated heat budget has a total 0.18 °C more warming than the observed temperature tendency; the difference is taken to be the residual. The daily averaged contribution of each net heat flux term and the sum of these (Figure 5.10c, brown line) show that I cannot close the heat budget with these methods of calculating advection and entrainment. The combination of net heat flux, advection and entrainment shown has the opposite sign to the observed temperature tendency after nine days. As was also seen with the heat budget and temperature tendency in Chapter 4, is not possible to close the budget within any individual day and the sign of the heat budget often disagrees with the sign of the temperature tendency. It seems likely that the explanation for the remaining discrepancy in the heat budget calculated here is that the entrainment term is unrealistically large as described above, and the horizontal advection from GLORYS may not be wholly accurate, discussed more in the next section.

5.4 Discussion and Conclusion

In Chapter 4, the mixed layer heat budget was closed to within 0.07 °C from the net heat flux contribution. When the time series is reduced to the nine full days from the 7th to 15th February (inclusive), the net heat flux contribution to the mixed layer heat budget is cumulatively 0.06 °C colder than the observed temperature tendency, equivalent to 19 $\mathrm{W\,m^{-2}}$ of unaccounted for heat transfer.In this chapter, I attempted to improve on this closure by accounting for advection and entrainment, to address the final question of this thesis; *'Considering air-sea interaction and ocean processes, can we close the heat budget on a local scale?'.* I focussed on advection and entrainment terms as a similarly short heat budget study found these to be important processes in closing the budget (Vijith et al., 2020). Advection is likely to be important in our budget because fluctuations in the heat content on daily timescales that cannot be explained by the net heat flux. The deepening of the mixed layer throughout this study indicates entrainment may also be important because entrainment will generate mixed layer warming in this region.

The advection calculated within this chapter contributes a sum total of −0.08 °C over the nine days of the study, such that heat is advected out of the study site. This value of advection comes from methods V2 and T3 such that the calculation is from GLORYS reanalysis data but is a very similar value to the time-averaged V2,T2 value. Figure 5.3b shows that with significant QC, observations of temperature gradients can be used to calculate the horizontal advection and feed into the heat budget (turquoise line). There is variability in the turquoise line budget on the 7th, 8th and 9th February, which is much larger than that in the brown line heat budget (using advection with V2 and T3). From the start of the campaign until 9th February, temperature variability between platforms (Figure 5.5a) shows differences in surface temperatures on the order of 0.2 °C at different times in those first three days, suggestive of a front being passed over by the vessels within the site. Between 9th and 14th February, the temperature differences between platforms are greatly reduced and become consistent across platforms. This indicates the temperature changes in the site after 9th February are no longer dominated by crossing a 'feature' within the site but by processes larger than the

10 km scale of the observations.

There are two potential explanations for the difference in heat exchange captured in the V2,T2 and V2,T3 horizontal advection on these first three days. The first is that despite the high resolution and eddy rich nature of GLORYS, it is unlikely to fully resolve submesoscale features. It is then possible that GLORYS will not be properly capturing the front passing through the study site, reducing the magnitude of the temperature gradient and subsequent heat exchange calculated in the mixed layer. This is supported by Figure 5.1 which shows the daily GLORYS surface level SST, with hourly 0.5m glider temperatures and hourly Caravela SST and daily means of the observations, where the gradients are not consistent with the vessel observations on every day. From 10th to the 13th February, GLORYS also appears cool biased compared to the vessel observations, indicating that GLORYS is not correctly representing the temperature at high spatial resolution. The second possibility is that the QC in the T2,V2 method eliminates some data, so may have obscured periods of strong advection of one sign or another, potentially biasing the daily means. Whilst there are evident discrepancies at the daily scale, over the nine day course of this campaign, horizontal advection estimates from GLORYS and observations are broadly consistent, indicating that horizontal advection is being represented accurately within this heat budget on the longer timescale.

The entrainment term calculated in this chapter (Figure 5.9) is likely to be an overestimate for the region. From the Seaglider temperature and salinity profiles of the top 75 m of the study site (Figures 4.9 and 4.10), the subsurface warm layer below the mixed layer visibly reduces in thickness and temperature throughout the study period, which indicates that some of the water is likely entrained into the mixed layer. It is possible the subsurface temperature maximum is mixed into the layer below or had been advected away from this region. Seasonal decay of the BL is not occurring here as that would not be anticipated until March-April, and would occur via shallowing of the ILD and MLD (Saha et al., 2021). I treat the estimates of entrainment as upper bound on the plausible entrainment as the lack of accounting for the third component of entrainment (lateral induction) is likely resulting in a positive bias in the calculated heating due to entrainment. During periods of strong horizontal stirring, lateral induction contributes significantly to the entrainment due to horizontal advection over a sloping mixed layer base (Vijith et al., 2020). One could argue that the front crossed in the site until 9th February is an example of where lateral induction would be important, and may have contributed to the overestimation of entrainment.

When assessing the heat budget including estimates of the effects of horizontal advection and entrainment, the heat budget closes with a $-0.18\,^{\circ}\mathrm{C}$ residual after nine days, i.e. the estimated sources of heat would lead to too much warming compared with the observed temperature change. With a mean mixed layer density of $1023\,\mathrm{kg/m^3}$ and mean mixed layer depth of $60\,\mathrm{m}$, this is equivalent to a $-56\,\mathrm{W/m^2}$ residual in the heat budget. The answer to Question 4 of this thesis is that the local heat budget has been closed with a $-0.18\,^{\circ}\mathrm{C}$ or $-56\,\mathrm{W/m^2}$ residual, over the short timescales and with the observational limitations of this study. This closure is not an improvement on the air-sea interactions only closure of Chapter 4 and could be improved upon with better sampling strategy and spatial SST information to inform the calculated ocean processes. The quality of the closure on a regional scale is sensitive to the processes considered and at the daily scale, explicit consideration on submesoscale processes may have benefitted this study.

Many studies investigate heat budgets around the globe; here I select two studies to compare with. Nogueira Neto et al. (2018) assess the heat budget in a large region of the NWTA which incorporates our study site. Vijith et al. (2020) look at the heat budget in the Bay of Bengal, a similar tropical environment, over a similar timescale and with a similar observational methodology to our study. I discuss each in turn.

Nogueira Neto et al. (2018) investigated the budget over a wider portion on the NWTA at annual timescales using Argo data from 2007-2012, with ERA-Interim, NOAA Optimum Interpolation Sea Surface Temperatures and two different current products (Section 5.1 for description of study region). Nogueira Neto et al. (2018) find and February mean surface heat fluxes and entrainment contribute to heat losses from the mixed layer, while advection contributes to heat gain to the mixed layer. Their February monthly mean surface flux is approx $-50\,\mathrm{W\,m^{-2}}$, and I find the observed contribution to be $-66\,\mathrm{W\,m^{-2}}$. Their temperature tendency is approx $-30\,\mathrm{W\,m^{-2}}$ and mine $-47\,\mathrm{W\,m^{-2}}$, such that our results are broadly consistent in these two terms, but smaller in magnitude than Foltz et al. (2003). I find the entrainment to be associated with heat gain up to $100\,\mathrm{W\,m^{-2}}$, whereas their February mean is a heat loss less than $-10\,\mathrm{W\,m^{-2}}$. Likewise our studies disagree of the overall behaviour of advection, with my advection showing heat loss of $-25\,\mathrm{W\,m^{-2}}$ and theirs heat gain of approx. $10\,\mathrm{W\,m^{-2}}$ but do agree that the zonal advection component is responsible for heat loss, as does Foltz et al. (2003). Seasonal variation in horizontal advection between 2001 and 2004 at the NTAS buoy shows horizontal advection varies month to month between heat gain and loss, but is always notably smaller than surface fluxes (Foltz and McPhaden, 2005). Studies further east and south have drawn differing conclusions on the importance of horizontal advection (Foltz et al., 2003; Peter et al., 2006; Yu et al., 2006; Giordani et al., 2013) and it appears the role of horizontal advection is similarly debated in our study region. The residual from Nogueira Neto et al. (2018) is $10\,\mathrm{W\,m^{-2}}$ in February, much smaller in magnitude than in my budget. It is difficult to determine exactly why the entrainment and advection for our studies differs so substantially. A time series of MLD is not available in their study, but the long term mean MLD from Argo for the region reaches maximum depths around 60 m over their box. If their ML was not deepening, this could lead to the given near negligible entrainment estimate. Unfortunately temperature profiles are also not available in their paper, so I cannot ascertain whether they detected the sub surface temperature inversion associated with barrier layers in the NWTA region, which leads to important ML warming in our study. Over longer timescales, entrainment is described as a cooling contributor over various tropical North Atlantic areas (Foltz and McPhaden, 2005; Nogueira Neto et al., 2018). I show with this thesis, the assumption that entrainment is responsible for heat loss must be applied with evidence and caution to the BL region of the NWTA. Overall we agree that surface processes are the dominant heat budget driver. The disagreement when quantifying the ocean processes lends evidence to the need for higher resolution spatial sampling in the NWTA, to better understand short term horizontal advection changes and further investigate BLs and their effect on entrainment.

Vijith et al. (2020) assess the heat budget in the Bay of Bengal and is relevant as a nine day short term study. Vijith et al. (2020) observe differences between glider-based temperature gradients and those from a ship's underway CTD, as well as seeing a 0.5 °C warm bias of their vessel observations compared to GHRSST (Group for High-Resolution Sea Surface Temperature) remote sensing observations (Vijith et al. (2020) Figure 5). This bias is thought to be due to aliasing of the diurnal cycle and cool skin SST measurements vs bulk observations. I see offsets between our observations and GLORYS (see Figure 5.1, with our observations warmer than Glorys by roughly 0.1 °C between 10th and 14th February) and expect these offsets to be due to the same reasons given by Vijith et al. (2020). Quantifying SST offsets is relevant in the case of a heat budget, as remote sensing or reanalysis SSTs can be used to give the temperature tendency of a region to close a heat budget against. Likewise using these products temperature gradient fields could introduce biases into horizontal advection estimates if the SSTs are biased. In terms of the heat budget, their entrainment term does contribute heat gain intermittently, up to approx 0.3 °C/day on any single day, which is a larger daily heat gain that seen in this thesis. Their study and ours both see entrainment vary between contributing to both heat loss and heat gain of the mixed layer at high temporal resolution. Horizontal advection in their paper is an important ocean process which can contribute considerably to heat transfer within any individual day (between −0.6 and 0.4 °C/day. Comparing with this study of similar temporal resolution highlights the variability in all heat budget process at short timescales and further highlights how in a surface flux dominant region, ocean processes can locally dominate the budget within a day, which is important to understand when scaling up flux parameterisations.

Because of the spatial distribution of the vessels within the study site, I was unable to calculate advection without large uncertainties or the lateral induction component of entrainment, affecting the ability to close the heat budget from observations. GLORYS reanalysis data does not capture the short fluctuations in temperature likely due to small-scale ocean advection. Ideally, these features would have been resolved by the observations, and if we had designed the experiment such that the platforms always maintained a near-optimal configuration, we may have been able to improve on the closure of the budget by including horizontal advection. A longer timeframe would also improve this study, allowing the cumulative temperature tendency and budget to be tested over a longer timescale and more robust assessment of processes on the timescales of months to be investigated, which would also help comparability of this study to monthly means in the regionally available literature.

To summarise, the ocean mixed layer processes calculated using the methods described in this chapter do not close the heat budget over the nine days investigated, nor am I able to fully explain the temperature tendency on any individual day with the net heat fluxes, advection and entrainment. The entrainment contributes to warming of the ocean mixed layer whilst the horizontal advection cools the mixed layer, such that these two processes in part cancel each other out. This behaviour is inconsistent with larger scale heat budget studies in the NWTA, highlighting the importance of smaller scale process studies in quantifying regional processes and their potential for larger scale heat budget impacts. Overall the best closure of the ocean heat budget comes from net surface heat fluxes alone, supporting the literature that this is the dominant driver of the heat budget in the tropics.

6

Conclusions

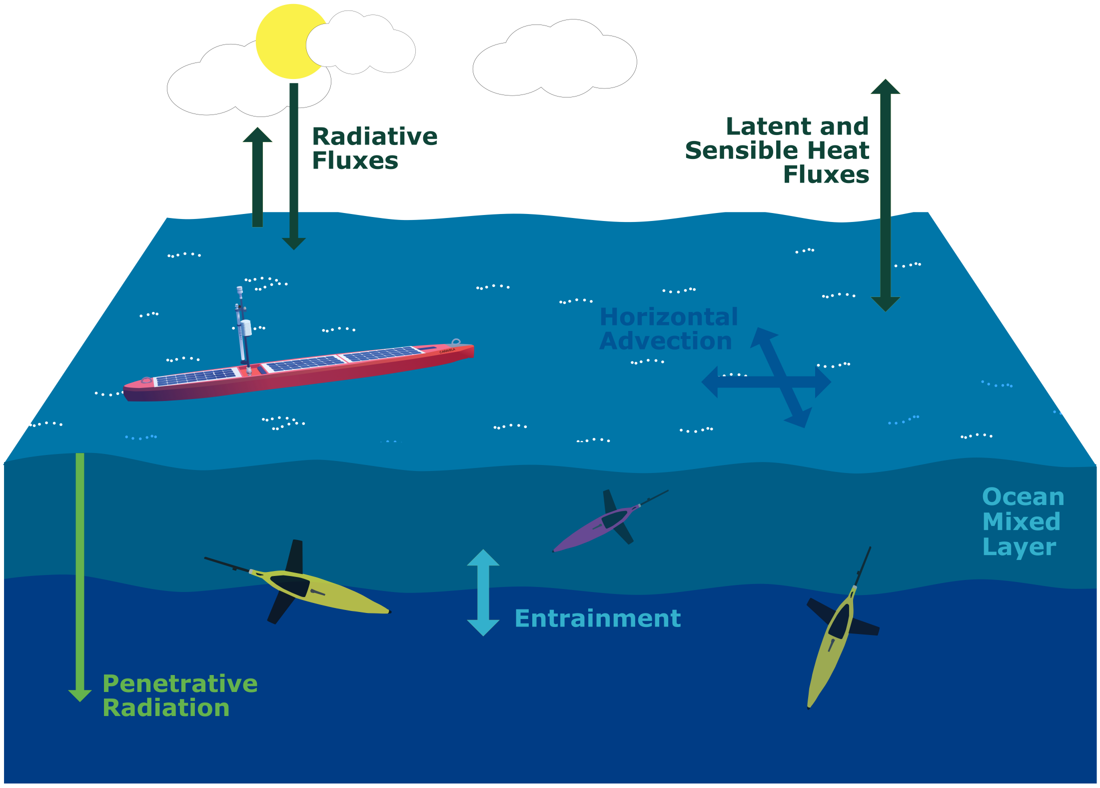

Figure 6.1: Schematic overview of the research contained within this thesis.

This thesis spans a wide arc, taking the challenge of quantifying air-sea interactions from observations and approaching the problem both technologically and scientifically. Chapter 2 presented an overview of our use of *Caravela* to study air-sea interactions within the EUREC^{4}A campaign. That chapter looked at the *Caravela* USV system, where even five years ago USV use for measurement of bulk air-sea flux variable was much less common. I presented some cross validations of data and aimed to enhance awareness of the technology and USV capabilities in the context of air-sea interactions. Chapter 3 took a more rigorous look at *Caravela* as a vessel. I like to think of both chapters 2 and 3 as forming a 'cookbook', a collection of recipes and pieces of advice for using the *Caravela* USV. I hope using these chapters as a base will allow future vessel users to understand the evolution of

Caravela , and be aided in navigating technological and data handling challenges associated with deploying *Caravela* . Chapter 3 itself discussed validation of many of the sensors, as well as specific problems overcome in data processing within the vessel architecture and in post processing for the user.

Chapters 4 and 5 focussed on the results and analysis of *Caravela* data, with the intention of closing a mixed layer heat budget to determine the dominant processes driving variability in SST in this region. In chapter 4, I calculated the bulk air sea-heat fluxes with the COARE 3.5 algorithm (Fairall et al., 1996*b*) using *Caravela* observations and ERA5 winds. These calculated fluxes were used to determine biases in ERA5 fluxes in the NWTA region. The air-sea heat fluxes were further used to test heat budget closure of the ocean mixed layer. In Chapter 5 I further investigated the mixed layer heat budget with the inclusion of horizontal advection and entrainment, to determine what dominated heat transfer in the NWTA over the nine whole days I observed at the site.

At the start of this thesis, I posed four research questions; the outcomes of these investigations are discussed in turn below.

Can an adapted autonomous surface vessel provide a viable platform for air-sea interaction studies?

The AutoNaut platform *Caravela* can be effectively used for studying mesoscale processes and submesoscale ocean features, studying air sea fluxes and deploying a Seaglider to target particular events of interest. *Caravela* was deployed on two large research campaigns, EUREC^{4}A and PICCOLO, and multiple short trial missions. With each time the *Caravela* vessel was used, new discoveries were made about how to optimise use of the vessel for bulk air-sea interaction studies. Across deployments, this included collaboration with AutoNaut to improve data handling and accessibility, refine (and occasionally repair) the vessel and upgrade and maintain sensors for optimal bulk flux calculation. While writing this thesis, my feedback to AutoNaut has also enabled these upgrades to be achieved as part of their continuous improvement. Specifically, I found an unpumped CTD experienced spiking in conductivity observations with variable motion of the *Caravela* vessel, and so this was replaced with a pumped CTD system. The bulk heat flux variables successfully observed by *Caravela* include SST; humidity; air temperature and downwelling shortwave radiation. Downwelling longwave radiation measurements were also successfully made, however with a root mean square difference between *Caravela* and the Barbados Cloud Observatory of

$46\,\mathrm{W\,m^{-2}}$ whilst completing sections near to Barbados, which points to the *Caravela* sensor needing recalibration. The vessel also successfully recorded data on ocean current velocities via an ADCP, however the group did not have capacity to process this data within this thesis time frame. Similarly the vessel is equipped to measure vessel-relative wind velocity and did successfully collect observations, however practical and time and data handling constraints meant these wind data were not further processed and used in this research. Many of the sensors ran at the high frequency of 1 Hz, such that a wealth of data exists to form the hourly averages used for comparison against ERA5 hourly resolution. Calculation of air-sea bulk fluxes with observed variables is possible at hourly resolution, and could be done to much higher temporal resolution if the observations are more rigorously quality controlled by the user.

There are currently no standardised measurement or processing guidelines across different USV types, so it can be difficult to directly compare vessels and their data output. Saildrones are one example of a USV for scientific research. Whilst *Caravela* reports a measurement at a repeated set frequency for each sensor, often 1 Hz, Saildrone takes a different strategy of sampling for a given period then turning off the sensor for a given period. For example their SST sensors run 2 seconds on, 2 seconds off (Gentemann et al., 2020). It is important as the USV scientific user base develops, to encourage creation of guidelines such that sampling strategies are clear and USVs inter-comparable. This discussion point is much larger than *Caravela* , but there is progress being made by groups like OASIS (Observing air-sea interactions strategy) (Cronin et al., 2023; Patterson et al., 2025).

Overall, I have found *Caravela* to be a great asset for observational air-sea flux studies, providing a reliable and user-friendly platform for investigating air-sea fluxes.

Are observational heat fluxes comparable to the global reanalysis product ERA5?

Observations from *Caravela* were supplemented with ERA5 10 m winds and used to calculate bulk turbulent fluxes with COARE 3.5 (Fairall et al., 1996*b*) and bulk radiative fluxes in Chapter 4. Upon comparison of bulk flux from observations to ERA5 fluxes, ERA5 was found to overestimate the magnitude of turbulent heat fluxes, such that they represent too much heat loss to the atmosphere. ERA5 sensible heat flux was $5\,\mathrm{W\,m^{-2}}$ larger than observations and ERA5 was $40\,\mathrm{W\,m^{-2}}$ larger for latent heat flux. Based on further analysis of the bulk flux components, air temperature was found to be underestimated by ERA5 and relative humidity derived from ERA5 2 m temperatures was on average 3.4% lower than observed humidity. A difference in the approximation between COARE3.5 and ERA5's transfer coefficients is though to play some role in the differences in fluxes, although the magnitude of this component was not quantified. SSTs were underestimated on certain days by ERA5 compared with observations. ERA5 uses SSTs from the OSTIA product as a boundary condition, so whilst having differences in ERA5 and our SSTs could be responsible for differences in the two fluxes, is not something directly resolvable in ERA5. For the radiative fluxes, I found the longwave radiation observations made on *Caravela* had an inconsistent offset for the Barbados Cloud Observatory observations and ERA5, such that potential biases in ERA5 longwave flux could not be tested. However the shortwave radiation measurements from *Caravela* allowed for calculation of an observed shortwave radiative flux to compare with the ERA5 product. Using satellite images to visualise cloud structure during the campaign, these observations support that ERA5 is overestimating surface irradiance during cloudy conditions seen on 14th and 15th February, in agreement with Urraca et al. (2018). The overestimate by ERA5 on these two days is $79\,\mathrm{W\,m^{-2}}$ and $43\,\mathrm{W\,m^{-2}}$ respectively. Assessment of irradiance over land in Urraca et al. (2018) indicates biases in ERA5 are due to poor cloud prediction. The EUREC^{4}A campaign (Bony et al., 2017; Stevens et al., 2021) was based around improving the understanding of tropical clouds, where results from EUREC^{4}A indicate that models misrepresent shallow trade cumulus cloud feedback due to the relative dependence of cloudiness on mixing and humidity and note an $8\,\%$ underestimate of relative humidity in ERA5 compared to dropsonde observations at 850 hPa (Vogel et al., 2022). The results of this thesis in terms of surface relative humidity being underestimated by ERA5 may then be of relevance to improving cloud parameterisations, but this would need further independent study. Based on the identified biases in ERA5, an optimal representation of the local net surface fluxes was chosen using observations from *Caravela* for shortwave and turbulent heat fluxes, with longwave fluxes from ERA5. The optimal net heat flux was compared with daily averaged heat fluxes from the ERA5 product. ERA5 both over- and underestimated daily net heat flux compared with observations. Mean daily net heat flux from ERA5 lost $30\,\mathrm{W\,m^{-2}}$ more heat to the atmosphere than our optimal estimate could account for.

Let us discuss the last two questions in tandem:

How well do observed surface processes alone close the heat budget?

and

Considering air-sea interactions and ocean processes, can we close the heat budget on a local scale?

One must start by highlighting how these answers are very dependent on the scope of the question asked. When the heat budget closure is approached on daily or at hourly scales, it becomes difficult to close the budget without explicit consideration of submesoscale processes and resolving all processes in the heat budget equation. However, if the budget closure is assessed over a longer time scale, i.e. the time spent in the study site from 6th to 16th February 2020, the heat budget can be closed to a much better extent under this thesis' methodology. In Chapter 4, I found that the heat budget closes remarkably well considering surface heat fluxes alone. Over the cumulative time spent in the study site from 6th February 12:30 UTC to 16th February 08:30 UTC, the net heat flux term closes the heat budget with a 0.07 °C residual. Surface heat fluxes alone are able to provide a good closure of the heat budget in the NWTA and shortwave and latent fluxes are the dominant driver of SST evolution, in agreement with Foltz et al. (2003). If I include estimates of advection and entrainment in the ocean heat budget and take the nine whole days spent in the study site from the 7th February to 15th February, the closure of the mixed layer heat budget becomes notably worse than with heat fluxes alone. The residual in this circumstance is −0.18 °C, such that this formulation of the ocean heat budget inputs too much heat into the mixed layer. There are multiple factors contributing to the residual being much larger with the additional budget terms. In part, it is due to the uncertainty in the heat budget calculation, where the inclusion of horizontal advection and entrainment brings additional uncertainties. Another reason for the large residual could be the methodology used for calculating the entrainment term, where the lateral induction component is neglected. Lastly the choice of GLORYS data fields could be contributing to the poor closure. As we are working at the limit of GLORYS resolution, it is possible that the temperature and velocity fields are a poor representation of the region at this scale. This study highlights the importance of targeted mission planning for an observational campaign to ensure reliable estimates of the ocean heat budget can be made from observations alone. Overall we are able to close the heat budget with a reasonably small residual when only considering the net heat flux contribution. Whilst it is possible to close (within uncertainties) an ocean mixed layer heat budget from observations (Vijith et al., 2020), in this thesis' particular campaign the sampling strategy prevented budget closure through spatial-temporal aliasing and spatial coverage constraints.

To summarise in the context of existing literature, the mean air-sea heat fluxes calculated in Chapter 4 are sensible $4\,\mathrm{W\,m^{-2}}$; latent $-181\,\mathrm{W\,m^{-2}}$; shortwave $197\,\mathrm{W\,m^{-2}}$ and longwave $-17\,\mathrm{W\,m^{-2}}$. This sensible flux is comparable to $-6.6\,\mathrm{W\,m^{-2}}$ of Iyer et al. (2022) and $-7\,\mathrm{W\,m^{-2}}$ of Bigorre and Plueddemann (2021) however this thesis finds a larger magnitude of latent flux than $-157\,\mathrm{W\,m^{-2}}$ from Iyer et al. (2022) and $-170\,\mathrm{W\,m^{-2}}$ from Bigorre and Plueddemann (2021). Bigorre and Plueddemann (2021) results are from February average fluxes from 2001-2012 using NTAS buoy data and Iyer et al. (2022) January - February 2020. Differences between studies are likely due Iyer et al. (2022) being over a larger and more easterly area, and spatial differences from (Bigorre and Plueddemann, 2021), where SSTs in these two studies may be cooler than our study site. Within this thesis, I find the dominant flux processes are shortwave and latent fluxes in alignment with Bigorre and Plueddemann (2021). Importantly these flux similarities to other studies justify our conclusions that ERA5 contains regional biases which should be more widely investigated.

For the heat budget of Chapter 5, the literature pointed to the importance of air-sea fluxes and/or horizontal advection on various timescales across the North Atlantic (Foltz et al., 2003; Foltz and McPhaden, 2005; Nogueira Neto et al., 2018). Consistent with the literature, I found air-sea fluxes to be the dominant process, in this case at short (days to weeks) timescales. I also identified horizontal advection to play an important role at short timescales (days). In the NWTA February mean, Nogueira Neto et al. (2018) identified entrainment as a near zero contributor to the heat loss and advection a contributor to heat gain. Both terms were small compared with surface fluxes. I find advection to play a larger role $-25\,\mathrm{W\,m^{-2}}$ of the opposite sign to their roughly $10\,\mathrm{W\,m^{-2}}$ heat gain from advection. They also identified the entrainment as a small cooling process, whereas our small scale study in the NWTA identifies entrainment as an important warming process of up to $100\,\mathrm{W\,m^{-2}}$. This is due to the subsurface temperature inversion identified within the ocean barrier layer of the study site. Whilst the exclusion of the lateral induction component of the entrainment suggests that entrainment is likely to be smaller than $100\,\mathrm{W\,m^{-2}}$, the sign and magnitude of entrainment are still significantly different from Nogueira Neto et al. (2018). The results of this thesis shows the importance of accurately representing ocean barrier layers of the NWTA (Mignot et al., 2007, 2012) as ocean barrier layers have the potential to significantly change local heat content through entrainment of localised temperature inversions. It also highlights the need for more short timescale observational campaigns, as comparing a short study with a longer or larger spatial study limits the comparability of the work. Small regional processes cannot necessarily be assumed to be the same at different locations, so more observations of this nature are vital.

6.1 Future work

6.1.1 *Caravela*

Throught the time spent on this work, there were a wide range of ideas and potential improvements that were imagined for *Caravela* . As a starting point for the next researchers who work with it, I include a summary of ideas and lessons that did not come to pass within the scope of this thesis.

The biggest upgrade made to *Caravela* after lessons learnt from the EUREC^{4}A deployment was the inclusion of a new GNSS system for better heading, pitch and roll information, for pairing with the ADCP. The first recommendation for a future user would be investigation into the data output of this system. As described in Chapter 3, data parsing from this vessel is often non-trivial. Whilst we have previously identified concerns with matching data from various sensors by timestamp, it is thought that this issue has now been rectified by the manufacturer and should not pose an issue with the PICCOLO dataset.

The next significant physical difference in the sensor package is the upgrading of the CTD to a pumped system. This system was tested in the 2022 trials and so the sensor is known to have produced data in advance of the PICCOLO 2024 deployment, however the data have not been validated. A recommendation before future use would be comparison of the *Caravela* vessel CTD with near surface data from the RRS Sir David Attenborough in the PICCOLO project, to ensure there are no offsets in the data. It is good practice to have an independent calibration for as many sensors as possible on any future deployment ,as well as ensuring post-deployment calibrations are undertaken to quantify sensor drift..

An area that would benefit the future user were it to be improved would be refining the data process such that the heading, pitch and roll are matched to the vessel relative wind and ADCP data by timestamp, such that these can be corrected and true currents and winds easily accessed by the end user. Developing code to automate this would be the preferable option, either to real time correct the the wind data or correct both in post processing.

During the time it has taken to produce this thesis, advances have been made in understanding quality control on moving platforms. Within the scope of this thesis, data were reduced to 10 minute medians in an effort to remove outliers whilst preserving high temporal resolution. Whilst taking 10 minute medians will have eliminated the majority of anomalous data points collected by *Caravela* , a QC process for each variable will give further insight into the effects of the vessel itself on measurement acquisition as well as improving data quality for scientific use. For example, it is known that platform movement introduces spurious variability into observations of downwelling shortwave radiation (Long et al., 2010; Riihimaki et al., 2024). For *Caravela* , at 45° roll, the uncertainty in the shortwave fluxes is +/- 2 % (approximately $20\,\mathrm{W\,m^{-2}}$ at peak insolation) (APOGEE INSTRUMENTS, INC., 2018). Pitch and roll values were far less than this (typically -10 to 15 degree pitch, -25 to +25 degree roll), and taking median values will have eliminated most of this variability. Therefore, I expect that the uncertainty introduced by the pitch and roll will be far less than the theoretical maximum of $20\,\mathrm{W\,m^{-2}}$ for any 10-minute median value, so this uncertainty will not have affected our conclusions pertaining to the shortwave flux biases in ERA5. However, to produce the most accurate shortwave observations, especially at high temporal frequency, I suggest following the recommendations of Riihimaki et al. (2024) and methodology of Long et al. (2010).

The *Caravela* vessel could additionally be enhanced in numerous ways. Firstly she would benefit from a power system upgrade. It is possible to greatly increase the battery storage capacity with the use of modern lithium ion batteries within the same footprint in the hull as the current battery array. This, paired with upgraded solar panels which sit curved on the hull surface to increase absorption and decrease panel heating would further increase energy availability for the science and system payloads. With an increased power set up, it would be possible to implement a Starlink antenna onto the vessel, such that the vessel systems and individual sensor data streams could be viewed by remotely accessing the *Caravela* system. Under the current set up, a limited selection of the sensor data involved in navigation and system monitoring can be accessed over Iridium, but the individual sensor outputs are not accessible. Other than power consumption to check a sensor is running, it is also not currently possible to monitor the sensor data outputs or retrieve data from some of the sensors during the deployment. Remote access into the *Caravela* PC system would greatly enhance operational capabilities. Access to the vessel systems allows data output to be checked to ensure there are no sensor drifts or errors, almost in real time. This is a substantial advance on waiting for vessel recovery to access most of the data in the current set up, and reduces the risk of data loss in the unfortunate event of vessel loss. Increased power capacity in the vessel also allows for the possibility of a camera for additional safety checks when being remotely piloted, which could help the vessel to comply with evolving safety requirements during deployment.

6.1.2 Heat fluxes and budgets

The heat budget yielded a residual, calculated to be −0.18 °C for the cumulative heat budget from 7th February 2020 to 15th February 2020. This residual accounts for terms omitted from the budget calculations made in this thesis and the uncertainty in the calculated terms. Let us first consider uncertainties. With observations of this type, it is difficult to resolve exactly how large the uncertainty in each term may be. In this circumstance, uncertainties consist not only of known measurement uncertainties but also unknown instrument biases (downwelling longwave offset), uncertainties in measurements due to vessel motion and sensor drifts due to time since last calibration, bio fouling and salt build up. Sampling uncertainties are also introduced in some terms, for example the horizontal advection surface drift where QC issues and GPS error may be affecting the values calculated. Mixed layer depth is also an important definition in a mixed layer heat budget, but the depth calculated is dependant on which of many methods one chooses to use, and there is temporal and spatial variability to consider in the calculated MLD. None of these quantities have a perfect ground truth observation available, so it is not possible to know all of these errors. Because of these difficulties, I do not explicitly resolve an uncertainty value for each air-sea flux or heat budget process within this thesis and instead choose to follow the approach of others (du Plessis et al., 2022) in having the uncertainty included in the residual. Were one to attempt to resolve the uncertainty in a measurement, an approach could be to take the uncertainty or accuracy for each of the sensors to determine an upper and lower bound on each of the bulk flux variables, however these measured uncertainties are likely a small component of the overall error. In the event of calculating uncertainties, they should be expressed as RMSE such that the total error is the square root of the sum of individual RMSE's squared. Quantifying the uncertainty in the heat budget components in this way would help to validate the heat budget closure and understand how much of the residual could be due to uncertainties.

For the entrainment and advection terms calculated in the heat budget, I earlier (Chapter 5) alluded to the sampling strategy and calculation of these terms playing a role in worsening the budget closure. To effectively calculate the temperature gradients between the three platforms for calculating the horizontal advection, the platforms must meet the conditions on each pair being spread out in latitude and longitude, the area of the triangle between the platforms being adequately large and the platform ideally forming a right angled triangle, but certainly not a line. Generally having a large triangle area forces the other conditions to be met too. Within this study, I was bound by the constraints of the bowtie sampling strategy and the effects of this were only realised during calculation of the temperature gradients needed for the advection term. Often the platforms were in a non-optimal arrangement, leading to unrealistic temperature gradients between platforms. Was I to address the question of a regional heat budget again, I would suggest using a fixed triangular arrangement of Seagliders with high vertical resolution in the top 50 m to calculate the ocean heat budget. Using Seagliders ensures data is retrieved during the campaign, which is not possible when using the alternative method of a mooring. Also the vertical resolution is higher with a Seaglider than with a mooring. In a region such as the NWTA, the mixed layer depth is variable within a day. The cost of a mooring with vertical sensor spacing high enough to resolve this MLD variation is not viable when Seaglider are available as an alternative. As well as three point locations, an additional surface vessel could then complete a bowtie pattern at the same location to cross submesoscale features which could be missed by a fixed arrangement of Gliders/moorings, and better investigate the ocean heat budget at daily timescales. In terms of the entrainment calculation, improving the sampling strategy as described above would also provide the spatial coverage to calculate the lateral induction component of entrainment. Given the deepening of the mixed layer in the observed timeseries and evidence in GLORYS that there is spatially variant in depth temperature inversion below the mixed layer, the inclusion of lateral induction may reduce the entrainment calculated in Chapter 5 and thus reduce the residual, further improving the budget closure.

The penetrative shortwave radiation is another term in the heat budget that may have been affected by our choice of calculation method. One of the Seagliders did make chlorophyll measurements during the EUREC^{4}A campaign. It would be interesting to process these and recalculate the Q_{pen} term according to a chlorophyll concentration methodology (Morel, 1988; Giddings et al., 2020, 2021), to see if the penetrative flux differs significantly from our estimation. Alternatively, PAR observations were made by SG579 and Q_{pen} could be calculated according to the methodology of Lotliker et al. (2016).

One could also consider the possible contributions of omitted terms from our budget and uncertainties to this residual. For the vertical mixing term, Sheehan et al. (2023) studied the same location as our study site, a few weeks prior to our research. They calculated an average vertical heat flux of $-1.4\,\mathrm{W\,m^{-2}}$ between 200-500 m depth. The shear sensor failed during this campaign so turbulence estimates were made from temperature microstructure. With the two methodologies they used, one discarded turbulence above 75 m and the other discarded many near surface bins in QC, such that I cannot confidently use their analysis to inform us about mixed layer specific turbulence. There is a profile available from Fernández-

Castro et al. (2014) in the NWTA which indicates a mixed layer average rate of turbulent kinetic energy (ϵ) value of around $10^{-8}\,\mathrm{W\,kg^{-1}}$ and diapycnal diffusivity of $10^{-3}\,\mathrm{m^2\,s^{-1}}$. I had hoped to estimate the vertical mixing component of the heat budget from the Seaglider, and if the campaign would be repeated, I would have liked to have deployed this glider for the same time period as the rest of the study with working microstructure shear probes.

The last suggestion for furthering this work would be running a 1-D mixed layer model, initialised with a glider T-S profile from the start of the time series and forced with wind observations from *Caravela* (were they obtained) or ERA5 winds in the case of this particular study. The heat fluxes from Chapter 4 would be applied as surface forcing to the model. This will test if SST and MLD evolution is consistent with being forced by surface fluxes of heat and momentum, as implied by the Chapter 4 heat budget. This would allow vertical mixing and entrainment to be simulated in the model, and could rule out the possibility of ML deepening being locally driven by the mixing, helping to clarify the processes behind the observed heat exchange.

6.2 Broader Implications of this thesis

6.2.1 Air-sea interactions and heat budgets

Air-sea interactions and ocean heat budgets are important for understanding the amount of heat exchanged by air-sea fluxes, as well as horizontal and vertical ocean processes. These processes in turn drive changes in SSTs at a range of timescales, which have significant climate implications. Improving the accuracy of SSTs at finer spatial and temporal resolutions may aid in better representation of atmosphere-ocean coupled phenomena in climate models as models begin to resolve rather than parametrise eddies and submesoscale processes. Open questions remain about whether mesoscale and submesoscale variability matter for air-sea heat and moisture fluxes. Only by investigating fluxes at these scales and quantifying the associated biases in reanalysis can one test whether explicitly resolving these small scales can improve the global budget closure. Within this work, I find even within the 1/12 °resolution of GLORYS, the small scale variability seen in our observations is not resolved in the GLORYS product, and GLORYS mixed layer depths are not consistent with those from observations. The results of this thesis would be useful in improving models and reanalysis products on small spatial scales, leading to further investigations on whether these small spatial biases compared with observations aided in global budget closure. At the smaller spatial and temporal scale of this thesis, the conclusion around the dominance of air-sea fluxes and importance of horizontal advection and entrainment at daily scales is a useful result for climate modellers and flux products. The wider implication for the ERA5 product could be improved parameterisations of tropical fluxes, particularly radiative fluxes, which have the potential to improve global budget closure. From the wider EUREC^{4}A project to which this thesis contributes, improvements in tropical cloud modelling have the potential to improve global radiative heat budgets.

6.2.2 USVs

Marine autonomy is a growing industry with the potential to impact multiple sectors. Within the scientific sector, the growth in uncrewed surface vessels brings alongside the potential for direct observation of extreme weather events including tropical cyclones (Lenain and Melville, 2014), volcanic activity (Tada et al., 2024) and hurricanes (Foltz et al., 2022), providing new insights that would not be available with conventional ship observations. Improvement in USVs and developments in interoperability with other vessels expands the potential capabilities of the ocean observing network. It is probable that the future of ocean observations involves a range of surface and underwater platforms communicating with one another in ways which optimise data return in real time. This thesis took the *Caravela* vessel and showed that with a basic QC regime of reducing data to 10 minute medians, it is possible to validate and bias test the ERA5 reanalysis product over short spatial scales. This result could have much wider global implications, where USVs could be used in the same way to bias test other important and difficult to quantify regions like the poles. The continued advancement of USVs, the systems and sensors could lead to longer endurance times as battery and solar panel technology develops, further enhancing out ability to leverage USV technology for efficient and climate friendly ocean monitoring. USV deployments of a few months are realistic achievements, particularly in lower latitudes with solar powered vessels. This could again bring valuable opportunity to increase ocean observational density in important tropical and subtropical regions. Whilst the scope of this thesis only begins to tackle the development of USV use for air-sea interactions, it is hoped that both the technical and scientific learnings about the *Caravela* USV contribute to the foundational knowledge for the future advancement of USV technology.

A

Appendices

A.1 Publications in this thesis

Chapter 2 includes the publication 'First measurements of ocean and atmosphere in the Tropical North Atlantic using Caravela, a novel uncrewed surface vessel' (Siddle et al., 2021). The contributions to this paper were as follows Elizabeth Siddle: Data curation; formal analysis; investigation; methodology; validation; visualization; writing-original draft; writing-review and editing. Karen Heywood: Conceptualization; investigation; project administration; resources; supervision; writing-review and editing. Benjamin Webber: Investigation; project administration; supervision; writing-review and editing. Peter Bromley: Supervision; writing-review and editing.

A.2 Software

This thesis used the standard Python library and the following additional packages

pandas (McKinney, 2010)

xarray (Hoyer and Hamman, 2017)

Cartopy (Met Office, 2010)

metpy (May et al., 2022)

pynmea2 (Knio, 2023)

numpy (Travis E. Oliphant, 2006)

matplotlib (Hunter, 2007)

Seaborn (Waskom, 2021)

cmocean (Thyng et al., 2016)

cmcrameri (Crameri, 2023)

Gibbs sea water (McDougall and Barker, 2011)

geographiclib (Karney, 2022)

scipy (Virtanen et al., 2020)

tqdm (Costa-Luis et al., 2024)

sklearn (Pedregosa et al., 2011)

The UEA Seaglider toolbox was used for processing of Seaglider data, UEA Seaglider toolbox commit version 3f16640, available from https://bitbucket.org/bastienqueste/uea-seaglider-toolbox/src/toolbox/.

Version 3.5 of the COARE algorithm was used in python (Fairall et al., 1996*b*, 2003; Edson et al., 2013).

GSHHG Global Self-consistent Hierarchical High-resolution Geography, GSHHG Version 2.3.7 June 15, 2017 shorelines were used in figures. Wessel, P., and W. H. F. Smith, A Global Self-consistent, Hierarchical, High-resolution Shoreline Database, *J. Geophys. Res., 101*, 8741-8743, 1996 [PDF]., data accessed via cartopy python package. (Wessel and Smith, 1996).
This thesis used GEBCO bathymetry data (GEBCO Bathymetric Compilation Group, 2020)

The World Ocean Atlas 2023 was consulted during creation of this thesis Reagan et al. (2023, 2024).

B

Glossary

B.1 List of Acronyms

20CR Twentieth Century Reanalysis

AIS Automatic Identification System

ATOMIC Atlantic Tradewind Ocean-atmosphere Mesoscale Interaction Campaign

AUV Autonomous Underwater Vehicle

BCO Barbados cloud observatory

BL Barrier Layer

BOMEX Barbados Oceanographic and Meteorological Experiment

CERES Clouds and the Earth's Radiant Energy System–Energy Balanced and Filled

CFSR Climate Forecast System Reanalysis

CT Conductivity, Temperature

CTD Conductivity, Temperature, Depth

DWL Diurnal Warm Layer

ECMWF European Centre for Medium-Range Weather Forecasts

ERA-20C European Centre for Medium-Range Weather Forecasts Twentieth Century

ERA-Interim European Centre for Medium-Range Weather Forecasts Interim

ERA5 European Centre for Medium-Range Weather Forecasts Fifth Generation

ESDIS Earth Science Data and Information System

EUC Equatorial Undercurrent

EUREC^{4}A Elucidating the Role of Cloud-Circulation Coupling in Climate

GHRSST Group for High-Resolution Sea Surface Temperature

GOOS Global Ocean Observing System

GPCP Global Precipitation Climatology Project

ILD Isothermal Layer Depth

ITCZ Inter Tropical Convergence Zone

JRA-55 Japanese 55-Year Reanalysis

MERRA Modern-Era Retrospective Analysis for Research and Applications

ML Mixed Layer

MLD Mixed Layer Depth

NASW North Atlantic Subtropical Water

NBC North Brazil Current

NCEP National centre for Environmental Prediction

NEC North Equatorial Current

NECC North Equatorial Counter Current

NEUC North Equatorial Undercurrent

NOC National Oceanography Centre

NWTA Northwestern Tropical Atlantic

OAFlux–1x1, 1 °gridded Objectively Analyzed Air–Sea Fluxes

OAFlux–HR3 high-resolution (0.25 °gridded) Objectively Analyzed Air–Sea Fluxes analysis computed from Coupled Ocean–Atmosphere Response Experiment (COARE) version 3

OAFlux–HR4, high-resolution (0.25 °gridded) Objectively Analyzed Air–Sea Fluxes analysis computed from Coupled Ocean–Atmosphere Response Experiment (COARE) version 4

OASIS Observing Air–Sea Interactions Strategy

OSTIA Operational Sea Surface Temperature and Ice Analysis

PICCOLO Processes Influencing Carbon Cycling: Observations of the Lower limb of the Antarctic Overturning

QC Quality Control

SAMS Scottish Association for Marine Science

SST Sea Surface Temperature

STUW Subtropical Under Water

TOGA COARE Tropical Ocean Global Atmosphere Coupled Ocean Atmosphere Response Experiment

TNA Tropical North Atlantic

UEA University of East Anglia

USV Uncrewed surface vessel

B.2 List of Symbols

Q_{sen} sensible heat flux

Q_{lat} latent heat flux

Q_{sw} net shortwave flux

Q_{lw} net longwave flux

Q_0 net heat flux

Q_{pen} penetrative shortwave heat flux

q_{-h} diffuse heat flux at depth h

ρ_{air} density of air

ρ density

c_p specific heat capacity

C_H sensible heat transfer coefficient

C_E latent heat transfer coefficient

S wind speed with respect to the ocean surface current

T temperature

T_s sea surface temperature (SST)

T_{air} air temperature

T_{skin} ocean skin temperature

T_a ocean temperature averaged between depth 0 and h

$T_{-h1.5}$ temperature interpolated at time 1 at the midpoint between the mixed layer depths at time 1 and 2.

$\hat{T}$ deviation from the vertically-averaged temperature

T_{-h} temperature at depth h

L_v latent heat of evaporation

q_{air} specific humidity

q_s saturation humidity at the SST

$SW \downarrow$ downwelling shortwave radiation

α albedo representing ocean surface reflection

ϵ surface emissivity

σ_{SB} Stefan-Boltzmann constant

$LW \downarrow$ the downwelling longwave radiation.

h depth

h_1 depth at timestep 1

h_2 depth at timestep 2

t time

$\frac{\partial T_a}{\partial t}$ temperature tendency

v_a horizontal velocity averaged between depth 0 and h

$\hat{v}$ deviation from the vertically-averaged horizontal velocity

v_{-h} horizontal velocity at depth h

w_{-h} vertical velocity at depth h

$k_{x,y}$ horizontal diffusion coefficients

k_z vertical diffusion coefficient

R Residual

S_A Absolute Salinity

Θ Conservative Temperature

Bibliography

Acquistapace, C., Meroni, A. N., Labbri, G., Lange, D., Späth, F., Abbas, S., and Bellenger, H. (2022) Fast Atmospheric Response to a Cold Oceanic Mesoscale Patch in the North-Western Tropical Atlantic, *Journal of Geophysical Research: Atmospheres*, **127**(21): p. e2022JD036,799, ISSN 2169-8996, doi:10.1029/2022JD036799.

Al Senafi, F., Anis, A., and Menezes, V. (2019) Surface Heat Fluxes over the Northern Arabian Gulf and the Northern Red Sea: Evaluation of ECMWF-ERA5 and NASA-MERRA2 Reanalyses, *Atmosphere*, **10**(9): p. 504, ISSN 2073-4433, doi:10.3390/atmos10090504.

APOGEE INSTRUMENTS, INC. (2018) *Apogee Instruments Owner's Manual Pyranometer Models SP-110 and SP-230 (including SS models)*, Apogee Instruments, Inc, 2018 edition.

Aristizábal Vargas, M. F., Kim, H.-S., Le Hénaff, M., Miles, T., Glenn, S., and Goni, G. (2024) Evaluation of the ocean component on different coupled hurricane forecasting models using upper-ocean metrics relevant to air-sea heat fluxes during Hurricane Dorian (2019), *Frontiers in Earth Science*, **12**, ISSN 2296-6463, doi:10.3389/feart.2024.1342390.

Bai, X., Li, B., Xu, X., and Xiao, Y. (2022) A Review of Current Research and Advances in Unmanned Surface Vehicles, *Journal of Marine Science and Application*, **21**(2): pp. 47–58, ISSN 1993-5048, doi:10.1007/s11804-022-00276-9.

Balaguru, K., Chang, P., Saravanan, R., and Jang, C. J. (2012) The Barrier Layer of the Atlantic warm pool: Formation mechanism and influence on the mean climate, *Tellus A: Dynamic Meteorology and Oceanography*, **64**(1), ISSN 1600-0870, doi:10.3402/tellusa.v64i0.18162.

Bellenger, H. and Duvel, J.-P. (2009) An Analysis of Tropical Ocean Diurnal Warm Layers, *Journal of Climate*, **22**(13): pp. 3629–3646, ISSN 1520-0442, 0894-8755, doi:10.1175/2008JCLI2598.1.

Bengtsson, L., Hodges, K. I., Koumoutsaris, S., Zahn, M., and Berrisford, P. (2013) The Changing Energy Balance of the Polar Regions in a Warmer Climate, *Journal of Climate*, **26**(10): pp. 3112–3129, ISSN 0894-8755, 1520-0442, doi:10.1175/JCLI-D-12-00233.1.

Bernie, D. J., Guilyardi, E., Madec, G., Slingo, J. M., and Woolnough, S. J. (2007) Impact of resolving the diurnal cycle in an ocean–atmosphere GCM. Part 1: a diurnally forced OGCM, *Climate Dynamics*, **29**(6): pp. 575–590, ISSN 1432-0894, doi:10.1007/s00382-007-0249-6.

Berry, D. I. and Kent, E. C. (2009) A New Air–Sea Interaction Gridded Dataset from ICOADS With Uncertainty Estimates, *Bulletin of the American Meteorological Society*, **90**(5): pp. 645–656, ISSN 0003-0007, 1520-0477, doi:10.1175/2008BAMS2639.1.

Berry, D. I. and Kent, E. C. (2011) Air–Sea fluxes from ICOADS: the construction of a new gridded dataset with uncertainty estimates, *International Journal of Climatology*, **31**(7): pp. 987–1001, ISSN 1097-0088, doi:10.1002/joc.2059.

Bigorre, S. P. and Plueddemann, A. J. (2021) The Annual Cycle of Air-Sea Fluxes in the Northwest Tropical Atlantic, *Frontiers in Marine Science*, **7**, ISSN 2296-7745, doi:10.3389/fmars.2020.612842.

Bishop, S. P., Small, R. J., Bryan, F. O., and Tomas, R. A. (2017) Scale Dependence of Midlatitude Air–Sea Interaction, *Journal of Climate*, **30**(20): pp. 8207–8221, ISSN 0894-8755, 1520-0442, doi:10.1175/JCLI-D-17-0159.1.

Black, P. G., D'Asaro, E. A., Drennan, W. M., French, J. R., Niiler, P. P., Sanford, T. B., Terrill, E. J., Walsh, E. J., and Zhang, J. A. (2007) Air–Sea Exchange in Hurricanes: Synthesis of Observations from the Coupled Boundary Layer Air–Sea Transfer Experiment, *Bulletin of the American Meteorological Society*, **88**(3): pp. 357–374, ISSN 0003-0007, 1520-0477, doi:10.1175/BAMS-88-3-357.

Bony, S., Stevens, B., Ament, F., Bigorre, S., Chazette, P., Crewell, S., Delanoë, J., Emanuel, K., Farrell, D., Flamant, C., Gross, S., Hirsch, L., Karstensen, J., Mayer, B., Nuijens, L., Ruppert, J. H., Sandu, I., Siebesma, P., Speich, S., Szczap, F., Totems, J., Vogel, R., Wendisch, M., and Wirth, M. (2017) EUREC4A: A Field Campaign to Elucidate the Couplings Between Clouds, Convection and Circulation, *Surveys in Geophysics*, **38**(6): pp. 1529–1568, ISSN 15730956, doi:10.1007/s10712-017-9428-0. ISBN: 1071201794.

Bourles, B., Molinari, R. L., Johns, E., Wilson, W. D., and Leaman, K. D. (1999) Upper layer currents in the western tropical North Atlantic (1989–1991), *Journal of Geophysical Research: Oceans*, **104**(C1): pp. 1361–1375, doi:https://doi.org/10.1029/1998JC900025.

Bourlès, B., Lumpkin, R., McPhaden, M. J., Hernandez, F., Nobre, P., Campos, E., Yu, L., Planton, S., Busalacchi, A., Moura, A. D., Servain, J., and Trotte, J. (2008) THE PIRATA PROGRAM: History, Accomplishments, and Future Directions, *Bulletin of the American Meteorological Society*, **89**(8): pp. 1111–1126, ISSN 0003-0007, 1520-0477, doi: 10.1175/2008BAMS2462.1.

Bourras, D., Branger, H., Reverdin, G., Marié, L., Cambra, R., Baggio, L., Caudoux, C., Caudal, G., Morisset, S., Geyskens, N., Weill, A., and Hauser, D. (2014) A New Platform for the Determination of Air–Sea Fluxes (OCARINA): Overview and First Results, *Journal of Atmospheric and Oceanic Technology*, **31**(5): pp. 1043–1062, ISSN 0739-0572, doi:10.1175/JTECH-D-13-00055.1.

Brock, F. V. (1986) A Nonlinear Filter to Remove Impulse Noise from Meteorological Data, *Journal of Atmospheric and Oceanic Technology*, **3**(1): pp. 51 – 58, doi:10.1175/1520-0426(1986)003⟨0051:ANFTRI⟩2.0.CO;2.

Böning, C. W. and Herrmann, P. (1994) Annual Cycle of Poleward Heat Transport in the Ocean: Results from High-Resolution Modeling of the North and Equatorial Atlantic, *Journal of Physical Oceanography*, **24**(1): pp. 91–107, ISSN 0022-3670, 1520-0485, doi: 10.1175/1520-0485(1994)024⟨0091:ACOPHT⟩2.0.CO;2.

Caccia, M., Bono, R., Bruzzone, G., Spirandelli, E., Veruggio, G., Stortini, A., and Capodaglio, G. (2005) Sampling sea surfaces with SESAMO: an autonomous craft for the study of sea-air interactions, *IEEE Robotics & Automation Magazine*, **12**(3): pp. 95–105, ISSN 1558-223X, doi:10.1109/MRA.2005.1511873.

Cai, W., Wu, L., Lengaigne, M., Li, T., McGregor, S., Kug, J.-S., Yu, J.-Y., Stuecker, M. F., Santoso, A., Li, X., Ham, Y.-G., Chikamoto, Y., Ng, B., McPhaden, M. J., Du, Y., Dommenget, D., Jia, F., Kajtar, J. B., Keenlyside, N., Lin, X., Luo, J.-J., Martín-Rey, M., Ruprich-Robert, Y., Wang, G., Xie, S.-P., Yang, Y., Kang, S. M., Choi, J.-Y., Gan, B., Kim, G.-I., Kim, C.-E., Kim, S., Kim, J.-H., and Chang, P. (2019) Pantropical climate interactions, *Science*, **363**(6430): p. eaav4236, doi:10.1126/science.aav4236.

Centurioni, L. R., Turton, J. D., Lumpkin, R., Braasch, L. J., Brassington, G. B., Chao, Y., Charpentier, E., Chen, Z., Corlett, G. K., Dohan, K., Donlon, C., Gallage, C., Hormann, V., Ignatov, A., Ingleby, B., Jensen, R. E., Kelly-Gerreyn, B. A., Koszalka, I. M., Lin, X., Lindstrom, E., Maximenko, N., Merchant, C. J., Minnett, P. J., O'Carroll, A. G., Paluszkiewicz, T., Poli, P., Poulain, P.-M., Reverdin, G., Sun, X., Swail, V. R., Thurston, S. W., Wu, L., Yu, L., Wang, B., and Zhang, D. (2019) Global in situ Observations of Essential Climate and Ocean Variables at the Air–Sea Interface, *Frontiers in Marine Science*, **6**: p. 419, ISSN 2296-7745, doi:10.3389/fmars.2019.00419.

Charnock, H. (1955) Wind stress on a water surface, *Quarterly Journal of the Royal Meteorological Society*, **81**(350): pp. 639–640, ISSN 1477-870X, doi:10.1002/qj.49708135027.

Clark, N. E., Eber, L. E., Laurs, R. M., Renneer, J. A., and Saur, J. F. T. (1974) Heat exchange between ocean and atmosphere in the eastern North Pacific for 1961-71, *NOAA Technical Report NMFS SSRF-682. U.S. Department of Commerce: Washington, DC*, p. 108 pp.

Cogley, J. G. (1979) The Albedo of Water as a Function of Latitude, *Monthly Weather Review*, **107**(6): pp. 775 – 781, doi:https://doi.org/10.1175/1520-0493(1979)107⟨0775:TAOWAA⟩2.0.CO;2.

Copernicus Climate Change Service (2023) ERA5 hourly data on single levels from 1940 to present, *Copernicus Climate Change Service (C3S) Climate Data Store (CDS)*, doi:10.24381/cds.adbb2d47. (Accessed on 2023-08-23).

Cornillon, P. and Stramma, L. (1985) The distribution of diurnal sea surface warming events in the western Sargasso Sea, *Journal of Geophysical Research: Oceans*, **90**(C6): pp. 11,811–11,815, doi:https://doi.org/10.1029/JC090iC06p11811.

Costa-Luis, C. d., Larroque, S. K., Altendorf, K., Mary, H., richardsheridan, Korobov, M., Yorav-Raphael, N., Ivanov, I., Bargull, M., Rodrigues, N., Shawn, Dektyarev, M., Górny, M., mjstevens777, Pagel, M. D., Zugnoni, M., JC, CrazyPython, Newey, C., Lee, A., pgajdos, Todd, Malmgren, S., redbug312, Desh, O., Nechaev, N., Boyle, M., Nordlund, M., MapleCCC, and McCracken, J. (2024) tqdm: A fast, Extensible Progress Bar for Python and CLI, doi:10.5281/zenodo.14231923.

Crameri, F. (2023) Scientific colour maps, doi:10.5281/zenodo.8409685.

Crawford, T. L., McMillen, R. T., Meyers, T. P., and Hicks, B. B. (1993) Spatial and temporal variability of heat, water vapor, carbon dioxide, and momentum air-sea exchange in a coastal environment, *Journal of Geophysical Research: Atmospheres*, **98**(D7): pp. 12,869–12,880, ISSN 2156-2202, doi:10.1029/93JD00628.

Cronin, M. F., Gentemann, C. L., Edson, J. B., Ueki, I., Bourassa, M., Brown, S., Clayson, C. A., Fairall, C., T. Farrar, J., Gille, S. T., Gulev, S., Josey, S., Kato, S., Katsumata, M., Kent, E. C., Krug, M., Minnett, P. J., Parfitt, R., Pinker, R. T., Stackhouse, P. W., Swart, S., Tomita, H., Vandemark, D., Weller, R. A., Yoneyama, K., Yu, L., and Zhang, D. (2019) Air-sea fluxes with a focus on heat and momentum, *Frontiers in Marine Science*, **6**(JUL), ISSN 22967745, doi:10.3389/fmars.2019.00430.

Cronin, M. F., Swart, S., Marandino, C. A., Anderson, C., Browne, P., Chen, S., Joubert, W. R., Schuster, U., Venkatesan, R., Addey, C. I., Alves, O., Ardhuin, F., Battle, S., Bourassa, M. A., Chen, Z., Chory, M., Clayson, C., de Souza, R. B., du Plessis, M., Edmondson, M., Edson, J. B., Gille, S. T., Hermes, J., Hormann, V., Josey, S. A., Kurz, M., Lee, T., Maicu, F., Moustahfid, E. H., Nicholson, S.-A., Nyadjro, E. S., Palter, J., Patterson, R. G., Penny, S. G., Pezzi, L. P., Pinardi, N., Reeves Eyre, J. E. J., Rome, N., Subramanian, A. C., Stienbarger, C., Steinhoff, T., Sutton, A. J., Tomita, H., Wills, S. M., Wilson, C., and Yu, L. (2023) Developing an Observing Air–Sea Interactions Strategy (OASIS) for the global ocean, *ICES Journal of Marine Science*, **80**(2): pp. 367–373, ISSN 1054-3139, doi:10.1093/icesjms/fsac149.

de Boyer Montégut, C., Madec, G., Fischer, A. S., Lazar, A., and Iudicone, D. (2004) Mixed layer depth over the global ocean: An examination of profile data and a profile-based climatology, *Journal of Geophysical Research: Oceans*, **109**(C12), doi:https://doi.org/10.1029/2004JC002378.

de Boyer Montégut, C., Mignot, J., Lazar, A., and Cravatte, S. (2007) Control of salinity on the mixed layer depth in the world ocean: 1. General description, *Journal of Geophysical Research: Oceans*, **112**(C6), ISSN 2156-2202, doi:10.1029/2006JC003953.

Dee, D. P., Uppala, S. M., Simmons, A. J., Berrisford, P., Poli, P., Kobayashi, S., Andrae, U., Balmaseda, M. A., Balsamo, G., Bauer, P., Bechtold, P., Beljaars, A. C. M., van de Berg, L., Bidlot, J., Bormann, N., Delsol, C., Dragani, R., Fuentes, M., Geer, A. J., Haimberger, L., Healy, S. B., Hersbach, H., Hólm, E. V., Isaksen, L., Kållberg, P., Köhler, M., Matricardi, M., McNally, A. P., Monge-Sanz, B. M., Morcrette, J.-J., Park, B.-K., Peubey, C., de Rosnay, P., Tavolato, C., Thépaut, J.-N., and Vitart, F. (2011) The ERA-Interim reanalysis: configuration and performance of the data assimilation system, *Quarterly Journal of the Royal Meteorological Society*, **137**(656): pp. 553–597, ISSN 1477-870X, doi:10.1002/qj.828.

Delnore, V. E. (1972) Diurnal Variation of Temperature and Energy Budget for the Oceanic

Mixed Layer During BOMEX, *Journal of Physical Oceanography*, **2**(3): pp. 239–247, ISSN 0022-3670, 1520-0485, doi:10.1175/1520-0485(1972)002⟨0239:DVOTAE⟩2.0.CO;2.

Domingues, R., Kuwano-Yoshida, A., Chardon-Maldonado, P., Todd, R. E., Halliwell, G., Kim, H.-S., Lin, I.-I., Sato, K., Narazaki, T., Shay, L. K., Miles, T., Glenn, S., Zhang, J. A., Jayne, S. R., Centurioni, L., Le Hénaff, M., Foltz, G. R., Bringas, F., Ali, M. M., DiMarco, S. F., Hosoda, S., Fukuoka, T., LaCour, B., Mehra, A., Sanabia, E. R., Gyakum, J. R., Dong, J., Knaff, J. A., and Goni, G. (2019) Ocean Observations in Support of Studies and Forecasts of Tropical and Extratropical Cyclones, *Frontiers in Marine Science*, **6**, ISSN 2296-7745, doi:10.3389/fmars.2019.00446.

Dong, J., Domingues, R., Goni, G., Halliwell, G., Kim, H.-S., Lee, S.-K., Mehari, M., Bringas, F., Morell, J., and Pomales, L. (2017) Impact of Assimilating Underwater Glider Data on Hurricane Gonzalo (2014) Forecasts, *Weather and Forecasting*, **32**(3): pp. 1143–1159, ISSN 1520-0434, 0882-8156, doi:10.1175/WAF-D-16-0182.1.

Dong, S., Gille, S. T., and Sprintall, J. (2007) An Assessment of the Southern Ocean Mixed Layer Heat Budget, *Journal of Climate*, **20**(17): pp. 4425–4442, ISSN 0894-8755, 1520-0442, doi:10.1175/JCLI4259.1.

Dong, S. and Kelly, K. A. (2004) Heat Budget in the Gulf Stream Region: The Importance of Heat Storage and Advection, *Journal of Physical Oceanography*, **34**(5): pp. 1214–1231, ISSN 0022-3670, 1520-0485, doi:10.1175/1520-0485(2004)034⟨1214:HBITGS⟩2.0.CO;2.

Dorling, S. (2019) Personal communication. Data supplied by Steve Dorling, WeatherQuest Ltd, 9th Septermber 2019.

du Plessis, M. D., Swart, S., Biddle, L. C., Giddy, I. S., Monteiro, P. M. S., Reason, C. J. C., Thompson, A. F., and Nicholson, S.-A. (2022) The Daily-Resolved Southern Ocean Mixed Layer: Regional Contrasts Assessed Using Glider Observations, *Journal of Geophysical Research: Oceans*, **127**(4): p. e2021JC017,760, ISSN 2169-9291, doi: 10.1029/2021JC017760.

Dumont, E. (2019) Personal Communication. Castaway Data, personal communication with Estelle Dumont, Scottish Association for Marine Science, 12/11/2019.

ECMWF (2024) Conversion table for accumulated variables (total precipitation/fluxes). Confluence.ecmwf.int/pages/viewpage.action?pageId=197702790 (accessed 02-Aug-2024).

Edson, J. B., Hinton, A. A., Prada, K. E., Hare, J. E., and Fairall, C. W. (1998) Direct Covariance Flux Estimates from Mobile Platforms at Sea*, *Journal of Atmospheric* *and Oceanic Technology*, **15**(2): pp. 547–562, ISSN 0739-0572, 1520-0426, doi:10.1175/1520-0426(1998)015⟨0547:DCFEFM⟩2.0.CO;2.

Edson, J. B., Jampana, V., Weller, R. A., Bigorre, S. P., Plueddemann, A. J., Fairall, C. W., Miller, S. D., Mahrt, L., Vickers, D., and Hersbach, H. (2013) On the Exchange of Momentum over the Open Ocean, *Journal of Physical Oceanography*, **43**(8): pp. 1589–1610, ISSN 0022-3670, 1520-0485, doi:10.1175/JPO-D-12-0173.1.

E.U. Copernicus Marine Service Information (CMEMS) (2023) Global Ocean Physics Reanalysis GLORYS12V1, *Marine Data Store (MDS).*, doi:https://doi.org/10.48670/moi-00021. (Accessed on 26-Nov-2023).

Fairall, C. W., Bradley, E. F., Godfrey, J. S., Wick, G. A., Edson, J. B., and Young, G. S. (1996*a*) Cool-skin and warm-layer effects on sea surface temperature, *Journal of Geophysical Research: Oceans*, **101**(C1): pp. 1295–1308, doi:10.1029/95JC03190.

Fairall, C. W., Bradley, E. F., Hare, J. E., Grachev, A. A., and Edson, J. B. (2003) Bulk parameterization of air-sea fluxes: Updates and verification for the COARE algorithm, *Journal of Climate*, **16**(4): pp. 571–591, ISSN 08948755, doi:10.1175/1520-0442(2003)016⟨0571:BPOASF⟩2.0.CO;2.

Fairall, C. W., Bradley, E. F., Rogers, D. P., Edson, J. B., and Young, G. S. (1996*b*) Bulk parameterization of air-sea fluxes for Tropical Ocean-Global Atmosphere Coupled-Ocean Atmosphere Response Experiment, *Journal of Geophysical Research: Oceans*, **101**(C2): pp. 3747–3764, doi:10.1029/95JC03205.

Fer, I., Nandi, P., Holbrook, W. S., Schmitt, R. W., and Páramo, P. (2010) Seismic imaging of a thermohaline staircase in the western tropical North Atlantic, *Ocean Science*, **6**(3): pp. 621–631, ISSN 1812-0784, doi:10.5194/os-6-621-2010.

Fer, I. and Peddie, D. (2013) Near surface oceanographic measurements using the SailBuoy, *in 2013 MTS/IEEE OCEANS - Bergen*, pp. 1–15, doi:10.1109/OCEANS-Bergen.2013.6607969.

Fernández, P., Speich, S., Bellenger, H., Lange Vega, D., Karstensen, J., Zhang, D., and Rocha, C. B. (2024) On the Mechanisms Driving Latent Heat Flux Variations in the Northwest Tropical Atlantic, *Journal of Geophysical Research: Oceans*, **129**(5): p. e2023JC020,658, ISSN 2169-9291, doi:10.1029/2023JC020658.

Fernández, P., Speich, S., Borgnino, M., Meroni, A. N., Desbiolles, F., and Pasquero, C. (2023) On the importance of the atmospheric coupling to the small-scale ocean in the modulation of latent heat flux, *Frontiers in Marine Science*, **10**: p. 1136,558, ISSN 2296-7745, doi:10.3389/fmars.2023.1136558.

Fernández-Castro, B., Mouriño-Carballido, B., Benítez-Barrios, V., Chouciño, P., Fraile-Nuez, E., Graña, R., Piedeleu, M., and Rodríguez-Santana, A. (2014) Microstructure turbulence and diffusivity parameterization in the tropical and subtropical Atlantic, Pacific and Indian Oceans during the Malaspina 2010 expedition, *Deep Sea Research Part I: Oceanographic Research Papers*, **94**: pp. 15–30, ISSN 09670637, doi:10.1016/j.dsr.2014.08.006.

Flatau, M., Flatau, P. J., Phoebus, P., and Niiler, P. P. (1997) The Feedback between Equatorial Convection and Local Radiative and Evaporative Processes: The Implications for Intraseasonal Oscillations, *Journal of the Atmospheric Sciences*, **54**(19): pp. 2373–2386, ISSN 0022-4928, 1520-0469, doi:10.1175/1520-0469(1997)054⟨2373:TFBECA⟩2.0.CO;2.

Foltz, G. R., Eddebbar, Y. A., Sprintall, J., Capotondi, A., Cravatte, S., Brandt, P., Sutton, A. J., Morris, T., Hermes, J., McMahon, C. R., McPhaden, M. J., Looney, L. B., Tuchen, F. P., Roxy, M. K., Wang, F., Chai, F., Rodrigues, R. R., Rodriguez-Fonseca, B., Subramanian, A. C., Dengler, M., Stienbarger, C., Bailey, K., and Yu, W. (2025) Toward an integrated pantropical ocean observing system, *Frontiers in Marine Science*, **12**, ISSN 2296-7745, doi:10.3389/fmars.2025.1539183.

Foltz, G. R., Grodsky, S. A., Carton, J. A., and McPhaden, M. J. (2003) Seasonal mixed layer heat budget of the tropical Atlantic Ocean, *Journal of Geophysical Research: Oceans*, **108**(C5), ISSN 2156-2202, doi:10.1029/2002JC001584.

Foltz, G. R. and McPhaden, M. J. (2005) Mixed Layer Heat Balance on Intraseasonal Time Scales in the Northwestern Tropical Atlantic Ocean, *Journal of Climate*, **18**(20): pp. 4168–4184, ISSN 0894-8755, 1520-0442, doi:10.1175/JCLI3531.1.

Foltz, G. R. and McPhaden, M. J. (2006) The Role of Oceanic Heat Advection in the Evolution of Tropical North and South Atlantic SST Anomalies, *Journal of Climate*, **19**(23): pp. 6122–6138, ISSN 0894-8755, 1520-0442, doi:10.1175/JCLI3961.1.

Foltz, G. R. and McPhaden, M. J. (2008) Seasonal mixed layer salinity balance of the tropical North Atlantic Ocean, *Journal of Geophysical Research: Oceans*, **113**(C2): p. 2007JC004,178, ISSN 0148-0227, doi:10.1029/2007JC004178.

Foltz, G. R. and McPhaden, M. J. (2009) Impact of Barrier Layer Thickness on SST in the

Central Tropical North Atlantic, *Journal of Climate*, **22**(2): pp. 285–299, ISSN 0894-8755, 1520-0442, doi:10.1175/2008JCLI2308.1.

Foltz, G. R., Schmid, C., and Lumpkin, R. (2013) Seasonal Cycle of the Mixed Layer Heat Budget in the Northeastern Tropical Atlantic Ocean, *Journal of Climate*, **26**(20): pp. 8169–8188, ISSN 0894-8755, 1520-0442, doi:10.1175/JCLI-D-13-00037.1.

Foltz, G. R., Zhang, C., Meing, C., Zhang, J. A., and Zhang, D. (2022) An Unprecedented View Inside a Hurricane. , Eos, 103, https://doi.org/10.1029/2022EO220228. Published on 6 May 2022.

Frajka-Williams, E., Eriksen, C. C., Rhines, P. B., and Harcourt, R. R. (2011) Determining Vertical Water Velocities from Seaglider, *Journal of Atmospheric and Oceanic Technology*, **28**(12): pp. 1641 – 1656, doi:https://doi.org/10.1175/2011JTECHO830.1.

Garau, B., Ruiz, S., Zhang, W. G., Pascual, A., Heslop, E., Kerfoot, J., and Tintoré, J. (2011) Thermal Lag Correction on Slocum CTD Glider Data, *Journal of Atmospheric and Oceanic Technology*, **28**(9): pp. 1065 – 1071, doi:https://doi.org/10.1175/JTECH-D-10-05030.1.

GEBCO Bathymetric Compilation Group (2020) The GEBCO_2020 Grid - a continuous terrain model of the global oceans and land, doi:10.5285/a29c5465-b138-234d-e053-6c86abc040b9.

Gentemann, C. L., Clayson, C. A., Lee, T., Brown, S., Subramanian, A., Bourassa, M., Lombardo, K., Parfitt, R., Seo, H., Gille, S., Farrar, T., Argrow, B., Whitaker, J., Kleist, D., May, J., Browne, P., Harris, C., Kachi, M., Tomita, H., and Bentamy, A. (2021) Butterfly: a satellite mission to reveal the oceans' impact on our weather and climate, doi:10.5281/zenodo.5120586.

Gentemann, C. L., Scott, J. P., Mazzini, P. L. F., Pianca, C., Akella, S., Minnett, P. J., Cornillon, P., Fox-Kemper, B., Cetinić, I., Chin, T. M., Gomez-Valdes, J., Vazquez-Cuervo, J., Tsontos, V., Yu, L., Jenkins, R., Halleux, S. D., Peacock, D., and Cohen, N. (2020) Saildrone: Adaptively Sampling the Marine Environment, *Bulletin of the American Meteorological Society*, **101**(6): pp. E744–E762, ISSN 0003-0007, 1520-0477, doi:10.1175/BAMS-D-19-0015.1.

Giddings, J., Heywood, K. J., Matthews, A. J., Joshi, M. M., Webber, B. G. M., Sanchez-Franks, A., King, B. A., and Vinayachandran, P. N. (2021) Spatial and temporal variability of solar penetration depths in the Bay of Bengal and its impact on sea surface temperature

(SST) during the summer monsoon, *Ocean Science*, **17**(4): pp. 871–890, ISSN 1812-0784, doi:10.5194/os-17-871-2021.

Giddings, J., Matthews, A. J., Klingaman, N. P., Heywood, K. J., Joshi, M., and Webber, B. G. M. (2020) The effect of seasonally and spatially varying chlorophyll on Bay of Bengal surface ocean properties and the South Asian monsoon, *Weather and Climate Dynamics*, **1**(2): pp. 635–655, doi:10.5194/wcd-1-635-2020.

Giordani, H., Caniaux, G., and Voldoire, A. (2013) Intraseasonal mixed-layer heat budget in the equatorial Atlantic during the cold tongue development in 2006, *Journal of Geophysical Research: Oceans*, **118**(2): pp. 650–671, ISSN 2169-9291, doi:10.1029/2012JC008280.

Godfrey, J. S. and Lindstrom, E. J. (1989) The heat budget of the equatorial western Pacific surface mixed layer, *Journal of Geophysical Research: Oceans*, **94**(C6): pp. 8007–8017, ISSN 0148-0227, doi:10.1029/JC094iC06p08007.

Grare, L., Statom, N. M., Pizzo, N., and Lenain, L. (2021) Instrumented Wave Gliders for Air-Sea Interaction and Upper Ocean Research, *Frontiers in Marine Science*, **8**, ISSN 2296-7745, doi:10.3389/fmars.2021.664728.

Grist, J. P., Josey, S. A., Marsh, R., Good, S. A., Coward, A. C., de Cuevas, B. A., Alderson, S. G., New, A. L., and Madec, G. (2010) The roles of surface heat flux and ocean heat transport convergence in determining Atlantic Ocean temperature variability, *Ocean Dynamics*, **60**(4): pp. 771–790, ISSN 1616-7228, doi:10.1007/s10236-010-0292-4.

Hadfield, R. E. (2007) The North Atlantic Study: An Argo Based Study, *PhD thesis, University of Southampton.*

Hadfield, R. E., Wells, N. C., Josey, S. A., and Hirschi, J. J.-M. (2007) On the accuracy of North Atlantic temperature and heat storage fields from Argo, *Journal of Geophysical Research: Oceans*, **112**(C1), doi:https://doi.org/10.1029/2006JC003825.

Halkides, D. J., Waliser, D. E., Lee, T., Menemenlis, D., and Guan, B. (2015) Quantifying the processes controlling intraseasonal mixed-layer temperature variability in the tropical Indian Ocean, *Journal of Geophysical Research: Oceans*, **120**(2): pp. 692–715, ISSN 2169-9291, doi:10.1002/2014JC010139.

Han, Y., Li, Y., Xu, C., Liu, L., Zhao, Y., Li, W., and Song, X. (2022) Coastal buoy observation of air-sea net heat flux in the East China Sea in summer 2020, *Journal of Oceanology and Limnology*, **40**(3): pp. 907–921, ISSN 2523-3521, doi:10.1007/s00343-021-1012-2.

Handegard, N. O., De Robertis, A., Holmin, A. J., Johnsen, E., Lawrence, J., Le Bouffant, N., O'Driscoll, R., Peddie, D., Pedersen, G., Priou, P., Rogge, R., Samuelsen, M., and Demer, D. A. (2024) Uncrewed surface vehicles (USVs) as platforms for fisheries and plankton acoustics, *ICES Journal of Marine Science*, **81**(9): pp. 1712–1723, ISSN 1054-3139, doi: 10.1093/icesjms/fsae130.

Hansen, D. V. and Paul, C. A. (1984) Genesis and effects of long waves in the equatorial Pacific, *Journal of Geophysical Research: Oceans*, **89**(C6): pp. 10,431–10,440, ISSN 2156-2202, doi:10.1029/JC089iC06p10431.

Hansen, D. V. and Poulain, P.-M. (1996) Quality Control and Interpolations of WOCE-TOGA Drifter Data, *Journal of Atmospheric and Oceanic Technology*, **13**(4): pp. 900–909, ISSN 0739-0572, 1520-0426, doi:10.1175/1520-0426(1996)013⟨0900:QCAIOW⟩2.0.CO;2.

Hersbach, H., Bell, B., Berrisford, P., Biavati, G., Horányi, A., Muñoz Sabater, J., Nicolas, J., Peubey, C., Radu, R., Rozum, I., Schepers, D., Simmons, A., Soci, C., Dee, D., and Thépaut, J.-N. (2018) ERA5 hourly data on single levels from 1940 to present, doi:10.24381/cds.adbb2d47.

Hersbach, H., Bell, B., Berrisford, P., Biavati, G., Horányi, A., Muñoz Sabater, J., Nicolas, J., Peubey, C., Radu, R., Rozum, I., Schepers, D., Simmons, A., Soci, C., Dee, D., and Thépaut, J.-N. (2023) ERA5 monthly data on single levels from 1940 to present, doi: 10.24381/cds.f17050d7.

Hersbach, H., Bell, B., Berrisford, P., Hirahara, S., Horányi, A., Muñoz-Sabater, J., Nicolas, J., Peubey, C., Radu, R., Schepers, D., Simmons, A., Soci, C., Abdalla, S., Abellan, X., Balsamo, G., Bechtold, P., Biavati, G., Bidlot, J., Bonavita, M., De Chiara, G., Dahlgren, P., Dee, D., Diamantakis, M., Dragani, R., Flemming, J., Forbes, R., Fuentes, M., Geer, A., Haimberger, L., Healy, S., Hogan, R. J., Hólm, E., Janisková, M., Keeley, S., Laloyaux, P., Lopez, P., Lupu, C., Radnoti, G., de Rosnay, P., Rozum, I., Vamborg, F., Villaume, S., and Thépaut, J.-N. (2020) The ERA5 global reanalysis, *Quarterly Journal of the Royal Meteorological Society*, **146**(730): pp. 1999–2049, doi:https://doi.org/10.1002/qj.3803.

Hine, R., Willcox, S., Hine, G., and Richardson, T. (2009) The Wave Glider: A Wave-Powered autonomous marine vehicle, *in OCEANS 2009*, pp. 1–6, doi:10.23919/OCEANS.2009.5422129. ISSN: 0197-7385.

Holte, J. and Talley, L. (2009) A new algorithm for finding mixed layer depths with applications to argo data and subantarctic mode water formation, *Journal of Atmospheric and Oceanic Technology*, **26**(9): pp. 1920 – 1939, doi:10.1175/2009JTECHO543.1.

Hormann, V., Lumpkin, R., and Foltz, G. R. (2012) Interannual North Equatorial Countercurrent variability and its relation to tropical Atlantic climate modes, *Journal of Geophysical Research: Oceans*, **117**(C4), ISSN 2156-2202, doi:10.1029/2011JC007697.

Hoyer, S. and Hamman, J. (2017) xarray: N-D labeled arrays and datasets in Python, *Journal of Open Research Software*, **5**(1), doi:10.5334/jors.148.

Hu, C., Montgomery, E. T., Schmitt, R. W., and Muller-Karger, F. E. (2004) The dispersal of the Amazon and Orinoco River water in the tropical Atlantic and Caribbean Sea: Observation from space and S-PALACE floats, *Deep Sea Research Part II: Topical Studies in Oceanography*, **51**(10): pp. 1151–1171, ISSN 0967-0645, doi:10.1016/j.dsr2.2004.04.001.

Hu, W., Duan, A., and Wu, G. (2015) Impact of Subdaily Air–Sea Interaction on Simulating Intraseasonal Oscillations over the Tropical Asian Monsoon Region, *Journal of Climate*, **28**(3): pp. 1057–1073, ISSN 0894-8755, 1520-0442, doi:10.1175/JCLI-D-14-00407.1.

Hunter, J. D. (2007) Matplotlib: A 2D Graphics Environment, *Computing in Science & Engineering*, **9**(3): pp. 90–95, ISSN 1558-366X, doi:10.1109/MCSE.2007.55.

Iyer, S., Drushka, K., Thompson, E. J., and Thomson, J. (2022) Small-Scale Spatial Variations of Air-Sea Heat, Moisture, and Buoyancy Fluxes in the Tropical Trade Winds, *Journal of Geophysical Research: Oceans*, **127**(10): p. e2022JC018,972, ISSN 2169-9291, doi:10.1029/2022JC018972.

Jansen, F., Schulz, H., and Stolla, K. (2021) EUREC4A BCO surface radiation data (v1.0.0), doi:https://doi.org/10.25326/230. Accessed 3rd Feb 2023.

Jean-Michel, L., Eric, G., Romain, B.-B., Gilles, G., Angélique, M., Marie, D., Clément, B., Mathieu, H., Olivier, L. G., Charly, R., Tony, C., Charles-Emmanuel, T., Florent, G., Giovanni, R., Mounir, B., Yann, D., and Pierre-Yves, L. T. (2021) The Copernicus Global 1/12° Oceanic and Sea Ice GLORYS12 Reanalysis, *Frontiers in Earth Science*, **9**, ISSN 2296-6463, doi:10.3389/feart.2021.698876.

Johns, W., Speich, S., Araujo, M., and lead authors (2021) Tropical Atlantic Observing System (TAOS) Review Report. CLIVAR, p. 218 pp.

Johnston, P. and Pierpoint, C. (2017) Deployment of a passive acoustic monitoring (PAM) array from the AutoNaut wave-propelled unmanned surface vessel (USV), *in OCEANS 2017 - Aberdeen*, pp. 1–4, doi:10.1109/OCEANSE.2017.8084780.

Johnston, P. and Poole, M. (2017) Marine surveillance capabilities of the AutoNaut wave-propelled unmanned surface vessel (USV), *in OCEANS 2017 - Aberdeen*, pp. 1–46, doi: 10.1109/OCEANSE.2017.8084782.

Josey, S. A. (2001) A Comparison of ECMWF, NCEP–NCAR, and SOC Surface Heat Fluxes with Moored Buoy Measurements in the Subduction Region of the Northeast Atlantic, *Journal of Climate*, **14**(8): pp. 1780–1789, ISSN 0894-8755, 1520-0442, doi: 10.1175/1520-0442(2001)014⟨1780:ACOENN⟩2.0.CO;2.

Josey, S. A., Kent, E. C., and Taylor, P. K. (1999) New Insights into the Ocean Heat Budget Closure Problem from Analysis of the SOC Air–Sea Flux Climatology, *Journal of Climate*, **12**(9): pp. 2856–2880, ISSN 0894-8755, 1520-0442, doi:10.1175/1520-0442(1999)012⟨2856:NIITOH⟩2.0.CO;2.

Josey, S. A., Oakley, D., and Pascal, R. W. (1997) On estimating the atmospheric longwave flux at the ocean surface from ship meteorological reports, *Journal of Geophysical Research: Oceans*, **102**(C13): pp. 27,961–27,972, ISSN 2156-2202, doi:10.1029/97JC02420.

Kara, A. B., Rochford, P. A., and Hurlburt, H. E. (2000) An optimal definition for ocean mixed layer depth, *Journal of Geophysical Research: Oceans*, **105**(C7): pp. 16,803–16,821, doi:https://doi.org/10.1029/2000JC900072.

Karlowska, E., Matthews, A. J., Webber, B. G. M., Graham, T., and Xavier, P. (2024) The effect of diurnal warming of sea-surface temperatures on the propagation speed of the Madden–Julian oscillation, *Quarterly Journal of the Royal Meteorological Society*, **150**(758): pp. 334–354, doi:https://doi.org/10.1002/qj.4599.

Karney, C. F. F. (2022) GeographicLib. Version 2.0, https://geographiclib.sourceforge.io/C++/2.0.

Kawai, Y. and Wada, A. (2007) Diurnal sea surface temperature variation and its impact on the atmosphere and ocean: A review, *Journal of Oceanography*, **63**(5): pp. 721–744, ISSN 1573-868X, doi:10.1007/s10872-007-0063-0.

Kent, E. C. and Berry, D. I. (2005) Quantifying random measurement errors in Voluntary Observing Ships' meteorological observations, *International Journal of Climatology*, **25**(7): pp. 843–856, ISSN 1097-0088, doi:10.1002/joc.1167.

Kent, E. C., Woodruff, S. D., and Berry, D. I. (2007) Metadata from WMO Publication No. 47 and an Assessment of Voluntary Observing Ship Observation Heights in ICOADS, *Journal of Atmospheric and Oceanic Technology*, **24**(2): pp. 214–234, ISSN 0739-0572, 1520-0426, doi:10.1175/JTECH1949.1.

Kim, S.-B., Fukumori, I., and Lee, T. (2006) The Closure of the Ocean Mixed Layer Temperature Budget Using Level-Coordinate Model Fields, *Journal of Atmospheric and Oceanic Technology*, **23**(6): pp. 840–853, ISSN 0739-0572, 1520-0426, doi:10.1175/JTECH1883.1.

Knio (2023) pynmea2: Python library for parsing the NMEA 0183 protocol. GitHub repository: https://github.com/Knio/pynmea2.

Kolodziejczyk, N. and Gaillard, F. (2013) Variability of the Heat and Salt Budget in the Subtropical Southeastern Pacific Mixed Layer between 2004 and 2010: Spice Injection Mechanism, *Journal of Physical Oceanography*, **43**(9): pp. 1880–1898, ISSN 0022-3670, 1520-0485, doi:10.1175/JPO-D-13-04.1.

Kum, B.-C., Shin, D.-H., Lee, J. H., Moh, T., Jang, S., Lee, S. Y., and Cho, J. H. (2018) Monitoring Applications for Multifunctional Unmanned Surface Vehicles in Marine Coastal Environments, *Journal of Coastal Research*, **85**(sp1): pp. 1381–1385, ISSN 0749-0208, 1551-5036, doi:10.2112/SI85-277.1.

Landwehr, S., O'Sullivan, N., and Ward, B. (2015) Direct Flux Measurements from Mobile Platforms at Sea: Motion and Airflow Distortion Corrections Revisited, *Journal of Atmospheric and Oceanic Technology*, **32**(6): pp. 1163–1178, ISSN 0739-0572, 1520-0426, doi:10.1175/JTECH-D-14-00137.1.

Lenain, L. and Melville, W. K. (2014) Autonomous Surface Vehicle Measurements of the Ocean's Response to Tropical Cyclone Freda, *Journal of Atmospheric and Oceanic Technology*, **31**(10): pp. 2169–2190, ISSN 0739-0572, 1520-0426, doi:10.1175/JTECH-D-14-00012.1.

L'Hégaret, P., Schütte, F., Speich, S., Reverdin, G., Baranowski, D. B., Czeschel, R., Fischer, T., Foltz, G. R., Heywood, K. J., Krahmann, G., Laxenaire, R., Le Bihan, C., Le Bot, P., Leizour, S., Rollo, C., Schlundt, M., Siddle, E., Subirade, C., Zhang, D., and Karstensen, J. (2023) Ocean cross-validated observations from R/Vs *L'Atalante*, *Maria S. Merian*, and *Meteor* and related platforms as part of the EUREC^{4}A-OA/ATOMIC campaign, *Earth System Science Data*, **15**(4): pp. 1801–1830, ISSN 1866-3508, doi:10.5194/essd-15-1801-2023. Publisher: Copernicus GmbH.

Li, J.-L. F., Xu, K.-M., Richardson, M., Jiang, J. H., Stephens, G., Lee, W.-L., Fetzer, E., Yu, J.-Y., Wang, Y.-H., and Wang, F.-J. (2021) Improved ice content, radiation, precipitation and low-level circulation over the tropical pacific from ECMWF ERA-interim to ERA5, *Environmental Research Communications*, **3**(8): p. 081,006, ISSN 2515-7620, doi:10.1088/2515-7620/ac1bfe.

Liu, H., Lin, W., and Zhang, M. (2010) Heat Budget of the Upper Ocean in the South-Central Equatorial Pacific, *Journal of Climate*, **23**(7): pp. 1779–1792, ISSN 0894-8755, 1520-0442, doi:10.1175/2009JCLI3135.1.

Liu, W. T., Katsaros, K. B., and Businger, J. A. (1979) Bulk Parameterization of Air-Sea Exchanges of Heat and Water Vapor Including the Molecular Constraints at the Interface, *Journal of the Atmospheric Sciences*, **36**(9): pp. 1722–1735, ISSN 0022-4928, 1520-0469, doi:10.1175/1520-0469(1979)036⟨1722:BPOASE⟩2.0.CO;2.

Liu, Y., He, R., and Lee, Z. (2021) Effects of Ocean Optical Properties and Solar Attenuation on the Northwestern Atlantic Ocean Heat Content and Hurricane Intensity, *Geophysical Research Letters*, **48**(13): p. e2021GL094,171, ISSN 1944-8007, doi:10.1029/2021GL094171.

Liu, Z., Zhang, Y., Yu, X., and Yuan, C. (2016) Unmanned surface vehicles: An overview of developments and challenges, *Annual Reviews in Control*, **41**: pp. 71–93, ISSN 1367-5788, doi:https://doi.org/10.1016/j.arcontrol.2016.04.018.

Long, C., Bucholtz, A., Jonsson, H., Schmid, B., Vogelmann, A., and Wood, J. (2010) A Method of Correcting for Tilt from Horizontal in Downwelling Shortwave Irradiance Measurements on Moving Platforms, *The Open Atmospheric Science Journal*, **4**: pp. 78–87, doi:10.2174/1874282301004010078.

Lotliker, A. A., Omand, M. M., Lucas, A. J., Laney, S. R., and Mahadevan, A. (2016) Penetrative Radiative Flux in the Bay of Bengal, *Oceanography*, **29**(2): pp. 214–221, doi:10.5670/oceanog.2016.53.

Lukas, R. and Lindstrom, E. (1991) The mixed layer of the western equatorial Pacific Ocean, *Journal of Geophysical Research: Oceans*, **96**(S01): pp. 3343–3357, ISSN 2156-2202, doi:10.1029/90JC01951.

Madden, R. A. and Julian, P. R. (1971) Detection of a 40–50 Day Oscillation in the Zonal Wind in the Tropical Pacific, *Journal of the Atmospheric Sciences*, **28**(5): pp. 702–708, ISSN 0022-4928, 1520-0469, doi:10.1175/1520-0469(1971)028⟨0702:DOADOI⟩2.0.CO;2.

Mainelli, M., DeMaria, M., Shay, L. K., and Goni, G. (2008) Application of Oceanic Heat Content Estimation to Operational Forecasting of Recent Atlantic Category 5 Hurricanes, *Weather and Forecasting*, **23**(1): pp. 3–16, ISSN 1520-0434, 0882-8156, doi:10.1175/2007WAF2006111.1.

Matthews, A. J. (2004) Atmospheric response to observed intraseasonal tropical sea surface temperature anomalies, *Geophysical Research Letters*, **31**(14), ISSN 1944-8007, doi:10.1029/2004GL020474.

Matthews, A. J., Baranowski, D. B., Heywood, K. J., Flatau, P. J., and Schmidtko, S. (2014) The Surface Diurnal Warm Layer in the Indian Ocean during CINDY/DYNAMO, *Journal of Climate*, **27**(24): pp. 9101–9122, doi:10.1175/JCLI-D-14-00222.1.

May, R. M., Goebbert, K. H., Thielen, J. E., Leeman, J. R., Camron, M. D., Bruick, Z., Bruning, E. C., Manser, R. P., Arms, S. C., and Marsh, P. T. (2022) MetPy: A Meteorological Python Library for Data Analysis and Visualization, *Bulletin of the American Meteorological Society*, **103**(10): pp. E2273 – E2284, doi:10.1175/BAMS-D-21-0125.1.

McDougall, T. and Barker, P. (2011) Getting started with TEOS-10 and the Gibbs Seawater (GSW) Oceanographic Toolbox, 28pp., SCOR/IAPSO WG127,.

McKinney, W. (2010) Data Structures for Statistical Computing in Python, *in* S. v. d. Walt and J. Millman (Editors), *Proceedings of the 9th Python in Science Conference*, pp. 51 – 56.

McPhaden, M. J. (2002) Mixed Layer Temperature Balance on Intraseasonal Timescales in the Equatorial Pacific Ocean, *Journal of Climate*, **15**(18): pp. 2632 – 2647, doi:https://doi.org/10.1175/1520-0442(2002)015⟨2632:MLTBOI⟩2.0.CO;2.

Met Office (2010) *Cartopy: a cartographic python library with a Matplotlib interface*, Exeter, Devon.

Mignot, J., de Boyer Montégut, C., Lazar, A., and Cravatte, S. (2007) Control of salinity on the mixed layer depth in the world ocean: 2. Tropical areas, *Journal of Geophysical Research: Oceans*, **112**(C10), ISSN 2156-2202, doi:10.1029/2006JC003954.

Mignot, J., Lazar, A., and Lacarra, M. (2012) On the formation of barrier layers and associated vertical temperature inversions: A focus on the northwestern tropical Atlantic, *Journal of Geophysical Research: Oceans*, **117**(C2), ISSN 2156-2202, doi: 10.1029/2011JC007435.

Moisan, J. R. and Niiler, P. P. (1998) The Seasonal Heat Budget of the North Pacific: Net Heat Flux and Heat Storage Rates (1950–1990), *Journal of Physical Oceanography*, **28**(3): pp. 401–421, ISSN 0022-3670, 1520-0485, doi:10.1175/1520-0485(1998)028⟨0401:TSHBOT⟩2.0.CO;2.

Monin, A. S. and Obukhov, A. M. (1954) Basic laws of turbulent mixing in the surface layer of the atmosphere, *Tr. Geofiz. Inst., Akad. Nauk SSSR*, **151**: pp. 163–187.

Monterey, 1954-1999, G. I. and Levitus, S. (1997) Seasonal variability of mixed layer depth for the world ocean.

Morel, A. (1988) Optical modeling of the upper ocean in relation to its biogenous matter content (case I waters), *Journal of Geophysical Research: Oceans*, **93**(C9): pp. 10,749–10,768, ISSN 2156-2202, doi:10.1029/JC093iC09p10749.

Mujumdar, M., Salunke, K., Rao, S. A., Ravichandran, M., and Goswami, B. N. (2011) Diurnal Cycle Induced Amplification of Sea Surface Temperature Intraseasonal Oscillations Over the Bay of Bengal in Summer Monsoon Season, *IEEE Geoscience and Remote Sensing Letters*, **8**(2): pp. 206–210, ISSN 1558-0571, doi:10.1109/LGRS.2010.2060183.

Nagamani, P. V., Ali, M. M., Goni, G. J., Pedro, D. N., Pezzullo, J. C., Udaya Bhaskar, T. V. S., Gopalakrishna, V. V., and Kurian, N. (2012) Validation of satellite-derived tropical cyclone heat potential with in situ observations in the North Indian Ocean, *Remote Sensing Letters*, **3**(7): pp. 615–620, ISSN 2150-704X, doi:10.1080/01431161.2011.640959.

Nagano, A., Geng, B., Richards, K. J., Cronin, M. F., Taniguchi, K., Katsumata, M., and Ueki, I. (2022) Coupled Atmosphere–Ocean Variations on Timescales of Days Observed in the Western Tropical Pacific Warm Pool During Mid-March 2020, *Journal of Geophysical Research: Oceans*, **127**(10): p. e2022JC019,032, ISSN 2169-9291, doi: 10.1029/2022JC019032.

NASA Worldview Snapshots (2020) NASA Worldview Snapshots. (https://worldview.earthdata.nasa.gov/) Accessed (2025-02-13).

Neelin, J. D., Battisti, D. S., Hirst, A. C., Jin, F.-F., Wakata, Y., Yamagata, T., and Zebiak, S. E. (1998) ENSO theory, *Journal of Geophysical Research: Oceans*, **103**(C7): pp. 14,261–14,290, ISSN 2156-2202, doi:10.1029/97JC03424.

Nemoto, Y. (2024) Navigation safety of Maritime Autonomous Surface Ships, *Australian Journal of Maritime & Ocean Affairs*, **0**(0): pp. 1–15, ISSN 1836-6503, doi:10.1080/18366503.2024.2393480.

Nicholson, S.-A., Whitt, D. B., Fer, I., du Plessis, M. D., Lebéhot, A. D., Swart, S., Sutton, A. J., and Monteiro, P. M. S. (2022) Storms drive outgassing of CO2 in the subpolar Southern Ocean, *Nature Communications*, **13**(1): p. 158, ISSN 2041-1723, doi:10.1038/s41467-021-27780-w.

Niiler, P. and Stevenson, J. (1982) The heat budget of tropical ocean warm-water pools, *Journal of Marine Research*, **40**(S).

Nogueira Neto, A. V., Giordani, H., Caniaux, G., and Araujo, M. (2018) Seasonal and Interannual Mixed-Layer Heat Budget Variability in the Western Tropical Atlantic From Argo Floats (2007–2012), *Journal of Geophysical Research: Oceans*, **123**(8): pp. 5298–5322, ISSN 2169-9291, doi:10.1029/2017JC013436.

Olivier, L., Boutin, J., Reverdin, G., Lefèvre, N., Landschützer, P., Speich, S., Karstensen, J., Labaste, M., Noisel, C., Ritschel, M., Steinhoff, T., and Wanninkhof, R. (2022) Wintertime process study of the North Brazil Current rings reveals the region as a larger sink for CO_2 than expected, *Biogeosciences*, **19**(12): pp. 2969–2988, ISSN 1726-4170, doi:10.5194/bg-19-2969-2022.

Osen, O. L., Liavåg, S. O., Sætre, L. E., Morken, O., and Zhang, H. (2019) Integration and Performance Study of Full Functional Sea Farm Inspection Platform for Aquaculture Application, *in OCEANS 2019 MTS/IEEE SEATTLE*, pp. 1–9, doi:10.23919/OCEANS40490.2019.8962801. ISSN: 0197-7385.

Pailler, K., Bourlès, B., and Gouriou, Y. (1999) The barrier layer in the western tropical Atlantic Ocean, *Geophysical Research Letters*, **26**(14): pp. 2069–2072, ISSN 1944-8007, doi:10.1029/1999GL900492.

Patterson, R. G., Cronin, M. F., Swart, S., Beja, J., Edholm, J. M., McKenna, J., Palter, J. B., Parker, A., Addey, C. I., Boone, W., Bhuyan, P., Buck, J. J. H., Burger, E. F., Burris, J., Camus, L., de Young, B., du Plessis, M., Flanigan, M., Foltz, G. R., Gille, S. T., Grare, L., Hansen, J. E., Hole, L. R., Honda, M. C., Hormann, V., Kohlman, C., Kosaka, N., Kuhn, C., Lenain, L., Looney, L., Marouchos, A., McGeorge, E. K., McMahon, C. R., Mitarai, S., Mordy, C., Nagano, A., Nicholson, S.-A., Nickford, S., O'Brien, K. M., Peddie, D., Ponsoni, L., Ramasco, V., Rozenauers, N., Siddle, E., Stienbarger, C., Sutton, A. J., Tada, N., Thomson, J., Ueki, I., Yu, L., Zhang, C., and Zhang, D. (2025) Uncrewed surface vehicles in the Global Ocean Observing System: a new frontier for observing and monitoring at the air-sea interface, *Frontiers in Marine Science*, **Volume 12 - 2025**, ISSN 2296-7745, doi:10.3389/fmars.2025.1523585.

Patterson, R. G., Lawson, E., Udyawer, V., Brassington, G. B., Groom, R. A., and Campbell, H. A. (2022) Uncrewed Surface Vessel Technological Diffusion Depends on Cross-Sectoral Investment in Open-Ocean Archetypes: A Systematic Review of USV Applications and Drivers, *Frontiers in Marine Science*, **8**, ISSN 2296-7745, doi:10.3389/fmars.2021.736984.

Payne, R. E. (1972) Albedo of the Sea Surface, *Journal of the Atmospheric Sciences*, **29**(5): pp. 959–970, ISSN 0022-4928, doi:10.1175/1520-0469(1972)029⟨0959:AOTSS⟩2.0.CO;2.

Pedregosa, F., Varoquaux, G., Gramfort, A., Michel, V., Thirion, B., Grisel, O., Blondel, M., Prettenhofer, P., Weiss, R., Dubourg, V., Vanderplas, J., Passos, A., Cournapeau, D., Brucher, M., Perrot, M., and Duchesnay, E. (2011) Scikit-learn: Machine Learning in Python, *Journal of Machine Learning Research*, **12**: pp. 2825–2830.

Peter, A.-C., Le Hénaff, M., du Penhoat, Y., Menkes, C. E., Marin, F., Vialard, J., Caniaux, G., and Lazar, A. (2006) A model study of the seasonal mixed layer heat budget in the equatorial Atlantic, *Journal of Geophysical Research: Oceans*, **111**(C6), ISSN 2156-2202, doi:10.1029/2005JC003157.

Philander, S. (2001) Atlantic Ocean Equatorial Currents, *in Encyclopedia of Ocean Sciences*, pp. 188–191, Elsevier, doi:10.1006/rwos.2001.0361.

Pinker, R. T., Bentamy, A., Grodsky, S. A., and Chen, W. (2020) Annual and seasonal variability of net heat flux in the Northern Indian Ocean, *International Journal of Remote Sensing*, **41**(17): pp. 6461–6483, ISSN 0143-1161, doi:10.1080/01431161.2020.1746858.

Pokhrel, S., Dutta, U., Rahaman, H., Chaudhari, H., Hazra, A., Saha, S. K., and Veeranjaneyulu, C. (2020) Evaluation of Different Heat Flux Products Over the Tropical Indian Ocean, *Earth and Space Science*, **7**(6): p. e2019EA000,988, ISSN 2333-5084, doi:10.1029/2019EA000988.

Prakash, K. R., Pant, V., and Nigam, T. (2019) Effects of the Sea Surface Roughness and Sea Spray-Induced Flux Parameterization on the Simulations of a Tropical Cyclone, *Journal* *of Geophysical Research: Atmospheres*, **124**(24): pp. 14,037–14,058, ISSN 2169-8996, doi:10.1029/2018JD029760.

Price, J. F., Weller, R. A., and Pinkel, R. (1986) Diurnal cycling: Observations and models of the upper ocean response to diurnal heating, cooling, and wind mixing, *Journal of Geophysical Research: Oceans*, **91**(C7): pp. 8411–8427, ISSN 0148-0227, doi:10.1029/JC091iC07p08411.

Quinn, P. K., Thompson, E. J., Coffman, D. J., Baidar, S., Bariteau, L., Bates, T. S., Bigorre, S., Brewer, A., de Boer, G., de Szoeke, S. P., Drushka, K., Foltz, G. R., Intrieri, J., Iyer, S., Fairall, C. W., Gaston, C. J., Jansen, F., Johnson, J. E., Krüger, O. O., Marchbanks, R. D., Moran, K. P., Noone, D., Pezoa, S., Pincus, R., Plueddemann, A. J., Pöhlker, M. L., Pöschl, U., Quinones Melendez, E., Royer, H. M., Szczodrak, M., Thomson, J., Upchurch, L. M., Zhang, C., Zhang, D., and Zuidema, P. (2021) Measurements from the RV *Ronald H. Brown* and related platforms as part of the Atlantic Tradewind Ocean-Atmosphere Mesoscale Interaction Campaign (ATOMIC), *Earth System Science Data*, **13**(4): pp. 1759–1790, ISSN 1866-3508, doi:10.5194/essd-13-1759-2021.

Reagan, J. R., Garcia, H. E., Boyer, T. P., Baranova, O. K., Bouchard, C., Cross, S. L., Dukhovskoy, D., Grodsky, A., Locarnini, R. A., Mishonov, A. V., Paver, C. R., Seidov, D., and Wang, Z. (2024) World Ocean Atlas 2023: Product Documentation, Technical Report, NOAA National Centers for Environmental Information.

Reagan, J. R., García, H. E., Boyer, T. P., Baranova, O. K., Bouchard, C., Cross, S. L., Dukhovskoy, D., Grodsky, A., Locarnini, R. A., Mishonov, A. V., Paver, C. R., Seidov, D., and Wang, Z. (2023) World Ocean Atlas. 2023 (NCEI Accession 0270533). [Salinity]. NOAA National Centers for Environmental Information. Dataset. https://www.ncei.noaa.gov/archive/accession/0270533. Accessed 25/06/2024.

Reed, R. K. (1977) On Estimating Insolation over the Ocean, *Journal of Physical Oceanography*, **7**(3): pp. 482–485, ISSN 0022-3670, 1520-0485, doi:10.1175/1520-0485(1977)007⟨0482:OEIOTO⟩2.0.CO;2.

Ren, L. and Riser, S. C. (2009) Seasonal salt budget in the northeast Pacific Ocean, *Journal of Geophysical Research: Oceans*, **114**(C12), ISSN 2156-2202, doi:10.1029/2009JC005307.

Reshma, M. and Singh, K. (2024) Role of PBL and air-sea flux parameterization schemes in the forecast of super cyclone Amphan and ESCS Phailin in the cloud-resolving scale using

WRF-ARW model, *Modeling Earth Systems and Environment*, **10**(4): pp. 5449–5467, doi: 10.1007/s40808-024-02072-6.

Riihimaki, L. D., Cronin, M. F., Acharya, R., Anderson, N., Augustine, J. A., Balmes, K. A., Berk, P., Bozzano, R., Bucholtz, A., Connell, K. J., Cox, C. J., di Sarra, A. G., Edson, J., Fairall, C. W., Farrar, J. T., Grissom, K., Guerra, M. T., Hormann, V., Joseph, K. J., Lanconelli, C., Melin, F., Meloni, D., Ottaviani, M., Pensieri, S., Ramesh, K., Rutan, D., Samarinas, N., Smith, S. R., Swart, S., Tandon, A., Thompson, E. J., Venkatesan, R., Verma, R. K., Vitale, V., Watkins-Brandt, K. S., Weller, R. A., Zappa, C. J., and Zhang, D. (2024) Ocean surface radiation measurement best practices, *Frontiers in Marine Science*, **11**, ISSN 2296-7745, doi:10.3389/fmars.2024.1359149.

Roberts, C. D., Palmer, M. D., Allan, R. P., Desbruyeres, D. G., Hyder, P., Liu, C., and Smith, D. (2017) Surface flux and ocean heat transport convergence contributions to seasonal and interannual variations of ocean heat content, *Journal of Geophysical Research: Oceans*, **122**(1): pp. 726–744, ISSN 2169-9291, doi:10.1002/2016JC012278.

Rodríguez, E., Bourassa, M., Chelton, D., Farrar, J. T., Long, D., Perkovic-Martin, D., and Samelson, R. (2019) The Winds and Currents Mission Concept, *Frontiers in Marine Science*, **6**, ISSN 2296-7745, doi:10.3389/fmars.2019.00438.

Roemmich, D., Alford, M. H., Claustre, H., Johnson, K., King, B., Moum, J., Oke, P., Owens, W. B., Pouliquen, S., Purkey, S., Scanderbeg, M., Suga, T., Wijffels, S., Zilberman, N., Bakker, D., Baringer, M., Belbeoch, M., Bittig, H. C., Boss, E., Calil, P., Carse, F., Carval, T., Chai, F., Conchubhair, D. , d'Ortenzio, F., Dall'Olmo, G., Desbruyeres, D., Fennel, K., Fer, I., Ferrari, R., Forget, G., Freeland, H., Fujiki, T., Gehlen, M., Greenan, B., Hallberg, R., Hibiya, T., Hosoda, S., Jayne, S., Jochum, M., Johnson, G. C., Kang, K., Kolodziejczyk, N., Körtzinger, A., Traon, P.-Y. L., Lenn, Y.-D., Maze, G., Mork, K. A., Morris, T., Nagai, T., Nash, J., Garabato, A. N., Olsen, A., Pattabhi, R. R., Prakash, S., Riser, S., Schmechtig, C., Schmid, C., Shroyer, E., Sterl, A., Sutton, P., Talley, L., Tanhua, T., Thierry, V., Thomalla, S., Toole, J., Troisi, A., Trull, T. W., Turton, J., Velez-Belchi, P. J., Walczowski, W., Wang, H., Wanninkhof, R., Waterhouse, A. F., Waterman, S., Watson, A., Wilson, C., Wong, A. P. S., Xu, J., and Yasuda, I. (2019) On the Future of Argo: A Global, Full-Depth, Multi-Disciplinary Array, *Frontiers in Marine Science*, **6**, ISSN 2296-7745, doi:10.3389/fmars.2019.00439.

Rollo, C., Heywood, K. J., and Hall, R. A. (2022) Glider observations of thermohaline staircases in the tropical North Atlantic using an automated classifier, *Geoscientific*

Instrumentation, Methods and Data Systems, **11**(2): pp. 359–373, ISSN 2193-0856, doi:10.5194/gi-11-359-2022.

Rudnick, D. L. (2016) Ocean Research Enabled by Underwater Gliders, *Annual Review of Marine Science*, **8**(Volume 8, 2016): pp. 519–541, ISSN 1941-1405, 1941-0611, doi:10.1146/annurev-marine-122414-033913.

Saha, A., Serra, N., and Stammer, D. (2021) Growth and Decay of Northwestern Tropical Atlantic Barrier Layers, *Journal of Geophysical Research: Oceans*, **126**(5): p. e2020JC016,956, ISSN 2169-9291, doi:10.1029/2020JC016956.

Sanchez-Franks, A., Kent, E. C., Matthews, A. J., Webber, B. G. M., Peatman, S. C., and Vinayachandran, P. N. (2018) Intraseasonal Variability of Air–Sea Fluxes over the Bay of Bengal during the Southwest Monsoon, *Journal of Climate*, **31**(17): pp. 7087–7109, ISSN 0894-8755, 1520-0442, doi:10.1175/JCLI-D-17-0652.1.

Scannell, H. A. and McPhaden, M. J. (2018) Seasonal Mixed Layer Temperature Balance in the Southeastern Tropical Atlantic, *Journal of Geophysical Research: Oceans*, **123**(8): pp. 5557–5570, ISSN 2169-9291, doi:10.1029/2018JC014099.

Seo, H., O'Neill, L. W., Bourassa, M. A., Czaja, A., Drushka, K., Edson, J. B., Fox-Kemper, B., Frenger, I., Gille, S. T., Kirtman, B. P., Minobe, S., Pendergrass, A. G., Renault, L., Roberts, M. J., Schneider, N., Small, R. J., Stoffelen, A., and Wang, Q. (2023) Ocean Mesoscale and Frontal-Scale Ocean–Atmosphere Interactions and Influence on Large-Scale Climate: A Review, *Journal of Climate*, **36**(7): pp. 1981–2013, ISSN 0894-8755, 1520-0442, doi:10.1175/JCLI-D-21-0982.1.

Seo, H., Subramanian, A. C., Song, H., and Chowdary, J. S. (2019) Coupled effects of ocean current on wind stress in the Bay of Bengal: Eddy energetics and upper ocean stratification, *Deep-Sea Research Part II: Topical Studies in Oceanography*, ISSN 09670645, doi:10.1016/j.dsr2.2019.07.005.

Sheehan, P. M. F., Damerell, G. M., Leadbitter, P. J., Heywood, K. J., and Hall, R. A. (2023) Turbulent kinetic energy dissipation rate and associated fluxes in the western tropical Atlantic estimated from ocean glider observations, *Ocean Science*, **19**(1): pp. 77–92, ISSN 1812-0784, doi:10.5194/os-19-77-2023.

Siddle, E., Heywood, K. J., Webber, B. G. M., and Bromley, P. (2021) First measurements of ocean and atmosphere in the Tropical North Atlantic using Caravela, a novel uncrewed surface vessel, *Weather*, **76**(6): pp. 200–204, doi:https://doi.org/10.1002/wea.4004.

Sivam, S., Zhang, C., Zhang, D., Yu, L., and Dressel, I. (2024) Surface latent and sensible heat fluxes over the Pacific Sub-Arctic Ocean from saildrone observations and three global reanalysis products, *Frontiers in Marine Science*, **11**, ISSN 2296-7745, doi:10.3389/fmars.2024.1431718.

Smith, S. D. (1988) Coefficients for sea surface wind stress, heat flux, and wind profiles as a function of wind speed and temperature, *Journal of Geophysical Research: Oceans*, **93**(C12): pp. 15,467–15,472, ISSN 2156-2202, doi:10.1029/JC093iC12p15467.

Soloviev, A. and Lukas, R. (1997) Observation of large diurnal warming events in the near-surface layer of the western equatorial Pacific warm pool, *Deep Sea Research Part I: Oceanographic Research Papers*, **44**(6): pp. 1055–1076, ISSN 0967-0637, doi:10.1016/S0967-0637(96)00124-0.

Song, X. (2020) The Importance of Relative Wind Speed in Estimating Air–Sea Turbulent Heat Fluxes in Bulk Formulas: Examples in the Bohai Sea, *Journal of Atmospheric and Oceanic Technology*, **37**(4): pp. 589–603, ISSN 0739-0572, 1520-0426, doi:10.1175/JTECH-D-19-0091.1.

Sprintall, J. and Tomczak, M. (1992) Evidence of the barrier layer in the surface layer of the tropics, *Journal of Geophysical Research: Oceans*, **97**(C5): pp. 7305–7316, ISSN 2156-2202, doi:10.1029/92JC00407.

Starkenburg, D., Metzger, S., Fochesatto, G. J., Alfieri, J. G., Gens, R., Prakash, A., and Cristóbal, J. (2016) Assessment of Despiking Methods for Turbulence Data in Micrometeorology, *Journal of Atmospheric and Oceanic Technology*, **33**(9): pp. 2001 – 2013, doi:10.1175/JTECH-D-15-0154.1.

Stevens, B., Bony, S., Brogniez, H., Hentgen, L., Hohenegger, C., Kiemle, C., L'Ecuyer, T. S., Naumann, A. K., Schulz, H., Siebesma, P. A., Vial, J., Winker, D. M., and Zuidema, P. (2020) Sugar, gravel, fish and flowers: Mesoscale cloud patterns in the trade winds, *Quarterly Journal of the Royal Meteorological Society*, **146**(726): pp. 141–152, ISSN 1477-870X, doi:10.1002/qj.3662.

Stevens, B., Bony, S., Farrell, D., Ament, F., Blyth, A., Fairall, C., Karstensen, J., Quinn, P. K., Speich, S., Acquistapace, C., Aemisegger, F., Albright, A. L., Bellenger, H., Bodenschatz, E., Caesar, K.-A., Chewitt-Lucas, R., de Boer, G., Delanoë, J., Denby, L., Ewald, F., Fildier, B., Forde, M., George, G., Gross, S., Hagen, M., Hausold, A., Heywood, K. J., Hirsch, L., Jacob, M., Jansen, F., Kinne, S., Klocke, D., Kölling, T., Konow, H., Lothon, M., Mohr, W., Naumann, A. K., Nuijens, L., Olivier, L., Pincus, R., Pöhlker, M., Reverdin, G., Roberts, G., Schnitt, S., Schulz, H., Siebesma, A. P., Stephan, C. C., Sullivan, P., Touzé-Peiffer, L., Vial, J., Vogel, R., Zuidema, P., Alexander, N., Alves, L., Arixi, S., Asmath, H., Bagheri, G., Baier, K., Bailey, A., Baranowski, D., Baron, A., Barrau, S., Barrett, P. A., Batier, F., Behrendt, A., Bendinger, A., Beucher, F., Bigorre, S., Blades, E., Blossey, P., Bock, O., Böing, S., Bosser, P., Bourras, D., Bouruet-Aubertot, P., Bower, K., Branellec, P., Branger, H., Brennek, M., Brewer, A., Brilouet, P.-E., Brügmann, B., Buehler, S. A., Burke, E., Burton, R., Calmer, R., Canonici, J.-C., Carton, X., Cato Jr., G., Charles, J. A., Chazette, P., Chen, Y., Chilinski, M. T., Choularton, T., Chuang, P., Clarke, S., Coe, H., Cornet, C., Coutris, P., Couvreux, F., Crewell, S., Cronin, T., Cui, Z., Cuypers, Y., Daley, A., Damerell, G. M., Dauhut, T., Deneke, H., Desbios, J.-P., Dörner, S., Donner, S., Douet, V., Drushka, K., Dütsch, M., Ehrlich, A., Emanuel, K., Emmanouilidis, A., Etienne, J.-C., Etienne-Leblanc, S., Faure, G., Feingold, G., Ferrero, L., Fix, A., Flamant, C., Flatau, P. J., Foltz, G. R., Forster, L., Furtuna, I., Gadian, A., Galewsky, J., Gallagher, M., Gallimore, P., Gaston, C., Gentemann, C., Geyskens, N., Giez, A., Gollop, J., Gouirand, I., Gourbeyre, C., de Graaf, D., de Groot, G. E., Grosz, R., Güttler, J., Gutleben, M., Hall, K., Harris, G., Helfer, K. C., Henze, D., Herbert, C., Holanda, B., Ibanez-Landeta, A., Intrieri, J., Iyer, S., Julien, F., Kalesse, H., Kazil, J., Kellman, A., Kidane, A. T., Kirchner, U., Klingebiel, M., Körner, M., Kremper, L. A., Kretzschmar, J., Krüger, O., Kumala, W., Kurz, A., L'Hégaret, P., Labaste, M., Lachlan-Cope, T., Laing, A., Landschützer, P., Lang, T., Lange, D., Lange, I., Laplace, C., Lavik, G., Laxenaire, R., Le Bihan, C., Leandro, M., Lefevre, N., Lena, M., Lenschow, D., Li, Q., Lloyd, G., Los, S., Losi, N., Lovell, O., Luneau, C., Makuch, P., Malinowski, S., Manta, G., Marinou, E., Marsden, N., Masson, S., Maury, N., Mayer, B., Mayers-Als, M., Mazel, C., McGeary, W., McWilliams, J. C., Mech, M., Mehlmann, M., Meroni, A. N., Mieslinger, T., Minikin, A., Minnett, P., Möller, G., Morfa Avalos, Y., Muller, C., Musat, I., Napoli, A., Neuberger, A., Noisel, C., Noone, D., Nordsiek, F., Nowak, J. L., Oswald, L., Parker, D. J., Peck, C., Person, R., Philippi, M., Plueddemann, A., Pöhlker, C., Pörtge, V., Pöschl, U., Pologne, L., Posyniak, M., Prange, M., Quiñones Meléndez, E., Radtke, J., Ramage, K., Reimann, J., Renault, L., Reus, K., Reyes, A., Ribbe, J., Ringel, M., Ritschel, M., Rocha, C. B., Rochetin, N., Röttenbacher, J., Rollo, C., Royer, H., Sadoulet, P., Saffin, L., Sandiford, S., Sandu, I., Schäfer, M., Schemann, V., Schirmacher, I., Schlenczek, O., Schmidt, J., Schröder, M., Schwarzenboeck, A., Sealy, A., Senff, C. J., Serikov, I., Shohan, S., Siddle, E., Smirnov, A., Späth, F., Spooner, B., Stolla, M. K., Szkó\lka, W., de Szoeke, S. P., Tarot, S., Tetoni, E., Thompson, E., Thomson, J., Tomassini, L., Totems, J., Ubele,

A. A., Villiger, L., von Arx, J., Wagner, T., Walther, A., Webber, B., Wendisch, M., Whitehall, S., Wiltshire, A., Wing, A. A., Wirth, M., Wiskandt, J., Wolf, K., Worbes, L., Wright, E., Wulfmeyer, V., Young, S., Zhang, C., Zhang, D., Ziemen, F., Zinner, T., and Zöger, M. (2021) EURECA, *Earth System Science Data*, **13**(8): pp. 4067–4119, doi:10.5194/essd-13-4067-2021.

Stevens, B., Farrell, D., Hirsch, L., Jansen, F., Nuijens, L., Serikov, I., Brügmann, B., Forde, M., Linne, H., Lonitz, K., and Prospero, J. M. (2016) The Barbados Cloud Observatory: Anchoring Investigations of Clouds and Circulation on the Edge of the ITCZ, *Bulletin of the American Meteorological Society*, **97**(5): pp. 787–801, ISSN 0003-0007, 1520-0477, doi:10.1175/BAMS-D-14-00247.1.

Stevenson, J. W. and Niiler, P. P. (1983) Upper Ocean Heat Budget During the Hawaii-to-Tahiti Shuttle Experiment, *Journal of Physical Oceanography*, **13**(10): pp. 1894 – 1907, doi:https://doi.org/10.1175/1520-0485(1983)013⟨1894:UOHBDT⟩2.0.CO;2.

Swart, S., Gille, S. T., Delille, B., Josey, S., Mazloff, M., Newman, L., Thompson, A. F., Thomson, J., Ward, B., Du Plessis, M. D., Kent, E. C., Girton, J., Gregor, L., Petra, H., Hyder, P., Pezzi, L. P., De Souza, R. B., Tamsitt, V., Weller, R. A., and Zappa, C. J. (2019) Constraining Southern ocean air-sea-ice fluxes through enhanced observations, *Frontiers in Marine Science*, **6**(JUL): pp. 1–10, ISSN 22967745, doi:10.3389/fmars.2019.00421.

Swenson, M. S. and Hansen, D. V. (1999) Tropical Pacific Ocean Mixed Layer Heat Budget: The Pacific Cold Tongue, *Journal of Physical Oceanography*, **29**(1): pp. 69–81, ISSN 0022-3670, 1520-0485, doi:10.1175/1520-0485(1999)029⟨0069:TPOMLH⟩2.0.CO;2.

Tada, N., Nagano, A., Tanaka, S., Ichihara, H., Suetsugu, D., Matsuoka, D., Ito, M., Kuwatani, T., and Honda, M. C. (2024) Challenge for multifaceted data acquisition around active volcanoes using uncrewed surface vessel, *Frontiers in Marine Science*, **11**, ISSN 2296-7745, doi:10.3389/fmars.2024.1406381.

Tanguy, Y., Arnault, S., and Lattes, P. (2010) Isothermal, mixed, and barrier layers in the subtropical and tropical Atlantic Ocean during the ARAMIS experiment, *Deep Sea Research Part I: Oceanographic Research Papers*, **57**(4): pp. 501–517, ISSN 0967-0637, doi:10.1016/j.dsr.2009.12.012.

Thomson, J. and Girton, J. (2017) Sustained Measurements of Southern Ocean Air-Sea Coupling from a Wave Glider Autonomous Surface Vehicle, *Oceanography*, **30**(2): pp. 104–109, ISSN 10428275, doi:10.5670/oceanog.2017.228.

Thyng, K. M., Greene, C. A., Hetland, R. D., Zimmerle, H. M., and DiMarco, S. F. (2016) True Colors of Oceanography: Guidelines for Effective and Accurate Colormap Selection, *Oceanography*, **29**(3): pp. 9–13, doi:10.5670/oceanog.2016.66.

Tilinina, N., Gavrikov, A., and Gulev, S. K. (2018) Association of the North Atlantic Surface Turbulent Heat Fluxes with Midlatitude Cyclones, *Monthly Weather Review*, **146**(11): pp. 3691–3715, ISSN 1520-0493, 0027-0644, doi:10.1175/MWR-D-17-0291.1.

Travis E. Oliphant (2006) *Guide to Numpy*. Http://archive.org/details/NumPyBook.

Treguier, A. M., de Boyer Montégut, C., Bozec, A., Chassignet, E. P., Fox-Kemper, B., McC. Hogg, A., Iovino, D., Kiss, A. E., Le Sommer, J., Li, Y., Lin, P., Lique, C., Liu, H., Serazin, G., Sidorenko, D., Wang, Q., Xu, X., and Yeager, S. (2023) The mixed-layer depth in the Ocean Model Intercomparison Project (OMIP): impact of resolving mesoscale eddies, *Geoscientific Model Development*, **16**(13): pp. 3849–3872, ISSN 1991-959X, doi: 10.5194/gmd-16-3849-2023.

Trolliet, M., Walawender, J. P., Bourlès, B., Boilley, A., Trentmann, J., Blanc, P., Lefèvre, M., and Wald, L. (2018) Downwelling surface solar irradiance in the tropical Atlantic Ocean: a comparison of re-analyses and satellite-derived data sets to PIRATA measurements, *Ocean Science*, **14**(5): pp. 1021–1056, ISSN 1812-0784, doi:10.5194/os-14-1021-2018.

Urraca, R., Huld, T., Gracia-Amillo, A., Martinez-de Pison, F. J., Kaspar, F., and Sanz-Garcia, A. (2018) Evaluation of global horizontal irradiance estimates from ERA5 and COSMO-REA6 reanalyses using ground and satellite-based data, *Solar Energy*, **164**: pp. 339–354, ISSN 0038-092X, doi:10.1016/j.solener.2018.02.059.

Vijith, V., Vinayachandran, P. N., Webber, B. G. M., and Matthews, A. J. (2020) Closing the sea surface mixed layer temperature budget from in situ observations alone : Operation Advection during BoBBLE, *Scientific Reports*, pp. 1–12, ISSN 2045-2322, doi:10.1038/s41598-020-63320-0.

Virmani, J. I. and Weisberg, R. H. (2003) Features of the Observed Annual Ocean–Atmosphere Flux Variability on the West Florida Shelf, *Journal of Climate*, **16**(4): pp. 734–745, ISSN 0894-8755, 1520-0442, doi:10.1175/1520-0442(2003)016⟨0734:FOTOAO⟩2.0.CO;2.

Virtanen, P., Gommers, R., Oliphant, T. E., Haberland, M., Reddy, T., Cournapeau, D., Burovski, E., Peterson, P., Weckesser, W., Bright, J., van der Walt, S. J., Brett, M., Wilson, J., Millman, K. J., Mayorov, N., Nelson, A. R. J., Jones, E., Kern, R., Larson, E., Carey, C. J., Polat, , Feng, Y., Moore, E. W., VanderPlas, J., Laxalde, D., Perktold, J., Cimrman, R., Henriksen, I., Quintero, E. A., Harris, C. R., Archibald, A. M., Ribeiro, A. H., Pedregosa, F., van Mulbregt, P., and SciPy 1.0 Contributors (2020) SciPy 1.0: Fundamental Algorithms for Scientific Computing in Python, *Nature Methods*, **17**: pp. 261–272, doi:10.1038/s41592-019-0686-2.

Vogel, R., Albright, A. L., Vial, J., George, G., Stevens, B., and Bony, S. (2022) Strong cloud–circulation coupling explains weak trade cumulus feedback, *Nature*, **612**(7941): pp. 696–700, ISSN 1476-4687, doi:10.1038/s41586-022-05364-y.

Wallcraft, A. J., Kara, A. B., Barron, C. N., Metzger, E. J., Pauley, R. L., and Bourassa, M. A. (2009) Comparisons of monthly mean 10 m wind speeds from satellites and NWP products over the global ocean, *Journal of Geophysical Research: Atmospheres*, **114**(D16), ISSN 2156-2202, doi:10.1029/2008JD011696.

Wang, J. and Carton, J. A. (2002) Seasonal Heat Budgets of the North Pacific and North Atlantic Oceans, *Journal of Physical Oceanography*, **32**(12): pp. 3474–3489, ISSN 0022-3670, 1520-0485, doi:10.1175/1520-0485(2002)032⟨3474:SHBOTN⟩2.0.CO;2.

Wang, W. and McPhaden, M. J. (1999) The Surface-Layer Heat Balance in the Equatorial Pacific Ocean. Part I: Mean Seasonal Cycle, *Journal of Physical Oceanography*, **29**(8): pp. 1812–1831, ISSN 0022-3670, 1520-0485, doi:10.1175/1520-0485(1999)029⟨1812:TSLHBI⟩2.0.CO;2.

Waskom, M. L. (2021) seaborn: statistical data visualization, *Journal of Open Source Software*, **6**(60): p. 3021, doi:10.21105/joss.03021.

Weller, R. A., Lukas, R., Potemra, J., Plueddemann, A. J., Fairall, C., and Bigorre, S. (2022) Ocean Reference Stations: Long-Term, Open-Ocean Observations of Surface Meteorology and Air–Sea Fluxes Are Essential Benchmarks, *Bulletin of the American Meteorological Society*, **103**(8): pp. E1968 – E1990, doi:10.1175/BAMS-D-21-0084.1.

Wells, N. C., Josey, S. A., and Hadfield, R. E. (2009) Towards closure of regional heat budgets in the North Atlantic using Argo floats and surface flux datasets, *Ocean Science*, **5**(2): pp. 59–72, ISSN 1812-0792, doi:10.5194/os-5-59-2009.

Wen, C., Xue, Y., Kumar, A., Behringer, D., and Yu, L. (2017) How do uncertainties in NCEP R2 and CFSR surface fluxes impact tropical ocean simulations?, *Climate Dynamics*, **49**(9): pp. 3327–3344, ISSN 1432-0894, doi:10.1007/s00382-016-3516-6.

Wessel, P. and Smith, W. H. F. (1996) A global, self-consistent, hierarchical, high-resolution shoreline database, *Journal of Geophysical Research: Solid Earth*, **101**(B4): pp. 8741–8743, ISSN 2156-2202, doi:10.1029/96JB00104.

Wills, S. M., Cronin, M. F., and Zhang, D. (2023) Air-Sea Heat Fluxes Associated With Convective Cold Pools, *Journal of Geophysical Research: Atmospheres*, **128**(20): p. e2023JD039,708, ISSN 2169-8996, doi:10.1029/2023JD039708.

Wong, A., Robert, K., Carval, T., and Team, A. D. M. (2023) Argo Quality Control Manual for CTD and Trajectory Data, Technical report, doi:https://doi.org/10.13155/33951.

Yan, Y., Song, X., Wang, G., and Li, X. (2023) Tropical Cool-Skin and Warm-Layer Effects and Their Impact on Surface Heat Fluxes, *Journal of Physical Oceanography*, **54**(1): pp. 45–62, ISSN 0022-3670, 1520-0485, doi:10.1175/JPO-D-23-0103.1.

Yu, L. (2019) Global Air–Sea Fluxes of Heat, Fresh Water, and Momentum: Energy Budget Closure and Unanswered Questions, *Annual Review of Marine Science*, **11**(Volume 11, 2019): pp. 227–248, ISSN 1941-1405, 1941-0611, doi:10.1146/annurev-marine-010816-060704.

Yu, L., Jin, X., and Weller, R. A. (2006) Role of Net Surface Heat Flux in Seasonal Variations of Sea Surface Temperature in the Tropical Atlantic Ocean, *Journal of Climate*, **19**(23): pp. 6153–6169, ISSN 0894-8755, 1520-0442, doi:10.1175/JCLI3970.1.

Yu, L., Jin, X., and Weller, R. A. (2007) Annual, Seasonal, and Interannual Variability of Air–Sea Heat Fluxes in the Indian Ocean, *Journal of Climate*, **20**(13): pp. 3190–3209, ISSN 0894-8755, 1520-0442, doi:10.1175/JCLI4163.1.

Zaghi, S., Dubbioso, G., Broglia, R., and Muscari, R. (2016) Hydrodynamic Characterization of USV Vessels with Innovative SWATH Configuration for Coastal Monitoring and Low Environmental Impact, volume 14, pp. 1562–1570, doi:10.1016/j.trpro.2016.05.121.

Zhang, C., Foltz, G. R., Chiodi, A. M., Mordy, C. W., Edwards, C. R., Meinig, C., Zhang, D., Mazza, E., Cokelet, E. D., Burger, E. F., Bringas, F., Goni, G. J., Hristova, H. G., Kim, H.-S., Trinanes, J. A., Zhang, J. A., Bailey, K. E., O'Brien, K. M., Morales-Caez, M., Lawrence-Slavas, N., Jenkins, R., Chen, S. S., and Chen, X. (2023) Hurricane Observations by Uncrewed Systems, *Bulletin of the American Meteorological Society*, **104**(10): pp. E1893 – E1917, doi:10.1175/BAMS-D-21-0327.1.

Zhang, D., Cronin, M., Meing, C., Farrar, J. T., Jenkins, R., Peacock, D., Keene, J., Sutton, A., and Yang, Q. (2019) Comparing Air-Sea Flux Measurements from a New Unmanned

Surface Vehicle and Proven Platforms During the SPURS-2 Field Campaign, *Oceanography*, **32**(2): pp. 122–133, ISSN 10428275, doi:10.5670/oceanog.2019.220.

Zhang, H.-M., Reynolds, R. W., Lumpkin, R., Molinari, R., Arzayus, K., Johnson, M., and Smith, T. M. (2009) An Integrated Global Observing System For Sea Surface Temperature Using Satellites and in Situ Data: Research to Operations, *Bulletin of the American Meteorological Society*, **90**(1): pp. 31–38, ISSN 0003-0007, 1520-0477, doi: 10.1175/2008BAMS2577.1.

Zhang, H.-M., Reynolds, R. W., and Smith, T. M. (2004) Bias characteristics in the AVHRR sea surface temperature, *Geophysical Research Letters*, **31**(1), ISSN 1944-8007, doi:10.1029/2003GL018804.

Zheng, Y., Kiladis, G. N., Shinoda, T., Metzger, E. J., Hurlburt, H. E., Lin, J., and Giese, B. S. (2010) Upper-Ocean Processes under the Stratus Cloud Deck in the Southeast Pacific Ocean, *Journal of Physical Oceanography*, **40**(1): pp. 103–120, ISSN 1520-0485, 0022-3670, doi:10.1175/2009JPO4213.1.